Modelling of Berry phase and Fermi-level topologies for emergent quantum phenomena prediction in selected solid state systems

by

Gaël-Pacôme Nguimeya Tematio
Student number: NGMPAC001

Supervised by:

Dr. Trisha Salagaram
Department of Physics, University of Cape Town, South Africa.
Dr. Aniekan Magnus Ukpong
School of Chemistry & Physics, University of Kwazulu Natal, South Africa.

A thesis Submitted to the Faculty of Science in fulfilment of the requirements for the degree of Doctor of Philosophy in Physics.

Department of Physics
University of Cape Town
South Africa

December 2024

Declaration

I, **Gaël-Pacôme Nguimeya Tematio**, hereby declare that the work on which this thesis is based is my original work (except where acknowledgements indicate otherwise) and that neither the whole work nor any part of it has been, is being, or is to be submitted for another degree in this or any other university.

I empower the university to reproduce for the purpose of research either the whole or any portion of the contents in any manner whatsoever.

Signed by candidate

- - - - - - - - - - - - - - - - - -

Dedication

This work is dedicated to my father, Mr. Augustin Nguimeya Tchoutezem, and my mother, Mrs. Marthe Madeleine Dongmo Nguimeya, who have always believed in me and never stopped making sacrifices to help me learn and move forward. Their unwavering support and encouragement have been a constant source of strength and inspiration throughout my journey.

Acknowledgements

I extend my sincere gratitude to my supervisors, Dr. Trisha Salagaram and Dr. Aniekan Magnus Ukpong, for their invaluable guidance, assistance, and support throughout my PhD journey. I am deeply thankful to Prof. Layla Martin-Samos for her support, which greatly contributed to the successful progress of my thesis. I am particularly grateful to the University of Cape Town for offering me the opportunity to pursue this research, and to the Physics Department for providing a comfortable and supportive environment where I could focus on my work. I also express my sincere appreciation to the Center for High-Performance Computing (CHPC) South Africa for granting me access to the Lengau Supercomputer for my computations and for their continuous technical support during my research. Lastly, I am profoundly thankful to my family, especially my father, Mr. Augustin Nguimeya Tchoutezem, and my mother, Mrs. Marthe Madeleine Dongmo Nguimeya, for their unwavering support and encouragement despite being thousands of miles away. Their constant motivation and steadfast belief in me kept me going and gave me the strength to persevere.

List of Conferences and Schools Attended

I have participated in the following academic activities during my PhD:

1. **2 - 6 Dec. 2018**, *12th CHPC National Conference*, Century City Convention Centre, Cape Town, South Africa.
2. **10 - 20 Jun. 2019**, *Southern African School on Electronic Structure Methods and Applications (SASESMA 2019)*, Department of Physics, University of Pretoria, South Africa.
3. **1 - 5 Dec. 2019**, *13th CHPC National Conference*, Birchwood Conference Centre, Kempton Park, Johannesburg, South Africa.

Table of contents

List of Figures

List of Abbreviations

- **BZ :** **B**rillouin **Z**one
- **DOS :** **D**ensity **O**f **S**tates
- **BOA :** **B**orn-**O**ppenheimer **A**pproximation
- **HA :** **H**artree **A**pproximation
- **HP :** **H**artree **P**roduct
- **HF :** **H**artree-**F**ock
- **KS :** **K**ohn-**S**ham
- **DFT :** **D**ensity **F**unctional **T**heory
- **XC :** **E**xchange-**C**orrelation
- **LDA :** **L**ocal **D**ensity **A**pproximation
- **GGA :** **G**eneralized **G**radient **A**pproximation
- **GEA :** **G**radient **E**xpansion **A**pproximation
- **PAW :** **P**rojector **A**ugmented **W**ave
- **PBE :** **P**erdew, **B**urke, and **E**rnzerhof
- **SOC :** **S**pin-**O**rbit **C**oupling
- **KM SOC :** **K**ane-**M**ele **S**pin-**O**rbit **C**oupling

❐ **DSMs :** **D**irac **S**emimetals

❐ **WSMs :** **W**eyl **S**emimetals

❐ **QPTs :** **Q**uantum **P**hase **T**ransitions

❐ **TQPTs :** **T**opological **Q**uantum **P**hase **T**ransitions

❐ **TIs :** **T**opological **I**nsulators

❐ **QE :** **Q**uantum **E**SPRESSO

❐ **TB :** **T**ight-**B**inding

❐ **MLWFs :** **M**aximally **L**ocalized **W**annier **F**unctions

❐ **WCCs :** **W**annier **C**harge **C**enters

❐ **2D :** **T**wo-**D**imensional

❐ **3D :** **T**hree-**D**imensional

❐ **MR :** **M**agnetoresistance

❐ **dHvA :** **D**e **H**aas-**v**an **A**lphen

❐ **SdH :** **S**hubnikov-**d**e **H**aas

❐ **RSW :** **R**arita-**S**chwinger-**W**eyl

❐ **STM :** **S**canning **T**unneling **M**icroscopy

❐ **CVT :** **C**hemical **V**apor **T**ransport

❐ **FFTs :** **F**ast **F**ourier **T**ransforms

❐ **DMFT :** **D**ynamical **M**ean-**F**ield **T**heory

❐ **CPGE :** **C**ircular **P**hotogalvanic **E**ffect

❐ **ARPES :** **A**ngle-**R**esolved **P**hotoemission **S**pectroscopy

Abstract

Topological materials host electronic states that remain robust against perturbations and offer routes to novel quantum functions. This thesis investigates three representative compounds - $SrSi_2$, CoSi, and NbP - to reveal how external stimuli, namely tensile strain and electric fields, tune their electronic bands and topological traits. By combining first-principles calculations with model Hamiltonian experiments, we aim to uncover mechanisms behind quantum phase transitions (QPTs) and to establish design principles for materials with tailored quantum states. We perform density functional theory (DFT) calculations within the plane-wave pseudopotential framework using the Quantum ESPRESSO (QE) suite. Spin-orbit coupling (SOC) is included to capture relativistic effects critical for topological properties. We generate maximally localized Wannier functions (MLWFs) with Wannier90 and construct tight-binding (TB) models to compute Berry curvature, surface state spectra, and Fermi arc patterns via WannierTools. To probe QPTs in $SrSi_2$, we employ the Quantum Lattice environment to simulate a renormalized graphene lattice, mapping analogies between external perturbations and topological responses in both systems. In $SrSi_2$, a 12% tensile strain opens a small band gap of ~ 0.055 eV along the Γ - X path, shifting the semimetal toward reduced metallic conductivity. Applying an electric field of 0.51 V/Å lifts degeneracies at Weyl nodes and creates small band gaps between them. Further increasing the field to 1.29 V/Å expands the gap at the Fermi level to ~ 0.058 eV and redistributes the Berry curvature near the node locations. These results highlight precise control over topological transitions in $SrSi_2$ via combined mechanical and electric tuning. CoSi exhibits strong directional sensitivity to strain and field. A 10% tensile strain induces a gap of ~ 0.035 eV at the Γ point, while the R point remains gapless. Raising the strain to 15% widens the Γ gap to ~ 0.11 eV without affecting the R point. Under an electric field of 0.51 V/Å, a selective gap of ~ 0.02 eV opens at the R point, leaving Γ unchanged. At 1.29 V/Å, the R gap widens to ~ 0.065 eV. These findings demonstrate that CoSi's band structure and surface Fermi arcs can be tuned anisotropically, enabling region-specific control of electronic transport. In NbP, a 4% tensile strain generates a band gap of ~ 0.05 eV in the Γ - Σ direction, reducing carrier density at the Fermi energy. Increasing the strain to

8% yields a gap of ~ 0.035 eV around the Fermi level, further suppressing states near the Fermi level. Electric fields exert subtler effects: at 0.51 V/Å, the band curvature shifts slightly, while at 1.29 V/Å, a gap of ~ 0.02 eV opens in the Γ - S direction. This field-driven gap opening suggests switchable electronic phases and highlights NbP as a promising candidate for tunable topological devices. Our model experiments draw clear parallels between $SrSi_2$ under an electric field and renormalized graphene under external pertubations. In both cases, increasing the perturbation opens topology-related band gaps at high-symmetry points, driving transitions from semimetallic to insulating phases. By further varying Kane-Mele SOC (KM SOC) and exchange interactions in the renormalized graphene model, we observe successive topological transitions marked by band closures, inversions, and reopenings. These analogies underscore universal principles of quantum phase control and emphasize the broad applicability of our approach. In summary, we demonstrate that strain and external electric fields can precisely engineer electronic and topological properties in $SrSi_2$, CoSi, and NbP. The observed band gap tuning and Berry curvature modifications point to applications in quantum computing elements, adaptable electronic switches, and sensitive detectors. By bridging atomistic DFT calculations with model Hamiltonian simulations, this work lays a comprehensive foundation for designing materials with targeted topological characteristics and for exploring emergent quantum phenomena.

Chapter 1

Introduction

Topological materials have emerged as a pivotal area of study in condensed matter physics, characterized by their unique electronic properties that are robust against perturbations. These materials are defined by topological invariants in their electronic band structures, leading to protected surface states that remain conductive even when the bulk is insulating. This phenomenon is described using the mathematical framework of topology, which captures properties that remain unchanged under continuous deformations. In the context of materials science, topology provides a framework for understanding phases of matter that cannot be described by traditional symmetry-breaking theories. The significance of topological materials lies in their potential applications in quantum computing, spintronics, and low-power electronics, owing to their ability to host dissipationless edge or surface states[1].

The drive for a fundamental understanding of the physical properties of topological materials is at the frontier of condensed matter physics research. This interest stems from the broad range of materials in which topological features can be realized, enabling testable theories, operable experiments, and viable technological applications. The field of topological electronic materials, particularly topological insulators (TIs), has seen rapid progress, enhancing the potential for future electronic devices and technologies. These materials possess electronic structures with nontrivial topological properties that are robust and insensitive to environmental perturbations, making them an essential focus for both fundamental and applied research.

A prominent example of topological materials is Dirac materials, which include graphene and three-dimensional (3D) Dirac semimetals (DSMs). In these systems, the conduction and valence bands touch at discrete points, known as Dirac points, around which the energy dispersion is linear, resembling the Dirac equation for relativistic particles. This linear dispersion leads to high carrier mobility and unique electronic properties. Graphene, a single layer of carbon atoms arranged in a hexagonal lattice, is the most well-known Dirac material and has been extensively studied for its exceptional electrical and mechanical properties[2]. Weyl semimetals (WSMs) represent another class of topological materials where the conduction and valence bands intersect at points called Weyl nodes. These nodes come in pairs with opposite chirality and act as monopoles of Berry curvature in momentum space. The separation of Weyl nodes in momentum space leads to the emergence of surface states known as Fermi arcs, which connect projections of Weyl nodes with opposite chirality on the surface Brillouin zone (BZ). These Fermi arcs are a hallmark of Weyl semimetals and have been observed experimentally in materials such as TaAs[3].

The concept of topological electronic states originates from the quantum Hall effect (QHE), which demonstrated that symmetry alone does not encompass all condensed matter phases. This introduced the necessity for topological numbers that extend beyond the Landau theory of symmetry breaking. Haldane's lattice model for QHE marked a significant theoretical breakthrough by suggesting that certain materials could exhibit a quantum anomalous Hall effect (QAHE) without requiring an external magnetic field or Landau levels. Furthermore, materials preserving time-reversal symmetry have been shown to support the quantum spin Hall effect (QSHE), characterized by a $\mathbb{Z}_2$ topological invariant, as demonstrated experimentally in HgTe/CdTe quantum well structures. The realization of QAHE in magnetically doped TIs highlights the practical implications of these theoretical advancements.

The study of topological materials also involves exploring the Berry of the electronic wave function, a critical geometric property that significantly influences material properties. This leads to emergent quantum phenomena, such as various Hall effects and quantum charge pumping, arising from the quantum geometry of electronic states and their responses to external perturbations. For instance, 2D materials like graphene have provided a versatile platform for studying topological phases in reduced dimensions. Beyond graphene, materials such as transition metal dichalcogenides (e.g., MoS_2) exhibit topological properties when subjected to specific conditions, such as strain or electric fields, presenting opportunities for applications in flexible electronics and optoelectronics[4].

The connections between these various classes of topological materials lie in their shared reliance on the topological properties of their electronic structures. Whether in 2D systems like graphene or 3D systems like WSMs, the robustness of their surface or edge states against perturbations is a unifying feature. This robustness is not only of fundamental scientific interest but also holds promise for technological applications where stability and low energy dissipation are crucial[5].

Controlling the electronic properties of topological materials is a central focus in condensed matter physics, with symmetry-breaking mechanisms playing a pivotal role. By intentionally disrupting symmetries such as time-reversal, spatial inversion, or SOC, researchers can induce novel quantum phases and manipulate carrier transport properties. For instance, breaking time-reversal symmetry in TIs can lead to the emergence of quantum anomalous Hall states, characterized by dissipationless edge currents without an external magnetic field. This phenomenon has been experimentally observed in magnetically doped TIs, where the introduction of magnetic impurities breaks time-reversal symmetry, resulting in quantized Hall conductance[6]. Spatial inversion symmetry breaking is another powerful tool for engineering topological phases. In materials lacking inversion symmetry, SOC can lift spin degeneracy, leading to spin-polarized electronic states. This effect is prominent in non-centrosymmetric materials, where the Rashba effect induces spin splitting in the electronic band structure. Such spin-polarized states are crucial for spintronic applications, as they allow for the manipulation of spin currents without external magnetic fields. Moreover, inversion symmetry breaking can give rise to topological superconductivity, where unconventional pairing mechanisms lead to the formation of Majorana bound states, which are of interest for fault-tolerant quantum computing[7]. Spin-orbit coupling itself serves as a symmetry-breaking mechanism that profoundly influences the topological properties of materials. In systems with strong SOC, the interplay between spin and orbital degrees of freedom can open band gaps at the Fermi level, leading to the realization of TIs. For example, in bismuth-based compounds, strong SOC drives the transition from a trivial insulator to a topological insulator phase, characterized by conducting surface states protected by time-reversal symmetry. Additionally, SOC can induce topological phase transitions in materials subjected to external perturbations, such as electric fields or strain, enabling dynamic control over their topological states[8].

The deliberate breaking of symmetries in topological materials not only facilitates the exploration of emergent quantum phases but also enables the design of materials with tailored electronic properties. By understanding and manipulating these symmetry-breaking mechanisms, researchers can engineer materials that exhibit desired functionalities, such as robust edge states, spin-polarized currents, and exotic superconducting phases. This approach holds promise for advancing technologies in quantum computing, spintronics, and low-power electronics, where control over electronic states at the quantum level is essential[8].

Quantum phase transitions are fundamental changes in the ground state of a quantum system driven by quantum fluctuations, occurring at absolute zero temperature. Unlike classical phase transitions, which can involve changes in phase or crystal structure and are influenced by factors such as temperature, pressure, and chemical composition, QPTs are governed by quantum fluctuations that arise due to changes in parameters like pressure, magnetic field, or interaction strength. In topological materials, QPTs can lead to transitions between distinct topological phases. These phases are characterized by changes in specific topological invariants, such as the Chern number or $\mathbb{Z}_2$ invariants, which describe the global electronic properties of the system. For example, such a transition might involve a change from a trivial insulating phase to a topological insulating phase, where phenomena like the quantum Hall state are observed. These transitions are often accompanied by the closing and reopening of energy gaps in the electronic band structure, signaling a change in the topological order. Understanding QPTs in topological materials is crucial for exploring novel quantum states and potential applications in quantum technologies[9].

External perturbations, such as tensile strain and electric fields, are effective tools for modulating the topological properties of materials. Applying tensile strain can alter the lattice parameters and symmetry of a material, leading to modifications in its electronic band structure. For instance, in certain 2D materials, strain can induce a transition from a trivial insulator to a topological insulator phase by closing and reopening the band gap. This strain-induced topological phase transition has been theoretically predicted and experimentally observed in materials like transition metal dichalcogenides[10]. Similarly, electric fields can influence the electronic structure of topological materials by breaking inversion symmetry and modifying SOC effects. In materials such as monolayer $MnBi_2Te_4$, an external electric field can induce a topological phase transition from a trivial to a nontrivial state by altering the band topology. This electric field-induced transition is associated with changes in magnetic anisotropy energy and Curie temperature, highlighting the interplay between electric fields and magnetic properties in topological materials[11].

The ability to control topological phase transitions through external biases like strain and electric fields opens avenues for designing materials with tunable topological properties. This tunability is essential for developing devices that leverage topological states for applications in quantum computing, spintronics, and low-power electronics. By precisely manipulating external parameters, researchers can engineer desired topological phases and transitions, paving the way for innovative quantum technologies[12].

1.1. Aims and objectives of the thesis

In this thesis, quantum mechanical principles are applied through computational methods, specifically DFT and TB models, to investigate the electronic ground state, Berry curvatures, and Fermi-level topologies in selected solid-state systems exhibiting emergent quantum phenomena. The Berry curvature is a local property of the parameter space that can be thought of as the field strength of the Berry connection. It describes the differential structure of the Berry phase across parameter space and determines how the Berry phase accumulates locally, providing a measure of the twisting or curvature of the quantum state manifold in response to parameter variations. It is worth noting that the Berry phase is the geometric phase acquired by a quantum system during adiabatic evolution around a closed loop in parameter space. The Berry connection, on the other hand, is a gauge-dependent quantity that can be understood as the vector potential in parameter space, constructed from the eigenstates of the Hamiltonian. Fermi-level topology, which refers to the arrangement and connectivity of electronic states at the Fermi energy, is crucial for understanding the stability of topological phases and their response to external factors such as strain, and electric field. These studies are essential for elucidating how such external factors influence QPTs by modifying the Berry curvature and Fermi-level topology. The objectives of this thesis are:

1. To utilize DFT calculations, implemented in QE, to capture the ground-state electronic properties of $SrSi_2$, CoSi, and NbP, including band structures, Fermi surfaces, and charge densities, and to refine these results using TB models developed with Wannier90 and WannierTools for accurate characterization of topological invariants such as the Chern number.

2. To investigate the Berry curvatures and Fermi-level topologies in $SrSi_2$, CoSi, and NbP, focusing on their response to external perturbations such as tensile strain and external electric fields, and to identify the mechanisms driving topological quantum phase transitions (TQPTs) in these materials.

3. To elucidate the tunability of topological phases in $SrSi_2$ through computational experiments using Quantum Lattice software, demonstrating parallels with renormalized graphene systems and revealing how SOC and magnetic interactions influence band structure and phase transitions.

4. To provide a detailed understanding of how topological properties such as Berry curvature and surface states in $SrSi_2$, CoSi, and NbP can be manipulated for potential applications in

spintronics and quantum technologies, establishing a theoretical framework for designing materials with customized topological characteristics.

The three systems $SrSi_2$, CoSi, and NbP were chosen to represent distinct classes of topological semimetals, each showcasing unique symmetry protections and exotic quasiparticles that are both theoretically intriguing and experimentally accessible. $SrSi_2$ crystallizes in a non-centrosymmetric space group $P4_332$ and hosts double-Weyl fermions with chiral charge ±2, offering a tunable platform via alloying or strain to explore topological phase transitions[13, 14]. CoSi, in the chiral cubic space group $P2_13$, stabilizes multifold fermions (spin-1 threefold and double spin-$\frac{1}{2}$ Weyl nodes) protected by crystal symmetries, making it an ideal system to study higher-order Berry curvature effects and the chiral anomaly in unconventional quasiparticles[15, 16]. NbP, a member of the noncentrosymmetric $I4_1md$ family, was among the first experimentally realized Weyl semimetals, with well-defined Fermi arcs and measurable Berry phases, providing a benchmark for transport and surface-state studies in systems with weak spin-orbit coupling[17, 18]. Together, these materials span a broad range of space groups and topological phenomena, enabling a comprehensive investigation of how external biases, such as strain and electric fields, modulate Berry curvature and Fermi surface topology as predictors of emergent quantum behavior.

1.2. Thesis Structure

This thesis is structured as follows:

- **Chapter 1** provides a general introduction to the study, including the motivation behind investigating Berry curvature and Fermi-level topologies for predicting emergent quantum phenomena in selected solid-state systems.
- **Chapter 2** presents a comprehensive literature review, discussing previous studies on the selected materials and their topological properties. This chapter highlights key advancements in the field and establishes the context for the current research.
- **Chapter 3** delves into the field of topological materials, merging concepts of topology with condensed matter physics. It explores the unique properties of topological phases and their relevance to the materials studied in this thesis, setting the stage for the theoretical and computational investigations that follow.

- **Chapter 4** lays out the theoretical framework essential for solving electronic structure problems in systems of interacting particles. This chapter focuses on DFT as a primary methodology for predicting physical properties from ground-state electron density. Additionally, the TB model is introduced as a complementary approach, particularly valuable for understanding graphene-like systems and the behavior of electrons in condensed matter.

- **Chapter 5** outlines the computational methods employed in this research. It details the ab initio calculations used to determine the electronic structure, density of states (DOS), and charge density of materials like $SrSi_2$, CoSi, and NbP. The chapter also describes how band structure data from DFT is utilized to develop TB models, enabling the computation of topological properties. Furthermore, this chapter explains the renormalization of $SrSi_2$'s electronic structure on a honeycomb lattice, using a TB model analogous to that of graphene.

- **Chapter 6** presents and discusses the results of our investigations into the physical and topological properties of bulk $SrSi_2$, CoSi, and NbP. It examines the effects of external fields on these materials, highlighting symmetry-breaking phenomena and quantum phase transitions. The chapter also explores the renormalization of $SrSi_2$'s electronic structure to a graphene-like honeycomb lattice, revealing Dirac-like physics and potential applications in two-dimensional topological systems.

- **Chapter 7** concludes the thesis, presenting the results of the study and discussing their implications. It also suggests potential directions for future research, building on the findings of this work.

Chapter 2

Literature Review

In this chapter, we gather and analyze the amount of research surrounding the topological materials: strontium disilicide ($SrSi_2$) with space group $P4_332$ (No. 212), cobalt monosilicide (CoSi) with space group $P2_13$ (No. 198), and niobium monophosphide (NbP) with space group $I4_1md$ (No. 109), with a specific focus on their characteristics, applications, and the implications of these findings on future technological advancements. This review will not only integrate and analyze existing knowledge but also identify gaps in current research, thus providing a comprehensive understanding of this rapidly evolving field.

2.1. Introduction

Topological materials, a novel class of materials, have drawn significant attention in recent years due to their unique electronic properties. These materials are distinguished by their robust surface states, which are a consequence of the topological order, a type of order different from the familiar one based on symmetry. The electronic properties of these materials are not easily perturbed by impurities or defects, making them highly stable and efficient. The topological nature of these materials leads to exotic electronic properties, such as conducting surface states with insulating bulk properties.

The significance of topological materials extends to various practical applications, especially in energy and electronics. For instance, $SrSi_2$ demonstrates potential, especially in the realms of advanced electronics, thermoelectrics, and sustainable technology development. Similarly, CoSi has been explored for its potential in spintronics, a field that could revolutionize data storage and processing by utilizing electron spin rather than charge. NbP exhibits exceptional conductivity and is a candidate for use in ultra-fast electronic devices. The study of these materials is crucial not only for the advancement of fundamental science but also for the development of novel technologies that can enhance energy efficiency, data storage, and electronic device performance.

Ultimately, this literature review aims to provide a detailed yet accessible overview of the topological materials mentionned above, focusing on their defining characteristics, the current state of research, and their potential applications in various fields. By doing so, it seeks to contribute to the broader understanding of these materials and their role in shaping future technological advancements.

2.2. Detailed Reviews of $SrSi_2$, CoSi, and NbP.

2.2.1. Strontium disilicide

Imai et al.[19] investigated the pressure dependence of the electrical resistance of the narrow-gap semiconductor $SrSi_2$. The measurements were performed at temperatures from 4.2 to 300 K and pressures from 0 to 3.6 GPa . The authors found that pressurization reduces the energy gap E_g, with a pressure coefficient $dE_g/dP = -8.8$ meV/GPa. By fitting the conductivity data, they determined $E_g = 43$ meV at ambient pressure. The deformation potential $a_g = dE_g/d\ln V = 0.50$ eV was also estimated. These values are in qualitative agreement with the band structure calculation by Imai and Watanabe[20], which predicted $SrSi_2$ to be an indirect gap semiconductor with E_g decreasing under pressure. The reduction of the energy gap with pressure suggests a potential pressure-induced semiconductor-metal transition around 5.0 GPa, where E_g extrapolates to zero. This transition would occur without any structural phase change, as evidenced by the earlier X-ray diffraction measurements. The authors also observed the appearance of a plateau in the temperature-resistance curve at high pressures, likely related to changes in ionization energy and wave function overlap of extrinsic charge carriers. Overall, this study elucidates the pressure response of the electronic structure of $SrSi_2$ through transport measurements. The results are significant for understanding the band structure and pressure-induced metallization of this narrow-gap silicide compound.

Chen and Tian[21] present first-principles calculations of the electronic, optical, and thermodynamic properties of $SrSi_2$ crystals. The study aims to clarify the basic physical properties of this material, which has shown ambiguity between experimental measurements indicating semiconducting behavior and some theoretical works predicting metallicity. Using DFT within the generalized gradient approximation, the authors determine an optimized lattice constant of 6.549 Å for cubic $SrSi_2$, agreeing closely with experiment. The electronic structure reveals an indirect band gap of 0.0618 eV, corroborating previous experimental suggestions of semiconducting character. This narrow gap results from Si $3p$ states at the valence band maximum and Sr $3d$ states at the conduction band minimum. Optical properties including the dielectric function and absorption spectra are calculated, predicting $SrSi_2$ as a promising dielectric material with strong absorption in the ultraviolet region. Finally, lattice dynamics computations provide thermodynamic properties such as the Debye temperature (408 K) and heat capacity. Summing up, this computational work helps reconcile previous conflicting reports on the properties of $SrSi_2$. By systematically examining its structural, electronic, optical and thermodynamic characteristics using first-principles methods, Chen and Tian confirm the material as an indirect narrow-gap semiconductor. Their detailed calculations also make predictions for optical behavior and thermophysical quantities that may guide future experimental investigations of this silicide.

Imai et al.[22] investigate the basic properties of $Sr_{1-x}Ba_xSi_2$, including the phase relationship, crystal structures, and energy gap E_g. They find that the $SrSi_2$-$BaSi_2$ pseudo-binary system has only two phases - the $SrSi_2$ and $BaSi_2$ phases. The $SrSi_2$ phase exists for $0 \leq x \leq 0.13$ and the $BaSi_2$ phase for $0.24 \leq x \leq 1.0$. The lattice parameters and volume increase with x in both phases. A volume jump of 13.7% occurs at the phase transition from the $SrSi_2$ to $BaSi_2$ phase. Notably, E_g shows opposite trends in the two phases - it increases with x in the $SrSi_2$ phase but decreases in the $BaSi_2$ phase. The authors attribute this to differences in the Si networks - the $SrSi_2$ phase has a continuous 3D Si network while the $BaSi_2$ phase has discrete Si tetrahedra. This also leads to differences in the homogeneity ranges. For Sr-rich $BaSi_2$-phase $Sr_{1-x}Ba_xSi_2$, Ba atoms at the A1 crystallographic site are preferentially substituted by Sr, similar to Ba-rich compositions. The study reveals basic structure-property relationships in alkaline earth metal disilicides, which are promising for energy applications.

Lue et al.[23] investigated the effects of partially substituting Ge at the Si sites in the $SrSi_2$ alloy on its thermoelectric properties. The motivation was to tailor the electronic structure and phonon scattering to improve the thermoelectric performance. Samples of $SrSi_{2-x}Ge_x$ with $x = 0 - 0.12$ were synthesized using arc melting and annealing. Temperature-dependent electrical resistivity ρ(T), Seebeck coefficient S(T), and thermal conductivity κ(T) were measured. Key findings show that with increasing Ge substitution up to $x = 0.06$, the room temperature ρ decreases while the band gap E_g increases due to negative chemical pressure. This composition dependence of ρ and E_g likely arises from modifications in the DOS near the Fermi level. The maximum S of $\sim 280\ \mu V/K$

occurs at $x = 0.03$ and T≈ 85 K. Analysis of κ(T) reveals the lattice thermal conductivity κL dominates, with the low-T peak dropping markedly with more Ge. This demonstrates enhanced phonon scattering due to mass fluctuations between Si and Ge. Ultimately, a peak $ZT \approx 0.13$ at room temperature was attained for $SrSi_{1.94}Ge_{0.06}$, ~ 3 times higher than pure $SrSi_2$. The improved thermoelectric performance is attributed to the combined effects of reduced ρ, moderately enhanced S, and decreased κL with controlled Ge substitution. This study reveals an effective route to optimize thermoelectric properties of $SrSi_2$ via isovalent Ge substitution. The modified electronic structure and strengthened phonon scattering open avenues to further improve ZT. To sum up, this research makes valuable progress toward establishing $SrSi_2$-based alloys as environmentally friendly and low-cost thermoelectric materials.

Rahman computationally studied the elastic and optical properties of the semiconducting compound $SrSi_2$ using first-principles DFT[24]. This is the first detailed theoretical examination of the elastic properties of this material, which has potential applications in photoelectric and thermoelectric devices. The author performed geometry optimizations and calculated the lattice constants, independent elastic constants (C_{11}, C_{12}, C_{44}), bulk modulus, shear modulus, Young's modulus, Poisson's ratio, and elastic anisotropy factor. Their analysis indicates $SrSi_2$ is mechanically stable with relatively low bulk modulus, suggesting it is a soft material. The obtained Poisson's ratio and Pugh ratio reveal brittle material behavior. The optical properties, including complex conductivity, reflectivity, refractive index, and absorption coefficient were also examined. Notably, the high low-energy reflectivity suggests suitability for solar cells, while the estimated band gap based on strong absorption onset agrees with typical semiconductor behavior. This comprehensive first-principles examination of $SrSi_2$ elastic and optical properties provides useful insights into its electronic structure and suitability for optoelectronic devices.

Huang et al.[14] propose $SrSi_2$ as a new type of Weyl semimetal with novel properties distinct from previous candidates like TaAs. They show using first-principles calculations that $SrSi_2$ hosts quadratically dispersing double Weyl fermions with higher chiral charge of ±2, enabled by the lack of inversion and mirror symmetries. Moreover, Weyl nodes of opposite chirality are positioned at different energies, facilitating experimental detection of the chiral magnetic effect. The robust, stoichiometric crystal structure of $SrSi_2$ and its distinctive topological properties open exciting possibilities to explore a rich variety of phenomena through tabletop experiments. The calculations reveal $SrSi_2$ is already a Weyl semimetal even without SOC due to band crossings along the $\Gamma - X$ direction. These crossings disperse linearly in all three directions, confirmed by the opposite chiral charges of +1 and -1 associated with two sets of nodes $W1$ and $W2$. Including spin-orbit interactions causes two Weyl cones with matching rotation eigenvalues to stick together, changing their dispersion from linear to quadratic. The emergent double Weyl fermions at $W1$ and $W2$ exhibit a higher chiral charge of ± 2. $SrSi_2$ lacks mirror symmetry, allowing Weyl nodes of opposite chirality to occur at different energies unlike previous candidates. By breaking crystalline symmetries, Huang et al. explicitly demonstrate the quadratic Weyl nodes in $SrSi_2$ are protected by fourfold rotational symmetry. They further calculate (001) surface states, finding topological Fermi arcs that terminate at the projection of the bulk double Weyl nodes. Their systematic characterization of $SrSi_2$ not only identifies a robust, feasible Weyl semimetal but also proposes realistic routes to detecting exotic phenomena and accessing new quadratic Weyl physics beyond TaAs. The simplicity of the stoichiometric $SrSi_2$ crystal and its distinctive properties open doors for exploring Weyl physics.

Singh et al.[13] computationally explored the topological electronic structure of the noncentrosymmetric cubic perovskite $SrSi_2$. They focused on elucidating the tunable double Weyl fermion semimetal state in this materials class using first-principles methods based on the Heyd-Scuseria-Ernzerhof hybrid functional. Their work underscores the potential of $SrSi_2$ materials family as a platform for investigating exotic Weyl physics. The authors' calculations revealed $SrSi_2$ hosts a pair of robust band inversion type double Weyl nodes carrying chiral charge ± 2. However, the small band inversion strength of -41 meV indicated proximity to a topological phase transition. By tuning the lattice constant in $SrSi_2$, a transition from the double Weyl semimetal to a trivial gapped insulator was induced. Further, alloying with Ca and Ba to obtain $Sr_{1-x}Ca_xSi_2$ and $Sr_{1-x}Ba_xSi_2$ enabled modulation of the band topology. Ca doping enhanced the band inversion strength, stabilizing the double Weyl state, while Ba doping suppressed it, eventually gaping the bulk bands. The (001) surface states showed double Fermi arcs connecting projected Weyl nodes, consistent with the bulk chiral charge. The tunable Weyl physics was reconciled with transport experiments on the Ca and Ba substituted alloys. This first-principles study establishes the $SrSi_2$ material class as a promising platform for investigating double Weyl fermion physics and related topological properties. The facile tunability of the topological semimetal state via strain and chemical substitution provides avenues for further exploration.

Singh and Imai synthesized cubic $Sr_{1-x}Ba_xSi_2$ with Ba content x higher than the solid solubility limit using spark plasma sintering[25]. They found that electrical resistivity ρ and Seebeck coefficient S increase with x, while thermal conductivity κ decreases. The dimensionless thermoelectric figure of merit ZT was enhanced by partial substitution of Sr with Ba, reaching a maximum value of 0.21 for $Sr_{0.81}Ba_{0.19}Si_2$ at 357 K. Detailed observations showed nonmonotonic temperature dependence of electrical resistivity ρ. With increasing x, the ρ value doubled around room temperature. The activation energy calculated from an Arrhenius plot of conductivity increased from 25 meV to 30 meV. Seebeck coefficient S also increased with x at all temperatures, indicating an increase in bandgap with substitution. Total thermal conductivity κ was found to decrease with x due to reduction in both electronic and lattice contributions. As a result, ZT showed higher values for Ba-substituted samples compared to unsubstituted $SrSi_2$. The study demonstrated enhancement in thermoelectric performance of cubic $SrSi_2$ by Ba substitution beyond solubility limit. This was attributed to increased electrical resistivity and Seebeck coefficient, combined with reduced thermal conductivity.

Shiojiri et al.[26] investigated the electronic structure and thermoelectric properties of the narrow-gap semiconducting α-$SrSi_2$ using a complementary experimental and computational approach. They grew high-purity α-$SrSi_2$ crystals using the vertical Bridgman method and estimated a bandgap of 13.1 meV from temperature-dependent carrier density measurements. First-principles calculations were performed using the Heyd-Scuseria-Ernzerhof hybrid functional, determining that a mixing parameter value of 18.7% for the Hartree-Fock (HF) contribution to exchange almost perfectly reproduced the experimentally measured bandgap of 13.1 meV. With this optimized computational model, the calculated Seebeck coefficient precisely matched experimental measurements when the calculations assumed a chemical potential shift due to unintentional doping. Overall, this combined approach enabled accurate prediction of the thermoelectric transport properties, with the calculations properly accounting for narrow-gap effects. The results highlight how first-principles modelling can overcome limitations of conventional DFT for narrow-gap semiconductors when an appropriate fraction of exact HF exchange is included. By growing highly pure crystals and systematically optimizing the computational parameters to match experimental data, Shiojiri et al. developed a predictive computational model for α-$SrSi_2$. This will enable extensive further analyses of doping effects and optimization strategies. With thermoelectrics research increasingly utilizing such multi-scale approaches combining precision experiments and computations, this work provides an exemplary methodology. The quantitative agreement achieved opens the prospect of computationally guided searches for altered compositions and nanostructures with enhanced performance.

Sadhukhan and Nag investigate $SrSi_2$, a noncentrosymmetric, nonmagnetic double WSMs[27]. This study focuses on the electronic structure, particularly the behavior of electron and hole pockets in the bulk Fermi surface, and examines the material's nonlinear optical responses, such as the circular photogalvanic effect (CPGE). This research is pivotal in understanding the properties of WSMs, which are materials with nontrivial topological properties that exhibit unique electronic behaviors not found in conventional semiconductors or metals. The authors detail their observations on $SrSi_2$'s electronic structure and its responses under various conditions. They find that the material can be characterized as a type-I WSM and explore its structural handedness, which influences the surface Fermi surface and the emergence of Fermi arcs. The study also delves into the SOC effects and their impact on the topological charge of the Weyl nodes. Interestingly, the CPGE response in $SrSi_2$ was found to be quantized only when the Fermi level is near a Weyl node with higher energy, contrasting with other types of WSMs where CPGE is quantized differently. These findings are supported by a comprehensive analysis using the three-band formula for CPGE, demonstrating the intricate interplay between the electronic structure and optical responses in topological semimetals. This study significantly advances the understanding of double WSMs, particularly in the context of nonlinear optical responses. The findings on $SrSi_2$'s electronic structure and CPGE behavior open new avenues for exploring topological materials in optoelectronic applications, such as high-efficiency solar cells and other photonic devices. The distinct behavior of CPGE in $SrSi_2$ compared to other WSMs suggests that varying topological charges and symmetries in such materials can lead to a range of novel optical phenomena.

Yao et al.[28] studied the Weyl semimetal candidate material $SrSi_2$ using angle-resolved photoemission spectroscopy (ARPES) and first-principles calculations. They introduced $SrSi_2$ as having a simple cubic structure lacking inversion and mirror symmetries, with previous theoretical works predicting it to host robust Weyl fermions. Their work aimed to experimentally verify these predictions. Through systematic ARPES measurements on $SrSi_2$ and Ca-doped $SrSi_2$ single crystals, the authors mapped the band structure and Fermi surfaces. They found no evidence of the theoretically predicted Weyl nodes at the $kz = 0$ plane. Specifically, only one hole-like band was observed along the $\Gamma - X$ direction, with their hybrid functional HSE calculations confirming a ~ 0.1 eV gap between this band and the higher-lying electron bands. The absence of band crossings suggests $SrSi_2$ may in fact be a topologically trivial semiconductor rather than a Weyl semimetal. Additionally, no signatures of topological surface states were found. Qualitatively similar results were obtained for the Ca-doped samples. This comprehensive study combining experiment and theory indicates $SrSi_2$ does not realize the Weyl semimetal state, contradicting previous predictions. The authors suggest improved theoretical treatment with hybrid functionals like HSE may better describe $SrSi_2$'s electronic structure. Further confirmation of the trivial band topology could come from higher-resolution ARPES accessing unoccupied states. More broadly, this work highlights the need for detailed measurements in assessing theoretical Weyl semimetal candidates, where subtle aspects of the band structure can determine topological properties.

Barua et al.[29] investigated various structural, electronic, optical, elastic, and thermophysical properties of the double Weyl semimetal $SrSi_2$ using DFT. The study reveals several hitherto unexplored properties of this noncentrosymmetric cubic silicide. The analysis shows $SrSi_2$ is a mechanically stable, ductile compound with significant metallic bonding. It has a semimetallic band structure with clear double Weyl nodes close to the Fermi level. The optical spectra suggest excellent broadband reflection ability, making $SrSi_2$ suitable as a solar reflector. It also absorbs ultraviolet efficiently and possesses high refractive index at lower photon energies. Furthermore, $SrSi_2$ exhibits comparatively soft elastic moduli, low Debye temperature, high thermal expansion, and small dominant phonon wavelengths. Overall, this comprehensive study unravels novel insights into the bulk properties of topological Weyl semimetal $SrSi_2$. The authors have systematically analyzed the material's potential for optoelectronic applications based on its favorable optical characteristics.

To conclude this part of the literature review on $SrSi_2$, it is worth noting that several fundamental questions persist regarding its nature and properties[13, 28]. While studies conducted on $SrSi_2$ have explored its basic properties[29], fundamental questions remain regarding its topological nature and eventually how its topological traits evolve under real-world conditions[28, 30]. A systematic investigation applying external bias potentials and monitoring the response of quantities like Berry curvatures and band topologies will provide crucial insights[13, 30]. The goal is to evaluate topological phase space and define quantifiable metrics capturing the robustness of observed phenomena[13, 14]. This approach will reveal new physics, facilitate applications leveraging topological characteristics, and further establish $SrSi_2$ as a versatile quantum materials platform.

2.2.2. Cobalt Monosilicide

Pshenay-Severin et al.[31] have delved into the unconventional electronic topology of CoSi, a semimetal known for defying traditional classifications within its crystalline structure. Their comprehensive ab initio calculations, which account for the intricacies of spin-orbit interactions, lay bare the exotic nature of CoSi's band structure. Their research paper exposes the existence of band-touching points within CoSi that demonstrate an extraordinary multiplicity in their degeneracy, carrying a nonzero Chern number. These points, harboring 'new fermions', embody a quantum state far removed from the well-charted territories of conventional Weyl and DSMs. It is the discovery of these topologically nontrivial nodes, some with fourfold and others with sixfold degeneracy, located at the high-symmetry Γ and R points of the BZ, that elevates the significance of their findings. The researchers utilized both linearized Hamiltonians and first-principles calculations to dissect and understand the topological features of these nodes. Remarkably, the fourfold degenerate multiplet found at the Γ point and the sixfold degenerate node at the R point exhibit total topological charges with magnitudes of 4, and intriguingly, they are of opposite signs despite the linear band dispersions. One of the salient revelations of Pshenay-Severin et al.'s study is the proximity of these multiplets to the Fermi energy, situated merely about 22 meV apart, suggesting that these features could have tangible effects on the material's physical properties. Furthermore, the reported cubic anisotropy of the Fermi surface adds another layer of complexity to the behavior of electrons in CoSi. This anisotropy is reflected in the formation of four Fermi arcs on the material's surface, which intriguingly start and end near the projections of the bulk Γ and R points on the surface BZ. This study of the electronic makeup of CoSi by Pshenay-Severin et al. shows how knowledge of topological materials keeps advancing. It not only challenges the boundaries of known electronic properties but also paves the way for potential applications that capitalize on these novel quantum phenomena.

Takane et al.[32] have shed light on the nature of electronic states in CoSi, making a remarkable leap in the field of topological quantum states by uncovering chiral fermions through their experiment. Utilizing the precision technique of ARPES, they have unearthed the existence of not one, but two types of chiral topological fermions within CoSi - a spin-1 chiral fermion at the center and a double Weyl fermion at the corner of the bulk BZ. The team's meticulous analysis reveals that the bulk Fermi surfaces of CoSi are exclusively constituted of energy bands that correspond to these novel fermions. Furthermore, their research has led to the identification of surface states that seamlessly bridge the Fermi surfaces pertinent to these fermions. This observation is particularly groundbreaking as it stands as the first experimental corroboration of the existence of Fermi-arc surface states-a theoretical concept until now. The importance of Takane et al.'s research cannot be overstated as it provides unprecedented experimental evidence of chiral topological fermions that extend beyond the realms of Dirac and Weyl fermions previously known in condensed-matter systems. Their findings not only validate theoretical predictions but also significantly advance the pursuit of new electronic phenomena that may arise from these unconventional chiral fermions. Takane et al. through Angle-Resolved Photoemission Spectroscopy (ARPE) measurements on CoSi have successfully captured the spectral fingerprints of these exotic fermions, manifesting themselves as unconventional multifold band crossings at the Γ and R points of the bulk BZ. The observed Fermi-arc surface states, tethered to these chiral fermions, cement the presence of topological fermions with a Chern number surpassing 1. The implications of this discovery are profound, offering a solid groundwork for the exploration of new physical properties inherent to chiral fermions such as unique photonic responses, anomalous transport phenomena, and potential applications in spintronics.

Tang et al.[33] unveiled a seminal study that pushes the frontier of our understanding of topological fermions in the realm of transition metal silicides. By leveraging the power of ab initio DFT, they peeled back the layers of these complex materials to reveal a fascinating tapestry of unconventional quasiparticles coexisting within. Their research focused on a family of transition metal silicides, including CoSi, RhSi, RhGe, and CoGe, particularly when SOC is incorporated into the equation. Within the crystalline confines of these materials, they observed not just the established entities of type-I and type-II Weyl fermions but also the presence of spin-1 excitations with threefold degeneracy and the enigmatic spin-$\frac{3}{2}$ Rarita-Schwinger-Weyl (RSW) fermions. These particles, with their nontrivial topology, were found to be connected by extensive Fermi arcs on the surface states, a phenomenon verified by the (001) surface electronic spectra of CoSi. Moreover, the significance of their findings is amplified by the stability and accessibility of these arc states, which span a broad energy range around the Fermi level-promising traits for future explorations using ARPES. Tang et al. underline a distinctive aspect of their findings: the topological features of these semimetals extend across a large energy window, contrasting with previous discoveries in the field that were more energetically restricted and localized in the BZ. This work by Tang et al. stands as a cornerstone contribution, setting a precedent for both theoretical prediction and experimental validation in the pursuit of novel quantum materials.

Yuan et al.[34] conducted a study in which they use scanning tunneling microscopy (STM) spectroscopy to investigate quasiparticle interference at various terminations of a CoSi single crystal. The single crystals were grown using a chemical vapor transport (CVT) method and carefully prepared before characterization. The experiments were performed at low temperatures using a commercial STM system, and the results were compared to DFT calculations. The researchers were able to confirm the presence of topological Fermi arc states on the (001) and (011) surfaces of CoSi, indicating the presence of chiral spin-$3/2$ RSW fermions and double spin-1 Weyl fermions. The observed quasiparticle interference patterns were consistent with theoretical simulations, providing strong evidence for the presence of these unconventional fermions. The chiral surface states of CoSi were found to exhibit a number of exotic properties, such as large spin-orbit splitting and a wide energy window. The researchers used a combination of experimental techniques and theoretical calculations to study the electronic structure of CoSi single crystals. They grew the crystals using a CVT method and carefully prepared the samples before characterization. The experiments were performed at low temperatures using a commercial STM system, and the results were compared to DFT calculations. The researchers were able to confirm the presence of topological Fermi arc states on the (001) and (011) surfaces of CoSi, indicating the presence of chiral spin-$3/2$ RSW fermions and double spin-1 Weyl fermions. This work provides valuable insights into the electronic structure of CoSi and the nature of chiral fermions.

Dutta and Pandey conducted a study to investigate the effect of electronic correlations on the fermions observed in the material CoSi[35]. They used a combination of DFT and dynamical mean-field theory (DMFT) to study the spectral functions of the bulk and surface of CoSi at a temperature of 100 K. They used the WIEN2k code, which is based on the full-potential plane wave method, to perform their DFT calculations. They also used the DMFT code implemented by Haule et al., which is interfaced with WIEN2k, to perform their DFT+DMFT calculations. They used a continuous-time quantum Monte Carlo impurity solver to solve the auxiliary impurity problem, and an exact double-counting scheme proposed by Haule. Their calculations showed the presence of extra hole pockets at the M points in the BZ, and the dispersion curves of CoSi showed both coherent and incoherent features, such as well-defined dispersive lines in the range -0.2 eV $\leq \omega \leq 0.2$ eV for coherent states with higher quasiparticle lifetimes, and smeared features at energies below -0.2 eV indicating incoherent states with shorter lifetimes. Notably, at $\omega \sim -30$ meV and $\omega \sim -186$ meV, these incoherent states correspond to calculated lifetimes of approximately 10^{-9} s and 10^{-12} s, respectively, when SOC is not included. This indicated the presence of quasiparticle-quasiparticle interactions, which affect the lifetime of the exotic fermionic quasiparticles. They also performed GW calculations using the Questaal package to calculate the quasiparticle energies. Overall, their work provides insight into the electronic correlations and quasiparticle interactions in CoSi.

Xu et al.[36] used different methods to grow single-crystalline CoSi and studied its electrical transport properties. The researchers used floating-zone, CVT, and flux methods to grow the crystals. In the floating-zone growth method, polycrystalline CoSi was first prepared by arc melting stoichiometric cobalt and silicon chunks, and then the crystal was grown in a Quantum Design 2-Mirror IR Image Furnace. In the standard CVT method, either CoSi powder or fresh cobalt and silicon powder was used as the starting material. About 1 g of the raw material was loaded into a fused silica tube, along with a transport agent such as I_2 or Br_2. The tube was then sealed in a vacuum and maintained at high temperatures for around 10 days. This process yielded shiny, millimeter-sized polyhedronlike crystals. For the flux growth method, the researchers used antimony, tin, and tellurium as the liquid solution. In the growth from tellurium flux, cobalt, silicon, and tellurium powder with a molar ratio of 1:1:20 were placed in an alumina crucible and sealed in a fused silica ampoule in a vacuum. The ampule was then heated to 1050 °C for a few hours, before being slowly cooled down to the centrifuging temperature of 700 °C at a rate of $3\ ^{\circ}\ \mathrm{C/h}$. This process yielded several single-crystalline chunks with large (111) facets. The electrical properties of the resulting crystals were then characterized using a range of techniques, including thermoelectric measurements and angle-dependent Nernst signals. The authors found that the CoSi crystals grown using a tellurium solution had the highest carrier mobility, enabling them to observe quantum oscillations in the thermoelectrical signals. Their analysis of these oscillations revealed two spherical Fermi surfaces in the crystal's BZ, consistent with the material's chiral charge. These results provide new insights into the electronic properties of CoSi and could potentially have applications in the field of topological materials.

Kudryavtsev et al.[37] prepared bulk Co_2Si, CoSi, and $CoSi_2$ alloys by melting together pieces of Co and Si of 99.99% purity in an arc furnace. The furnace was purged with argon gas, and the ingot was remelted multiple times to promote volume homogeneity. The researchers also prepared amorphous and crystalline CoSi and $CoSi_2$ films by flash evaporation of crushed alloy powders onto a cooled glass substrate. Kudryavtsev et al. characterized the structural and optical properties of the bulk and film samples using a variety of techniques, including X-ray diffraction, spectroscopic ellipsometry, and four-probe resistivity measurements. They found that the lattice constants of the bulk alloys agreed well with previous reports, and that the optical properties of the alloys could be explained in terms of their electronic structures. To do this, the researchers performed ab-initio electronic structure calculations using the WIEN2K code, which utilizes an all-electron full-potential linearized-augmented-plane-wave method. The calculations included the effects of SOC and employed the generalized gradient approximation (GGA) version of Perdew et al. for the exchange-correlation (XC) functional. The team found that the optical conductivity spectra of the Co_2Si, CoSi, and $CoSi_2$ alloys showed a number of peaks in the visible and near-infrared regions, which they attributed to transitions between different electronic states. They also found that the temperature dependence of the electrical resistivity of CoSi films followed a power-law behavior, indicating the presence of electron-electron scattering. Overall, the study provides new insights into the optical properties of Co_2Si, CoSi, and $CoSi_2$ alloys, and demonstrates the utility of ab-initio electronic structure calculations in explaining these properties.

Wang et al.[38] conducted an insightful study into the magnetic transport properties and electronic structures of the topological chiral semimetal CoSi, using de Haas-van Alphen (dHvA) quantum oscillation measurements and first-principles calculations. This research contributes significantly to the understanding of fermionic excitations and their implications in condensed matter physics, particularly focusing on the large-Chern-number properties of CoSi and its electronic structure. The team observed prominent dHvA oscillations in CoSi, which led to the identification of three fundamental frequencies. These findings were corroborated by first-principles calculations. Their study research revealed a low-frequency oscillation (F_α), first detected in quantum oscillation measurements, representing the contribution from a hole pocket at the BZ center. Additionally, two high frequencies (F_β and F_γ) with asymmetrical peaks were confirmed to stem from electron pockets with SOC at the BZ corner R point. These results underscored the complex electronic structure of CoSi, particularly when considering the effects of SOC. The asymmetry in the peaks was attributed to SOC-induced band splitting and irregular Fermi pockets, highlighting the intricate nature of electronic interactions in this material. This study paves the way for further experimental and theoretical exploration into topological materials with large Chern numbers. The detailed understanding of the electronic structure and fermionic excitations in CoSi, as revealed by this research, is crucial for future studies in the field. The observations made about SOC effects and the identified frequencies provide a foundational understanding that could be instrumental in developing new materials and exploring novel quantum phenomena. This research not only adds to the existing knowledge about topological chiral semimetals but also opens up avenues for investigating the practical applications of these materials in technology and fundamental science.

Wieder et al.[39] review progress in the discovery of topological materials, from early predictions of quantum spin Hall insulators and TIs to recent large-scale searches identifying over 25,000 candidate topological materials. The authors detail key developments enabling topological materials research, including topological band theory diagnosing band topology through symmetry indicators or Wilson loop methods and discoveries of various topological phases like topological crystalline insulators protected by crystal symmetries. A crucial breakthrough was the theory of topological quantum chemistry systematically enumerating atomic limits realizable in crystal structures, allowing identification of topologically non-trivial bands. The authors highlight major frontiers including topological materials discovery in noncentrosymmetric crystals, incorporation of magnetism, investigation of few-layer and heterostructure devices manifesting fragile topology, and exploration of intertwined charge-density-wave order and topology. Overall, the explosive growth and bright outlook of topological materials research is presented, driven by synergistic advances in band theory, crystallography, and high-throughput computation. Key opportunities are raised in refining theoretical classification, investigating complex quantum materials, and realizing next-generation electronic, spintronic and quantum technologies.

Nikolaev et al.[40] investigate the influence of uniaxial deformation on the band structure and topological properties of CoSi. Cobalt monosilicide belongs to non-centrosymmetric space group $P2_13$ (No. 198) and features multifold band crossings with large topological charges of ±4. The change in crystal symmetry under external stress can lift the degeneracy and modify the topological properties. Using ab initio calculations and symmetry analysis, the authors construct k.p Hamiltonians near the Γ and R points to describe the low-energy excitations. The results reveal splitting of the multifold nodes into band crossings of different types and topological charges depending on the strain direction. Along [100], the 4-fold degenerate node at Γ splits into Weyl nodes of unit charge, while at R there is no splitting. For [110] strain, Γ node splits into 4 effective spin-$1/2$ nodes with total charge ±2, shifted along tilted directions. At R, the 4-fold degenerate node becomes 2 double spin-$1/2$ crossings with charges ±1. Most peculiarly, [111] strain induces transitions to quadratic double-Weyl nodes of charge ±2 at Γ and R, resembling but distinct from regular double Weyl points. Additional conventional Weyl nodes appear around Γ and R. The shifting and tilting of band dispersions is analyzed using the k.p model. Surface states and their modifications are also discussed. This work demonstrates tunable transitions between different topological semimetallic phases in CoSi purely by mechanical deformation. The understanding of strain effects lays the foundation to utilize topological properties in devices.

Fecher et al.[41] provide an extensive overview and classification of chiral structures and space groups in crystalline solids. They introduce chirality measures to quantify and distinguish between chiral structures, focusing on the Hausdorff distance and continuous chirality measure. The authors discuss chirality in bulk crystals and at surfaces, where four different situations can arise regarding the bulk and surface chirality. They further analyze how basic electronic structure properties like the band structure and Berry curvature relate to chirality, finding that the band structure is unaffected by changing the handedness while the Berry curvature does depend on it. However, the Berry curvature is not an indicator of chirality since it changes sign under inversion of achiral structures too. Finally, Fecher et al. propose that circular dichroism in the angular distribution of photoelectron spectroscopy can be used to distinguish the handedness of chiral crystals, which they demonstrate through calculated spectra for the surfaces of FeSi and VSi_2. The authors provide a comprehensive analysis that clearly distinguishes between chiral structures, space groups, and properties, while introducing quantitative measures of chirality and demonstrating signatures in electronic structure properties. Their proposed dichroic photoelectron spectroscopy method offers new possibilities for experimentally probing chirality in crystalline solids.

To summarize this part of the literature concerning CoSi, we note that several studies have elucidated rich topological phenomena intrinsic to CoSi, yet opportunities remain to further probe the bias dependence of key metrics capturing this non-trivial band topology[42, 43]. Systematically applying external potentials and tracking the evolution of Berry curvatures, Fermi surface topologies, and related topological invariants can reveal new exotic phases and control mechanisms for emergent chiral surface states[43, 44]. Quantifying robustness to perturbations via bias-dependent topological metrics also promises deeper insights into the inherent landscape of this topological semimetal[3].

2.2.3. Niobium monophosphide

Sun et al. performed first-principles calculations to systematically study the topological surface states and Fermi arcs in four recently discovered WSMs - TaAs, TaP, NbAs, and NbP[45]. These noncentrosymmetric semimetals were predicted to exhibit unclosed Fermi arcs, instead of closed Fermi surfaces, due to the presence of topological Weyl nodes in their bulk band structures. The calculations reveal that the shape and topology of the Fermi arcs depend sensitively on the surface termination, although the fundamental topology remains unchanged. On the polar (001) surface, the arc shapes for cation (Ta/Nb) and anion (As/P) terminations differ considerably. Comparisons to experiments suggest the anion-terminated surfaces best match the measured band structures. Through analysis of the surface state spin polarization and odd number of Fermi surface crossings along closed loops, the actual Fermi arcs are identified out of intertwined surface states at the

Fermi level. The evolution of surface states with increasing spin-orbit coupling strength is also examined, showing the transition from trivial spin-degenerate Fermi circles to non-closed spin-split arcs as Weyl nodes emerge. Additionally, the sensitivity of the arc shapes to perturbations is demonstrated via calculated Fermi surfaces with potassium adsorbates. Overall, this work provides valuable microscopic insight into the exotic topological Fermi arcs in WSMs. The authors highlight the intricate interplay between bulk and surface electronic structures that underlies the rich variety of observable arc shapes. These results motivate future studies examining responses to other perturbations and connections to transport anomalies in WSMs.

Lee et al.[46] present a comprehensive first-principles study of the electronic structure and Fermi surface topology of the TaAs class of WSMs, including TaAs, TaP, NbAs and NbP. The significance of this work lies in providing fundamental knowledge of band structure and charge carrier properties in these materials, which is crucial for understanding and interpreting experimental observations and for realizing predicted exotic Weyl physics phenomena. The authors perform detailed DFT calculations to investigate the band structure both with and without spin-orbit coupling. Their analysis reveals 24 Weyl nodes in the BZ arising from the spin-orbit induced lifting of nodal rings. Importantly, the calculations determine energies, locations and velocities of two distinct types of Weyl nodes, finding significant anisotropy. The complex interconnectivity and topology of multiple electron and hole pockets at the Fermi energy is also established. Areas, carrier concentrations and velocities of the Fermi surfaces are reported, highlighting a rich, tunable electronic behavior. Notably, the small energy separation between Weyl nodes in TaAs explains its relatively low carrier concentrations, contrasting with larger separations and higher concentrations in TaP, NbAs and NbP. The comprehensive analysis of band structure and interconnected Fermi surfaces provides fundamental knowledge for realizing exotic physics predicted for WSMs. The tunable electronic properties suggest excellent potential for engineering applications via doping, strain or external fields. This work forms a platform for future theoretical and experimental studies involving spectroscopic, transport, optical and thermal phenomena in TaAs-class topological semimetals.

Shekhar et al.[47] investigate the exotic semimetal NbP which combines features of both a normal semimetal and a Weyl semimetal. They find NbP exhibits an extremely large, nonsaturating magnetoresistance of $8.5 \times 10^5\%$ at 1.85 K in a 9 T field, among the highest reported for any material. Additionally, NbP demonstrates an ultrahigh carrier mobility reaching 5×10^6 $\mathrm{cm^2V^{-1}s^{-1}}$ at 1.85 K, comparable to Cd_3As_2. Through Shubnikov-de Haas (SdH) oscillation measurements, the authors determine NbP has a very low cyclotron effective mass of 0.076 m_0 leading to the high mobility. Shubnikov-de Haas frequencies correspond to small Fermi surface pockets with areas $< 1\%$ of the BZ, consistent with their DFT calculations which show both hole pockets from normal bands and electron pockets from linear Weyl bands crossing the Fermi level. This coexistence of hole and electron pockets enables the extremely large, nonsaturating magnetoresistance (MR) under an applied magnetic field. By combining features of topological WSMs and conventional semimetals, NbP presents unique transport phenomena including ultrahigh carrier mobilities from Weyl bands and extremely large MR from electron-hole resonance. The authors propose NbP as a platform to explore exotic physics arising from the interplay of these topological and normal electronic phases. NbP offers intriguing possibilities for both fundamental physics studies and potential device applications.

Dos Reis et al.[48] investigate the pressure evolution of the Fermi surface topology in the non-centrosymmetric Weyl semimetal NbP. They combined experimental studies of SdH oscillations and band structure calculations up to 2.8 GPa. Although they observed a drastic effect on the amplitudes of the quantum oscillations, the frequencies exhibit only a weak pressure dependence. The changes in oscillation frequencies agree with their band structure calculations showing the stability of NbP's electronic structure. They related the amplitude changes to small Fermi surface modifications. The high-field MR variation for current I parallel to the a-axis results from an altered charge carrier balance and shift of the W2 Weyl points towards the Fermi energy shown in their calculations. Their good agreement between experimental and calculated SdH frequencies demonstrates quantum oscillations and band structure calculations effectively probe pressure-induced Fermi surface changes in WSMs. In detail, they performed electrical transport and SdH oscillation measurements on high-quality NbP crystals up to 2.8 GPa and 9 T. Although the MR magnitude stayed almost unchanged for B along the c-axis, it showed a double-well structure for B and electrical current I applied parallel to the a-axis, dropping from $8\times10^4\%$ at ambient pressure to $2.3\times10^4\%$ at 1 GPa before increasing again. This indicates the electron-hole balance tuning with pressure seen from the antisymmetrized MR. Pronounced SdH oscillations occurred above 1 T revealing small cyclotron masses between 0.034 m_e and 0.112 m_e almost constant under pressure. Fast Fourier transforms (FFTs) yielded four fundamental frequencies changing little under pressure. Comparison with band structure calculations showed they arise from two electron and two hole pockets remaining stable. The FFTs amplitudes decreased strongly due to increased Fermi surface curvature near the extremal cross sections according to the calculations. The calculations also demonstrated the W2 Weyl points shift towards the Fermi energy with pressure while the W1 points stay fixed. Dos Reis et al. work provided extensive evidence for NbP's robust electronic structure up to 2.8 GPa from precise SdH oscillation frequency tracking. Agreement between experiment and theory proves quantum oscillations' power for resolving pressure-induced Fermi surface changes. The high-field MR variation likely originates from the W2 Weyl point shift tuning the chiral anomaly contribution. Their approach sets an exemplary standard for investigating pressure effects on Weyl semimetals' topological properties.

Sergelius et al.[17] investigated the quantum oscillations and band topology of the Weyl semimetal NbP. They performed dHvA measurements on a single crystal sample along the major crystal axes. The raw oscillation data contained contributions from multiple conduction bands. By fitting to a summation of damped sine functions, they extracted parameters for the individual bands. Two bands with low cyclotron masses of 0.048 m_0 and 0.086 m_0 displayed non-trivial π Berry phases, indicating Dirac-type dispersions. The remaining bands had higher effective masses and trivial Berry phases, suggesting conventional parabolic bands. One Dirac band sat just 3.74 meV from the Fermi level, agreeing with predictions that a small shift could activate exotic Weyl node properties. Despite simplicity of the measurement technique, fitting the complex data enabled thorough characterization of band topology and scattering, unattainable by transport methods alone. The significance of this work is twofold. Firstly, it demonstrates that quantum oscillation analysis, complemented by topological band theory, can deeply probe the electronic structure of WSMs even when multiple conduction channels are present. Secondly, it provides experimental evidence that the intrinsic Fermi level in NbP lies remarkably close to the Weyl nodes. This substantiates theoretical predictions that slight electron doping could stimulate exotic chirality-based transport phenomena. This research highlights how specialized measurement and fitting procedures can uncover rich physics even in quantum materials with complex band structures. The results motivate further efforts to access and control topological band crossings in Weyl semimetals. Clever analysis to disentangle overlapping quantum oscillation frequencies promises deeper insight into these states of matter.

Guo et al.[49] systematically investigated the high pressure phase diagrams of the TaAs family compounds (NbP, NbAs, TaP and TaAs) using ab initio random structure searching and DFT calculations. They found that NbAs and TaAs undergo similar structural transitions from the ambient pressure $I4_1md$ phase to high pressure hexagonal P-6m2, monoclinic P21/c and finally cubic Pm-3m phases under compression. Interestingly, the electronic structure of the P-6m2 phase in

NbAs contains both Weyl points and triple degenerate points, analogous to high pressure P-6m2 TaAs[50]. In contrast, NbP and TaP display different high pressure behaviors, transitioning to Cmcm and Pmmn phases before forming the P21/c structure at higher pressures. All the predicted high pressure phases were found to be metallic. The results systematically map out pressure-induced topological phase transitions across the TaAs family of WSMs. The emergence of mixed Weyl and triple point topological states in the intermediate hexagonal phase highlights opportunities for realizing unusual transport phenomena.

Wu et al.[51] investigate a recently discovered Weyl semimetal, NbP, which was presumed to exhibit exclusively type-I Weyl points. Their study reveals that a group of Weyl points in NbP are actually type II. This has important implications for properties like the chiral anomaly and large photocurrents. By analyzing the electronic structure of NbP, Shu et al. find strong tilting of the Weyl cone approximately 17° off the k_z axis for one group of Weyl points. At these type-II Weyl points, the bulk Fermi surface forms linearly touching electron and hole pockets instead of shrinking to a point. Surface calculations reveal linearly crossing surface state bands terminating at projections of the type-II Weyl points. While NbP was previously considered to host only type-I Weyl points, the results definitively identify coexistence of type-I points near $k_z = 0$ and type-II points at $k_z = \pm\pi/c$. The discovery that NbP hosts type-II in addition to type-I Weyl points is significant, as the emergent Weyl fermions will exhibit distinct properties. With possible electron doping to access the type-II Weyl points experimentally, observations of an anisotropic chiral anomaly and large photocurrents are now feasible in NbP. More broadly, the results challenge conventional assumptions about band topology equivalency among Weyl semimetal compounds, motivating further searches for hidden type-II Weyl points in related materials.

Niemann et al.[52] explored chiral MR in the Weyl semimetal NbP. Weyl semimetals host exotic quasiparticles called Weyl fermions, which exhibit the chiral anomaly - negative MR when electric and magnetic fields are parallel. Intrinsic NbP's Weyl points lie far from the Fermi energy, hindering observation of this effect. By lowering the Fermi energy via Ga doping, the authors activated the W2 Weyl points just 5 meV above the Fermi level. Consequently, they observed a robust negative MR up to room temperature when the magnetic field was parallel to the current, considered a signature of the chiral anomaly. Analysis of quantum oscillations and band structure calculations confirmed the Weyl point positions and Fermi level shift. Activating Weyl points by materials engineering could enable applications and further explore Weyl physics. Through Ga-focused ion beam etching, the authors fabricated NbP microribbons with average 2% Ga incorporation, lowering the Fermi energy 10 meV above intrinsic levels. Magnetotransport measurements revealed six SdH oscillation frequencies, matched to calculated orbits to identify band positions. Non-metallic temperature-dependent resistivity and linear transverse MR were also observed. Tilting the magnetic field parallel to the applied current yielded negative MR obeying $\cos^2(\phi)$ angle-dependence and quadratic-to-linear positive magnetoconductance with magnetic field, confirming chiral anomaly origin. The effect persisted up to room temperature, attributed to further Ga ionization at higher temperatures. This realization of chiral anomaly and activation of Weyl points by strategic doping opens possibilities for accessing Weyl physics and applications. The robust negative MR could be interesting for Weyl electronics.

Fu et al.[53] investigated the topological properties of the Weyl semimetal NbP after hydrogen and helium ion irradiation using DFT simulations. This study focuses on analyzing the changes in electronic band structures and DOS caused by different types of point defects, revealing their effects on protected band crossing nodes known as Weyl points. Understanding defect influences is significant for potential low-energy electronic applications of WSMs. The authors simulated the irradiation process and defect formation in NbP using time-dependent DFT. They determined the most stable defect configuration to be an interstitial H atom. Calculations of the electronic structures show that various defects impact the Weyl points to different extents. Interstitial H and He lift the Fermi level and break four-fold degenerate bands into two-fold, slightly opening some band crossings when including SOC. Nb vacancies also reduce topological properties, but P vacancies leave Weyl points intact. While substituted H atoms at Nb sites do not repair vacancies, substituted He at P sites does break topology. Overall, defects cause band splitting and Fermi level shifts, disrupting symmetrically-protected degeneracies. Formation energy analysis further confirms H interstitials as the most easily formed and stable defects. This study elucidates the microscopic mechanisms modifying topological electronic properties in a WSMs via point defects. The results suggest defect engineering may enable controlled manipulation of electronic band structures.

Tilmann et al.[54] investigate the linear and nonlinear optical properties of epitaxially grown NbP thin films. They compare the performance of the NbP films to NbP bulk crystals, aiming to assess the potential of Weyl semimetal thin films for on-chip applications. The authors first characterize a 16 nm thick NbP (001) film grown on an MgO substrate. Spectral ellipsometry reveals a relatively wavelength-independent refractive index combined with a large, semimetallic extinction coefficient. Notably, the thin film exhibits a very high third-harmonic generation efficiency exceeding $10^{-4}\%$, over 12 times greater than the bulk crystal. Moreover, sub-10 fs pump-probe measurements demonstrate an ultrafast modulation depth reaching 1%, completely decaying within 100 fs. This contrasts the bulk crystal dynamics dominated by optical absorption effects. The enhanced nonlinear optical response is attributed to interaction with the topological surface states in the penetrating pump light. This study reveals NbP thin films as a promising platform for nanophotonic devices, outperforming bulk crystals. The combination of efficient frequency conversion, ultrafast modulation capabilities, and integrability with top-down fabrication could enable applications in on-chip all-optical switching and processing. The results motivate future research into Weyl semimetal nanophotonics harnessing strong light-topology interactions.

In wrapping up this part of the literature review concerning NbP, we point out that several studies have elucidated details of the electronic band structure, Fermi surface topologies, and associated topological properties of NbP[47]. However, opportunities remain to further investigate the dependence of these fundamental quantum properties on external perturbations[43]. Targeted computational and experimental work quantifying the evolution of topological invariants, Berry curvatures, and intricate Fermi surfaces in NbP under varied bias potentials conditions constitutes a promising research direction[55]. Advancing techniques to map phase boundaries and characterize emergent phenomena linked to underlying band topology changes will uncover new means of dynamically controlling exotic transport properties in NbP[47, 52].

Chapter 3

Topological Materials Overview

In this chapter, we explore the intricate world of topological materials, a field that combines the concepts of topology with the study of condensed matter physics. We start with an exploration of topology in physics, setting the stage for a detailed examination of topological semimetals, including DSMs and WSMs. We delve into the topological signatures of Weyl points, emphasizing the roles of the Berry phase, Berry curvature, Chern number, and the emergence of Fermi arcs. The chapter then transitions to discussing the two-dimensional material graphene. Following this, we analyze carrier transport in topological materials, emphasizing their unique properties. The discussion culminates in a comprehensive look at QPTs, particularly focusing on TQPTs. Throughout this chapter, we adopt the convention of setting the reduced Planck constant $\hbar = 1$.

3.1. Topology in Physics

Topology is a branch of mathematics that deals with properties preserved under continuous deformations. Its introduction into physics, particularly in understanding quantum states, marks a paradigm shift in how we comprehend materials and their phases. Unlike traditional views which rely on symmetry-breaking, topological concepts offer a novel perspective, focusing on global properties that remain invariant under continuous transformations. This shift in approach is exemplified by the famous topological invariant, the Chern number[56], which characterizes distinct quantum states in a non-trivial manner.

The significance of topology in physics was historically rooted in the study of quantized Hall effects, where the Hall conductance was quantized in units of e^2/h, with e being the electron charge and h the Planck constant. This quantization, as Thouless et al. demonstrated[57], can be linked to a topological invariant, specifically the Chern number, which underlies the quantized Hall conductance and exemplifies how topological concepts significantly enhance our understanding of physical phenomena. The concept of Berry phase, a geometrical phase acquired over a cycle in parameter space, further enriched this understanding[58]. In condensed matter, this manifests in the robustness of edge states in TIs, defying the conventional wisdom of band theory and opening a new frontier in material science.

Furthermore, the application of topological concepts in physics extends beyond theoretical elegance; it has practical implications in the search for novel materials. For instance, the prediction and subsequent discovery of TIs, materials that are insulating in the bulk but conduct electricity on their surfaces or edges, have opened avenues for revolutionary applications in electronics and spintronics[59]. These materials exhibit edge states that are protected by topological invariants, leading to robustness against disorder and potential use in quantum computing.

3.2. Topological Semimetals

In recent years, the study of electronic structure topology of crystalline materials has become a significant area of interest in condensed matter physics. This shift in focus was initially sparked by the groundbreaking discovery of TIs[59–61]. More recently, the attention has turned to topological semimetals, which are closely related to TIs but with some key differences. Topological semimetals have a continuous, or 'gapless', spectrum, meaning they don't have the energy gap found in TIs. Instead, a transition is needed to create a gap in these materials.

The unique characteristic of topological semimetals lies in their gapless nature, which is protected by specific properties within their structure, known as topological charges. These charges are found in the BZ and are defined by topological invariants. While TIs and semimetals differ in their energy gap properties, they share a common feature: both are significantly influenced by SOC. This coupling plays a crucial role in the formation of their distinct structures.

Another interesting aspect of topological semimetals is their role as a transitional phase between different types of insulators. They are seen as a bridge linking two insulating phases, each characterized by fully gapped bands. During this transition, a band closing is necessary to change the topology of the material. In the bulk of these materials, there's an intersection of two or more bands at certain points, leading to linear dispersion near these crossing points. A well-known example of this phenomenon is the appearance of Dirac cones, which are seen in materials like graphene[62]. These cones are points where four bands meet and require the presence of both time-reversal (T) and inversion (I) symmetry. Additional symmetries may also be involved to protect these nodal points from perturbations.

Topological semimetals are categorized into two main types based on the crystal's symmetry: DSMs and WSMs[63–76]. The experimental realization of both types[77–81] has significantly advanced the field of condensed matter research, placing it at the forefront of contemporary scientific exploration. This progress has not only expanded our understanding of these materials but also opened up new possibilities for their application in various technological fields.

3.2.1. Dirac Semimetals

Dirac semimetals have significantly influenced the field of condensed matter physics, especially in the realm of topological phases of matter. These materials are characterized by the existence of Dirac points (or Dirac nodes) where the conduction and valence bands intersect linearly. This intersection creates relativistic Dirac fermions as low-energy excitations, a phenomenon originally proposed in the context of quantum field theory[68]. The realization of these quasiparticles in a solid-state system represents a notable achievement, bridging high-energy physics and condensed matter physics, and enriching our understanding of the quantum mechanical nature of electrons[77].

This intersection of bands is protected by symmetry, resulting in a robust, gapless state under specific conditions, such as the presence of T and I symmetry[70]. The theoretical underpinnings of DSMs can be traced back to Dirac's pioneering work in 1928, where he presented a complete quantum theory that was consistent with the postulates of special relativity[82]. The Dirac equation, formulated in a 3D space with the speed of light set to $c = 1$, is[83]:

$$\left(i\gamma^{\mu}\partial_{\mu} - m\right)\psi = 0, \tag{3.1}$$

where $\mu = 0, 1, 2, 3$ label time and space dimensions, γ^{μ} are the 4×4 Dirac matrices, m is the mass of an electron, and ψ represents a 4-component wave-function describing the electron. This equation describes the dynamics of the electron as a relativistic quantum particle, introducing the concept of spin and laying the groundwork for the understanding of topological materials[82, 83].

The Hamiltonian derived from Eq. 3.1 plays a central role in the theory of topological materials. In the presence of T and I symmetry, a 3D Dirac fermion emerges at the topological phase boundary between a normal insulator and a topological insulator (TI)[84]. This is described by the

Hamiltonian[85–87]:

$$H(\boldsymbol{k}) = \begin{pmatrix} +v_F \boldsymbol{\sigma}.\boldsymbol{k} & m \\ m & -v_F \boldsymbol{\sigma}.\boldsymbol{k} \end{pmatrix}, \tag{3.2}$$

where $\boldsymbol{k}$ is the momentum vector, v_F is the Fermi velocity, m is the mass, and $\boldsymbol{\sigma}$ represents the Pauli matrices, describing spin degrees of freedom.

This Hamiltonian describes two Weyl fermions of opposite chirality at the same time-reversal invariant momentum point in the BZ. Its off-diagonal entry, m, mixes the two Weyl fermions and opens up a gap of magnitude $2m$[84, 88]. At the critical point of the transition, defined by $m = 0$, the mass term vanishes, indicating the closure of the bulk gap and the disappearance of the intrinsic energy scale that separates gapped and gapless regimes[89]. In the framework of quantum criticality, the vanishing mass defines the quantum critical point where the correlation length diverges and scale invariance emerges, reflecting the absence of any finite energy cost for particle-hole excitations at $k = 0$[90]. This parallels the standard QPT phase diagram, in which tuning a non-thermal control parameter to its critical value drives a continuous transition characterized by the collapse of an energy gap and the onset of long-range critical fluctuations[91]. Near $m = 0$, low-energy excitations exhibit linear dispersion across all length scales, marking a scale-invariant Dirac semimetal that sits at the boundary between topologically distinct insulating phases[92]. Renormalization-group analyses further show that the mass term is the only relevant perturbation at this fixed point, so its vanishing corresponds directly to the collapse of a tuning parameter energy scale at the QCP[93]. Thus, $m = 0$ not only signals gap closing but also pinpoints the disappearance of the characteristic mass energy scale at the quantum critical point, unifying the topological transition with the broader theory of continuous quantum phase transitions. In fact, at the critical point of the transition, defined by $m = 0$, the spectrum of Eq. 3.2 is gapless at $k = 0$, resulting in a 4-fold degenerate point node with linear dispersion, called a Dirac point[68–70, 94–97], leading to a stable DSM phase.

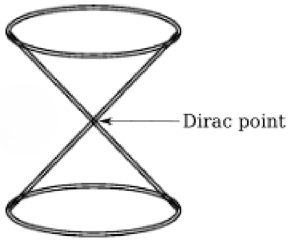

Figure 3.1: Dirac semimetal with T and I symmetry consisting of two copies of identical Weyl cones. The Dirac point lies between two doubly degenerate levels[98].

As a bridge between topological and normal insulators, DSMs represent a phase of matter where the conduction and valence bands touch only at discrete points, leading to a zero band gap. Additionally, a DSM can undergo phase transitions into exotic phases, such as WSMs, making it an ideal candidate as a parent compound for studying these states and the phase transitions that occur[68–70].

3.2.2. Weyl Semimetals

In 1929, Hermann Weyl proposed a seminal concept in the realm of quantum mechanics and particle physics. He noted that the Dirac equation, which describes the behavior of fermions, simplifies notably when the mass term is set to zero, leading to the theoretical conception of Weyl fermions[99, 100]. These massless particles are characterized by a distinctive property known as chirality, making them either left-handed or right-handed. This conceptual framework laid the foundation for understanding the behavior of fermions in various physical systems, including condensed matter.

The significance of Weyl fermions extends beyond theoretical physics into the realm of condensed matter, particularly in the study of WSMs. In these materials, the concept of chirality is not merely a theoretical construct but manifests in the form of Weyl nodes (or Weyl points). These nodes, which are points where conduction and valence bands touch, carry topological charges that can be conceptualized as monopoles and anti-monopoles of Berry flux in momentum space[75]. Remarkably, these topological charges are protected only by the translational invariance of the crystal. This unique feature implies that the topological Weyl phase can only be disrupted by annihilating Weyl nodes with opposite charges in k-space, without breaking any symmetries.

The emergence of Weyl fermions as low-energy excitations in WSMs is conditioned on the breaking of either Time-reversal (T) or Inversion (I) symmetry, or both. This condition is critical as it prevents the bands from being double degenerate throughout the system, which would otherwise result in a Dirac material characterized by a 4-fold degenerate touching point. In a 3D system, the occurrence of Weyl nodes, or points of band touching, is thus a direct consequence of the broken symmetries, with these nodes appearing at an even number of momenta close to the Fermi energy.

A deeper understanding of Weyl fermions is gained by examining the Dirac equation in the case of a massless particle ($m = 0$). In this case, the Dirac equation simplifies to:

$$i\partial_t \psi_\pm = H(\boldsymbol{k})\psi_\pm, \tag{3.3}$$

where ψ_+ and ψ_- (or $\psi_\pm$) are two component Weyl spinors and the massless Hamiltonian, known as Weyl's Hamiltonian, is written:

$$H(\boldsymbol{k}) = \pm v_F \boldsymbol{\sigma}.\boldsymbol{k}, \tag{3.4}$$

where the ± sign represents the chirality of the Weyl points. This formulation not only outlines the existence of two types of fermions with opposite chirality but also reveals that chiral particles have their spin direction locked to momentum, as evident in Eq. 3.4. The energy eigenvalues at the Weyl nodes are given by $E = \pm v_F p$, depicting right or left-moving particles. These nodes intersect at $p = 0$ and are central to the study of WSMs.

In the ultrarelativistic limit, where the mass term m approaches zero, the Dirac equation evolves to represent the dynamics of Weyl fermions. The energy dispersion of the Dirac equation given by:

$$E^2 = c^2 p^2 + m^2 c^4, \tag{3.5}$$

becomes linear, and the off-diagonal terms vanish. As a result, the 4×4 Dirac equation can be viewed as a combination of two 2×2 Weyl equations with opposite signs but shared momentum p. This separation leads to the concept of chirality, a fundamental property in particle physics, indicating the parallel or antiparallel movement of a Weyl fermion to its spin direction. In order to transition from a DSM to a WSM, the breaking of T and/or I symmetry (I) is required. This process causes each Dirac node to split into two separate Weyl nodes of opposite chirality, as shown in the figure below, at opposite momenta $\pm\boldsymbol{k}_0$.

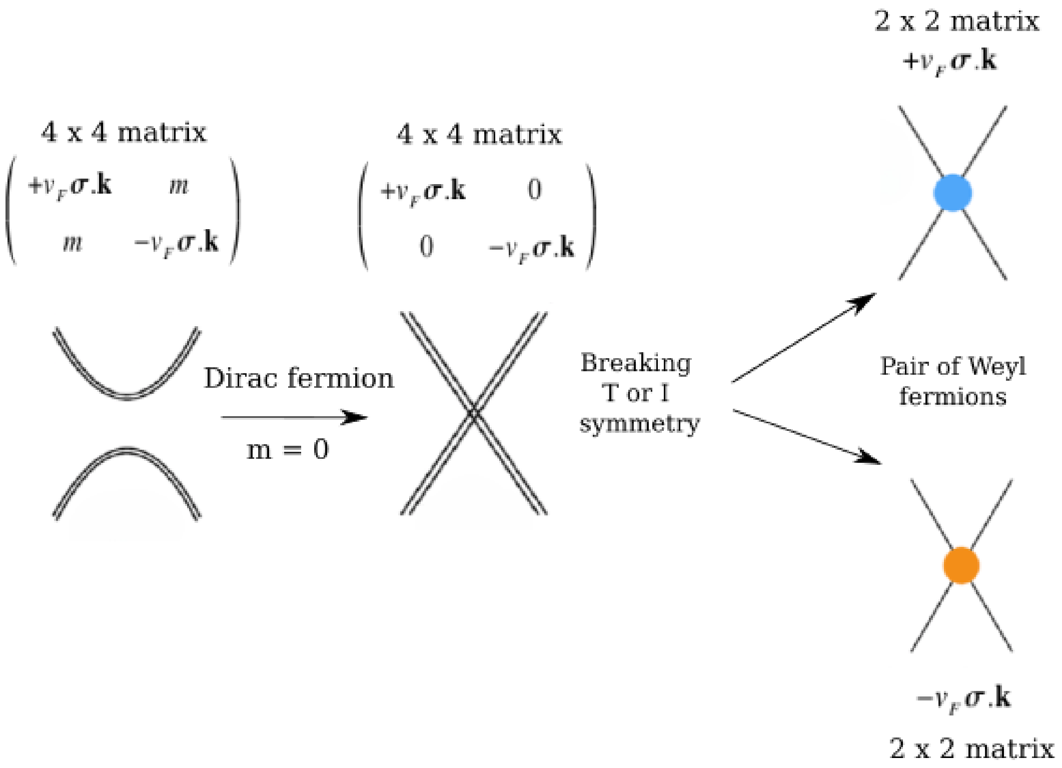

Figure 3.2: From a DSM to a WSM: The breaking of time-reversal symmetry causes a Dirac node, described by four-component Dirac spinors, to split into two separate Weyl nodes, each described by two-component Weyl spinors, of opposite chirality[85, 86].

The presence of chiral electrons in materials like WSMs leads to the phenomenon known as the Chiral anomaly[75]. This describes the adiabatic electron pumping induced by the combined effect of external magnetic and electric fields between Weyl points with opposite chirality. This results in a current along the magnetic field direction, manifesting as negative magneto resistance when the magnetic and electric fields are aligned.

In solid-state physics, chirality manifests through the charge of the Weyl point, characterizing the system's topology. This is particularly evident in the behavior of WSMs, where the non-trivial topology is indicated by the presence of unique surface states known as Fermi arcs. These arcs, represented by open lines on a surface, connect the projection of two Weyl nodes, highlighting the profound interplay between topology and the physical properties of these materials. The topological nature of WSMs is further elucidated by the Berry curvature[101], which provides a means to calculate the chirality and topological invariant. Furthermore, Eq. 3.4 illustrates the resilience of a Weyl node to generic external perturbations. The only way to annihilate a Weyl point is by merging it with another of opposite chirality at the same crystal momentum $\boldsymbol{k}$, highlighting their topological robustness against generic external perturbations. The unique electronic structure of WSMs, characterized by Weyl nodes and protected by topological invariants, serves as an ideal system for investigating Berry phase curvatures and Fermi-level topologies. In this thesis, we examine how these topological features respond to external bias potentials, aiming to identify topologically robust metrics that can predict emergent quantum phenomena.

3.3. Topological signature of Weyl points

Weyl points, essentially monopoles of Berry curvature in momentum space, are characterized by their topological invariants and associated surface states. Understanding these properties requires a grasp of key concepts like the Berry phase, Berry curvature, Chern number, and Fermi arcs.

3.3.1. Berry phase

In quantum mechanics, the concept of wave functions is pivotal, yet their phase is usually not physically significant as it doesn't affect observable quantities. However, in 1984, Berry introduced the concept of a geometric phase with potential observable impacts in certain conditions. This occurs when a quantum system undergoes adiabatic, cyclic transformations.

To understand this phenomenon, consider a quantum system in a stable (or stationary) state, governed by a Hamiltonian $H(\boldsymbol{k})$. According to the Adiabatic Theorem, as described by Messiah[102], if such a system is slowly varied, it remains in an eigenstate of its Hamiltonian. When the Hamiltonian returns to its initial state, the system does too, but with an added phase factor - the Berry phase[58, 103]. Suppose we start with a state $|\psi(t)\rangle$ in an initial eigenstate $\left|\psi\left(t_0\right)\right\rangle = \left|n\left(\boldsymbol{k}\left(t_0\right)\right)\right\rangle$. As this state evolves over time, following the eigenstate $|n(\boldsymbol{k}(t))\rangle$, its representation at time t is given by:

$$|\psi(t)\rangle = e^{i\gamma_n(\boldsymbol{k}(t))} e^{-i\int_{t_0}^{t} dt' E_n(\boldsymbol{k}(t'))} \left|n\left(\boldsymbol{k}\left(t'\right)\right)\right\rangle . \tag{3.6}$$

In this equation, the second exponential term describes the time evolution of the state $|n(\boldsymbol{k}(t))\rangle$. The first phase factor is an additional phase encompassing effects beyond the dynamical phases. Applying the Schrödinger equation to this state, the Berry phase $\gamma_n(t)$ can be expressed as:

$$\gamma_n(t) = i\int_{t_0}^{t} dt' \left\langle n\left(\boldsymbol{k}\left(t'\right)\right)\middle|\frac{d}{dt'}\middle|n\left(\boldsymbol{k}\left(t'\right)\right)\right\rangle = i\int_{k\left(t_0\right)}^{k(t)} d\boldsymbol{k}' \left\langle n\left(\boldsymbol{k}'\right)\middle|\nabla_{\boldsymbol{k}'}\middle|n\left(\boldsymbol{k}'\right)\right\rangle . \tag{3.7}$$

In the context of the BZ, when $\boldsymbol{k}\left(t_0\right) = \boldsymbol{k}(t)$, this corresponds to a closed loop in parameter space:

$$\gamma_n(C) = i \oint_C d\boldsymbol{k} \left\langle n(\boldsymbol{k}) \left| \nabla_{\boldsymbol{k}} \right| n(\boldsymbol{k}) \right\rangle, \tag{3.8}$$

where the wave vector $\boldsymbol{k}$ represents the set of parameters undergoing adiabatic changes and the closed path C defines the boundary of the BZ. This equation represents the Berry phase, a key element in understanding the wave function's topology and its implications for transport properties in topological materials.

Using the Kelvin-Stokes theorem[104, 105], we can express the Berry phase in a more tangible form as follows:

$$\gamma_n(C) = i \oint_C d\boldsymbol{k} \left\langle n(\boldsymbol{k}) \middle| \nabla_{\boldsymbol{k}} \middle| n(\boldsymbol{k}) \right\rangle = \oint_C d\boldsymbol{k} \boldsymbol{A}_n(\boldsymbol{k}). \tag{3.9}$$

Here, $\boldsymbol{A}_n(\boldsymbol{k})$ denotes the Berry connection, analogous to a vector potential in this context. An important aspect of the Berry connection is its behavior under gauge transformations, which are transformations of the form $|n(\boldsymbol{k})\rangle \rightarrow e^{i\phi n(\boldsymbol{k})}|n(\boldsymbol{k})\rangle$. Under such a transformation, the Berry connection changes according to the rule

$$\boldsymbol{A}_n(\boldsymbol{k}) \rightarrow \boldsymbol{A}_n(\boldsymbol{k}) - \nabla_{\boldsymbol{k}} \phi_n(\boldsymbol{k}). \tag{3.10}$$

This change highlights the non-invariance of the Berry connection under gauge transformations, a critical point in understanding its properties and implications

3.3.2. Berry curvature

The Berry curvature emerges as a pivotal attribute encapsulating the geometric properties of eigenstates within the BZ. Its essence lies in the quantification of the Berry phase. In essence, it's akin to an effective, pseudo magnetic field, but intriguingly, it exists in the reciprocal space, a realm fundamental to understanding wave phenomena in solids. This unique perspective allows for a deeper insight into the behavior of electronic states in various materials, particularly those exhibiting topological properties.

To delve into its mathematical formulation, we express the Berry curvature using the curl of the Berry connection $\boldsymbol{A}_n(\boldsymbol{k})$. This is elegantly captured by the equation:

$$\Omega_n(\boldsymbol{k}) = \nabla_{\boldsymbol{k}} \times \boldsymbol{A}_n(\boldsymbol{k}). \tag{3.11}$$

Here, $\Omega_n(\boldsymbol{k})$ represents the Berry curvature for the n^{th} band at a given wave vector $\boldsymbol{k}$. The term $\nabla_{\boldsymbol{k}}$ denotes the gradient with respect to the wave vector, symbolizing the change of the phase space across the BZ.

This formulation offers a window into the geometric nature of quantum states. By exploring the distribution and behavior of the Berry curvature, we gain valuable insights into the electronic properties of materials. It aids in understanding phenomena like the anomalous Hall effect and TIs, where the interplay of geometry and electronic structure leads to exotic and potentially useful electronic behavior.

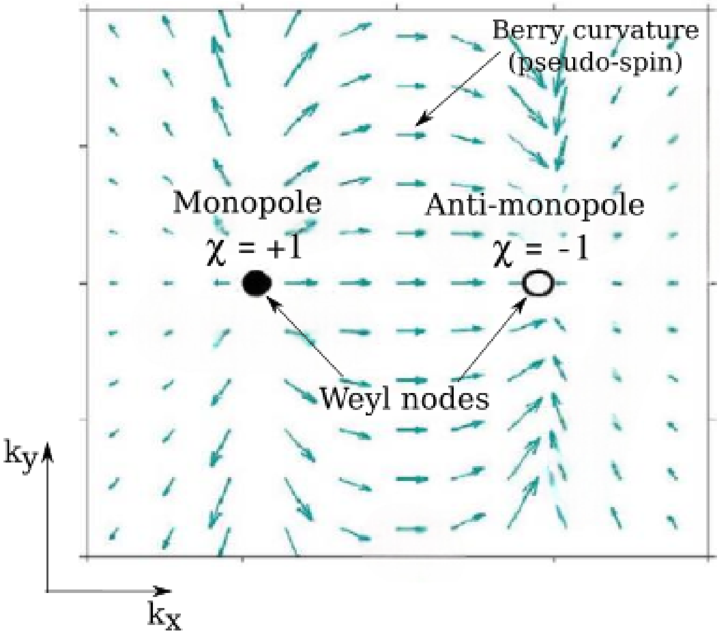

Figure 3.3: The vector plot of the Berry curvature in two-dimensional (2D) momentum space. The arrows indicate that the flux of the Berry curvature flows from the source (monopole) to the drain (anti-monopole) of the Berry connection, defining the non-trivial topological properties of a topological semimetal[86].

Applying Stoke's theorem transforms the Berry phase, as presented in Eq. 3.12, into a function of the Berry curvature, $\Omega(\boldsymbol{k})$:

$$\gamma_n(C) = \oint_C d\boldsymbol{k}\boldsymbol{A}_n(\boldsymbol{k}) = \iint_S d^2\boldsymbol{k}\Omega_n(\boldsymbol{k}). \tag{3.12}$$

This is analogous to Gauss's law in magnetism, where the total Berry curvature flux across the entire BZ equals zero. However, it is possible to choose closed surfaces within the BZ where this flux is non-zero. For example, Weyl points in the BZ behave similarly to magnetic monopoles in momentum space. They either emit or absorb Berry curvature flux. The net flux passing through a surface that encloses a Weyl point gives us an important topological invariant, known as the Chern number. This invariant is crucial for understanding the topological properties of the material.

Understanding and calculating the Berry curvature is not just a theoretical endeavor; it has practical implications. For instance, in the growing field of topological materials, the study of Berry curvature helps in predicting and explaining novel quantum phenomena that could be harnessed for advanced technological applications, such as spintronics and quantum computing. This exploration deepens our understanding of the electronic behavior of materials, paving the way for the development of new materials with tailored electronic properties.

3.3.3. Chern number

In the study of band structures of topological materials, the Chern number emerges as a fundamental concept. This integer value, deeply rooted in topological invariants, serves to distinguish the global characteristics of a band structure. For a given band, the Chern number is determined by integrating the Berry curvature across the full BZ. In a 2D space, the Chern topological invariant for the n^{th} band, also known as the first Chern number, is defined as follows[101, 106]:

$$C_n = \frac{1}{2\pi} \oint_C d\boldsymbol{k} \boldsymbol{A} n(\boldsymbol{k}) = \frac{1}{2\pi} \iint \boldsymbol{S} d^2 \boldsymbol{k} \Omega_n(\boldsymbol{k}). \tag{3.13}$$

This expression reveals that the Chern invariant is effectively a Berry phase, normalized by a factor of 2π.

The Chern number assumes only integer values. Its sign also indicates the chirality of the node. Notably, a Chern number of $|C| = 1$, computed for a single node, correlates with linear band dispersion. Conversely, a higher value, like $|C| = 2$, suggests parabolic or more complex dispersion patterns. It's important to mention that the curvature's flux through the entire BZ boundary must be zero to prevent curvature divergences, implying that the system can only have an even number of Weyl points. Additionally, the minimum number of Weyl nodes in the system depends on the presence of specific symmetries, either T or I.

It's worth nothing that the Chern invariant is not always uniquely defined; in cases of band degeneracies, its value can depend on the chosen gauge. Nevertheless, the total Chern invariant, which sums the Chern invariants of all occupied bands, remains a unique integer, provided there's a finite gap between filled and empty bands:

$$C = \sum_n^{occ.} C_n. \tag{3.14}$$

This concept of the Chern number not only encapsulates the intricate relationship between topology and band theory but also paves the way for understanding and predicting novel phenomena in materials science. Its implications extend to various applications, from explaining the unique properties of topological materials to aiding in the design of materials with tailored electronic properties.

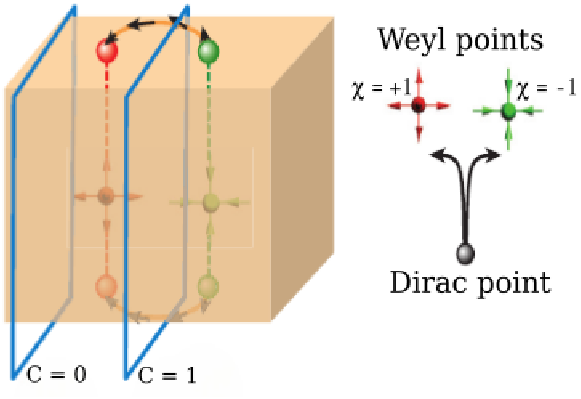

Figure 3.4: Illustration of Chern number calculation in the BZ depicting topological trivial (C = 0) and non-trivial (C = 1) phases. The Chern number in non-zero between the Weyl points and zero everywhere else. A non-zero Chern number indicates the existence of edge states in topologically non-trivial materials[107].

3.3.4. Fermi arcs

In WSMs, a distinctive phenomenon known as Fermi arcs arises, characterized by open-ended arcs on the surface BZ. These arcs are crucial in linking the projections of Weyl points with opposing chirality and serve as a hallmark of the nontrivial topological characteristics inherent in the bulk band structure of these materials. Specifically, Fermi arcs epitomize the unique electronic states that emerge due to this intricate topology[63].

Similarly, topological materials are known for their surface states, which are inherently linked to the boundaries of the material. These states' properties are directly influenced by the topological nature of the bulk band structure. In the context of WSMs, these surface states materialize as Fermi arcs. These arcs are not just structural features; they provide tangible evidence of the non-trivial topological properties inherent in these materials.

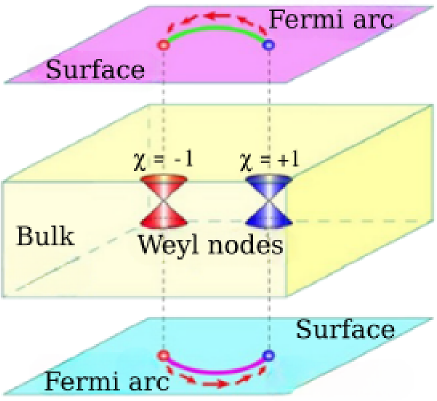

Figure 3.5: Schematic representation of a WSM featuring spin-polarized Fermi arcs on its surfaces, linking the projections of two oppositely chiral weyl nodes. The red arrows on the surfaces depict the spin texture of the Fermi arcs[108].

It should be mentioned that DSMs also exhibit Fermi arcs as surface states. However, in DSMs, these Fermi arcs present a more nuanced characteristic. This subtlety arises because the bulk Dirac points in these materials possess a zero Chern number, distinguishing them from their counterparts in WSMs. Conceptually, one can interpret a Dirac point as a stable convergence of two Weyl points of opposite chirality, occurring at the same momentum $\boldsymbol{k}_0$. This interpretation leads to an understanding of the surface states in DSMs as a projection of the two Weyl node-derived arcs onto the same surface momentum. This phenomenon results in what are termed as double Fermi arcs[76].

This intricate interplay between the topological properties of the bulk band structure and the resulting surface states, whether in WSMs or DSMs, not only underscores the complex nature of these materials but also highlights the profound implications of topology in dictating the behavior of quantum materials.

3.4. Exploring the plane of graphene

The relationship between symmetry, dimensionality, and material properties forms a cornerstone in condensed matter physics. A key process in the transition from 3D bulk materials to planes of atomic thickness is exfoliation, which enables the creation of monolayer materials. Through exfoliation, materials are thinned to single atomic layers, leading to quantum confinement effects where electrons are limited to movement within a 2D plane. This confinement significantly alters electronic behavior, offering distinct properties unseen in their 3D counterparts. Such changes are exemplified in the class of 2D materials, which are the focus of considerable scientific inquiry following the pioneering isolation of graphene[109, 110], as shown in Fig. 3.6.

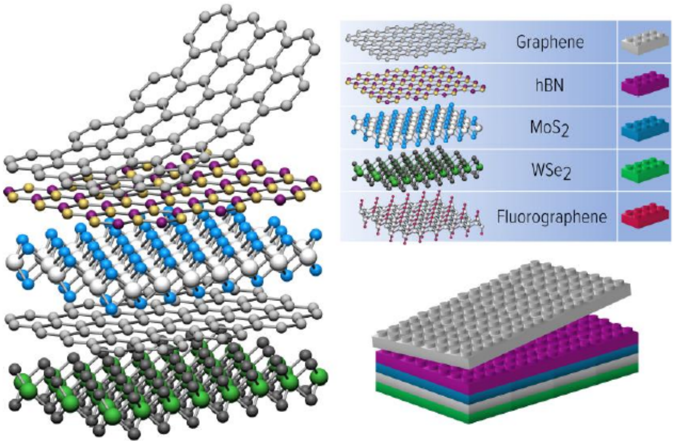

Figure 3.6: Layered structures of 2D materials[111].

Despite initial doubts about the stability of 2D materials, the successful isolation and analysis of graphene in 2004 overturned previous assumptions[112]. It was once thought that materials with lower dimensionalities could not withstand thermal vibrations at nonzero temperatures, likely disintegrating[113]. This theory seemed supported by observations of reduced melting points in materials as their thickness was reduced[114, 115]. Yet, the extraordinary mechanical and thermal stability observed in graphene countered these theories, solidifying its status as a robust 2DM. The process of peeling graphene layers from graphite is illustrated in Fig. 3.7[109, 110].

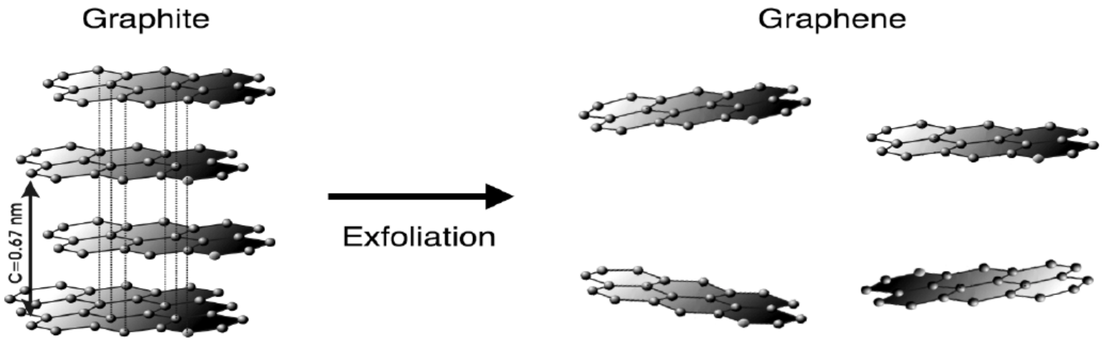

Figure 3.7: The exfoliation of graphene from Graphite[116].

Graphene is renowned not only for its thinness but also for its exceptional strength. It is composed of a honeycomb lattice where each carbon atom is connected to three others[117, 118], giving rise to a myriad of remarkable properties. These include high electrical and thermal conductivity, due to its efficient carrier mobility, and superior mechanical flexibility[119]. The diverse applications of graphene span from electronic devices like transistors[120] and integrated circuits[121], to novel uses in sensors[122], energy storage[123], DNA sequencing[124], and water purification[125]. Its utility extends further into developments in flat-panel displays, solar cells, and spintronic devices[126].

The unique quasi-particle dynamics within graphene's lattice are characterized by massless electrons moving ballistically, described by the Dirac equation[62, 127]. This peculiar movement was evidenced with the observation of the anomalous quantum Hall effect in 2005, which confirmed the presence of a Berry phase in massless Dirac fermion systems[128–130].

Building on the foundational studies of graphene, this thesis explores the implications of reduced dimensionality on the electronic properties of $SrSi_2$. It is hypothesized that $SrSi_2$ adapted onto a graphene-like lattice exhibits similar transport phenomena due to akin energy spectra, despite the presence of massless fermions and lifted degeneracies at the nodal points. This study also delves into the changes in quasi-particle behavior transitioning from Dirac to Weyl fermions due to symmetry breaking and significant SOC, which is crucial for spintronics[131–136].

3.5. Carrier transport in topological materials

Topological materials, particularly DSMs and WSMs, represent a frontier in condensed matter physics, offering unique electron transport characteristics due to their non-trivial band topology. These materials, characterized by their gapless band structures and linear dispersion relations near the Dirac or Weyl points, exhibit fascinating electronic properties with significant implications for next-generation electronic devices[76].

In DSMs, electrons behave as Dirac fermions due to the linear crossing of conduction and valence bands at discrete points in the BZ. The Hamiltonian describing these Dirac points is given in Eq. 3.2. This linear dispersion leads to a high mobility of charge carriers and unusual quantum phenomena such as the Klein tunneling[73]. Weyl semimetals, a subset of Dirac materials, lack T or I symmetry, leading to pairs of Weyl points with opposite chirality. The low-energy excitations near these points can be described by the Weyl Hamiltonian in Eq. 3.4. The chiral anomaly in these materials enables unusual transport phenomena like the chiral magnetic effect and negative MR[137].

The unique band structures of DSMs and WSMs also lead to anomalous Hall effects, where transverse conductivity arises even without an external magnetic field, governed by the Berry curvature of the bands[58]. This effect is particularly pronounced in WSMs, where the Berry curvature diverges at the Weyl points, contributing significantly to their anomalous Hall conductivity.

Furthermore, these materials exhibit a strong sensitivity to external perturbations like strain or electromagnetic fields, which can be used to engineer their electronic properties. This tunability, combined with the high mobility of carriers and robustness against disorder, positions Dirac and Weyl materials as promising candidates for applications in high-speed electronics and spintronics[107]. The transport properties of DSMs and WSMs are a testament to the intricate interplay between their topological aspects and electronic structure. Their study not only advances our understanding of fundamental physics but also opens up avenues for innovative material applications in technology.

3.6. Topological quantum phase transitions

In the realm of condensed matter physics, the study of phase transitions, where materials alter their physical state under varying conditions such as temperature or pressure, reveals fascinating insights. A notable example is the QPT, which occurs not from thermal fluctuations but from quantum fluctuations at absolute zero temperature (0 K). These transitions mark changes between different quantum states and are crucial in understanding the behavior of materials under extreme quantum conditions[89, 138, 139].

Unlike classical phase transitions that depend primarily on temperature variations, QPTs are driven by changes in quantum mechanical parameters such as pressure, magnetic field, or the chemical composition through doping. Here, the quantum properties of materials come to the forefront. For instance, at zero temperature, materials like metals can transition into superconductors or from a metallic to an insulating state - a phenomenon driven by the underlying quantum mechanics rather than thermal energy[140].

The theoretical understanding of these phenomena relies on concepts such as scale invariance, criticality, and universality. Techniques such as the renormalization group theory are instrumental in exploring these transitions across different scales, providing a cohesive picture from microscopic quantum fluctuations to macroscopic observable properties[141].

Building upon the foundation of QPTs, the discourse extends into the domain of TQPTs, which involve changes in the topological order of a system's ground state. These transitions are characterized by the topological invariants, quantifiable metrics that remain robust against perturbations and are insensitive to local disturbances[59, 142, 143].

In the context of electronic materials, topological changes are often initiated by SOC, which can alter the topology of the electronic bands, as depicted in Fig. 3.8. SOC can cause the band structure to invert, transitioning a system from a trivial insulator to a metallic state or even to a topological insulator, showcasing a new bandgap opened by topological changes[144].

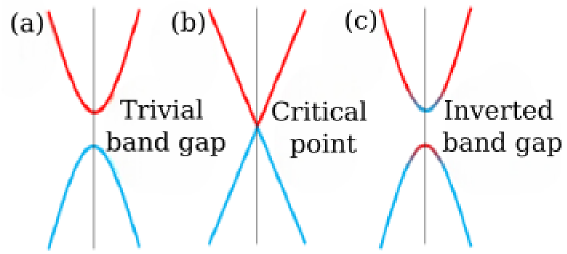

Figure 3.8: Topological QPT in the electronic band structure. (a) Trivial band insulator, (b) Closure of the gap at a critical point, and (c) Inverted band with orbital character swap of the two states at the symmetry point.

Experimentally observing these transitions often requires precise manipulation of conditions to induce and detect changes in the band structure, with tools like electromagnetic fields or piezoelectric responses being crucial[57, 145–147]. Such experiments not only confirm theoretical predictions but also contribute to the development of technologies leveraging the unique properties of topological materials, such as energy-efficient electronic devices that operate with minimal power loss[73].

Moreover, integrating materials with topological properties, like graphene and other Dirac materials, into devices ensures the stability of their quantum states against disturbances. This attribute is particularly beneficial in applications like spintronics and nanophotonics, where maintaining coherence and reducing energy loss are paramount[148, 149].

Chapter 4

Theoretical Framework

In this chapter, we cover the essential theoretical groundwork required for computationally solving the electronic structure challenges in systems composed of many interacting particles. We focus on DFT, a central methodology used in this thesis, to predict physical properties based on the ground state electron density. Additionally, we discuss the TB model, a key approach to understanding graphene's characteristics and the behavior of electrons in solid materials. For our discussions, we use atomic units, where the values of fundamental constants are simplified to unity. In this system, the electron charge (e*), the electron mass (*m_e*), the reduced Planck constant (*$\hbar$*), and the permittivity of free space (*$1/4\pi\epsilon_0$*) are all set equal to one:* $e = m_e = \hbar = 1/4\pi\epsilon_0 = 1$.

4.1. The many-body problem in quantum mechanics

In the realm of quantum mechanics, the electronic structure of quantum-mechanical systems, such as atoms, molecules, and crystalline solids, is fundamentally governed by the Schrödinger equation. The time-dependent Schrödinger equation provides a comprehensive framework for these systems, but for practical purposes, especially in the absence of time-dependent interactions, the time-independent Schrödinger equation is often the focus of study.

4.1.1. The Schrödinger equation in quantum mechanics

The journey into the electronic structure of quantum-mechanical systems begins with the full many-body time-independent Schrödinger equation:

$$\hat{H}\Psi(\mathbf{x}_i, \mathbf{R}_k) = E\Psi(\mathbf{x}_i, \mathbf{R}_k), \tag{4.1}$$

where $\hat{H}$ denotes the exact Hamiltonian operator of the system, and $\Psi(\mathbf{x}_i, \mathbf{R}_k)$ represents the exact many-body wavefunction, formulated with space-spin coordinates $\mathbf{x}_i = \mathbf{r}_i, \sigma_i$ (where $\sigma_i = \pm\frac{1}{2}$) for electrons indexed by i (with $i = 1, 2, 3, ..., N$), and $\mathbf{R}_k$ for nuclei indexed by k (with $k = 1, 2, 3, ..., M$). This equation encapsulates the entire complexity of the quantum system, linking the wavefunction with its associated energy eigenvalue E.

4.1.2. The complexity of quantum systems

Quantum systems are inherently complex, comprising nuclei and electrons, each contributing to a web of interactions. For a crystalline solid, this complexity escalates with a large number of particles, leading to a problem involving $(3N + 3M)$ degrees of freedom, where N and M are the numbers of electrons and nuclei, respectively. The exact Hamiltonian, detailed in its explicit form, represents all interactions within such a system[150–159]:

$$\hat{H} = -\frac{1}{2}\sum_{i=1}^{N}\nabla_i^2 - \frac{1}{2m_n}\sum_{k=1}^{M}\nabla_k^2 - \sum_{i=1}^{N}\sum_{k=1}^{M}\frac{Z_k}{|\mathbf{r}_i - \mathbf{R}_k|} + \frac{1}{2}\sum_{\substack{i,j=1\\ i\neq j}}^{N}\frac{1}{|\mathbf{r}_i - \mathbf{r}_j|} + \frac{1}{2}\sum_{\substack{k,l=1\\ k\neq l}}^{M}\frac{Z_k Z_l}{|\mathbf{R}_k - \mathbf{R}_l|}, \tag{4.2}$$

where m_n represents the nuclear mass in atomic units and Z_k represents the atomic number of each nucleus. This Hamiltonian can be broken down into components representing kinetic and potential energy terms, revealing the intricate nature of the interactions between particles:

$$\hat{H} = \hat{T}_e + \hat{T}_n + \hat{V}_{en} + \hat{V}_{ee} + \hat{V}_{nn}, \tag{4.3}$$

where $\hat{T}_e$ is the kinetic energy operator of the electrons, $\hat{T}_n$ is the kinetic energy operator of the nuclei, $\hat{V}_{ee}$ represents the interaction within pairs of electrons, $\hat{V}_{en}$ represents the electron-nucleus interactions and $\hat{V}_{nn}$ represents the interaction of nuclei with each other.

$$\hat{T}_e = -\frac{1}{2}\sum_{i=1}^{N}\nabla_i^2, \tag{4.4}$$

$$\hat{T}_n = -\frac{1}{2m_n}\sum_{k=1}^{M}\nabla_k^2, \tag{4.5}$$

$$\hat{V}_{en} = -\sum_{i=1}^{N}\sum_{k=1}^{M}\frac{Z_k}{|\mathbf{r}_i - \mathbf{R}_k|}, \tag{4.6}$$

$$\hat{V}_{ee} = +\frac{1}{2}\sum_{\substack{i,j=1\\ i\neq j}}^{N}\frac{1}{|\mathbf{r}_i - \mathbf{r}_j|}, \tag{4.7}$$

$$\hat{V}_{nn} = +\frac{1}{2}\sum_{\substack{k,l=1\\ k\neq l}}^{M}\frac{Z_k Z_l}{|\mathbf{R}_k - \mathbf{R}_l|}. \tag{4.8}$$

Solving the Schrödinger equation for many-body systems is a formidable challenge. The complexity arises not only from the computational difficulties but also from the inherent limitations of current quantum mechanics methods, which are not equipped to solve multi-particle problems directly. Therefore, to make progress, it becomes essential to introduce approximations that reduce the many-body problem to a more tractable form, often by considering independent particle systems. These approximations, while simplifying the problem, must be judiciously chosen to maintain the physical relevance and accuracy of the solutions.

Understanding and solving the many-body problem in quantum mechanics is a critical step in unraveling the mysteries of the electronic structure of materials. The Schrödinger equation serves as the cornerstone of this endeavor, but its complexity necessitates the use of sophisticated methods and approximations to extract meaningful and accurate information about the system under study.

4.2. The Born-Oppenheimer approximation

The Born-Oppenheimer approximation (BOA) is a fundamental approach in addressing many-body problems in quantum mechanics, particularly in the context of molecular systems. This approximation is predicated on a key physical insight: the mass of nuclei is significantly greater than that of electrons ($m_e \ll m_n$). This disparity in mass leads to a corresponding disparity in the mobility of these particles - electrons being far more agile than the comparatively sluggish nuclei. The essence of the BOA lies in exploiting this difference in mobility. Electrons, due to their lighter mass and higher velocity, can rapidly adjust their positions in response to the slower movements of the nuclei. In the BOA, we take this dynamism to its logical extreme: the electrons are considered to instantaneously adapt to the positions of the nuclei. This leads to a critical simplification: the nuclei can be considered as essentially stationary (or 'frozen') during the electronic motion, reducing their dynamical role to mere parameters in the system ($\mathbf{R}_k = \text{constant, for each } k$). Mathematically, this approximation manifests in the neglect of the kinetic energy of the nuclei ($\hat{T}_n$) in the Hamiltonian. Furthermore, the potential energy of the nuclei ($\hat{V}_{nn}$), in this static framework, becomes a mere constant. This simplification allows for the decoupling of nuclear and electronic motions, transforming the complex many-body problem into a more manageable electronic problem. With the nuclei considered static, the original Hamiltonian (Eq. 4.2) is reduced to an electronic Hamiltonian, $\hat{\mathcal{H}}$, concerned solely with the electronic structure[160, 161]:

$$\hat{\mathcal{H}} = -\frac{1}{2}\sum_{i=1}^{N}\nabla_i^2 - \sum_{i=1}^{N}\sum_{k=1}^{M}\frac{Z_k}{|\mathbf{r}_i - \mathbf{R}_k|} + \frac{1}{2}\sum_{\substack{i,j=1\\ i\neq j}}^{N}\frac{1}{|\mathbf{r}_i - \mathbf{r}_j|}, \tag{4.9}$$

which can be succinctly expressed as

$$\hat{\mathcal{H}} = \hat{T}_e + \hat{V}_{en} + \hat{V}_{ee}. \tag{4.10}$$

The task then becomes to solve the N-electron non-relativistic Schrödinger equation:

$$\hat{\mathcal{H}}\psi(\mathbf{r}_i) = \varepsilon\psi(\mathbf{r}_i), \tag{4.11}$$

where $\psi(\mathbf{r}_i)$ is the N-electron wave function corresponding to the total electronic energy eigenvalue ε.

This equation, though significantly simplified from the full many-body problem, still presents considerable challenges. Except in the simplest cases (like the hydrogen atom), an exact analytical solution remains elusive. Consequently, further approximations and computational methods are often employed to make progress in solving this equation.

4.3. Hartree-Fock approximation

The Hartree approximation (HA) is a foundational method in quantum mechanics for solving the N-electron problem. It simplifies the many-electron problem into N independent one-electron problems. In HA, each electron is treated as moving independently in an effective potential formed by the combined effects of nuclear attraction and the average repulsion of all other electrons. This results in the Hartree product (HP), a simple product of one-electron wavefunctions:

$$\psi_{\mathrm{HP}}(\mathbf{r}_i) = \prod_{i=1}^{N}\psi_i(\mathbf{r}_i). \tag{4.12}$$

This approach simplifies the complex multi-electron problem into N independent one-electron problems. Each electron problem is governed by the following Schrödinger-like equation:

$$\left(-\frac{1}{2}\nabla^2 + \mathcal{V}_{\mathrm{eff}}(\mathbf{r})\right)\psi_i(\mathbf{r}) = \varepsilon_i\psi_i(\mathbf{r}), \tag{4.13}$$

where $\psi_i(\mathbf{r})$ denotes the orbital for the i-th electron, associated with the energy eigenvalue ε_i, and $\mathcal{V}_{\mathrm{eff}}(\mathbf{r})$ represents the effective potential. The effective potential includes the nuclear potential,

$$V_{\text{ext}}(\mathbf{r}) = -\sum_{k=1}^{M} \frac{Z_k}{|\mathbf{r}-\mathbf{R}_k|}, \tag{4.14}$$

and the electrostatic Hartree potential due to the average electronic density $n(\mathbf{r})$ of the other $(N-1)$ electrons:

$$\mathcal{V}_H(\mathbf{r}) = \int d^3\mathbf{r}' \frac{n(\mathbf{r}')}{|\mathbf{r}-\mathbf{r}'|}, \tag{4.15}$$

where $n(\mathbf{r}) = \sum_{j\neq i}^{N} |\psi_j(\mathbf{r})|^2$.

The N one-electron equations in Eq. 4.13 are then given by[150–159]:

$$\left[-\frac{1}{2}\nabla^2 - \sum_{k=1}^{M} \frac{Z_k}{|\mathbf{r}-\mathbf{R}_k|} + \sum_{j\neq i}^{N} \int d^3\mathbf{r}' \frac{|\psi_j(\mathbf{r}')|^2}{|\mathbf{r}-\mathbf{r}'|}\right] \psi_i(\mathbf{r}) = \varepsilon_i \psi_i(\mathbf{r}). \tag{4.16}$$

This set of equations, known as Hartree's equations, must be solved iteratively to obtain self-consistent solutions for the one-electron wavefunctions $\psi_i(\mathbf{r})$ and their corresponding energies ε_i.

The HA makes it possible to reduce the complexity of the initial problem. However, the HP fails to properly describe the behavior of molecular species because it does not adequately account for the Pauli exclusion principle, which requires that no two electrons in a many-electron system occupy the same quantum state. The Pauli exclusion principle requires that the wave-function must be antisymmetric when any pair of electron coordinates are permuted, but the HP does not have the correct antisymmetry character for exchange of space and spin coordinates of any two electrons. This observations were made independently by Fock and Slater and a correction was brought to improve this approach leading to what is known as the Hartree-Fock approximation.

Fock[162] improved on Hartree's method by writing the wave-function as an antisymmetrized products of spin-orbitals, as suggested by Slater[163], in order to satisfy the Pauli principle instead of just a simple product of one-electron wave-functions like in the Hartree method. The wavefunction in the HFA then reads:

$$\psi_{HF}(\mathbf{x}_i) = \frac{1}{\sqrt{N!}} \begin{vmatrix} \psi_1(\mathbf{x}_1) & \psi_1(\mathbf{x}_2) & \cdots & \psi_1(\mathbf{x}_N) \\ \psi_2(\mathbf{x}_1) & \psi_2(\mathbf{x}_2) & \cdots & \psi_2(\mathbf{x}_N) \\ \vdots & \vdots & \ddots & \vdots \\ \psi_N(\mathbf{x}_1) & \psi_N(\mathbf{x}_2) & \cdots & \psi_N(\mathbf{x}_N) \end{vmatrix}, \tag{4.17}$$

where $\frac{1}{\sqrt{N!}}$ is the normalization constant which ensures that the wavefunction remains properly scaled irrespective of the number of electrons in the system. Each element within the Slater de-

terminant, $\psi_i(\mathbf{x}_i)$, represents a spin-orbital, which is a product of a spatial part, $\phi_i(\mathbf{r}_i)$, and a spin part, $\chi_i(\sigma)$. The spin function, takes one of two possible values: α or β. These values correspond to the two possible spin states of an electron: spin-up ($m_s = +\frac{1}{2}$), denoted by α, and spin-down ($m_s = -\frac{1}{2}$), denoted by β, with the properties $\langle\alpha\rangle\,\alpha = \langle\beta\rangle\,\beta = 1$ and $\langle\alpha\rangle\,\beta = \langle\beta\rangle\,\alpha = 0$.
Using the variational principle[164], we obtain the HF equations[150–159]:

$$\left[-\frac{1}{2}\nabla^2 + V_{ext}(\mathbf{r}) + \underbrace{\sum_{j\neq i}^{N}\int d^3\mathbf{r}'\frac{|\psi_j(\mathbf{r}')|^2}{|\mathbf{r}-\mathbf{r}'|}}_{\text{Hartree potential}}\right]\psi_i(\mathbf{r}) - \underbrace{\sum_{j=1}^{N}\int d^3\mathbf{r}'\frac{\psi_j^*(\mathbf{r}')\psi_j(\mathbf{r})}{|\mathbf{r}-\mathbf{r}'|}}_{\text{Fock potential}}\psi_i(\mathbf{r}') = \varepsilon_i\psi_i(\mathbf{r}), \tag{4.18}$$

where the second term

$$\mathcal{V}_X = -\sum_{j=1}^{N}\int d^3\mathbf{r}'\frac{\psi_j^*(\mathbf{r}')\psi_j(\mathbf{r})}{|\mathbf{r}-\mathbf{r}'|} \tag{4.19}$$

represents the non-local exchange potential acting on the j^{th} orbital. The HF equations above are nonlinear and can be solved iteratively to find the spin-orbitals that minimize the total energy of the system.
The HFA offered a good description of the atomic and molecular cases. However, it has limitations. It often overestimates the energy due to its neglect of electron correlation, leading to inaccuracies in predicting properties like ionization energies and electron affinities. The band gaps in solids are often overestimated, and cohesive energies in metals are underestimated. A completely different approach for introducing the electron correlation, based on the electron density, was elaborated to accurately describe quantum-mechanical systems.

4.4. Density functional theory

Density Functional Theory stands as a pivotal quantum mechanical method in the realms of physics, chemistry, and materials science. It is primarily utilized to investigate and predict properties, predominantly of the ground state, of many-body systems such as atoms, molecules, and crystalline solids. Unlike HF theory, which describes the interaction of electrons with both an external field from nuclei and the average field of all other electrons, DFT offers a more comprehensive approach. It relies on a holistic description of the entire system, thus providing a superior approximation for solving many-electron problems. Density Functional Theory's efficacy in treating crystalline solids stems from its foundation on the Hohenberg-Kohn theorems, advancing beyond the HFA by incorporating correlation effects in its analysis of the physical properties of the ground state in many-electron systems. These theorems hinge on describing the external potential of the nuclei, $\hat{V}_{\text{ext}}(\mathbf{r})$, and thus the total energy, as a unique functional of the electronic density, expressed as

$$n(\mathbf{r}) = N \int \left|\psi(\mathbf{x}, \mathbf{x}_2, \ldots, \mathbf{x}_N)\right|^2 d\mathbf{x}_2 \ldots d\mathbf{x}_N, \tag{4.20}$$

where $\mathbf{x} = (\mathbf{r}, \sigma)$ represents both the spatial and spin coordinates of an electron. This density is normalized to the number of electrons, such that

$$\int n(\mathbf{r}) d^3\mathbf{r} = N. \tag{4.21}$$

The foundational principles of DFT were first laid out in 1964 by Hohenberg and Kohn[165], who demonstrated that the ground-state energy of an electron gas could be entirely described by a functional of the electronic density, even in the presence of an external potential. Following this, Kohn and Sham in 1965[166] established that the complex many-body problem could be simplified to a set of self-consistent equations. These equations pertain to a system of single electron orbitals $\phi(\mathbf{r})$, with a total density mirroring that of the actual system. This breakthrough transformed DFT into a practical electronic structure theory. While DFT indicates the feasibility of calculating the total energy of a many-electron system based on its electronic density, the process from density to energy, as we will discuss, is not straightforward. Notably, DFT operates within the BOA, wherein the Hamiltonian of the system is represented by

$$\hat{\mathcal{H}} = -\frac{1}{2}\sum_{i=1}^{N} \nabla^2 + \frac{1}{2}\sum_{j\neq i}^{N} \frac{1}{|\mathbf{r} - \mathbf{r}'|} + \hat{V}_{ext}(\mathbf{r}). \tag{4.22}$$

In its practical implementations, various approximations are employed to calculate the electronic structure[167], from which diverse ground-state properties like structural, magnetic, and optical characteristics of materials can be derived[168].

4.4.1. The Hohenberg-Kohn theorems

The foundation of contemporary DFT is anchored in the two seminal mathematical theorems formulated by Hohenberg and Kohn[165, 166, 169]. This significant breakthrough simplified the complex many-body problem, traditionally reliant on a high-dimensional approach, by transposing it back to a more manageable 3D space. Central to this simplification is the use of electronic density, denoted as $n(\mathbf{r})$, as the primary variable. In contrast to the wave function of a system with

N electrons, which is contingent on $3N$ variables (representing three spatial dimensions for each electron), the electronic density is a function of merely three spatial variables. This reduction to a 3D perspective renders the electronic density a far more tractable entity in the study of many-body systems, streamlining the complexities inherent in analyzing such systems.

Theorem 1. *For any electronic system in an external potential $V_{ext}(\mathbf{r})$, the potential $V_{ext}(\mathbf{r})$ is uniquely determined, up to an additive constant, by the ground-state electronic density $n_0(\mathbf{r})$.*

The first HK theorem plays a pivotal role in DFT by establishing a direct correspondence between the electronic density $n_0(\mathbf{r})$ of a system in its ground state and the external potential $\hat{V}_{ext}[n_0]$[150–159]. This relationship is crucial as it enables the characterization of any observable within the system as a unique functional of the exact electronic density, which is specific to the ground state. The rationale behind using electronic density in place of the wave function stems from a fundamental principle: for each N-electron system, there exists a singular external potential. This unique external potential is instrumental in formulating the specific Hamiltonian for the system. Solving the Schrödinger equation for this Hamiltonian yields a unique wave function, and consequently, a singular electronic density. This electronic density encapsulates as much information about the system as its corresponding wave function. In essence, each external potential corresponds to a specific electronic density, and this one-to-one correspondence forms the core of the first HK theorem, underpinning the theoretical framework of DFT.

Proof. To prove this theorem, we will proceed by *reductio ad absurdum*. Let $V_{ext}(\mathbf{r})$ be the external potential of a system with associated ground-state electronic density $n_0(\mathbf{r})$, the total number of particles N, the Hamiltonian $\hat{\mathcal{H}}$, the ground-state wave function ψ and the ground-state energy $E = \langle\psi|\mathcal{H}|\psi\rangle$. Similarly, let us consider a second system of N particles with associated ground-state electronic density $n_0(\mathbf{r}')$, Hamiltonian $\hat{\mathcal{H}}'$, ground-state energy $E' = \langle\psi'|\mathcal{H}|\psi'\rangle$ and where $V_{ext}(\mathbf{r}) \neq V'_{ext}(\mathbf{r}) + const$ and so $\psi \neq \psi'$.

1) Let assume that $\hat{\mathcal{H}}$ and $\hat{\mathcal{H}}'$ have the same ground-state wave-function ψ, that is, $\hat{\mathcal{H}}\,|\psi\rangle = E\,|\psi\rangle$ and $\hat{\mathcal{H}}'\,|\psi\rangle = E'\,|\psi\rangle$. Subtracting these two equations gives

$$(\hat{V}_{ext} - \hat{V}'_{ext})\,|\psi\rangle = (E - E')\,|\psi\rangle\,, \tag{4.23}$$

which implies $V_{ext}(\mathbf{r})$ - $V'_{ext}(\mathbf{r}) = const$, in contradiction with the initial hypothesis. We conclude, therefore, that external potentials differing by more than an additive constant cannot share the same ground-state wave-function.

2) Let us now assume that ψ and ψ' have the same ground-state electronic density $n_0(\mathbf{r})$. Because of the variational principle[170], no wavefunction can give an energy that is less than the energy

of ψ for the Hamiltonian $\hat{\mathcal{H}}$. That is

$$E = \langle\psi|\hat{\mathcal{H}}|\psi\rangle < \langle\psi'|\hat{\mathcal{H}}|\psi'\rangle\,. \tag{4.24}$$

Assuming that the ground-state is non-degenerate, the inequality in above strictly holds. Taking $|\psi'\rangle$ as a trial wave-function for the Hamiltonian $\hat{\mathcal{H}}$, we obtain from Eq. 4.24 that

$$\begin{aligned} E < \langle\psi'|\hat{\mathcal{H}}|\psi'\rangle &= \langle\psi'|\hat{\mathcal{H}}'|\psi'\rangle + \langle\psi'|(\hat{\mathcal{H}} - \hat{\mathcal{H}}')|\psi'\rangle\,, \\ &= E' + \int d^3\mathbf{r} n_0(\mathbf{r})[V_{ext}(\mathbf{r}) - V'_{ext}(\mathbf{r})], \end{aligned} \tag{4.25}$$

whereas taking $|\psi\rangle$ as a trial wave-function for the Hamiltonian $\hat{\mathcal{H}}'$ gives

$$\begin{aligned} E' < \langle\psi|\hat{\mathcal{H}}'|\psi\rangle &= \langle\psi|\hat{\mathcal{H}}|\psi\rangle + \langle\psi|(\hat{\mathcal{H}}' - \hat{\mathcal{H}})|\psi\rangle\,, \\ &= E - \int d^3\mathbf{r} n_0(\mathbf{r})[V_{ext}(\mathbf{r}) - V'_{ext}(\mathbf{r})]. \end{aligned} \tag{4.26}$$

Summing Eqs. 4.25 and 4.26 up results in the contradiction inequality

$$E + E' < E + E', \tag{4.27}$$

and we can conclude by *reductio ad absurdum* that the assumption of the existence of $V'_{ext}(\mathbf{r})$ is wrong. Therefore, there cannot exist two external potentials V_{ext} and V'_{ext} that yield the same ground-state electronic density $n_0(\mathbf{r})$ □.

So, the ground-state electronic density $n_0(\mathbf{r})$ uniquely specifies the external potential V_{ext}, which in turn uniquely determines the Hamiltonian, and thus everything about the many-electron problem. This theorem thereby ensures that the ground-state wave-function ψ for the potential $V_{ext}(\mathbf{r})$ is itself a functional of $n_0(\mathbf{r})$, denoted by $\psi[n_0]$, which was utilized by HK to define the universal (that is, independent from the external potential) functional

$$F_{HK}[n_0] = \left\langle\psi[n_0]\middle|\hat{T} + \hat{V}_{int}\middle|\psi[n_0]\right\rangle, \tag{4.28}$$

which can be used to define the total electronic energy functional of the ground-state of the system. If this theorem shows that all the properties of the system are formally determined by the ground-state electronic density, it does not say anything about how we can be assured that a certain density is truly the ground-state electronic density that we are looking for. A formal prescription on how this problem can be addressed has been given in a second theorem

Theorem 2. *A universal functional for the energy $E[n]$ can be defined in terms of the ground-state electronic density $n_0(\mathbf{r})$, which is valid for any external potential. For any particular $V_{ext}(\mathbf{r})$, the exact ground-state energy of the system is the global minimum value of this functional, and the electronic density $n_0(\mathbf{r})$ that minimizes the functional is the exact ground-state electronic density.*

The second HK theorem is a cornerstone in the field of DFT, particularly for understanding the ground-state properties of an N-electron system[150–159]. It asserts that the total energy of the system's ground-state can be expressed as a functional of its electronic density, denoted by $E \equiv E[n]$. This theorem is crucial because it establishes that the electronic density, which minimizes this total energy functional, corresponds exactly to the true electronic density of the system's ground-state, represented as $n_o(\mathbf{r})$. Furthermore, it underscores a fundamental principle: all ground-state properties of the system can be derived as functionals of this specific electronic density. This theorem not only provides a theoretical underpinning for the calculation of the ground-state energy but also signifies that other intrinsic properties of the ground-state are inherently linked to and can be determined from this optimal electronic density.

Proof. Since all observables of the system such as kinetic energy, etc., are completely determined if the electronic density is specified, then each such observable can be regarded as unique functional of the electronic density, including the total electronic energy functional $E[n]$. The best way to write this energy in term of the electronic density is through to the so-called Levy's constrained-search formulation[171–173]

$$F[n] = \min_{\psi \to n} \langle \psi | \hat{T} + \hat{V}_{int} | \psi \rangle = \langle \psi[n] | \hat{T} + \hat{V}_{int} | \psi[n] \rangle\, r), \tag{4.29}$$

which establishes that the total electronic energy functional can be obtained by minimizing over all the states ψ that yield the electronic density $n(\mathbf{r})$

$$\begin{aligned} E_{HK}[n] &= \min_{\psi \to n} \langle \psi | \hat{\mathcal{H}} | \psi \rangle\,, \\ &= \min_{\psi \to n} \langle \psi | \hat{T} + \hat{V}_{int} + \hat{V}_{ext} | \psi \rangle\,, \\ &= \min_{\psi \to n} \langle \psi | \hat{T} + \hat{V}_{int} | \psi \rangle + \int d^3\mathbf{r} V_{ext}(\mathbf{r}) n(\mathbf{r}), \\ &= \langle \psi[n] | \hat{T} + \hat{V}_{int} | \psi[n] \rangle + \int d^3\mathbf{r} V_{ext}(\mathbf{r}) n(\mathbf{r}), \\ &= T[n] + V_{int}[n] + \int d^3\mathbf{r} V_{ext}(\mathbf{r}) n(\mathbf{r}), \end{aligned} \tag{4.30}$$

which can be separated into a universal $F_{HK}[n]$ part and a system dependent part, that is, depends on the external potential

$$E_{HK} = F_{HK}[n] + \int d^3\mathbf{r}V_{ext}(\mathbf{r})n(\mathbf{r}). \tag{4.31}$$

The universal functional $F_{HK}[n]$, however, is not known and finding its exact form remains the holy grail of DFT. One can then obtain the ground-state energy E_0 by minimizing the energy functional $E[n]$ with respect to N-electron densities n that are ground-state densities associated with some local potential (referred to as V-representable densities)

$$E_0 = \min_n \left(F_{HK}[n] + \int d^3\mathbf{r}V_{ext}(\mathbf{r})n(\mathbf{r}) \right), \tag{4.32}$$

the minimum being reached for a electronic ground-state density $n_0(\mathbf{r})$ corresponding to the potential $V_{ext}(\mathbf{r})$ □.

While the HK theorems allow to reformulate the many-body problem in terms of the electronic density, which reduces the dimensionality and complexity of the many-electron problem, they do not offer a way in which the minimization of the energy functional can be done in practice. Kohn and Sham proposed a method which allows the minimization to be done in self consistence way.

4.4.2. Kohn-Sham equations

To apply DFT to real systems, Kohn and Sham developed in 1965 a method which transformed DFT into a practical electronic structure theory. Faced with the difficulty to evaluate the universal functional $F_{HK}[n]$, they suggested to replace the original system of interacting electrons by a fictitious reference system of N non-interacting electrons moving in an effective external potential v_s defines in order to generate a ground-state electronic density identical to the exact electronic density of the ground-state of the original system. The Hamiltonian $\hat{\mathcal{H}}_s$ of this fictitious system reads

$$\hat{\mathcal{H}}_s = \sum_{i=1}^{N} \left(-\frac{1}{2}\nabla_i^2 + \hat{v}_s(\mathbf{r}_i) \right), \tag{4.33}$$

and the ground-state ψ_s, assuming it is non-degenerate, is given by the Slater determinant

$$\psi_s(\mathbf{x}_i) = \frac{1}{\sqrt{N!}} det_{ij}\psi_j(\mathbf{r}_i, \sigma_i), \tag{4.34}$$

where the ψ_i are the N lowest eigenstates of one-electron Hamiltonian

$$\hat{h}_s = -\frac{1}{2}\nabla_i^2 + \hat{v}_s(\mathbf{r}_i), \tag{4.35}$$

satisfying

$$\hat{h}_s \psi_i = \varepsilon_i \psi. \tag{4.36}$$

By inserting this Slater determinant into Eq. 4.34 and performing spin integration, we get the particle density of the non-interacting system

$$n(\mathbf{r}) = \sum_{i=1}^{N} \left|\phi_i(\mathbf{r})\right|^2, \tag{4.37}$$

where $\phi_i(\mathbf{r})$ are Kohn-Sham (KS) single-particle orbitals. The total energy of the non-interacting system is expressed by the functional

$$\begin{aligned} E_{V_s}[n] &= F[n] + \int d^3\mathbf{r} v_s(\mathbf{r}) n(\mathbf{r}), \\ &= T_s[n] + \int d^3\mathbf{r} v_s(\mathbf{r}) n(\mathbf{r}). \end{aligned} \tag{4.38}$$

Since there is no interaction between the electrons, the functional $F[n]$ is equal to the kinetic energy $T_s[n]$ of the electrons

$$T_s[n] = \langle \psi_s[n] | \hat{T}_s | \psi_s[n] \rangle = -\frac{1}{2} \sum_{i=1}^{N} \int \psi_i^*(\mathbf{r}) \nabla^2 \psi_i(\mathbf{r}). \tag{4.39}$$

Bearing the discussion of the non-interacting system above in mind, we get back to the original system with electron-electron interaction. We split the universal functional $F_{HK}[n] = T[n] + V_{int}[n]$ into three parts as follow

$$F_{KS}[n] = T_s[n] + E_H[n] + E_{XC}[n], \tag{4.40}$$

where $E_H[n]$ is the Hartree energy which describes the classical part of the electron-electron repulsion

$$E_H[n] = \frac{1}{2} \int \int d^3\mathbf{r} d^3\mathbf{r}' \frac{n(\mathbf{r}) n(\mathbf{r}')}{|\mathbf{r} - \mathbf{r}'|}, \tag{4.41}$$

and $E_{XC}[n]$ is the XC energy accounting for all the non-classical exchange and correlation effect which remains to be approximate. The total energy in Eq. 4.31 then becomes

$$E_{KS}[n] = T_s[n] + E_H[n] + E_{XC}[n] + \int d^3\mathbf{r} V_{ext}(\mathbf{r}) n(\mathbf{r}). \tag{4.42}$$

In order to obtain the KS orbitals $\{\phi_j\}$ which give rise to the ground-state energy, we need to minimize the total energy above with respect to the orbitals, subject to the orthonormalization constraints

$$\int d^3\mathbf{r} \psi_i^*(\mathbf{r}) \psi_j(\mathbf{r}) = \delta_{ij}. \tag{4.43}$$

In that view, we define the following Lagrangian

$$L_V\left[\psi_i\right] = E_{KS}[n] - \sum_{j=1}^{N} \varepsilon_{ij}\psi_j(\mathbf{r}), \tag{4.44}$$

where ε_{ij} are Lagrange multipliers to ensure $\{\psi_i\}$ are orthonormal. It should be underlined that Eq. 4.21 is satisfied automatically if $\{\psi_i\}$ are orthonormal. The Lagrangian above must be stationary with respect to variations of the KS orbitals $\psi_i(\mathbf{r})$

$$\frac{\delta L_V\left[\psi_i\right]}{\delta\psi_i^*(\mathbf{r})} = 0. \tag{4.45}$$

A quick calculation of this functional derivative leads to the following set of one-electron equations

$$\left(-\frac{1}{2}\nabla^2 + \mathcal{V}_{KS}(\mathbf{r})\right)\psi_i'(\mathbf{r}) = \sum_{j=1}^{N} \varepsilon_{ij}\psi_j'(\mathbf{r}), \tag{4.46}$$

where $\mathcal{V}_{KS}(\mathbf{r})$, the KS effective potential, is given by

$$\begin{aligned}\mathcal{V}_{KS} &= V_{ext} + \frac{\delta E_H[n(\mathbf{r})]}{\delta n(\mathbf{r})} + \frac{\delta E_{XC}[n(\mathbf{r})]}{\delta n(\mathbf{r})},\\ &= V_{ext} + V_H + V_{XC}.\end{aligned} \tag{4.47}$$

Since the KS effective potential above is real then the KS effective Hamiltonian

$$\hat{h}_i^{KS} = -\frac{1}{2}\nabla^2 + \hat{\mathcal{V}}_{KS}(\mathbf{r}), \tag{4.48}$$

is hermitian. Therefore, the matrices ε_{ij} are also hermitian and they can be diagonalize. Transforming the orbitals $\{\psi_j'\}$ by the unitary transformation diagonalizing ε_{ij} leads to new set of orbitals $\{\psi_i\}$ obtained from one-electron Schrödinger-like equations known as KS equations

$$\left(-\frac{1}{2}\nabla^2 + \mathcal{V}_{KS}(\mathbf{r})\right)\psi_i(\mathbf{r}) = \varepsilon_i\psi_i(\mathbf{r}), \tag{4.49}$$

where the ε_i's are then the KS eigenvalues and the KS effective potential $\mathcal{V}_{KS}$, as it can been in Eq. 4.47 includes the external potential $V_{ext}(\mathbf{r})$, Hartree potential $V_H(\mathbf{r})$ and XC potential $V_{XC}(\mathbf{r})$ which is responsible to correctly account for all quantum many-body effects such as electron spin-dependent effects, Van der Waals Interactions, or electron-hole pair creation.

Therefore, if $\mathcal{V}_{KS}$ is given, by simply solving the KS equations above we obtain the ground-state density as

$$n(\mathbf{r}) = \sum_{i=1}^{N} \left|\psi_i(\mathbf{r})\right|^2, \tag{4.50}$$

The total energy of the reference system $E_{V_s}[n]$, which is the sum of the KS eigenenergies ε_i, can be obtain by minimizing the KS effective Hamiltonian over the KS sates $|\psi_i\rangle$ and we get

$$\begin{aligned} E_{V_s}[n] &= \sum_{i=1}^{N} \varepsilon_i, \\ &= \sum_{i=1}^{N} \langle\psi_i| \hat{h}^{KS} |\psi_i\rangle, \\ &= T_s[n] + \int\int d^3\mathbf{r} d^3\mathbf{r}' \frac{n(\mathbf{r})n(\mathbf{r}')}{|\mathbf{r}-\mathbf{r}'|} + \int d^3\mathbf{r} V_{ext}(\mathbf{r})n(\mathbf{r}) + \int d^3\mathbf{r} V_{XC}(\mathbf{r})n(\mathbf{r}). \end{aligned} \tag{4.51}$$

Since the KS approach preserves the electronic density of the interacting system, then the total electronic energy in Eq. 4.42 is representative of the real system. This energy can be reformulated using Eq. 4.51 as

$$E_{KS}[n] = \sum_{i=1}^{N} \varepsilon_i - \frac{1}{2}\int\int d^3\mathbf{r} d^3\mathbf{r}' \frac{n(\mathbf{r})n(\mathbf{r}')}{|\mathbf{r}-\mathbf{r}'|} - \int d^3\mathbf{r} V_{XC}(\mathbf{r})n(\mathbf{r}) + E_{XC}[n], \tag{4.52}$$

which is the formula use to calculate the ground-state energy of a physical system from the solution of the KS equations. Due to the nonlinearity of the KS, the electron density needs to be solved in a self-consistent manner, where the equations are iteratively updated until the input and output densities converge.

The challenge in utilizing the KS energy functional lies in the fact that the exact form of E_{XC} is not known. This term is essential because it accounts for complex electron-electron interactions beyond classical electrostatics, specifically incorporating exchange interactions, which arise from the Pauli exclusion principle, and correlation effects, which reflect the dynamic interactions between electrons due to their mutual repulsion. The absence of a precise analytical form for E_{XC} necessitates the use of approximations, which is a focal point of extensive research in DFT.

In practical applications of the KS equations, an approximate form of the XC energy functional must be employed. Since the inception of DFT, a multitude of approximations for E_{XC} have been proposed. These approximations vary in their complexity and the physical phenomena they attempt to capture. Among these, two approximations have gained widespread acceptance and usage: the Local Density Approximation (LDA) and the GGA.

The LDA, introduced in the foundational work of Hohenberg and Kohn, treats an inhomogeneous system as a collection of infinitesimal volumes with constant electronic density, akin to a uniform electron gas. The XC energy in LDA ($E_{XC}^{LDA}[n]$) and its corresponding potential ($V_{XC}^{LDA}(\vec{r})$) are derived analytically, leveraging the known XC energy per particle of a homogeneous electron gas ($\epsilon_{XC}^{LAD}[n]$). This approach, despite its simplicity and effectiveness in certain systems like free atoms, molecules, and metals, shows limitations in describing solids with non-homogeneous electronic densities, often leading to overestimations in cohesive energies and underestimations in lattice constants, particularly in semiconductors.

To address these limitations, the Gradient Expansion Approximation (GEA) was proposed as an extension to LDA, considering local density gradients as an additional variable[165]. However, GEA's practical effectiveness was limited, paving the way for the development of GGA. The GGA, a more flexible and refined approach, includes gradient corrections to LDA, expressed through a functional form $f\,(n(\vec{r}), \nabla n(\vec{r}))$ that accounts for both exchange ($E_X^{GGA}[n]$) and correlation energies ($E_C^{GGA}[n]$)[158]. The GGA, particularly the Perdew, Burke, and Ernzerhof (PBE) functional[174, 175] used in this thesis, introduces an exchange enhancement factor ($F_X(s)$) and parameters (κ and μ) obtained from physical constraints, thereby improving upon LDA's limitations.

4.5. Ab initio modeling of materials

4.5.1. Bloch's theorem and plane wave basis set

The complexity of the Schrödinger equation in condensed matter systems, due to the infinite number of electrons, is significantly simplified by Bloch's theorem. Introduced by Felix Bloch in 1928, this theorem allows for a tractable description of electron behavior in periodic potentials, which is essential for understanding the properties of matter on a large scale, including electronic, magnetic, and optical properties of materials[176, 177].

Bloch's theorem states that the wave function of an electron in a periodic potential can be expressed as a product of a plane wave (PW) and a lattice periodic function. This is mathematically represented as[178]:

$$\psi_k(\boldsymbol{r}) = e^{i\boldsymbol{k}\cdot\boldsymbol{r}} u_k(\boldsymbol{r}), \tag{4.53}$$

where $\boldsymbol{k}$ denotes the wave vector within the first BZ, $\boldsymbol{r}$ is the position vector, and $u_k(\boldsymbol{r})$ is a periodic lattice function, invariant under lattice translation:

$$u_k(\boldsymbol{r} + \boldsymbol{R}) = u_k(\boldsymbol{r}), \tag{4.54}$$

with $\boldsymbol{R}$ representing the translation vector. The periodic function $u_k(\boldsymbol{r})$ can be expanded using Fourier series:

$$u_{\boldsymbol{k}}(\boldsymbol{r}) = \sum_{\boldsymbol{G}} c_{\boldsymbol{G},\boldsymbol{k}} e^{i\boldsymbol{G}\cdot\boldsymbol{r}}, \tag{4.55}$$

where $\boldsymbol{G}$ is the reciprocal lattice vector defined by:

$$\boldsymbol{G} \cdot \boldsymbol{b} = 2\pi m, \tag{4.56}$$

with $\boldsymbol{b}$ denoting the translation vector in the crystal lattice, and m an integer. This approach simplifies the understanding of electron behavior in crystals, which are periodic and regular arrangements of atoms.

The PW basis set is instrumental in describing the properties of solids due to its several advantages, such as the ease of implementation of periodic boundary conditions and the straightforward calculation of matrix elements. When coupled with the KS equations, which embody the translational symmetry of the solid, Bloch's theorem provides a framework for solving these equations efficiently. The KS orbitals, expressed in terms of plane waves, become:

$$\psi_{\boldsymbol{k}}(\boldsymbol{r}) = \sum_{\boldsymbol{K},\boldsymbol{G}} c_{\boldsymbol{K},\boldsymbol{G}} e^{i(\boldsymbol{K}+\boldsymbol{G})\cdot\boldsymbol{r}}. \tag{4.57}$$

Substituting these plane waves into the KS equation results in the secular equation:

$$\sum_{\boldsymbol{G}} \left[\frac{\hbar}{2m} |\boldsymbol{K}+\boldsymbol{G}|^2 \delta_{\boldsymbol{G}\boldsymbol{G}'} + V^{\sigma}_{KS}(\boldsymbol{G}-\boldsymbol{G}') \right] c_{i,\boldsymbol{K}+\boldsymbol{G}'} = E_i c_{i,\boldsymbol{K}+\boldsymbol{G}'}, \tag{4.58}$$

where $V^{\sigma}_{KS}(\boldsymbol{G}-\boldsymbol{G}')$ is the Fourier transform of the KS potential. The accuracy of computations is enhanced by determining an appropriate energy cut-off E_{cut}, which limits the number of $\boldsymbol{G}$-vectors in the Fourier expansion:

$$\frac{1}{2}|\boldsymbol{K}+\boldsymbol{G}|^2 < E_{\text{cut}}. \tag{4.59}$$

In DFT computations, the selection of plane PWs hinges on the Bloch wave vector, denoted as $\boldsymbol{K}$. Knowing $\boldsymbol{K}$ allows for the precise determination of the electron's many-body quantum state, confined numerically within an appropriate plane wave basis. As outlined in Eq. 4.59, the cut-off energy defines the upper limit of the $\boldsymbol{G}$ vector lengths. This limitation results in a finite-dimensional matrix representation of the Hamiltonian. Consequently, the expansion truncation within the plane wave basis restricts the kinetic energy term to remain below the cut-off energy threshold. This discrepancy in energy representation may lead to errors in estimating the total energy of certain systems. To ensure the accuracy of total energy calculations, a convergence test is performed by incrementally increasing the cut-off energy E_{cut} and evaluating the resulting total energy. This process continues until the computed total energy converges to a stable value within an acceptable tolerance. Such convergence testing determines the minimum cut-off energy required to achieve the desired accuracy, effectively reducing truncation errors in the Fourier expansion.

The interplay of Bloch's theorem and the plane wave basis set forms the backbone of computational approaches in condensed matter physics. They allow for a detailed and accurate description of electron behavior in materials, crucial for understanding their large-scale properties and phenomena.

4.5.2. Reciprocal space and Brillouin zone

The BZ is fundamental in the context of wave representation within a periodic medium. Bloch's seminal work demonstrated that the solutions of electron states in a periodic lattice are effectively characterized by the behavior of plane waves within the BZ[176]. This understanding is crucial in the computation of the total energy of a many-body system using the KS equation, where the eigenvalues are self-consistently derived from the k-dependence of the Hamiltonian. In the realm of DFT, the first BZ is sampled by defining a continuous array of points in reciprocal space, denoted as $\boldsymbol{k}$-space. These points, referred to as k-points, are essential in representing the BZ. The computation of the total energy within DFT necessitates an integration over the first BZ, which, in practice, is transformed into a summation over discrete $\boldsymbol{k}$-space points. For instance, the calculation of density at BZ points is expressed as:

$$n(\boldsymbol{r}) = \sum \int_{BZ} F(\boldsymbol{k}) d^3\boldsymbol{k}, \tag{4.60}$$

where $F(\boldsymbol{k})$ is a periodic function. In periodic systems, this integral is approximated by a sum over a finite number of k-points, which are the specific points in the first BZ at which DFT calculations are performed to ascertain the electronic state in a solid system. The selection of k-points is pivotal for enhancing the numerical accuracy of the calculation while balancing computational efficiency. The adoption of a dense k-point grid minimizes errors in self-consistency calculations. The tetrahedron method[179, 180], recognized for its efficacy in integrating over the BZ, partitions the BZ volume into non-overlapping small tetrahedra. Additionally, a simple yet effective integration technique involves sampling the BZ with a limited k-point grid, such as the Monkhorst-Pack mesh[181]. This approach provides a uniform distribution of points within the BZ for DFT calculations, offering an unbiased method for selecting k-points. Moreover, the use of sets of irreducible points in the BZ serves as a potent tool for integrating periodic functions. Consequently, a denser k-point grid ensures that the accuracy of the discrete sum closely approximates the integral in Eq. 4.60. However, it's noteworthy that achieving good convergence for some properties might necessitate a significantly large $\boldsymbol{k}$-point grid size.

4.6. Pseudopotential

The pseudopotential approach in computational condensed matter physics involves replacing the actual Coulomb potential from the nucleus and core electrons with an effective potential that influences only the valence electrons. This method is based on the principle that core electrons shield the nucleus, thus altering the potential experienced by valence electrons. By focusing solely on valence electrons through the frozen core approximation, computational efficiency is significantly enhanced. Pseudo-wavefunctions, which require fewer Fourier modes, are used to represent valence states, enabling the use of a plane wave basis and reducing the computational burden. This approach simplifies the system to a one-electron scheme, allowing for the incorporation of additional effects like spin-orbit and relativistic interactions. Various methods to compute pseudopotentials have been developed, including norm-conserving[182, 183] and ultrasoft[184, 185] pseudopotentials.

4.6.1. Projector augmented wave method

The projector augmented wave (PAW) method was developed by Blöchl[186] as a method to calculate the electronic structure of materials within the framework of DFT with accuracy and greater computational efficiency[187–191]. It generalizes and combines all-electron and pseudopotential approaches through projector functions. The main idea of the PAW method is to transform physically relevant all-electron wave-functions $\psi(\vec{r})$ onto computationally convenient smooth auxilary wave-functions $\tilde{\psi}(\vec{r})$, that can be represented in a PW expansion. We start by defining a transformation operator $\hat{\mathcal{T}} = \hat{\mathcal{U}}^{-1}$ such that

$$\psi_n(\vec{r}) = \hat{\mathcal{T}}\tilde{\psi}_n(\vec{r}), \tag{4.61}$$

which implies that

$$\tilde{\psi}_n(\vec{r}) = \hat{\mathcal{U}}\psi_n(\vec{r}). \tag{4.62}$$

We expand auxilary wave-functions in PWs

$$\tilde{\psi}_n(\vec{r}) = \sum_{\vec{G}} e^{i\vec{G}.\vec{r}} \tilde{\psi}_n(\vec{G}). \tag{4.63}$$

Next, we define a complete set $\{|\phi_i\rangle\}$ of initial and final states of the transformation operator $\hat{\mathcal{T}}$ such that, for all i,

$$|\phi_i\rangle = \hat{\mathcal{T}}\, |\tilde{\phi}_i\rangle, \tag{4.64}$$

and find the transformation operator $\hat{\mathcal{T}}$ so that the auxiliary wave-functions are well behaved

$$\hat{\mathcal{T}} = 1 + \sum_j \left(|\phi\rangle - |\tilde{\phi}\rangle \langle \tilde{p}_j| \right), \tag{4.65}$$

where the projector function satisfies the bi-orthogonality

$$\langle \tilde{p}_i \rangle \, \tilde{\phi}_j = \delta_{ij}. \tag{4.66}$$

Using the above transformation operator, the relevant all-electron wave function takes the form

$$|\psi_n\rangle = |\tilde{\psi}_n\rangle + \sum_j \left(|\phi_j\rangle - |\tilde{\phi}_j\rangle \right) \langle \tilde{p}_j \rangle \, \tilde{\psi}_n. \tag{4.67}$$

The PAW formalism, uses many ideas similar to those developed by Vanderbilt[184] in his ultra-soft pseudopotential formalism and by Blöchl[192] in his earlier work on generalized separable potentials and has been successfully demonstrated for several interesting materials[186, 193–195]. We used this method within this thesis.

4.6.2. The spin-orbit coupling

Spin-orbit coupling constitutes a critical relativistic effect that connects an electron's spin to its orbital angular momentum. Pioneering work by Taylor et al.[196] has emphasized the significance of SOC in understanding electron dynamics. In the realm of DFT, recognizing the influence of relativistic adjustments is essential when examining the electronic structures of solid materials. For metals, where the Fermi level signifies the highest filled state at zero temperature, the disparity between the Fermi energy and the electron's rest mass energy, approximately 10^{-5} times smaller, underscores the importance of considering relativistic effects, especially for materials with significant atomic mass and narrow band gaps.

Introduced by Dirac to describe the behavior of relativistic electrons[82], the Dirac equation articulates the dynamics of electrons through a multi-component wave equation:

$$(\beta mc^2 + c \sum_{n=1}^{3} \alpha_n p_n)\psi(x,t) = i\hbar \frac{\partial \psi(x,t)}{\partial t}, \tag{4.68}$$

establishing a framework that incorporates the periodic potential of crystal lattices, akin to Schrödinger's formulation. Utilizing this equation, we apply the orthogonalized plane wave (OPW) method by Herring[197], which employs plane waves to form valence electron states orthogonal to core electron states. In its simplest form, the Dirac equation's non-relativistic limit separates into components for electrons and positrons, simplified through the Foldy-Wouthuysen transformation[198, 199], rendering a simplified two-component electron wavefunction. The transformed Hamiltonian appears as:

$$\begin{aligned} H = \frac{1}{2m}\left(\mathbf{p} - \frac{e}{c}\mathbf{A}\right)^2 - \frac{1}{8m^3c^2}\mathbf{p}^2 + V(\boldsymbol{r}) - \frac{e}{mc}\mathbf{S}\cdot\boldsymbol{\nabla}\times\mathbf{A} \\ + \frac{1}{2m^2c^2}\mathbf{S}\cdot\left[\boldsymbol{\nabla}V(\boldsymbol{r})\times\left(\mathbf{p}-\frac{e}{c}\mathbf{A}\right)\right] + \frac{\hbar^2}{8m^3c^2}\boldsymbol{\nabla}^2 V. \end{aligned} \tag{4.69}$$

This model accounts for modifications due to **A**, a symmetry-breaking field, incorporating the spin's influence explicitly.

Further exploration into the practical implications of SOC within modern quantum field theory reveals how relativistic phenomena influence material properties in unexpected ways. Contrary to Dirac's initial interpretations surrounding negative-energy states, modern theoretical physics reinterprets these as interactions between different electron states and the quantum vacuum, rather than time-reversal symmetry violations[200]. Such reevaluations are crucial for understanding materials like DSMs.

Addressing SOC in non-relativistic methods like the KS approach necessitates adjustments to the typical Hamiltonian expressions, as seen in:

$$\hat{H}_{so} = \frac{e\hbar}{4m^2c^2}\hat{\boldsymbol{\sigma}}\cdot[\mathbf{E}(\boldsymbol{r})\times\hat{\mathbf{p}}], \tag{4.70}$$

where SOC is treated as a perturbation and involves the calculation of the electric field **E** at the electron's position $\boldsymbol{r}$, illustrating the interaction:

$$\mathbf{E}(\boldsymbol{r}) = \frac{1}{2m^2c^2}\frac{1}{r}\frac{dV}{dr}. \tag{4.71}$$

In DFT calculations, employing relativistic pseudo-potentials allows for a nuanced inclusion of SOC, highlighting its role in lifting Kramers' degeneracy and influencing the electronic structure and physical properties of materials. The treatment of SOC as a first-order perturbation, along with PAW potentials, provides insight into the emergence of magnetic anisotropy, spin relaxation[201], and phenomena such as the anomalous Hall effect[202]. Our results elucidate how SOC affects transport properties and the manifestation of spin-dependent phenomena, emphasizing the necessity of its inclusion for accurate material characterization.

4.7. Tight Binding Approximation

Considering the fundamentals of electron behavior in solids, we address electrons and atomic nuclei distinctly due to their different masses and velocities, consistent with the BOA. For Dirac materials such as graphene, electron dynamics can be analyzed using a Schrödinger-like framework, where the electron's quantum state evolution is driven by the Hamiltonian as described by the Ehrenfest Theorem[203]. If the initial state of an electron is known, its future state at any time t can be determined with the evolution operator $U(t)$, expressed as:

$$\psi(\tilde{\boldsymbol{r}}, t) = U(t)\psi(0), \tag{4.72}$$

where the operator $U(t)$ is given by:

$$U(t) = e^{-i\hat{H}t/\hbar}, \tag{4.73}$$

assuming a time-invariant Hamiltonian $\hat{H}$.

To explore the electron dynamics under various external conditions, the TB model serves as a vital tool, especially significant for materials like graphene when studying their response to external stimuli in what is known as the adiabatic regime-characterized by slow changes relative to the system's response. The TB approximation, integrating time-dependent DFT, models the electron behavior using atomic orbitals to simulate electrons in a variety of structures from small molecules to large crystalline solids. This method proves useful in understanding how electrons interact with external elements such as SOC, electric, and electromagnetic fields. A practical example includes the interaction of laser light with the electronic dipole moments, which may induce symmetry-breaking effects in the material's ground state.

Initially introduced by Slater and Koster[204], the TB model suggests that a material's eigenstates are localized and resemble atomic orbitals - a concept also referred to as the linear combination of atomic orbitals. This approach is frequently utilized to compute the electronic band structure and define Bloch states within the same framework used by DFT ab initio methods. One of the TB model's strengths lies in its parameterization, where electronic structure parameters are tailored to experimental data concerning a material's characteristics or the results from detailed ab initio calculations. These parameters, however, are usually not transferable to other materials, highlighting a limitation of the TB model.

The application of the TB model is particularly effective for studying materials where the bonding is primarily defined by the electron states in the s and p orbitals. This model simplifies the computational process compared to ab initio methods by employing the two-center approximation, which simplifies multicenter integrals typical in solid-state HF calculations[205]. By focusing on nearest-neighbor interactions, the TB approach accelerates the determination of electronic structures, although it may compromise the accuracy in depicting orbital extents and bond lengths.

4.8. Tight Binding Model of Graphene

Graphene is recognized as a one-atom-thick planar sheet, comprising a hexagonal honeycomb lattice, which is visually represented in Figure 4.1. This configuration is achieved through each carbon atom forming strong σ-bonds with three neighboring atoms, resulting from s-p hybridization. These bonds are purely covalent, featuring no ionic characteristics. The lattice structure of graphene can be viewed as two interlaced triangular sublattices.

The electron dynamics within this material, specifically the transition of electrons to adjacent sites, is simplified in our analysis by defining a single parameter t. This parameter focuses exclusively on electron transitions between these sublattices, disregarding transitions within the same sublattice. The effective use of this parameter is critical in our representation of electron motion across graphene's lattice[206].

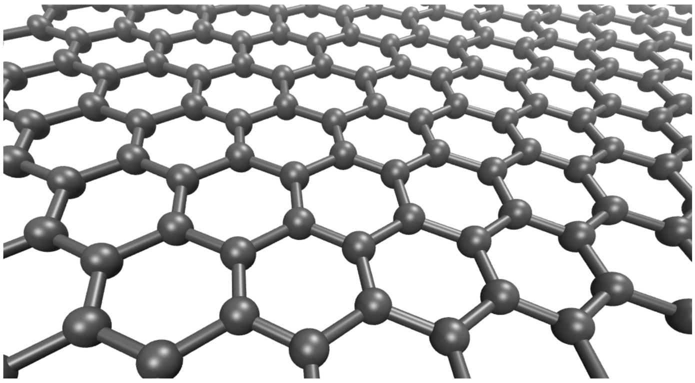

Figure 4.1: Ball-and-Stick Model of Graphene: Hexagonal (honeycomb) Carbon Lattice[207].

Our Hamiltonian for graphene's lattice, formulated within the tight binding approximation, is delineated as[98]:

$$\hat{H} = -t \sum_{\langle i,j \rangle} \left[\hat{a}_i^\dagger \hat{b}_j + \hat{b}_j^\dagger \hat{a}_i \right]. \tag{4.74}$$

In this expression, t signifies the electron hopping energy, estimated to be about 2.7 eV for graphene[208].

The notation $\langle i, j\rangle$ represents neighboring interactions between sublattices A and B, and $\hat{a}_i^\dagger$ and $\hat{a}_i$ denote creation and annihilation operators, respectively. This is expanded to include:

$$\sum_{\langle i,j\rangle}\left[\hat{a}_i^\dagger \hat{b}_j + \hat{b}_j^\dagger \hat{a}_i\right] = \sum_{i\in A}\sum_{\delta}\left[\hat{a}_i^\dagger \hat{b}_{i+\delta} + b_{i+\delta}^\dagger \hat{a}_i\right]. \tag{4.75}$$

In this model, δ refers to the vector positions of nearest neighbors, specifically δ_1, δ_2, and δ_3. Consequently, the Hamiltonian in Eq. 4.74 becomes:

$$\hat{H} = \frac{-t}{N/2}\sum_{i\in A}\sum_{\delta,k,k'}\left[e^{i(\boldsymbol{k}-\boldsymbol{k}')\cdot \boldsymbol{r}_i} e^{-i\boldsymbol{k}'\cdot\boldsymbol{\delta}}\hat{a}_{\boldsymbol{k}}^\dagger \hat{b}_{\boldsymbol{k}'} + h.c.\right]. \tag{4.76}$$

Here, $N/2$ is the count of sites in sublattice A. Simplifying, we have:

$$\hat{H} = \sum_{\boldsymbol{k}} \psi^\dagger h(\boldsymbol{k})\psi, \tag{4.77}$$

where ψ and $\psi^\dagger$ consist of:

$$\psi \equiv \begin{pmatrix} \hat{a}_{\boldsymbol{k}} \\ \hat{b}_{\boldsymbol{k}} \end{pmatrix}, \tag{4.78}$$

$$\psi^\dagger = \begin{pmatrix} \hat{a}_{\boldsymbol{k}} & \hat{b}_{\boldsymbol{k}} \end{pmatrix}, \tag{4.79}$$

and $h(\boldsymbol{k})$ is defined as:

$$h(\boldsymbol{k}) \equiv -t\begin{pmatrix} 0 & \triangle_k \\ \triangle_k^* & 0 \end{pmatrix}, \tag{4.80}$$

with $\triangle_{\boldsymbol{k}}$ calculated as:

$$\triangle_{\boldsymbol{k}} = e^{i\boldsymbol{k}\cdot\boldsymbol{\delta}_1} + e^{i\boldsymbol{k}\cdot\boldsymbol{\delta}_2} + e^{i\boldsymbol{k}\cdot\boldsymbol{\delta}_3}. \tag{4.81}$$

The eigenvalues of this matrix result in energy bands:

$$\varepsilon_\pm(\boldsymbol{k}) = \pm t\sqrt{\triangle_{\boldsymbol{k}}\triangle_{\boldsymbol{k}}^*}. \tag{4.82}$$

Graphically represented in Figure 4.2, this model underlines how the energy bands converge at the Fermi level, characterized by zero energy at the K and K' points of the BZ, demonstrating a significant aspect of graphene's electronic properties.

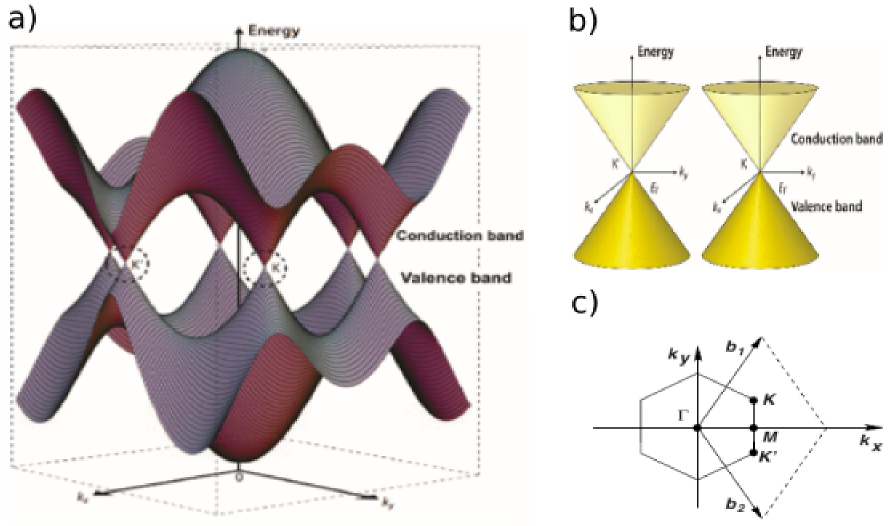

Figure 4.2: Electronic structure of monolayer graphene: a) Energy bands near the Fermi level in graphene, b) Conic energy bands in the vicinity of the K and K' points, and c) Corresponding reciprocal lattice of graphene with primitive vectors (b_1 and b_2), and the high-symmetry points Γ, K, K', and M[62, 209].

4.9. Wannier functions in the tight-binding approach

Wannier functions are a cornerstone in the study of electronic structures in computational condensed matter phsics and materials science, offering a real-space perspective to the otherwise momentum-space dominated descriptions. Originating from the work of Gregory Wannier in the 1930s[210], these functions are localized in real space and are used to provide insightful understanding of electronic behavior in crystals.

Mathematically, a Wannier function $W_n(\mathbf{r} - \mathbf{R})$ is defined through the Fourier transformation of Bloch functions $\psi_{n\mathbf{k}}(\mathbf{r})$, which are solutions to the Schrödinger equation in a periodic potential[211]. The transformation is given by:

$$W_n(\mathbf{r} - \mathbf{R}) = \frac{V}{(2\pi)^3} \int_{BZ} e^{-i\mathbf{k}\cdot\mathbf{R}} \psi_{n\mathbf{k}}(\mathbf{r}) d\mathbf{k}, \tag{4.83}$$

where $\mathbf{R}$ is a lattice vector, V is the volume of the unit cell, and the integration is over the BZ.

In computational studies, the challenge lies in determining these functions accurately, as they are not directly observable. Advanced algorithms, such as the MLWFs method, have been developed to compute Wannier functions that are as spatially localized as possible, enhancing both their physical interpretability and computational efficiency[212].

In the realm of TB models, Wannier functions play a pivotal role. They serve as a basis for constructing Hamiltonians that describe the electronic structure of materials with remarkable simplicity and accuracy. The TB Hamiltonian in terms of Wannier functions is expressed as:

$$H_{TB} = \sum_{nm\mathbf{R}} t_{nm}(\mathbf{R}) c^{\dagger}_{n\mathbf{0}} c_{m\mathbf{R}}, \tag{4.84}$$

where $t_{nm}(\mathbf{R})$ are the hopping parameters between sites, and $c^{\dagger}_{n\mathbf{0}}$, $c_{m\mathbf{R}}$ are creation and annihilation operators.

The application of Wannier functions extends notably to the study of topological properties in materials. Topological insulators and semimetals, characterized by their unique boundary states and protected by topological invariants, can be effectively analyzed using Wannier functions[213]. These functions provide a localized basis, making it feasible to calculate topological invariants directly from the electronic structure.

A key aspect of this approach is the utilization of Wannier charge centers (WCCs). The WCCs are calculated as the expectation values of position operators in the space of Wannier functions. They are crucial in determining the Chern number, a topological invariant, which is crucial to understanding the quantum Hall effect in materials[214].

In TIs, the existence of edge or surface states, which are immune to scattering by non-magnetic impurities, can be inferred from the non-trivial topology of the bulk band structure. The bulk-boundary correspondence principle links these surface states with the bulk electronic properties, a relationship that Wannier functions help to elucidate. This is particularly useful in predicting material properties that are sensitive to topological aspects, such as electrical conductivity and magnetoelectric effects[215].

Furthermore, Wannier functions are instrumental in studying the topological phase transitions. By tracking the evolution of WCCs across phase transitions, one can witness the change in topological character of the material. This method provides a powerful tool for probing and understanding the emergence of topological phases in various materials.

In conclusion, Wannier functions not only serve as a bridge between theoretical models and computational practices in condensed matter physics and material science but also play a crucial role in unveiling the topological nature of materials. Their application in determining topological invariants and studying boundary states opens new avenues in the exploration of novel quantum materials and devices.

Chapter 5

Computational Methods

This chapter outlines the computational techniques employed in this thesis, focusing on ab initio calculations used to analyze the electronic structure, DOS, and charge density of bulk materials $SrSi_2$, CoSi, and NbP. Next, the band structure data obtained from DFT calculations serve as the foundation for constructing TB models, further enabling the calculation of their topological properties. Additionally, this chapter details the process of renormalizing the electronic structure of $SrSi_2$ on a honeycomb lattice, using a TB model analogous to that of graphene. This approach facilitates a deeper understanding of the intrinsic behaviors and properties of these materials, essential for advancing the field of topological materials.

5.1. Ab initio calculations using Quantum Espresso

Quantum ESPRESSO is a pivotal tool in the computational materials science field, providing an integrated suite of open-source codes for electronic-structure calculations and materials modeling at the nanoscale. It is based on DFT, plane waves, and pseudopotentials, including norm-conserving, ultrasoft, and PAW types, all of which are supported by QE. The significance of QE lies in its wide applicability for the study of the electronic structure and related properties of materials, ranging from isolated molecules to complex solids[216].

At its core, QE facilitates the solution of the KS equations of DFT. The plane-wave basis set offers an efficient and accurate approach for representing wavefunctions, particularly useful for periodic systems such as crystals[217]. Pseudopotentials simplify the calculation by removing core electrons from the quantum mechanical treatments, focusing on valence electrons which are most relevant for bonding and other material properties.

Quantum ESPRESSO stands out not only for its efficient use of parallel computing, which enables large-scale simulations, but also for its comprehensive range of functionalities, comparable to those of proprietary DFT software packages, all within an open-source framework. This feature is particularly beneficial for investigating complex materials and phenomena such as phase transitions, mechanical properties, and energy transport, which are crucial for designing novel materials for energy and electronic applications[218, 219].

Quantum ESPRESSO offers a comprehensive and flexible platform for the investigation of a wide range of material properties. Its blend of accuracy, efficiency, and versatility makes it an indispensable tool in the field of computational materials science.

5.1.1. Methodology

In the computational investigation of materials using the QE framework, a systematic methodology is employed to ensure accurate and reproducible results. This approach is characterized by a meticulous setup of computational parameters, including pseudopotentials, XC functionals, and convergence tests[216, 220, 221].

The initial phase of the computational process involves the relaxation of the material's structures. This step is crucial for obtaining the optimized geometry of the material under investigation. Collinear calculations, which do not include the SOC, are performed to achieve this. The electron-ion interactions are represented using PAW pseudopotentials[188], and the XC effects are addressed using the GGA as formulated by PBE[175]. These pseudopotentials and functionals are carefully selected for their proven reliability in representing electronic structures. Regarding the computational parameters, a plane-wave basis set is employed, with convergence tests conducted using a charge density cut-off energy (ecutwfc) set to eight times the kinetic energy cut-off (ecutrho), ensuring the accuracy of all calculations. The convergence of electronic energies is confirmed with a high precision threshold, achieving an accuracy of 10^{-3} eV/Å on the total forces, using the converged Monkhorst-Pack[222–224] k-point meshes. To ensure a comprehensive exploration of the electronic properties, denser k-point grids are utilized for BZ sampling[181].

Time-reversal symmetry is a critical consideration in these calculations, particularly for materials where spin plays a significant role. To address this, the electronic states are treated as spinors, adhering to double group symmetry and utilizing the Methfessel-Paxton smearing scheme with an appropriate width[223]. This approach promotes accurate convergence of the electronic structure, favoring a non-magnetic ground state unless magnetic ordering is explicitly introduced. Post relaxation, the optimized structures undergo further analysis to study non-collinear magnetic states, incorporating fully relativistic pseudopotentials that inherently include SOC. This step is essential for revealing the subtle effects of SOC on the material's electronic structure, particularly in lifting Kramers' degeneracy and splitting degenerate electron states.

The methodology outlined here, characterized by its rigorous and systematic approach, is foundational in the computational study of various materials. It ensures the reliability and reproducibility of the results, thereby providing a solid basis for further theoretical and practical explorations in materials science.

5.1.2. Convergence tests for the bulk $SrSi_2$, CoSi, and NbP.

An essential step in DFT calculations is determining the appropriate cut-off energy and k-point grid for the crystal system under consideration. Figures 5.1(a) and 5.1(b) illustrate the convergence behavior of the total energy with respect to these parameters for bulk $SrSi_2$. The convergence tests were performed by gradually increasing the cut-off energy and k-point density, observing changes in the total energy until further adjustments resulted in negligible variations. From the plots, a cut-off energy of 65 Ry and a $9 \times 9 \times 9$ k-point mesh provide stable total energy values, indicating good convergence for the computational setup.

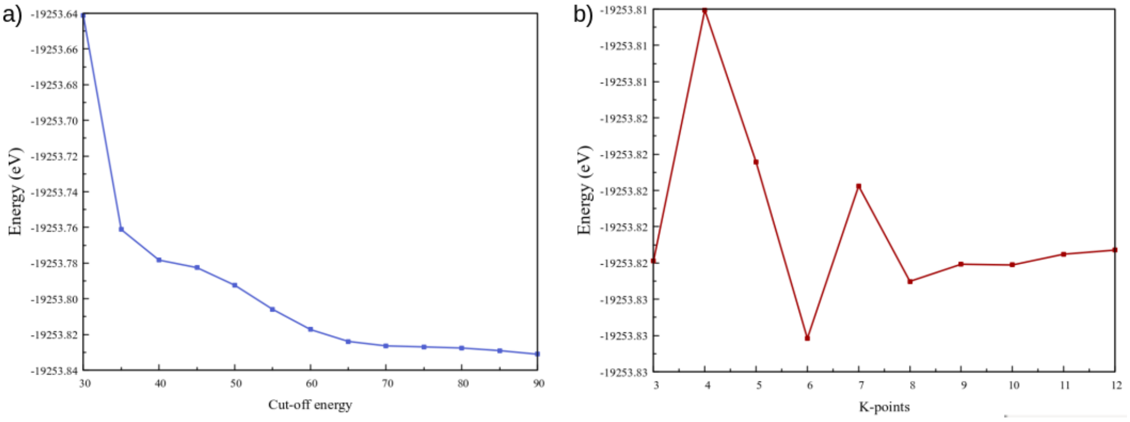

Figure 5.1: Convergence test for $SrSi_2$ showing the variation in total energy as a function of (a) cut-off energy and (b) k-point grid size. The selected values of 65 Ry for the cut-off energy and a $9 \times 9 \times 9$ k-point mesh ensure reliable convergence for further calculations.

For the CoSi structure, Figures 5.2(a) and 5.2(b) show the variation in total energy as a function of cut-off energy and k-points, respectively. As shown in the plots, the total energy stabilizes effectively when a cut-off energy of 50 Ry and a k-point mesh of $9 \times 9 \times 9$ are employed. These values ensure minimal fluctuations in energy, indicating reliable convergence.

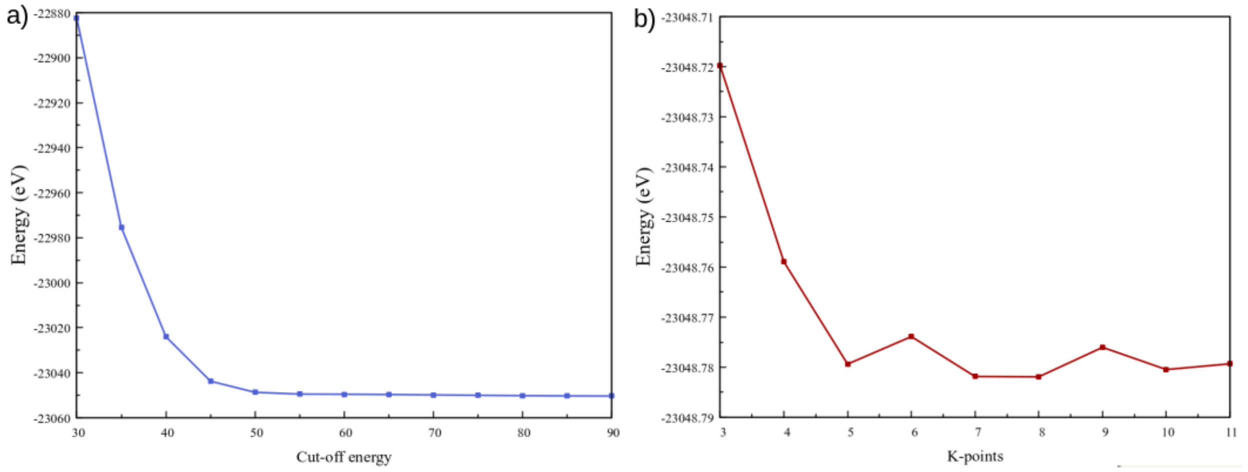

Figure 5.2: Convergence test for CoSi showing the dependence of total energy on (a) cut-off energy and (b) k-point grid size. Converged values of 50 Ry for the cut-off energy and a $9 \times 9 \times 9$ k-point mesh provide stability in the total energy, establishing a solid basis for subsequent analyses.

For the NbP structure, Figures 5.3(a) and 5.3(b) display the changes in total energy as influenced by variations in cut-off energy and k-points, respectively. As seen in the graphs, stable convergence is achieved at a cut-off energy of 65 Ry and a k-point grid of $7 \times 7 \times 7$, where the total energy fluctuations become minimal.

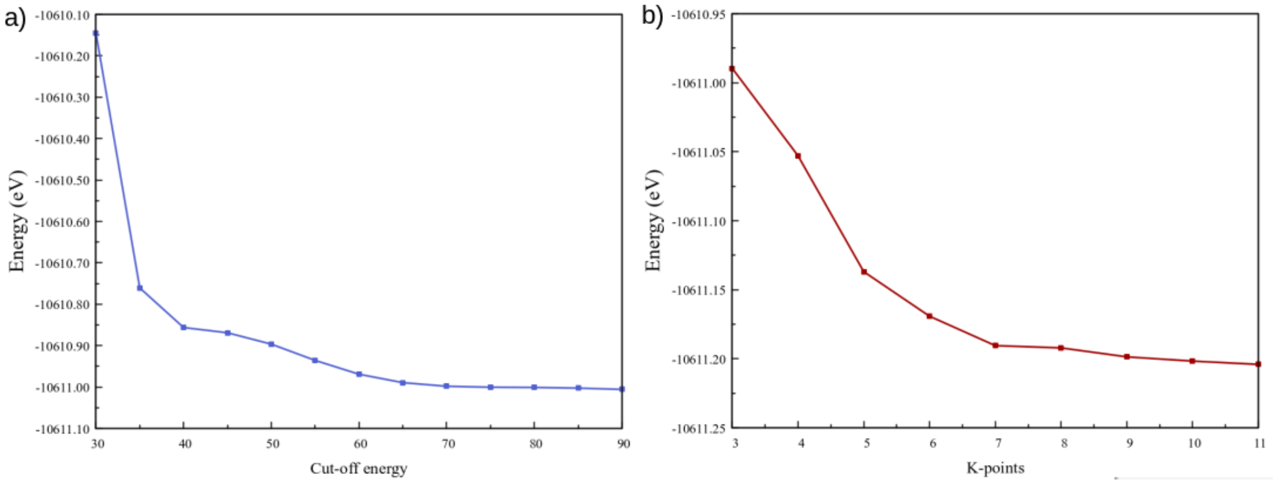

Figure 5.3: Convergence test for NbP illustrating the variation in total energy as influenced by (a) cut-off energy and (b) k-point grid size. A cut-off energy of 65 Ry and a $7 \times 7 \times 7$ k-point mesh achieve minimal energy fluctuations, ensuring reliable settings for further calculations.

In $SrSi_2$ the total energy varies up and down more strongly as the k-point mesh is increased because its semimetallic band structure hosts multiple Weyl crossings very near the Fermi level. At low to moderate mesh densities each incremental Monkhorst-Pack grid will sample these band-crossing regions unevenly, sometimes capturing a critical pocket of states and sometimes missing it, which leads to the overshoot-undershoot behavior seen in Fig. 5.1(b). By contrast, CoSi and NbP have fewer or more smoothly dispersing states at E_n, so each new k-point simply refines an already-sampled Fermi surface and the energy converges more monotonically (Figs. 5.2(b) and 5.3(b)). In addition, $SrSi_2$'s primitive cell in $P4_332$ is larger (ten atoms per cell) than those of CoSi ($P2_13$) or NbP ($I4_1md$), giving a smaller Brillouin zone and thus a coarser reciprocal-space sampling step for each added k-point - another factor that amplifies the oscillations in total energy during convergence testing[225, 226]

In summary, the convergence tests for $SrSi_2$, CoSi, and NbP highlight the importance of carefully selecting the cut-off energy and k-point grid in achieving reliable computational accuracy. Each structure required fine-tuning these parameters to minimize fluctuations in total energy, with the chosen values providing a stable basis for subsequent calculations. This approach underscores the effectiveness of the plane-wave basis set, where accurate results can be obtained by systematically adjusting key parameters. The converged values for each material ensure that these settings will yield consistent and reliable outcomes in further analyses, as observed in the figures below.

5.1.3. Band structure analysis

Analyzing a material's band structure is essential in computational condensed matter and materials science, as it reveals the energy levels of electrons within a crystal, thereby determining the material's electronic and optical properties. To compute the band structure, we solve the KS equations (see Eq. 4.49 in Chapter 4) of DFT at each **k**-point in the BZ:

$$\hat{H}_{\mathrm{KS}}\psi_{\mathbf{k}n}(\mathbf{r}) = \varepsilon_{\mathbf{k}n}\psi_{\mathbf{k}n}(\mathbf{r}), \tag{5.1}$$

where $\hat{H}_{\mathrm{KS}}$ is the KS Hamiltonian, $\varepsilon_{\mathbf{k}n}$ are the eigenvalues corresponding to the energy levels of the electrons, and $\psi_{\mathbf{k}n}(\mathbf{r})$ are the KS orbitals. The KS Hamiltonian comprises terms representing the kinetic energy, electron-electron interactions, electron-ion interactions, and the XC energy, which is crucial for capturing the quantum mechanical nature of electron interactions. Due to the periodic nature of the crystal lattice, the KS potential $V_{\mathrm{KS}}(\mathbf{r})$ inherits this periodicity, allowing the application of Bloch's theorem. According to Bloch's theorem, the wavefunctions of electrons in a periodic potential can be expressed as:

$$\psi_{\mathbf{k}n}(\mathbf{r}) = e^{i\mathbf{k}\cdot\mathbf{r}} u_{\mathbf{k}n}(\mathbf{r}), \tag{5.2}$$

where **k** is the wavevector within the first BZ, and $u_{\mathbf{k}n}(\mathbf{r})$ is a function that shares the periodicity of the crystal lattice, satisfying $u_{\mathbf{k}n}(\mathbf{r}+\mathbf{R}) = u_{\mathbf{k}n}(\mathbf{r})$ for any lattice vector **R**. This formulation simplifies the problem by reducing it to the first BZ and enables the use of plane-wave basis sets for computational efficiency. The band structure is then constructed by plotting the eigenvalues $\varepsilon_{\mathbf{k}n}$ against the wavevector **k** for various bands n.

Analyzing a material's band structure is essential for understanding its electronic properties. Key features such as band gaps, band curvatures, and special points like Dirac or Weyl nodes provide insights into the material's behavior. For example, a band gap between the valence and conduction bands indicates insulating or semiconducting properties, while its absence suggests metallic behavior[227]. The effective mass of electrons, which affects charge transport, can be determined from the curvature of the bands near the Fermi level using the relation:

$$m^* = \hbar^2 \left(\frac{\partial^2 \mathcal{E}}{\partial k^2}\right)^{-1}, \tag{5.3}$$

where $\hbar$ is the reduced Planck constant[224]. Additionally, understanding whether bands originate from s, p, d, or f orbitals sheds light on the material's bonding nature and optical characteristics. By applying DFT and examining the resulting band dispersion, researchers can predict a material's conductive behavior, carrier effective masses, and suitability for various applications. This approach is fundamental in theoretical materials science, informing experimental research and the development of new materials.

5.1.4. Density of states computation

In materials science, understanding how electrons are distributed across energy levels is key to exploring a material's electronic characteristics. This distribution is captured by the concept of the DOS, which essentially counts the number of electron states available per unit volume within a specific energy range[224]. Mathematically, the number of electron states N within an energy range $\mathcal{E}$ to $\mathcal{E}+\delta\mathcal{E}$ is expressed as $N(\mathcal{E})\delta\mathcal{E}$[227]. The DOS helps in deciphering how different electron orbitals contribute to energy levels within this range, and it plays a crucial role in determining the electronic transport properties of materials[217].

The relationship between energy $\mathcal{E}$ and wave-vector $\boldsymbol{k}$, crucial for understanding the DOS, is given by the dispersion relation:

$$\mathcal{E} = \frac{\hbar^2}{2m}k^2. \tag{5.4}$$

Here, $\mathcal{E}$ represents the energy of a free electron with wavevector $\mathbf{k}$ and mass m. In a three-dimensional setting, the total DOS can be described by the formula[224]:

$$D(\mathcal{E}) = \frac{1}{2\pi^2}\left(\frac{2m}{\hbar^2}\right)^{\frac{3}{2}}\mathcal{E}^{\frac{1}{2}}. \tag{5.5}$$

This expression indicates that the DOS increases with the square root of energy, reflecting the greater number of available states at higher energies.

To avoid confusion between the free-electron model and actual material DOS, we clarify as follows: Eqs. 5.4 and 5.5 give, respectively, the energy dispersion $\mathcal{E}(k)$ and the corresponding density of states $D(\mathcal{E})$ for an ideal 3D free Fermi gas, assuming a uniform potential and a simple parabolic dispersion relation, and therefore apply only to nearly free electrons in simple metals[228]. This analytic form captures the $D(\mathcal{E}) \propto \mathcal{E}^{1/2}$ behavior of parabolic bands but does not include the energy gaps or the detailed band curvature induced by a crystal's periodic potential[229]. In contrast, semiconductors and insulators exhibit a true band gap - so the DOS is strictly zero over that range - and their valence and conduction bands each have distinct DOS shapes, including step-like onsets and van Hove singularities at BZ critical points[230]. Density functional theory DOS curves incorporate the full band structure of the material, but standard KS functionals systematically underestimate gap magnitudes by 30-40% due to XC approximations[231]. Real materials therefore deviate from the simple $\mathcal{E}^{1/2}$ law, especially near band extrema and singularities[14]. Finally, external perturbations such as strain or electric fields shift band edges and introduce new DOS features - effects that must be evaluated with material-specific DOS calculations rather than the free-electron model[232].

5.1.5. Charge density mapping

In materials science, accurately determining the charge density, denoted as $\rho(\mathbf{r})$, is essential for understanding a material's electronic structure and properties. Charge density represents the spatial distribution of electrons within a material and is pivotal in predicting various physical characteristics. Within the framework of DFT, the charge density is derived from the KS orbitals, $\psi_{\mathbf{k}n}(\mathbf{r})$, obtained by solving the KS equations. The expression for charge density is:

$$\rho(\mathbf{r}) = \sum_{\mathbf{k},n} f_{\mathbf{k}n} |\psi_{\mathbf{k}n}(\mathbf{r})|^2, \tag{5.6}$$

where the summation extends over all wavevectors $\mathbf{k}$ in the BZ and all bands n. The term $f_{\mathbf{k}n}$ represents the occupation number of the state characterized by $\mathbf{k}$ and n, which is determined by the Fermi-Dirac distribution[217].

Analyzing charge density offers valuable insights into bonding characteristics and electron distribution within a material. For example, regions with elevated charge density between atoms often indicate strong covalent bonding, while areas with lower charge density may suggest ionic interactions. Visualizing charge density aids in identifying electron-rich and electron-poor regions, which is crucial for understanding chemical reactivity and catalytic behavior.

Charge density mapping also facilitates the visualization of electron clouds in molecules and solids, providing information about symmetry, electron delocalization, and the shapes of molecular orbitals. In complex materials, such as those exhibiting topological properties or intricate electron correlation effects, charge density analysis becomes even more critical. It helps elucidate the underlying mechanisms driving the material's unique properties and can reveal changes associated with phase transformations.

By thoroughly analyzing charge density derived from first-principles calculations, researchers can gain significant information about bonding, electronic distribution, and potential functionalities of materials. This understanding is instrumental in designing novel materials with tailored properties for specific applications.

5.2. Application of symmetry breaking fields

Symmetry considerations are fundamental in physics, particularly in understanding the electronic properties of crystalline materials. At absolute zero temperature, perturbations that alter the inherent symmetries of Bloch states can induce new quantum phases. For instance, the presence of time-reversal (T) symmetry ensures that both the orbital magnetic moment and Berry curvature of Bloch states are zero, provided inversion symmetry is also maintained. Therefore, both T and I symmetries are crucial in determining the electronic characteristics of crystals[233].

In our research, we intentionally break these symmetries by incorporating SOC and applying external perturbations such as strain and electric fields in our calculations. These external fields serve as tunable disorder potentials, modifying the ground state symmetry and allowing us to explore the resulting electronic properties. By systematically varying these perturbations, we aim to understand how symmetry breaking influences the emergence of new quantum phases and the overall behavior of the material[234].

5.2.1. Application of tensile strain to the ground states

Applying tensile strain to a material is a methodical approach for exploring changes in its electronic properties and ground state. This study focuses on tensile strain in the z-direction, achieved by adjusting the lattice constant in that direction. Here, we express the tensile strain as a percentage relative to the original lattice constant c, resulting in a modified lattice constant,

$$c' = c + \%\Delta c, \tag{5.7}$$

where $\%\Delta c$ denotes the percentage extension. By stretching the crystal lattice along the z-axis, this controlled alteration allows for a systematic examination of strain's effect on the material.

To implement tensile strain along the z-axis, we first compute the distorted lattice constant from Eq. 5.7. In the QE input file, this is realized by replacing the third lattice vector under the **CELL_PARAMETERS** card with the scaled value. All deformations were imposed by altering the crystal lattice vectors to achieve the target strain; no external stress tensor was used. For example, if the unstrained cell is

```
CELL_PARAMETERS {bohr}
12.4037    0.0000    0.0000
 0.0000   12.4037    0.0000
 0.0000    0.0000   12.4037
```

imposing a lattice deformation corresponding to a 5% tensile strain by modifying the cell vectors in the z-direction produces

```
CELL_PARAMETERS {bohr}
12.4037    0.0000    0.0000
 0.0000   12.4037    0.0000
 0.0000    0.0000   12.4037*(1.05)
```

so that the c-vector becomes 12.4038×1.05 bohr. This simple scaling preserves in-plane lattice constants and symmetry (with **ibrav = 0**), while exerting uniaxial tension in z.

Tensile strain alters both the atomic spacing and the corresponding orbital overlaps, thereby tuning the hopping amplitudes in our TB models and reshaping the DFT band structure. As c increases, certain band crossings near the Fermi level shift in energy or move in k-space, which directly modifies the local Berry curvature peaks and can shift or gap Weyl/Dirac nodes. In practice, we observe that modest z-strain enhances the magnitude of Berry curvature peaks - reflecting reduced band inversions - while larger strain can open small gaps at formerly degenerate points, thus driving transitions between semimetallic and insulating topologies. By systematically varying $\%\Delta c$, we map out how the Fermi-surface connectivity, Berry phase distributions, and topological invariants evolve, providing a clear picture of strain as an effective tuning parameter for emergent quantum phases in $\mathrm{SrSi_2}$, CoSi, and NbP.

The influence of tensile strain on electronic characteristics is significant. Strain modifies the spacing between atoms, which directly impacts the electronic band structure. To analyze these changes, DFT models are applied, enabling calculation of the adjusted charge density $\rho(\mathbf{r})$ under strain. For the strained material, the charge density is represented as

$$\rho'(\mathbf{r}) = \sum_{\mathbf{k},n} f'_{\mathbf{k}n} |\psi'_{\mathbf{k}n}(\mathbf{r})|^2, \tag{5.8}$$

with $\psi'_{\mathbf{k}n}(\mathbf{r})$ representing the wavefunctions and $f'_{\mathbf{k}n}$ the occupation values in the strained structure[217]. This analytical approach provides insight into how strain affects electron distribution and bonding properties.

Applying tensile strain along the z-axis alters the lattice constant, which changes interatomic spacing and thus the electronic band structure. These modifications can vary the band gap width - shifting the material between semiconducting and insulating behavior - affect electrical conductivity and optical response, and even trigger phase transitions. By examining the strained charge density and band structure together, we gain clear insights into how mechanical deformation influences ground-state properties. This understanding guides the design of materials with tailored electronic characteristics and supports future experimental studies of stress-driven phenomena.

To clarify the choice of strain mode, we initially tested both compressive and tensile distortions on $\mathrm{SrSi_2}$, CoSi, and NbP. In each case, modest compressive strain produced only minimal shifts in the band extrema - implying negligible changes in topological markers such as Berry curvature distributions and Fermi-surface connectivity - even though we did not explicitly compute those metrics at this stage. By contrast, tensile strain consistently modulated interatomic distances in a way that altered band crossings near the Fermi level and enhanced sensitivity of topological invariants to external bias. Consequently, we have focused our discussion on tensile strain - introduced by uniformly scaling the lattice vectors according to Eq. 5.7 - since it provides a clear tuning parameter for the emergent quantum phases in these materials.

According to the Hellmann-Feynman theorem[235], the force on each atom - or, by extension, the stress on the crystal lattice - can be obtained directly as the derivative of the total electronic energy with respect to atomic positions or strain, without needing finite-difference energy calculations. In our DFT workflow, we impose a given tensile strain by deforming the lattice vectors, then relax all internal atomic coordinates until the Hellmann-Feynman forces vanish. At each strain step, the resulting stress tensor, computed as the derivative of the energy with respect to strain, exactly captures how the applied deformation alters the interatomic Coulomb forces and the total energy of the system. Thus, the changes in band structures and topological metrics we observe under strain arise naturally from the modified interatomic forces that the Hellmann-Feynman theorem predicts. In practice, we scanned strain values, relaxed the atoms via Hellmann-Feynman forces, and recorded the energy and stress response. This procedure ensures that our strain-dependent electronic and topological results for $SrSi_2$, CoSi, and NbP are fully consistent with the underlying quantum-mechanical forces dictated by the Hellmann-Feynman theorem.

5.2.2. Application of an external electric field to the ground states

To apply an external electric field in computational simulations, various methods are utilized, depending on the specific system under study. In QE, an external electric field is introduced by adding a sawtooth potential to the KS Hamiltonian[236–238]. This allows for the simulation of materials in homogeneous electric fields while using periodic boundary conditions. This method is particularly useful in the study of dielectric properties and polarization effects in materials.

The external electric field introduces an additional potential energy term, $V_{\text{ext}}(\mathbf{r})$, defined as:

$$V_{\text{ext}}(\mathbf{r}) = -\mathbf{E} \cdot \mathbf{r}. \tag{5.9}$$

Here, **E** represents the external electric field vector, and **r** is the position vector. The negative sign indicates that the potential energy of a positive charge decreases in the direction of the electric field, aligning with physical expectations[217, 224, 239]. To maintain periodicity in simulations, the potential is reset at the boundaries of each unit cell, resulting in a 'sawtooth' profile.

In DFT, the total energy of a system subjected to an external electric field is expressed as:

$$E_{\text{total}}[\rho] = E_{\text{DFT}}[\rho] + \int \rho(\mathbf{r}) V_{\text{ext}}(\mathbf{r})\, d\mathbf{r}. \tag{5.10}$$

In this equation, $E_{\text{DFT}}[\rho]$ denotes the standard DFT energy functional, and $\rho(\mathbf{r})$ is the electron density[217]. Implementing the sawtooth potential in QE allows for accurate first-principles simulations of materials and interfaces under external electric fields, aiding in the investigation of phenomena such as polarization, dielectric properties, and field-induced phase transitions[175].

The strength of the applied electric field in these simulations is measured in atomic units (a.u.), where 1 a.u. corresponds to approximately 5.14×10^{11} V/m. During simulations, the total energy of each structure is calculated and converged under the modified potential. However, it is important to note that the atomic positions are typically not re-optimized for each new electric field value, which should be considered when interpreting the results of such simulations.

5.3. Tight-binding modeling and topological analysis

To advance our understanding of the electronic and topological properties of SrSi_2, CoSi, and NbP, we extend our computational study beyond standard DFT techniques. This exploration is supported by using Wannier90[240] and WannierTools[241], which enable the construction of highly detailed TB models for each material. Through these TB models, we gain a more nuanced view of their electronic structures, as well as a clearer framework for examining their topological characteristics. Building on this foundation, we further map the ground states of SrSi_2, CoSi, and NbP onto a graphene-like lattice using Quantum Lattice software[242]. This approach allows us to investigate how these materials might behave within a lattice environment that mirrors the characteristics of graphene, providing new insights into their structural and topological properties under such conditions.

5.3.1. Construction of the TB Hamiltonian with Wannier90

To construct a TB Hamiltonian that accurately reflects the electronic properties of SrSi_2, CoSi, and NbP, we utilize Wannier90[240], a powerful tool that generates MLWFs from DFT results. Wannier90 is particularly valuable for its ability to transform electronic band structure data obtained from first-principles calculations into a real-space framework, which provides an insightful view of electronic behavior in terms of localized orbitals. This real-space representation is fundamental for examining complex electronic and topological characteristics in materials.

The construction of the TB Hamiltonian begins by using DFT to compute the Bloch wavefunctions, $\psi_{\mathbf{k}n}$, where $\mathbf{k}$ represents the wave vector within the BZ, and n is the band index. These Bloch states, generated through QE in this study, serve as input for Wannier90, which then applies an iterative localization process to convert them into Wannier functions. The localization of these functions is crucial for generating TB models, as it allows electronic properties to be expressed in terms of interactions among localized orbitals, making it possible to capture essential features of the material's band structure and topology.

The transformation from Bloch functions to Wannier functions follows a mathematical framework in which Wannier90 minimizes the spatial spread of the functions. The transformation is mathematically expressed as:

$$w_{\mathbf{R}n}(\mathbf{r}) = \frac{V}{(2\pi)^3} \int_{BZ} e^{-i\mathbf{k}\cdot\mathbf{R}} \psi_{\mathbf{k}n}(\mathbf{r})\, d\mathbf{k}, \tag{5.11}$$

where the integration occurs over the BZ. Here, $w_{\mathbf{R}n}(\mathbf{r})$ represents the Wannier function associated with lattice vector $\mathbf{R}$ and band index n, and V is the volume of the unit cell. This transformation yields localized orbitals that retain key electronic characteristics derived from the DFT-calculated Bloch states.

Using these localized Wannier functions, the TB Hamiltonian, H_{TB}, can then be constructed. This Hamiltonian represents the electronic structure in terms of hopping parameters between Wannier functions located on different lattice sites, which provides a simplified yet comprehensive model of the system's electronic behavior. The TB Hamiltonian takes the form:

$$H_{TB} = \sum_{\mathbf{R},\mathbf{R}',n,m} t_{\mathbf{R}n,\mathbf{R}'m} c^{\dagger}_{\mathbf{R}n} c_{\mathbf{R}'m}, \tag{5.12}$$

where $t_{\mathbf{R}n,\mathbf{R}'m}$ denotes the hopping parameter between Wannier functions centered at sites $\mathbf{R}$ and $\mathbf{R}'$, and $c^{\dagger}_{\mathbf{R}n}$, $c_{\mathbf{R}'m}$ represent creation and annihilation operators, respectively. This TB framework serves as a foundation for further studies of topological characteristics, facilitating calculations of properties such as Berry curvature and surface states with tools like WannierTools[241].

The ability of Wannier90 to produce MLWFs that bridge DFT results and TB models is essential for exploring topological properties in materials. By mapping complex electronic structures into real space, it enables a deeper understanding of how electronic states interact locally, which is critical for studying materials with potential topological phases. Consequently, the TB Hamiltonian constructed through this approach provides a versatile platform to explore a variety of topological phenomena, making it an invaluable tool for modern condensed matter research.

5.3.2. Calculation of Topological Properties via WannierTools

WannierTools, an advanced computational toolkit, is tailored for investigating the intricate topological features of materials based on TB Hamiltonians derived from Wannier90[241]. It serves as a bridge between first-principles calculations and the analysis of topological invariants by translating electronic structure data into forms suitable for topology-focused exploration. The software offers a structured framework to analyze and visualize phenomena inherent to topological materials, such as Berry curvature, Chern numbers, Fermi arcs, and surface states.

A crucial aspect of studying topological materials is calculating the Berry curvature, a vector field in momentum space that captures the geometric phase of electronic states. In WannierTools, this quantity, represented by $\Omega(\mathbf{k})$, is derived from the wavefunction characteristics of each electronic band. Specifically, the Berry curvature at a given $\mathbf{k}$-point is defined as:

$$\Omega(\mathbf{k}) = \nabla_{\mathbf{k}} \times \langle u_{\mathbf{k}n} | i\nabla_{\mathbf{k}} | u_{\mathbf{k}n} \rangle, \tag{5.13}$$

where $|u_{\mathbf{k}n}\rangle$ denotes the periodic part of the Bloch function. This formulation provides essential insights into the electronic band topology by serving as a precursor to computing the Chern number, an integer that classifies bands based on their topological order. The Chern number is derived by integrating the Berry curvature over the BZ, and its non-zero value indicates a nontrivial topological phase.

WannierTools also specializes in the simulation of surface states, which are the hallmark of topological insulators and semimetals. By constructing a surface Green's function from the TB Hamiltonian, the software models the localized electronic states that emerge at the boundaries of a material. This computational approach leverages iterative methods to evaluate the local density of states at the surface, which is particularly useful for identifying and visualizing the presence of Fermi arcs. These arcs, characteristic of WSMs, appear as disconnected segments in momentum space and provide direct evidence of the material's topological structure. This surface-based analysis allows researchers to probe the interface-specific properties of topological materials that are not apparent in bulk calculations.

In summary, WannierTools is an indispensable resource for computationally exploring the topological attributes of materials. Its extensive toolkit, which includes Berry curvature and Chern number calculation, surface state analysis, etc ... provides a comprehensive platform for analyzing topological phases. By integrating with TB Hamiltonians generated from DFT, WannierTools enables an in-depth examination of the electronic properties central to topological materials research[241].

5.4. SrSi$_2$ ground state renormalization to graphene's TB model and topological phase emergence

The study of TQPTs presents significant challenges because these phases are not characterized by conventional local order parameters. To explore quantum phases effectively, we focus on understanding the topological order that emerges when ground-state data from DFT calculations, applied to materials such as SrSi$_2$ is projected onto a graphene-based lattice through a TB model. This projection approach leverages the semi-metallic nature of these materials, which have zero-temperature carrier transport behaviors similar to graphene's. However, this similarity pertains only to transport properties and does not imply identical atomic structures, bonding chemistry, or symmetry of crystal lattices.

For the present study, Quantum Lattice software was utilized to model the transport and topological characteristics of SrSi$_2$ within the TB framework[242, 243]. This required carefully adjusting scaling parameters to align the observed transport properties of this material with its band structures under SOC, as represented on a graphene-like lattice. By adjusting these scaling factors, we achieved alignment between the DFT-calculated band properties and those produced by our TB model, allowing for a meaningful comparison.

Our renormalization approach draws upon the Kane-Mele model used for bulk systems, with an additional exchange field term incorporated to fit specific observed band gaps[244, 245]. This extra term allowed us to reproduce the band structures of the selected material in the presence of SOC, particularly for cases where the Kane-Mele model alone would not suffice. This approach is vital as the low-energy carrier excitations near the Fermi level have a significant impact on the transport characteristics of Dirac materials, which include graphene-like systems and some TIs.

In condensed matter physics, understanding quantum transport phases at absolute zero is fundamental, especially the emergence of topological order in the presence of symmetry-breaking mechanisms, such as applied fields, and the ability to manipulate transitions across different topological quantum phases (TQPs). The development of graphene in 2004, along with a growing range of 2D materials, has introduced new theoretical possibilities in quantum materials research. The unique band topologies and confinement effects of 2D materials make them ideal platforms for examining QPTs and their response to external fields, holding potential applications in optics and optoelectronics.

Using Quantum Lattice, we induced topological phase transitions by adjusting parameters like the exchange field, Rashba SOC, KM SOC, and Haldane model parameters. This allowed us to construct topological phase diagrams, identifying the zero-temperature phases through the calculated Chern number C. Variations in these metrics indicate shifts between distinct topological phases[246, 247]. Both invariants are related to the Berry connection $A^{(j)}$ for the j^{th} band, the Berry curvature $\Omega^{(j)}(\boldsymbol{k})$, and the Chern number $C^{(j)}$. A non-zero Chern number signals topological activity in the wavefunction, providing a basis for differentiating between quantum phases. This property, intrinsic to the band structure, strongly influences carrier transport within the material. The inclusion of SOC in our TB calculations was essential, as it lifts degeneracies in bulk bands, demonstrating the significant role spin plays as a quantum degree of freedom in these systems.

Overall, this chapter establishes the computational groundwork and tools necessary to explore topological materials and sets the stage for deeper analysis in subsequent chapters. Through DFT calculations in QE, the effects of symmetry-breaking fields, and TB modeling using Wannier90 and WannierTools, we have mapped key electronic and topological properties. Additionally, by employing Quantum Lattice to model phase transitions, we gained insights into the emergence of topological phases in selected material. These methods provide a robust framework for analyzing complex quantum properties, enabling a thorough investigation of the unique topological characteristics of these materials in later chapter.

Chapter 6

Results and Discussion

In this chapter, we present and discuss the results of our investigations into the physical, and topological properties of bulk $SrSi_2$*, CoSi, and NbP structures. We discuss how external fields impact these materials by breaking the symmetry of their ground states and inducing quantum phase transitions. Our investigation was conducted using a range of fields. However, here we only present the results for which we observed significant changes. Additionally, present and discuss the results from our study on the renormalization of the bulk* $SrSi_2$ *band structure to graphene.*

6.1. Bulk $SrSi_2$ structure

6.1.1. Structural properties

$SrSi_2$ crystallizes in a simple cubic structure, belonging to the chiral space group $P4_332$ (No. 212), which lacks inversion and mirror symmetries[14, 248, 249]. The lattice constant a = 6.563 Å[248–251]. As shown in Fig. 6.1(a), $SrSi_2$ crystal structure comprises a unit cell containing four strontium (Sr) atoms at Wyckoff positions 4a and eight silicon (Si) atoms at positions 8c. The lack of I symmetry is crucial in $SrSi_2$ for the potential realization of a Weyl semimetal phase under the condition that time-reversal (T) symmetry is preserved. The bulk BZ of $SrSi_2$ is showcased in Fig. 6.1(c). The X, Y, and Z points, which hold equivalent positions, are situated at the centers of the square faces, while the M points are located at the centers of the edges, and the R points can be found at the corners of the cubic structure. The 001 surface projection represented on top of the BZ intersects with the critical high-symmetry lines and is an essential aspect in the investigation of surface states intrinsic to topological phases of matter.

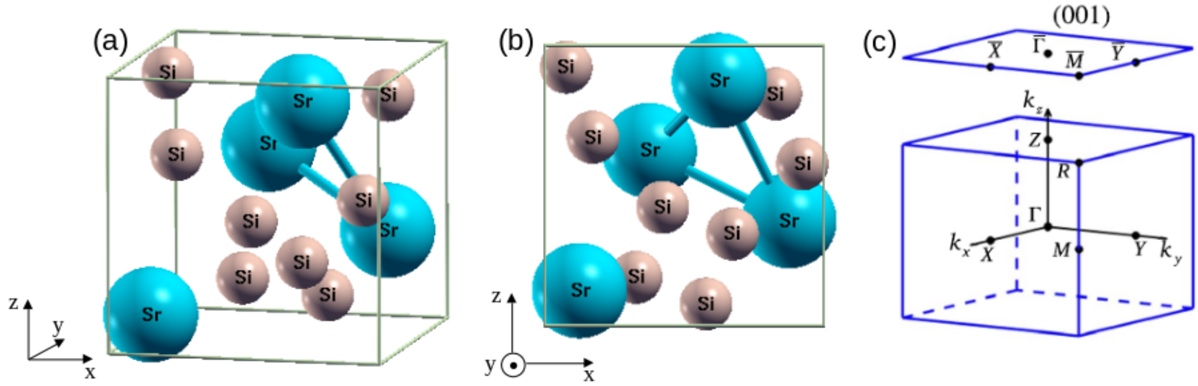

Figure 6.1: Bulk crystal structure of $SrSi_2$. Panel (a) illustration of the bulk crystal structure. Panel (b) visualization of the bulk crystal structure along the $x - z$ plane. Panel (c) depiction of the primitive bulk BZ highlighting four inequivalent high-symmetry k-points, and the projected (001) surface BZ with identified high-symmetry points.

6.1.2. Ground state electronic properties

The analysis of $SrSi_2$'s band structure in Figs. 6.2(a) and 6.2(b) offers insights into its topological properties and the role of SOC. In Fig. 6.2(a), without SOC, the band structure displays semimetallic characteristics with an inverted configuration along the Γ - X direction, where Weyl nodes manifest at points W1 and W2. These nodes, carrying opposite chiral charges, highlight the inherent chirality and potential topological non-triviality of the system. This behavior is indicative of Weyl semimetals, where the linear dispersion of these nodes suggests potential for unusual electronic transport properties. Incorporating SOC, as shown in Fig. 6.2(b), transforms the landscape significantly. The introduction of SOC leads to the hybridization of bands carrying the same rotational eigenvalues, while those with opposing eigenvalues develop robust Weyl nodes (W3 and W4) with enhanced chiral charges of ±2[13, 14, 27], indicative of a double-Weyl semimetal state. This higher order topology results in a quadratic dispersion along two axes and linear along the third, further distinguishing the electronic properties of $SrSi_2$ under external influences. These results are consistent with the previous study[13, 14, 27].

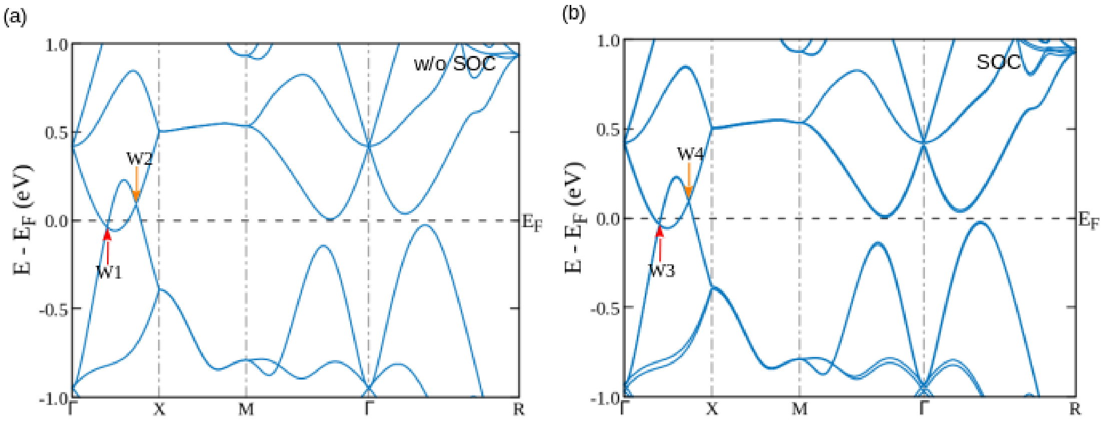

Figure 6.2: Band structure of $SrSi_2$ calculated along high-symmetry lines in the BZ. Panel (a) without the inclusion of SOC, illustrating the electronic states in the absence of relativistic effects. Panel (b) with SOC, showing the splitting of bands due to relativistic interactions. The horizontal dotted line represent the Fermi level.

These observations are critical as they not only reinforce the semimetallic nature of $SrSi_2$ but also emphasize the sensitivity to SOC, which can be exploited to stabilize and manipulate its topological states. This sensitivity is crucial for predicting and controlling emergent quantum phenomena in such non-centrosymmetric systems, potentially paving the way for novel electronic applications based on the unique topological features of $SrSi_2$. The distinct behavior of the band structure under different conditions underscores the importance of external perturbations in tailoring material properties, a key aspect in the design and application of new quantum materials[14].

6.1.3. Effect of applied strain

a) Electronic Properties

Band structure and Fermi surface

Figure 6.3(a) presents the band structure of $SrSi_2$ with no tensile strain. At 0% strain, the bands display a semimetallic character, with notable band crossings between the valence and conduction bands along the Γ - X line. This configuration suggests the presence of Weyl nodes, a hallmark of topological non-triviality in the electronic structure. In Fig. 6.3(b), with an 8% tensile strain, the band structure begins to alter significantly. The strain reduces the separation (Δk) between the Weyl nodes of opposite chiral charge, from 0.168 at 0% strain to 0.092. This compression of the band features indicates a modification in the electronic properties, affecting electron mobility and overall material reactivity. Figure 6.3(c) showcases a more dramatic change at 12% tensile strain. Here, a gap of approximately 0.055 eV opens up in the Γ - X direction, effectively breaking the symmetry that supports the semimetallic state. The disappearance of Δk (0 at this strain level) suggests a complete elimination of Weyl nodes, transitioning the material towards reduced metallic conductivity. This could imply significant changes in the electronic properties and the potential emergence of different quantum phenomena due to reduced electron density at the Fermi level. Turning to the Fermi surface results, Fig. 6.3(d) illustrates the Fermi surface topology at 0% strain. It is complex, with multiple pockets indicating a high degree of electron mobility and potential areas for high conductance. At 8% tensile strain (Fig. 6.3(e)), the Fermi surfaces begin to deform, reflecting the band structure alterations observed. The surfaces show increased localization of electron density, which may indicate shifts in electron delocalization phenomena, possibly enhancing material anisotropy in electronic conduction. Figure 6.3(f) at 12% strain depicts a further evolved Fermi surface, with more isolated and distinct pockets. This transformation correlates with the observed gap opening in the band structure, signifying reduced electronic states available at the Fermi level. Such changes could affect the material's conductivity and electro-mechanical properties, opening up new applications based on strain-induced property tuning.

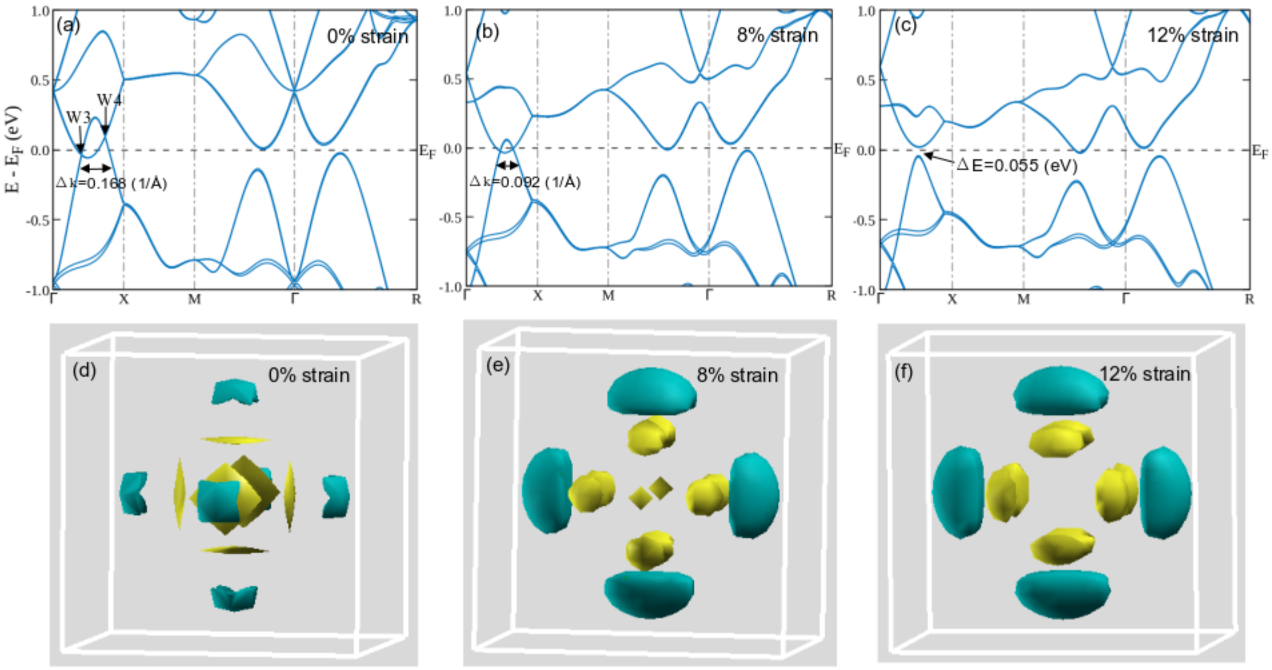

Figure 6.3: Band structure and Fermi surface of $SrSi_2$ under varying applied strains. Panels (a) and (d) with no applied strain, serving as the baseline electronic configuration. Panels (b) and (e) under 8% tensile strain, illustrating the modifications in electronic states and Fermi surface topology due to moderate strain. Panels (c) and (f) under 12% tensile strain, highlighting the further changes in electronic structure and Fermi surface with increased strain.

In Fig. 6.3(a-c), the separation between the W3 and W4 Weyl nodes along the X - Γ line decreases notably with tensile strain, from $\Delta k = 0.168$ Å^{-1} at zero strain to $\Delta k = 0.092$ Å^{-1} at 8% strain, yielding an anisotropic ratio $\mathcal{R} = \frac{\Delta k(8\%)}{\Delta k(0\%)} \approx 0.55$. By 12% strain the nodes no longer display a well-defined momentum separation but instead exhibit an energy splitting $\Delta E = 0.055$ eV. This sharp reduction in Δk under strain highlights the strong directional sensitivity of the Fermi-surface topology in $\mathrm{SrSi_2}$ and matches first-principles predictions of strain-driven topological transitions in this materials class[13, 30]. The modification observed suggest a shift from semimetallic to insulating state, highlighting the potential for using tensile strain to explore and induce novel quantum phenomena in this material. These findings underscore the utility of tensile strain as a potent tool for customizing electronic properties in $\mathrm{SrSi_2}$, with significant implications for developing new electronic devices[252, 253].

Charge density

Figure 6.4(a) depicts the charge density distribution in $\mathrm{SrSi_2}$ under no tensile strain. The plot reveals a relatively uniform distribution with subtle variations around the Sr and Si atomic sites. The presence of magenta color around the atomic sites indicates regions of high electron concentration, reflecting the intrinsic semimetallic nature of $\mathrm{SrSi_2}$. The homogeneous color gradient across the material suggests minimal localization of charge, characteristic of an unstrained lattice where electron mobility is high and evenly distributed. With the introduction of 8% tensile strain, as shown in Fig. 6.4(b), there is a noticeable shift in the charge density. The color intensities around the Sr atoms become more pronounced, indicating an increased localization of charge. This strain-induced redistribution of electrons results from the energy levels around the Fermi surface being altered, pushing electrons to lower energy states that are more localized. The increased electron density near the Sr atoms suggests that tensile strain may enhance the material's electronic interactions at these sites, impacting its electronic properties and usefulness in applications like semiconductors. At 12% strain, depicted in Fig. 6.4(c), the charge density further evolves, demonstrating even more significant localization. The deeper color saturation suggests that the gap opening at the Fermi level has considerably reduced the electron density at higher energy states, confining the available electrons to more localized regions. This alteration not only confirms the insulating behavior induced by the high tensile strain but also highlights specific sites where electronic properties might be significantly changed, affecting the material's reactivity and conductivity.

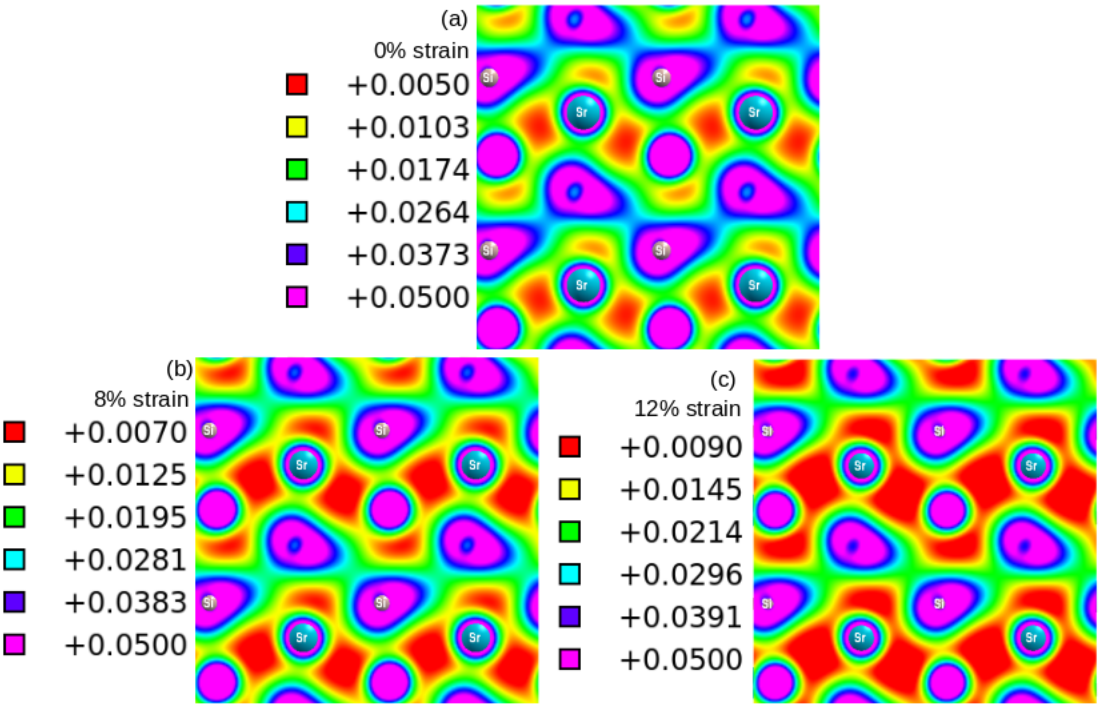

Figure 6.4: Charge density distribution of $SrSi_2$ under varying applied strains. Panel (a) with no applied strain, showing the baseline electronic configuration. Panel (b) under 8% tensile strain, illustrating the modifications in electronic density due to moderate deformation. Panel (c) under 12% tensile strain, highlighting the further changes in electronic density with increased deformation.

The evolution in charge density from Figs. 6.4(a) - (c) correlates closely with the modifications observed in the band structures previously discussed. As tensile strain increases, the electron redistribution and the increasing localization of charge density reflect the changes in the electronic structure, where band gap openings and modifications at the Fermi level decrease the density of states at these energy levels. This complex interplay between the band structure and charge density under external strain underscores the sensitive nature of $SrSi_2$'s electronic properties to mechanical deformations, offering valuable insights for tailoring material properties through strain engineering[253].

b) Topological properties

Berry curvature and surface state

In Fig. 6.5(a), the Berry curvature for $SrSi_2$ under no tensile strain is illustrated. The diagram shows a pronounced localization of the Berry curvature around the monopole and anti-monopole points, indicative of the Weyl points in the material. This distribution is symmetrical, reflecting the inherent symmetry properties of the crystalline structure without strain. The significant peaks in curvature at these points underscore the topological nature of the material, suggesting robust topological characteristics under normal conditions. As shown in Fig. 6.5(b), with an 8% tensile strain applied, there is a noticeable shift and reduction in the symmetry of the Berry curvature distribution. The curvature still peaks near the original Weyl points but becomes less pronounced and more spread out in momentum space. This spreading indicates a perturbation in the topological invariants due to strain, affecting the localization and possibly altering the overall topological charge distribution. Such changes can influence the electron transport properties and the topological protection mechanisms within the material. At 12% tensile strain, depicted in Fig. 6.5(c), further changes are observed. The Berry curvature becomes more dispersed, and the regions of high curvature are less defined, suggesting a substantial alteration or even a possible reversal in the topological features of the material. This dispersion can lead to a significant modification in the electronic response and potentially new electronic phases, driven by the breakdown of symmetry and the alteration of topological protections. Fig. 6.5(d) highlights the surface states of $SrSi_2$ at no strain. The dispersion relations show clear, well-defined surface states connecting the bulk bands, indicative of a strong topological character. The energy gap where these surface states exist is well maintained, suggesting stable topological surface states under no strain conditions. In Fig. 6.5(e), with an 8% strain, the surface states begin to show variations. The dispersion curves shift, and the energy regions where these states exist expand slightly, indicating changes in the energy landscape of the material due to the strain. This change can affect the connectivity between surface and bulk states, altering the material's surface conductivity and its reaction to external stimuli. Finally, at 12% strain, shown in Fig. 6.5(f), The surface states have almost disappeared. The vanishing of surface states indicates a removal of Weyl nodes, pushing the material toward a state with reduced metallic conductivity. These changes suggest a strain-induced transition that could modify the material's electronic properties, particularly at surfaces, which are critical for applications involving surface interactions.

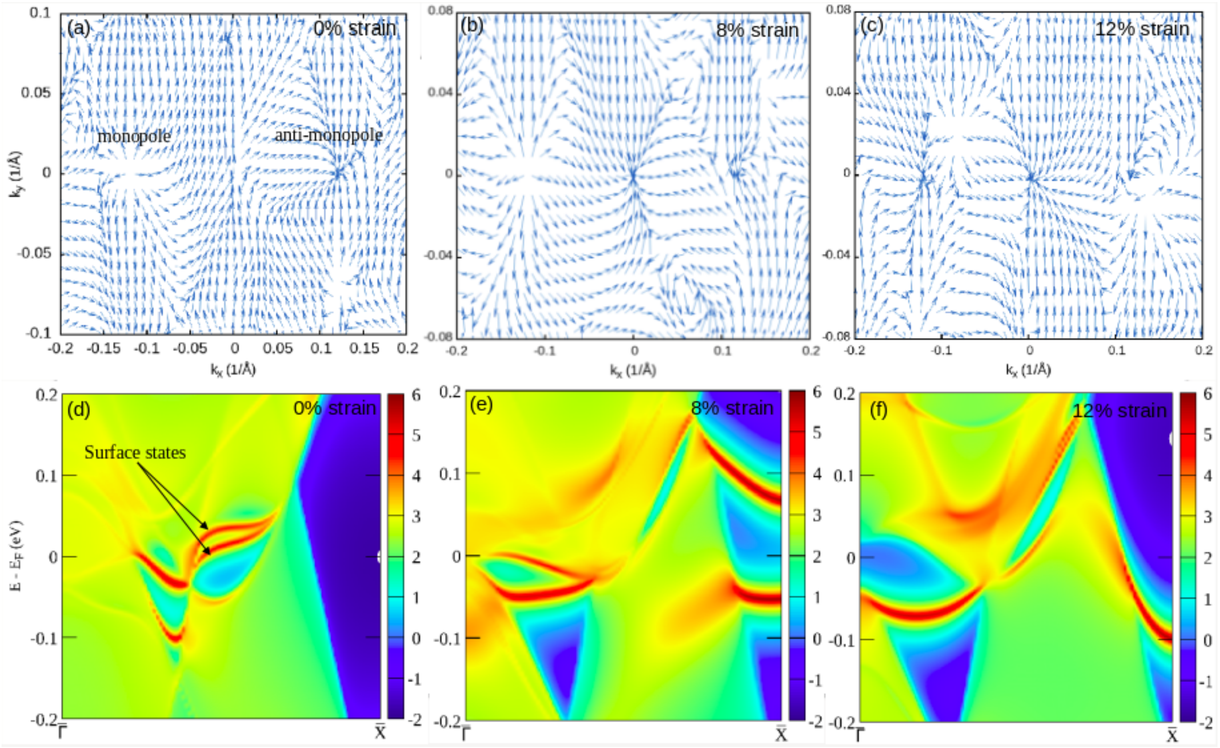

Figure 6.5: Berry curvature and (001) surface state characteristics of $SrSi_2$ under varying applied strains. Panels (a) and (d) with no applied strain, serving as the reference configuration. The Chern number $C \neq 0$. Panels (b) and (e) under 8% tensile strain, illustrating the strain-induced changes in topological properties. The Chern number $C \neq 0$. Panels (c) and (f) under 12% tensile strain, highlighting the further evolution of these properties with increased strain. The Chern number $C = 0$.

The examination of Berry curvature and surface states for $SrSi_2$ under varying tensile strain reveals how mechanical strain can be strategically utilized to manipulate the electronic and topological properties of this material. The changes induced by strain demonstrate the potential for precisely controlling these properties, thereby enabling the design of materials with tailored electronic behaviors[254].

Fermi arc

Figure 6.6(a) displays the Fermi arcs in $SrSi_2$ with no applied strain. The arcs are distinct and form closed loops around the Γ point, characteristic of a topologically non-trivial structure. These loops suggest robust Fermi arcs that are well-defined and extend significantly across the momentum space, connecting Weyl points with opposite chiralities. The clarity and completeness of these arcs indicate strong topological stability under unstrained conditions, essential for maintaining specific electronic properties such as high surface conductivity and unique quantum behaviors. With an 8% tensile strain, as shown in Fig. 6.6(b), the Fermi arcs undergo noticeable transformations. The arcs appear to elongate and become less distinct, with increased spread in momentum space. This deformation suggests a disruption in the topological order and a potential reorientation of the Weyl points. The change in shape and extent of the Fermi arcs signify a shift in the electronic structure, affecting the stability of surface states and the overall electronic transport properties of the material. At 12% strain, illustrated in Fig. 6.6(c), the Fermi arcs demonstrate further evolution, showing a return towards more defined loops but with altered configurations compared to the unstrained state. The arcs reconnect around the Γ point, which lies in a region with very low electron mobility, indicating a significant restructuring of the surface state connectivity. This behavior reflect a topological transition induced by strain leading to a state with reduced metallic conductivity.

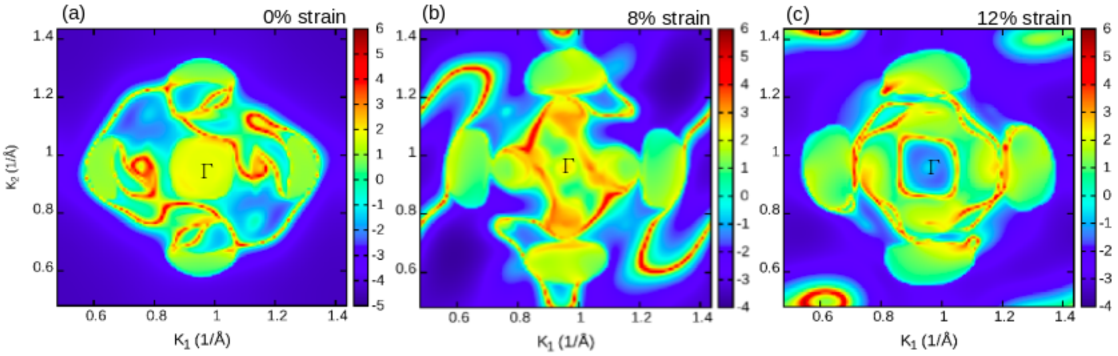

Figure 6.6: Visualization of the Fermi arcs in $SrSi_2$ under varying applied strains. Panel (a) with no applied strain, showing the baseline topological state. Panel (b) under 8% tensile strain, illustrating the changes in the Fermi arc structure due to moderate strain. Panel (c) under 12% tensile strain, highlighting the further evolution and deformation of the Fermi arcs with increased strain.

The observed changes in the Fermi arcs from Figs. 6.6(a) - (c) reflect a dynamic response of $SrSi_2$'s surface states to mechanical strain. The evolution of these arcs under increasing strain levels highlights the sensitivity of topological features to external perturbations, crucial for applications where control over material properties via strain is desired. Notably, the alterations in the Fermi arcs' shape and robustness under strain correlate with the previously discussed changes in band structure and Berry curvature, illustrating a comprehensive picture of how tensile strain impacts the electronic properties of $SrSi_2$. These findings are integral to understanding and leveraging the interplay between mechanical and electronic properties in topological materials, providing a foundation for designing devices that exploit these unique characteristics[255]. For example, broadband infrared photodetectors based on nanostructured Weyl semimetals exploit their linear dispersion for high sensitivity and fast response[256, 257]. Spin-field-effect transistors using spin-momentum locking in topological insulator surface states enable dissipationless spin currents for low-power spintronic memory and logic devices[258, 259]. Thermoelectric generators built from Bi_2Te_3 alloys leverage topological band inversion to enhance the Seebeck coefficient while suppressing thermal conductivity[260, 261]. Topological photonic crystals with mechanically tunable interfaces offer robust light guiding immune to defects, suited for optical communication and on-chip sensing applications[257, 262]. Piezoelectric energy harvesters integrating topological phononic crystals convert ambient vibrations into electrical power with enhanced efficiency and broadband response[263, 264].

6.1.4. With an external electric field applied

a) Electronic Properties

Band structure and Fermi surface

Figure 6.7(a) illustrates the band structure of $SrSi_2$ without an applied electric field. The structure exhibits typical Weyl semimetal characteristics with band crossings near the Fermi level, specifically around the Weyl nodes W3 and W4 along the Γ - X direction. The absence of an electric field shows a balanced electronic environment, with no significant band gap at the Fermi level, indicating a robust semimetallic nature conducive to high electron mobility. With an external electric field of $E = 0.51\ V/Å$, the symmetry in the band structure begins to break, notably opening up gaps between the Weyl nodes as depicted in Fig. 6.7(b). This alteration suggests a shift towards an insulating state under moderate electric field strengths. As the field increases to $E = 1.29\ V/Å$, shown in Fig. 6.7(c), a more significant gap of approximately 0.058 eV opens up around the Fermi level. This gap further supports the transition from a conductive state to one with reduced metallic conductivity, highlighting the electric field's effectiveness in tuning the electronic properties of $SrSi_2$. Correspondingly, Fig. 6.7(d) displays the Fermi surface of $SrSi_2$ at zero electric field, characterized by complex and interconnected electron pockets that are indicative of a high degree of electronic delocalization. This complexity supports the semimetallic behavior observed in the band structure. Under an electric field of $E = 0.51\ V/Å$, as seen in Fig. 6.7(e), the Fermi surface undergoes significant modifications. The electron pockets start to shrink and show signs of electron localization, reflecting the initial stages of gap formation observed in the band structure. At a higher field of $E = 1.29\ V/Å$ (Fig. 6.7(f)), the Fermi surface reveals a drastic change, with further reduced and isolated pockets. These changes correlate with the increased gap at the Fermi level, indicating a decrease in the DOS available for conduction and a notable shift in electronic properties.

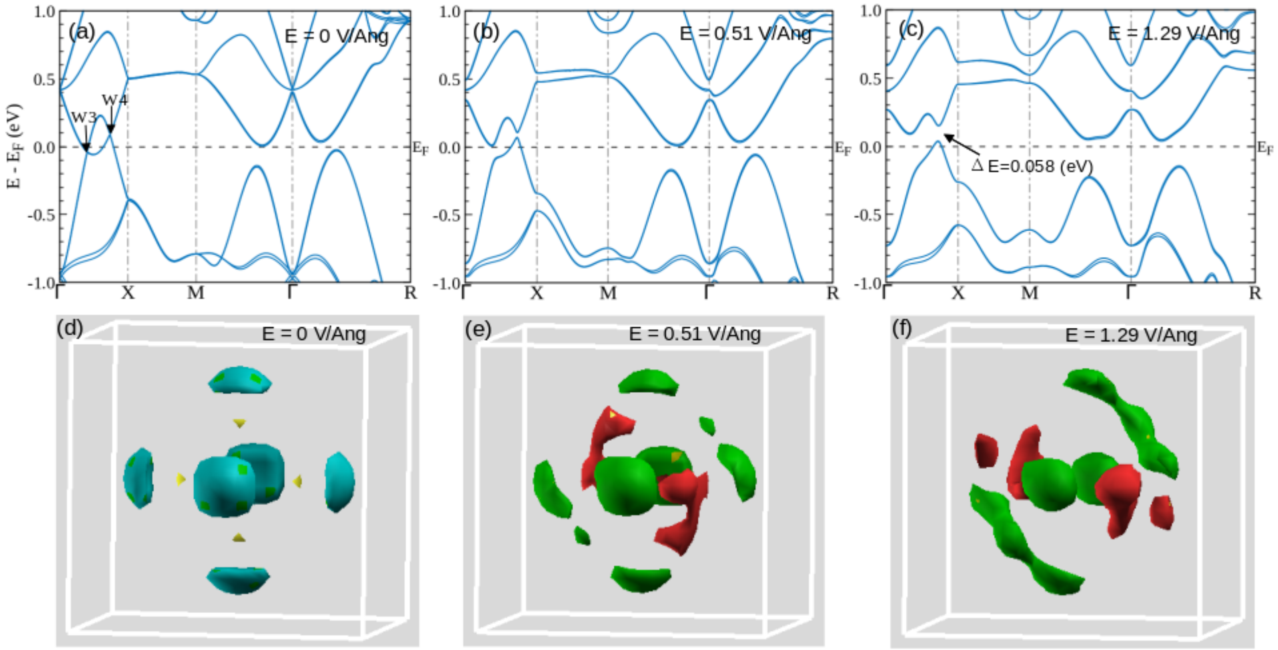

Figure 6.7: Band structure and Fermi surface of $SrSi_2$ under varying external electric fields. Panels (a) and (d) display the band structure and Fermi surface at $E = 0$ V/Å, serving as the baseline state. Panels (b) and (e) demonstrate the band structure and Fermi surface at $E = 0.51$ V/Å, illustrating adjustments in electronic states and alterations in Fermi surface topology induced by the electric field. Panels (c) and (f) reveal the band structure and Fermi surface at $E = 1.29$ V/Å, highlighting the significant modifications in electronic properties due to increased electric field strength.

The evolution of the electronic band structure and Fermi surface of $SrSi_2$ in Fig. 6.7 under external electric fields from 0 $V/$Å to 1.29 $V/$Å demonstrates a clear field-dependent modulation of its electronic properties. The transition from a semimetallic state to one with reduced metallic conductivity under increasing electric field strengths is marked by band gap openings and significant alterations in the Fermi surface topology. These observations not only confirm the sensitivity of $SrSi_2$'s topological and electronic properties to external electric fields but also highlight the potential for utilizing such fields to engineer specific electronic behaviors, crucial for applications in electronic switching and quantum computing technologies[265]. This control mechanism provides a valuable tool for manipulating the quantum phenomena in WSMs, paving the way for advanced material functionalities in technological applications[266].

Charge density

Figure 6.8(a) presents the charge density distribution in $SrSi_2$ without any applied electric field. The visualization shows a uniform and symmetrical distribution of charge around the Sr and Si atomic sites, indicating a balanced electronic environment typical of an unstrained and unbiased state. The colors are evenly distributed, reflecting a stable electronic structure with high electron delocalization across the material. With the application of an external electric field of $E = 0.51\ V/\text{Å}$, as depicted in Fig. 6.8(b), there is a noticeable alteration in the charge density. The colors begin to intensify around specific regions, particularly around the Sr atoms, suggesting an increase in electron localization. This shift signifies a redistribution of electrons, moving from higher to lower energy states as the electric field begins to influence the electronic structure. The emergence of these localized areas indicates changes in the electronic interactions within $SrSi_2$, leading to altered physical properties such as electrical conductivity and reactivity. At a higher electric field of $E = 1.29\ V/\text{Å}$, shown in Fig. 6.8(c), the charge density undergoes further significant changes. The redistribution becomes more pronounced, with stark contrasts in color intensity indicating a substantial localization of charge density. This condition correlates with the opening of a gap around the Fermi level, as evidenced in the band structure analysis. The reduced electron density in regions previously occupied by states at the Fermi level highlights a decrease in the DOS, a factor critical for understanding changes in the material's electronic properties under strong external fields.

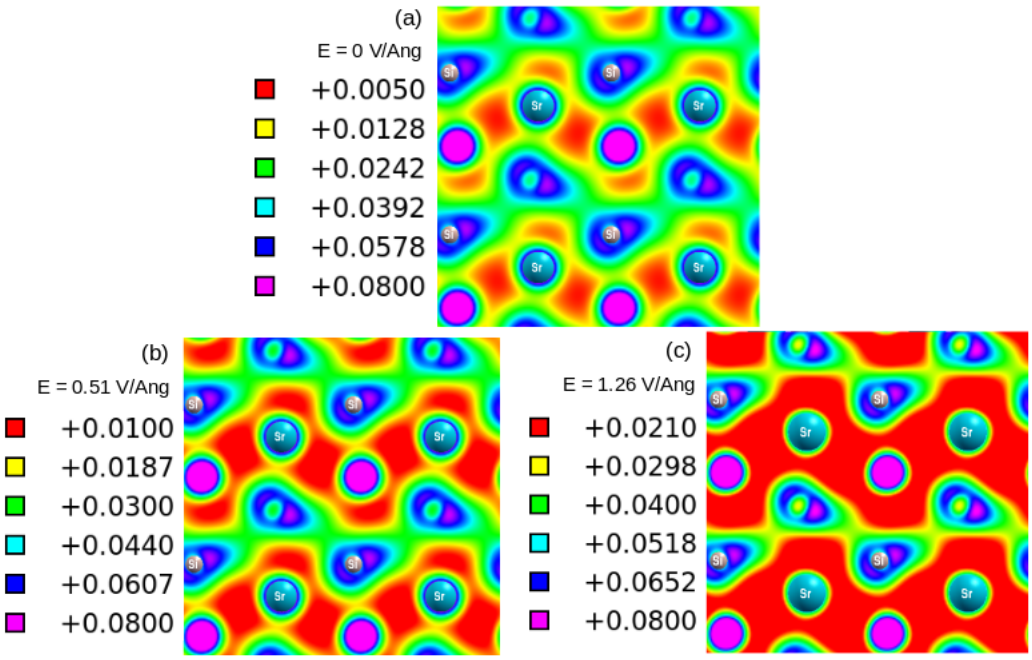

Figure 6.8: Charge density distribution in $SrSi_2$ under varying external electric fields. Panel (a) without any applied electric field, depicting the baseline electronic configuration. Panel (b) under an external electric field of $E = 0.51\ V/Å$, illustrating modifications in electronic density that reflect changes in electronic environment due to the moderate electric field. Panel (c) under an external electric field of $E = 1.29\ V/Å$, highlighting further alterations in electronic density as a response to increased electric field strength.

The evolution of the charge density in $SrSi_2$ in Fig. 6.8 under increasing strengths of external electric fields from 0 $V/Å$ to 1.29 $V/Å$ elucidates significant shifts from a delocalized to a more localized electronic structure. These changes are indicative of the electric field's capacity to manipulate electron distribution within the material, influencing its electronic and chemical properties. Such control is crucial for applications where precise tuning of electronic properties is required, such as in semiconductor devices. Understanding these transformations helps in predicting the behaviour of the material under operation conditions, enhancing the design and development of electronic materials with tailored properties.

b) Topological properties

Berry curvature and surface state

Fig. 6.9(a) shows the Berry curvature for $SrSi_2$ with no external electric field applied. The curvature is symmetrically distributed around the Weyl points, indicating a balanced topological configuration with well-defined chiral properties. The localization at these points suggests robust topological characteristics that support specific electronic properties like high conductivity and unique quantum behaviors under equilibrium conditions. With an electric field of $E = 0.51\ V/Å$, depicted in Fig. 6.9(b), there is a subtle shift in the distribution of the Berry curvature. Although the overall symmetry is preserved, the intensity and spread of the curvature around the Weyl points start to adjust, indicating a response to the external bias. At a higher field of $E = 1.29\ V/Å$ (Fig. 6.9(c)), more pronounced changes are evident with significant alterations in the distribution of the curvature. This indicates disruptions in the topological invariants and suggests a modification of the material's topological phase, leading to new electronic and quantum properties. The surface states for $SrSi_2$ at zero electric field, shown in Fig. 6.9(d), exhibit clear and continuous energy bands connecting the bulk states, a hallmark of strong topological surface states. The absence of external disturbance allows these states to manifest distinctly, reinforcing the material's inherent topological protection and stability. Under an electric field of $E = 0.51\ V/Å$, as shown in Fig. 6.9(e), the surface states begin to show deviations in their dispersion relations. The bands start to shift, indicating an influence of the electric field on the energy landscape. This shift can affect the connectivity and penetration depth of these states into the bulk material. At $E = 1.29\ V/Å$ (Fig. 6.9(f)), these changes are more extensive, with notable disruptions in the band connectivity and the emergence of new features within the energy bands. This evolution suggests a transition of $SrSi_2$ from the topological phase toward a state with reduced metallic conductivity.

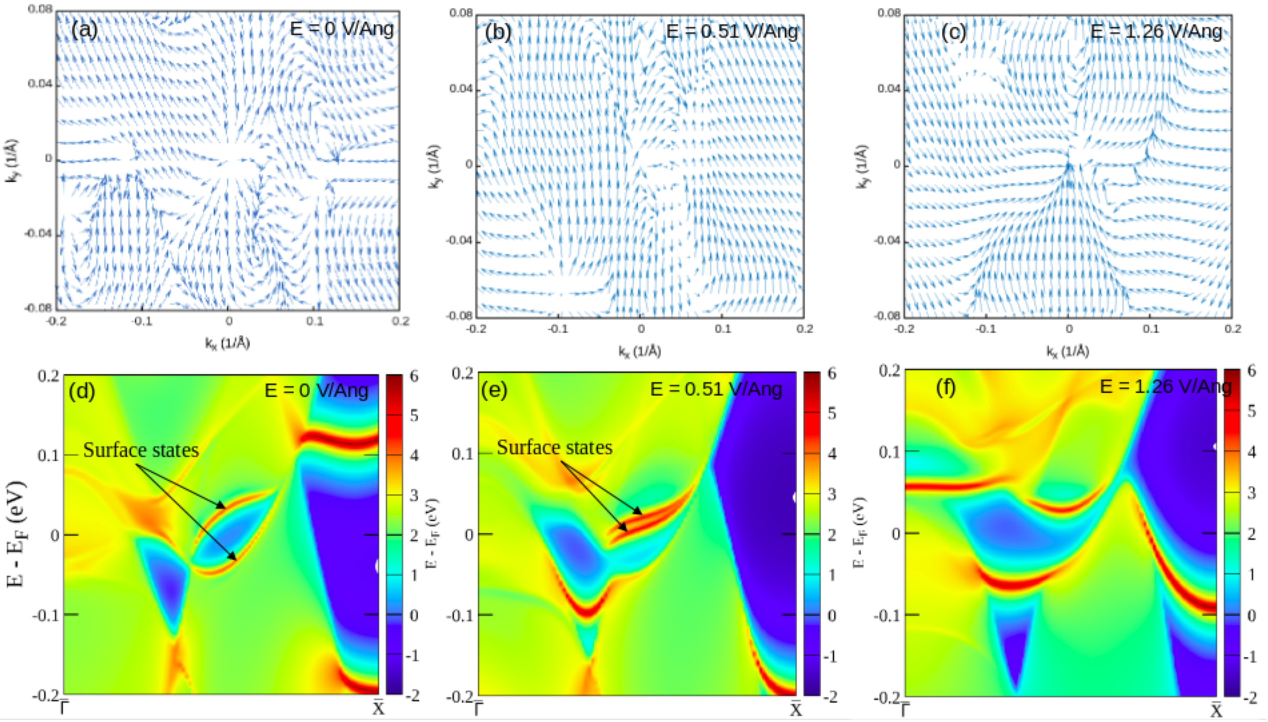

Figure 6.9: Berry curvature and surface state characteristics of SrSi$_2$ under varying external electric fields. Panels (a) and (d) without any applied electric field, establishing the reference configuration. The Chern number $C \neq 0$. Panels (b) and (e) under an electric field of $E = 0.51\ V/\text{Å}$, depicting the modifications in topological properties induced by the electric field. The Chern number $C \neq 0$. Panels (c) and (f) under a higher electric field of $E = 1.29\ V/\text{Å}$, highlighting the progressive evolution of topological features with increasing electric field strength. The Chern number $C = 0$.

The analysis of Berry curvature and surface states in SrSi$_2$ in Fig. 6.9 under varying electric fields reveals a dynamic interplay between the external electric bias and the material's topological and electronic properties. As the electric field strength increases, both the Berry curvature and surface states undergo significant transformations, indicating a shift in the material's electronic structure and topological attributes. These changes highlight the sensitivity of SrSi$_2$ to external perturbations and underscore the potential for controlling its properties through electric field applications[265].

Fermi arc

Figure 6.10(a) showcases the Fermi arcs in SrSi$_2$ with no external electric field applied. The arcs are prominently defined, creating a continuous and coherent path connecting Weyl points around the Γ point. This configuration underscores a stable topological state, with the Fermi arcs acting as a bridge between different topological features within the crystal, indicative of robust and intact topological properties in the absence of external perturbations. With a moderate electric field of

$E = 0.51\ V/\text{Å}$, as depicted in Fig. 6.10(b), there is a visible alteration in the Fermi arcs' shape and connectivity. The arcs begin to distort, showing some degree of elongation and slight disconnection from their original paths. This deformation suggests an initial response to the electric field, affecting the electronic structure and the topological connectivity. The slight disruption indicates a beginning of topological transition, which may alter the material's inherent quantum properties. At a higher electric field of $E = 1.29\ V/\text{Å}$, shown in Fig. 6.10(c), the Fermi arcs undergo significant transformations. The arcs are more fragmented and extensively reoriented, demonstrating a substantial modification from their original state. This extensive reconfiguration implies a robust influence of the electric field, leading to a topological phase transition where the nature and stability of the Fermi arcs are critically altered. Such changes are indicative of a new electronic phase.

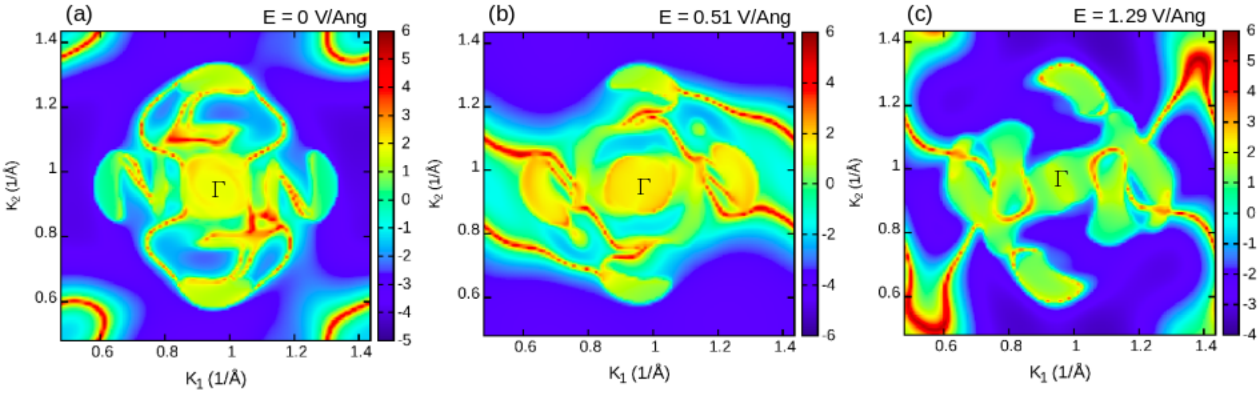

Figure 6.10: Visualization of the Fermi arcs in $SrSi_2$ under varying external electric fields. Panel (a) with no applied electric field, depicting the baseline topological state. Panel (b) under an electric field of $E = 0.51\ V/\text{Å}$, illustrating changes in the Fermi arc structure that suggest modifications in topological characteristics due to the moderate electric field. Panel (c) under an increased electric field of $E = 1.29\ V/\text{Å}$, highlighting the further evolution and deformation of the Fermi arcs under stronger field conditions.

The evolution of the Fermi arcs in $SrSi_2$ in Fig. 6.10 under increasing electric field strengths from $0\ V/\text{Å}$ to $1.29\ V/\text{Å}$ illustrates a profound sensitivity to external electric biases. The observed changes from well-defined connectivity at zero field to significant distortion and reorientation at higher fields highlight the dynamic nature of topological features under external influences. These alterations in the Fermi arcs reflect corresponding changes in the material's band structure and Berry curvature, reinforcing the interconnected nature of these topological properties[255].

6.2. Bulk CoSi structure

6.2.1. Structural properties

CoSi crystallizes in a simple cubic structure with a lattice constant of 4.45 Å. It is characterized by the non-symmorphic space group $P2_13$ (No. 198), which lacks I symmetry.[31, 34, 44]. As depicted in Fig. 6.11(a), each unit cell consists of four cobalt (Co) and four silicon (Si) atoms, with each Co atom forming covalent bonds with six neighboring Si atoms, and vice versa. The absence of I symmetry in $SrSi_2$ plays a pivotal role for the possible emergence of a Weyl semimetal phase, provided that T symmetry remains intact. The bulk BZ of CoSi displaed in Fig. 6.11(c), essential for understanding its electronic structure, is simple cubic with high-symmetry points designated as Γ (at the center), R (at the vertices), X (at the face centers), and M (at the edge centers). The 001 surface projection, depicted on top of the BZ, intersects with critical high-symmetry lines, making it an essential aspect in the investigation of surface states inherent to topological phases of matter.

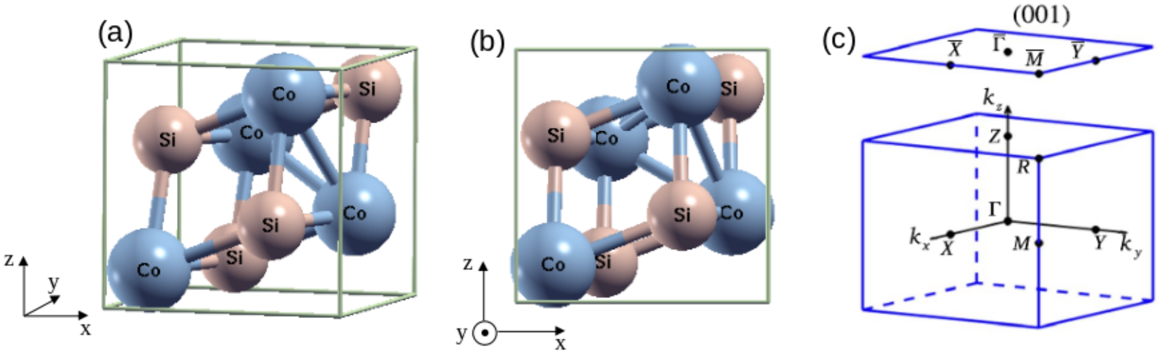

Figure 6.11: Bulk crystal structure of CoSi. Panel (a) 3D representation of the bulk crystal lattice. Panel (b) cross-sectional view along the $x - z$ plane. Panel (c) detailed mapping of the primitive bulk BZ with four inequivalent high-symmetry k-points and projection of the (001) surface BZ showcasing key high-symmetry locations.

6.2.2. Ground state electronic properties

Exploring the band structure of CoSi in Fig. 6.12(a) and Fig. 6.12(b) reveals key details about its topological characteristics and the impact of SOC. In the absence of SOC, as depicted in Fig. 6.12(a), the electronic structure of CoSi is characterized by notable features at critical points in the BZ. Notably, at the Γ point, there is a threefold degenerate point that corresponds to spin-1 excitations, manifesting a crossing point with a topological charge of ±2[33, 267, 268]. This observation aligns with the predictions of unconventional crossings in chiral crystal structures and the presence of symmetry-protected fermionic states, which contribute significantly to the topological landscape of CoSi . Alongside, the R point hosts a double Weyl fermion with a fourfold degeneracy and a Chern number of ±2[269–271], a configuration that respects the 'no-go theorem'[272] by balancing the total Chern number across the Fermi surface to zero. With the introduction of SOC in Fig. 6.12(b), the electronic topology undergoes a transformative shift. The SOC's influence is noticeably pronounced at non-time-reversal invariant points within the BZ, lifting degeneracies and reshaping the band crossings. At the BZ center, the previously sixfold degenerate point splits into two distinct crossings: a twofold and a fourfold degenerate point, attributed to a Weyl fermion and a spin-$3/2$ RSW fermion, respectively, with the latter carrying a substantial topological charge of ±4[33, 267, 268].These results are in good agreement with previous works[31, 33, 35]. The presence of these higher-charge fermions underlines the critical impact of SOC on CoSi's electronic structure, highlighting a unique topology that deviates significantly from more commonly studied Weyl and Dirac fermions, which generally exhibit topological charges of ±1 or zero .

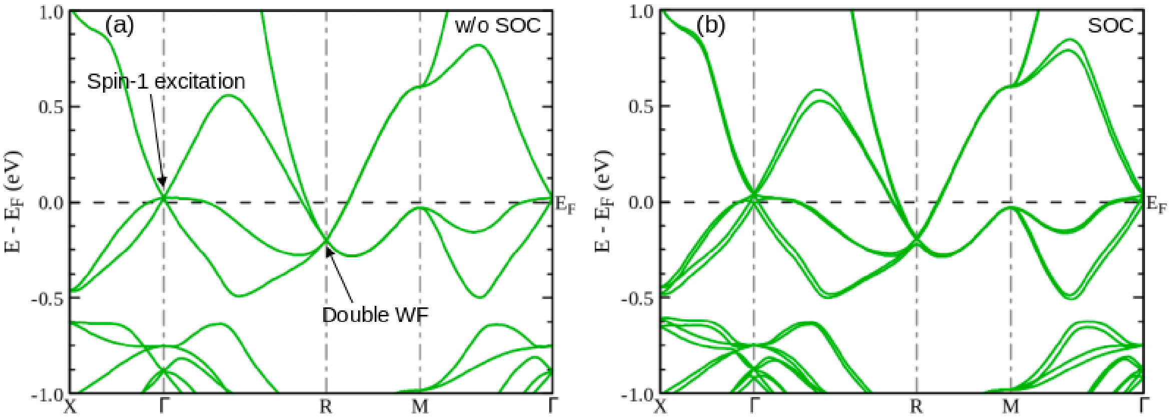

Figure 6.12: Band structure of CoSi calculated along high-symmetry lines in the BZ. Panel (a) without the inclusion of SOC, illustrating the electronic states in their baseline configuration, devoid of relativistic effects. Panel (b) with SOC implemented, showing the splitting of bands as a direct consequence of relativistic interactions. The horizontal dotted lines mark the Fermi level.

This intricate interplay between SOC and the crystal symmetries of CoSi not only alters the fundamental electronic properties but also introduces complex topological nuances that could potentially influence emergent quantum phenomena in this systems. Such detailed understanding is pivotal in harnessing the material's properties for technological applications, particularly in devices exploiting topological characteristics at the quantum scale[273].

6.2.3. Effect of applied strain

a) Electronic Properties

Band structure and Fermi surface

In Fig. 6.13(a), we observe the band structure of CoSi under no tensile strain. This initial configuration serves as a baseline for understanding the intrinsic electronic properties of the material. The bands near the Fermi level are closely packed, suggesting a rich electronic structure conducive to various quantum phenomena. Moving to Fig. 6.13(b), the application of a 10% tensile strain introduces notable changes in the band structure, particularly around the Γ point where a gap of approximately 0.035 eV emerges. This opening signifies a shift in the electronic states, altering the electronic properties of the material. The absence of a gap at the R point indicates localized strain effects, highlighting the anisotropic response of the electronic structure to external deformation at that point. Further strain intensification to 15%, as shown in Fig. 6.13(a), widens the gap at the Γ point to 0.11 eV. This alteration suggests a strengthening of the band splitting induced by the strain, which could lead to changes in the electronic transport properties of the material. The continued absence of a gap at the R point underscores the robustness of certain band features against strain, possibly linked to symmetry or local electronic structure characteristics. Corresponding to these band structure modifications, the Fermi surfaces in Figs. 6.13(d), (e), and (f) undergo significant transformations. Figure 6.13(d) displays a complex Fermi surface at zero strain, characterized by interconnected electron pockets that facilitate high electron mobility. With the application of 10% strain in Fig. 6.13(e), the Fermi surface fragments, indicating a localization of electron states. This fragmentation correlates with the reduced electronic conductivity, as fewer states are available at the Fermi level. At 15% strain, shown in Fig. 6.13(f), the Fermi surface further evolves, exhibiting increased localization and reduction of electron pockets. This evolution is indicative of a more pronounced electronic insulation state, supported by the increased band gap observed in the band structure analysis. The alterations in the Fermi surface are crucial for understanding the material's electronic response under extreme conditions and could have implications for its use in strain-engineered electronic devices.

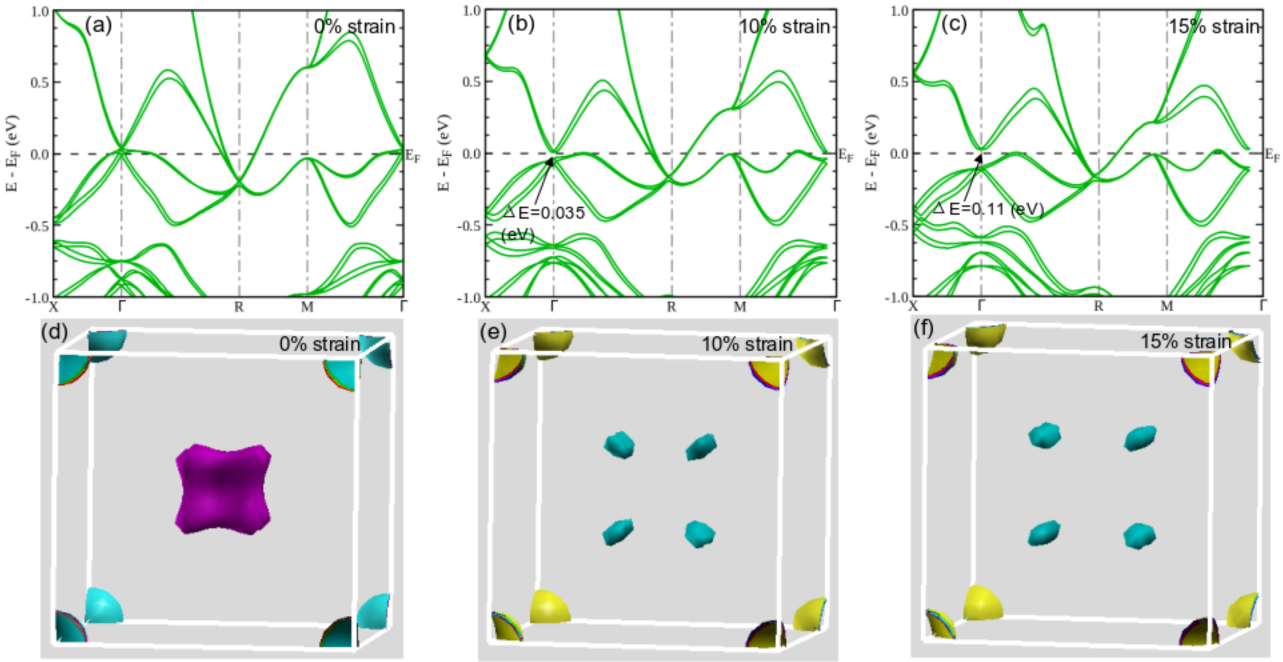

Figure 6.13: Band structure and Fermi surface of CoSi under varying tensile strains. Panels (a) and (d) without strain. Panels (b) and (e) depict changes under 10% tensile strain, illustrating adjustments in electronic states and Fermi surface topology. Panels (c) and (f) demonstrate further modifications under 15% tensile strain.

These observations collectively highlight the sensitivity of CoSi's electronic properties to mechanical strain, suggesting avenues for tailoring material properties through controlled strain applications. The evolution of the band structure and Fermi surface with increasing tensile strain underscores the potential for discovering novel quantum phenomena in this material system[274].

Charge density

In Fig. 6.14(a), the charge density distribution of CoSi under no tensile strain shows a relatively uniform electron distribution around both Co and Si atoms. The color scale indicates regions of higher electron density in pink and lower density in blue, suggesting a balanced electron environment conducive to the material's intrinsic properties. This baseline state provides a critical reference for understanding changes under subsequent strain conditions. Moving to Fig. 6.14(b), which depicts the charge density at 10% tensile strain, there is a noticeable shift towards higher electron localization around the Co atoms. This redistribution suggests that electrons are moving away from higher energy states around the Fermi level, where a gap has opened, to more stable lower energy states. This change is particularly significant as it not only affects the local electronic interactions but also alters the overall electronic structure, impacting the material's conductivity and reactivity. In Fig. 6.14(c), at 15% strain, the localization becomes even more pronounced. The regions of high electron density are more sharply defined, particularly around the Co atoms, while the Si atoms show a relative decrease in surrounding electron density. This trend points to a significant alteration in electronic behavior, where the strain induces a more distinct separation of charge densities, thereby enhancing the material's potential for varied electronic applications. The increased electron localization could lead to modified electronic properties such as reduced conductivity or altered magnetic properties, depending on the nature of the localized states.

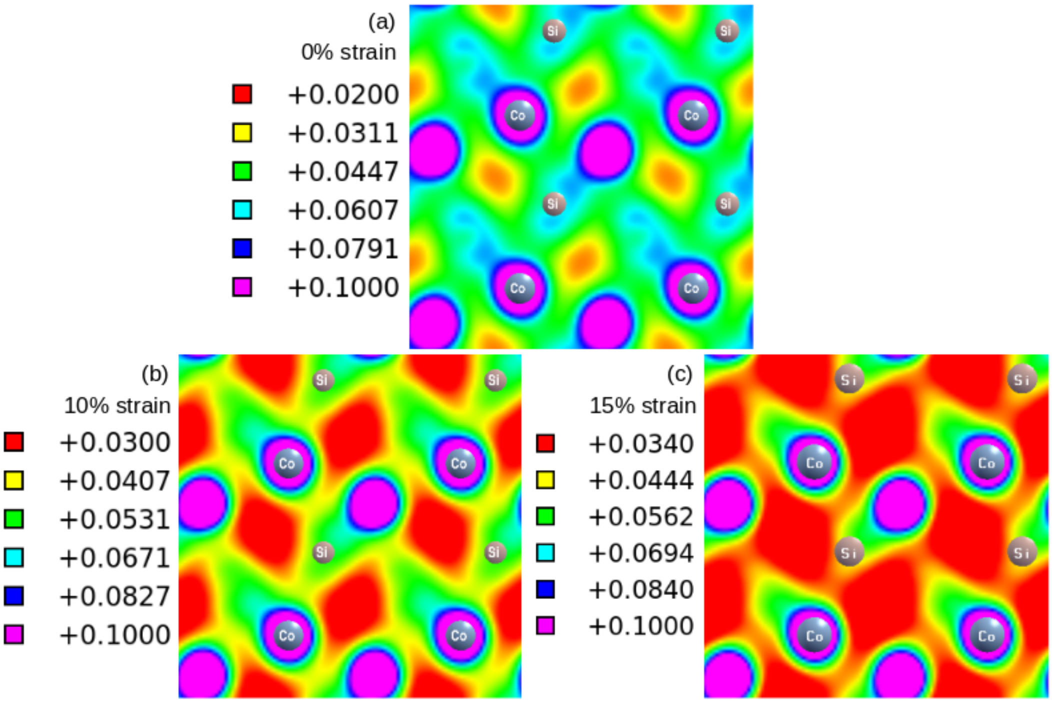

Figure 6.14: Charge density distribution of CoSi under different tensile strains. Panel (a) presents the baseline electronic configuration without strain. Panel (b) shows changes in electronic density at 10% tensile strain, illustrating moderate deformation effects. Panel (c) further highlights alterations in electronic density at 15% tensile strain.

These insights from the charge density plots correlate closely with the changes observed in the band structures discussed earlier. The gap openings around the Fermi level reduce the charge density at these energy levels, as reflected in the altered charge density landscapes. This comprehensive analysis links the mechanical strain to electronic structural changes, offering insights into how CoSi might be engineered through strain for specific electronic applications. The detailed understanding of charge redistribution and localization under varying strain conditions is essential for designing materials with tailored electronic properties, suitable for applications in semiconductors or advanced electronic devices.

b) Topological properties

Berry curvature and surface state

In Fig. 6.15(a), depicting the Berry curvature of CoSi without any applied strain, we observe a relatively uniform distribution across the momentum space. This indicates a balanced electronic structure under no external influence, with Weyl points subtly manifesting within the distribution. The absence of pronounced peaks suggests that the intrinsic topological features of CoSi are stable and less affected by external perturbations. With the introduction of a 10% tensile strain in Fig. 6.15(b), significant modifications become apparent in the Berry curvature distribution. The curvature is now more concentrated around specific regions near the Weyl points, indicating a shift towards higher topological activity due to strain-induced modifications in the electronic structure. This strain level also impacts the symmetry properties of the Berry curvature, as evident from the changes in localization and magnitude, which suggests an alteration in the topological characteristics of the material. At a higher tensile strain of 15%, shown in Fig. 6.15(c), the Berry curvature exhibits further intensification in localization and changes around the Weyl points. These changes are indicative of a robust manipulation of the material's topological properties through strain, leading to new electronic behaviors and novel quantum phenomena. Regarding the surface states, in Fig. 6.15(d) at 0% strain, CoSi shows well-defined surface states with clear dispersion relations. These states are robust and smoothly connected to the bulk states, which is characteristic of topologically protected surface states. Upon increasing the strain to 10% in Fig. 6.15(e), the surface states undergo noticeable transformations. The dispersion curves shift, indicating a modification in the energy bands due to strain. This alteration affects the connectivity between the surface and bulk states, with implications for the surface electronic properties, such as altered surface conductivity or chemical reactivity. At 15% strain, shown in Fig. 6.15(f), the changes in surface states become even more pronounced. The dispersion relations show significant warping, and the gaps between surface and bulk states widen, suggesting a deep modification of the surface electronic structure. This strain level markedly influences the penetration depth and nature of the surface states, leading to distinct changes in surface-related phenomena.

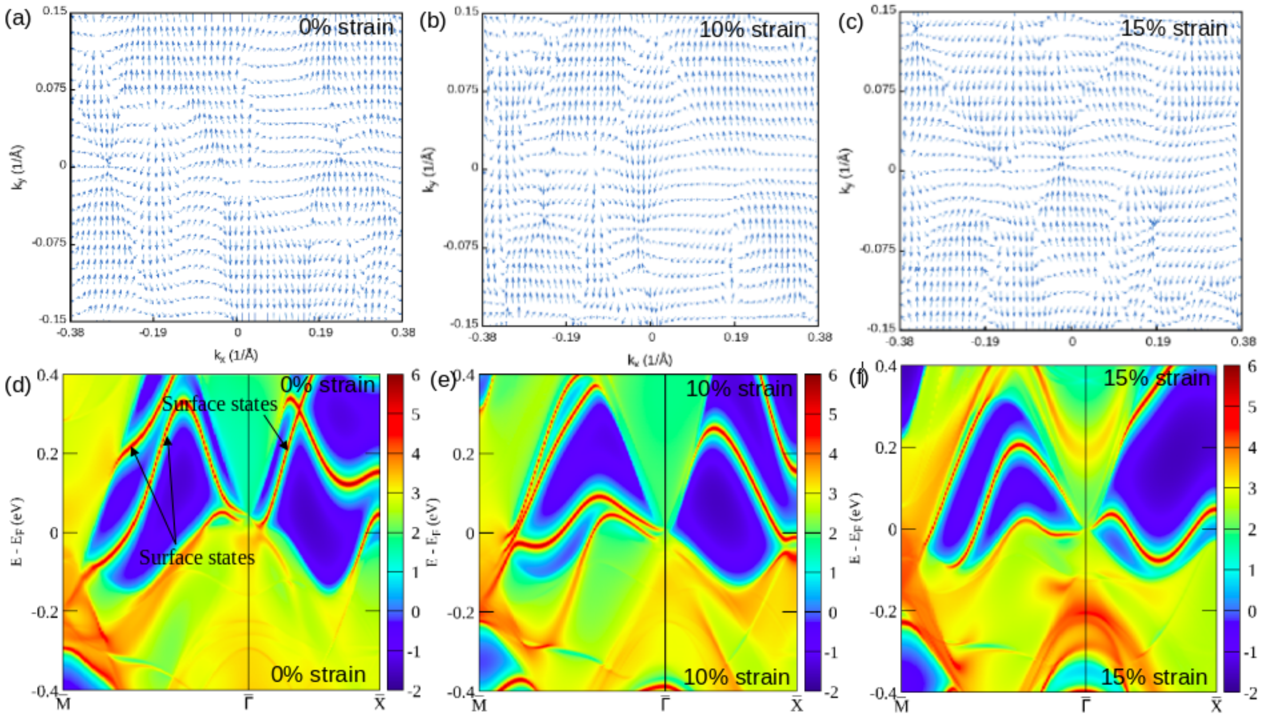

Figure 6.15: Berry curvature and surface state characteristics of CoSi under increasing tensile strains. Panels (a) and (d) depict the reference state without strain. The Chern number $C \neq 0$. Panels (b) and (e) show the effects of 10% tensile strain on topological properties. The Chern number $C = 0$. Panels (c) and (f) demonstrate further topological changes at 15% strain. The Chern number $C = 0$.

These results underline the sensitive interplay between tensile strain and the topological and surface electronic properties of CoSi. The Berry curvature and surface states' under strain provide critical insights into how mechanical deformations can be employed to tailor material properties for specific electronic and quantum applications[274].

Fermi arc

In Fig. 6.16(a), depicting the Fermi arc of CoSi at 0% strain, the arcs are distinctly visible, smoothly connecting the Weyl points. The arcs exhibit a broad, continuous curve, illustrating a robust topological structure under unstrained conditions. This configuration provides a stable electronic environment conducive to maintaining CoSi's intrinsic topological characteristics. As shown in Fig. 6.16(b), where a 10% tensile strain is applied, the Fermi arcs start to show notable alterations in their shape and extent. The arcs become elongated and slightly reoriented, indicating a strain-induced modification in the electronic structure near the Weyl points. These changes suggest a dynamic response of the Fermi arcs to external mechanical deformations, affecting their topological connectivity and stability. At 15% strain, shown in Fig. 6.16(c), the Fermi arcs undergo further transformations. The arcs are not only elongated but also appear to be more fragmented, indicating a significant alteration in their connectivity between Weyl points. This fragmentation may signal topological transitions or modifications in the stability of the Fermi arcs, which could influence the overall robustness of the topological features in CoSi.

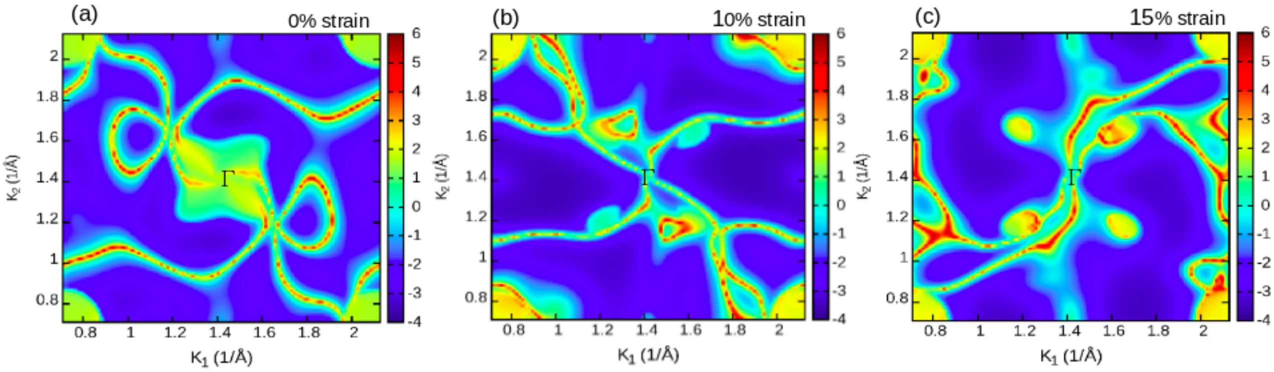

Figure 6.16: Visualization of Fermi arcs in CoSi under different tensile strains. Panel (a) shows the baseline state without strain. Panel (b) illustrates the Fermi arc structure under 10% strain, showing moderate changes. Panel (c) displays further evolution and deformation of Fermi arcs under 15% strain. These images demonstrate how tensile strain impacts the topological surface states of CoSi.

These observations from the analysis of the Fermi arcs under varying levels of tensile strain illustrate how mechanical deformations can critically influence the topological landscape of materials like CoSi. The changes in the shape, extent, and connectivity of the Fermi arcs are indicative of how external strains could be utilized to tailor material properties for specific applications in electronics and quantum technology. The correlation with band structure changes further highlights the intricate relationship between strain, electronic structure, and topological properties, providing a comprehensive understanding of the material's behavior under strain[274].

The comparison of Fermi arcs for $SrSi_2$ (see Fig. 6.6) and CoSi (see Fig. 6.16) under different tensile strains reveals distinct responses in the electronic structure of these materials. In $SrSi_2$, the application of strain appears to induce elongated features in the Fermi surface without forming continuous lines across momentum space, suggesting an absence of nodal-line formation. Conversely, in CoSi, the strained Fermi arcs exhibit a noticeable evolution towards continuous, extended features, which resemble nodal lines where conduction and valence bands approach each other closely. This phenomenon, indicative of nodal-line behavior, signifies regions in momentum space with persistent degeneracy, characteristic of topologically protected nodal-line semimetals. The difference in response to strain between $SrSi_2$ and CoSi suggests that the nodal-line conducting states are unique to CoSi under strain, highlighting its potential as a topological material with implications for advanced technological applications. This insight underscores the distinctive electronic properties that strain can unlock in CoSi, as opposed to $SrSi_2$, marking a significant contribution to understanding strain-induced topological phenomena in materials.

6.2.4. With an external electric field applied

a) Electronic Properties

Band structure and Fermi surface

In Fig. 6.17(a), CoSi exhibits its electronic band structure under no external electric field ($E = 0\ V/\text{Å}$), serving as the baseline for observing how electric fields influence the material's electronic properties. The band structure shows multiple crossings at the Fermi level, particularly around the M and R points, indicating a rich and complex electronic environment conducive to various electronic and quantum phenomena. Upon the application of a moderate electric field of $E = 0.51\ V/\text{Å}$ in Fig. 6.17(b), notable changes occur in the band structure. A gap of approximately 0.02 eV opens up at the R point, illustrating the field's effectiveness in breaking symmetry and influencing electronic properties. However, the Γ point remains gapless, indicating selective sensitivity of band structure regions to external electric fields. This partial gap opening suggests modifications in the electronic transport and optical properties of CoSi, enabling the material's use in electronic devices where control of electron flow at specific points is required. As the electric field increases to $E = 1.29\ V/\text{Å}$ in Fig. 6.17(c), the gap at the R point further widens to about 0.065 eV. This significant modification under a stronger electric field underscores a substantial alteration in the material's electronic structure, enhancing the material's potential for applications in field-effect devices, sensors, and other technologies requiring controlled electronic responses to high electric fields. Correspondingly, the Fermi surfaces in Figs. 6.17(d), (e), and (f) evolve markedly under these conditions. At $E = 0\ V/\text{Å}$, Fig. 6.17(d) shows a complex Fermi surface with multiple interconnected electron pockets, indicative of high electronic mobility and interactivity. With the application of $E = 0.51\ V/\text{Å}$ in Fig. 6.17(e), these surfaces start to show signs of electron localization, reducing the complexity of connections and slightly shrinking the electron pockets. This transition points to a decrease in electron mobility, corresponding to the opening of electronic gaps observed in the band structure. At $E = 1.29\ V/\text{Å}$, Fig. 6.17(f) further illustrates the impact of the electric field on the Fermi surface, where greater localization and a notable reduction in the size and number of electron pockets are observed. This change reflects the decreased number of electrons at the Fermi level due to the wider gap at the R point, significantly altering the material's electronic transport properties.

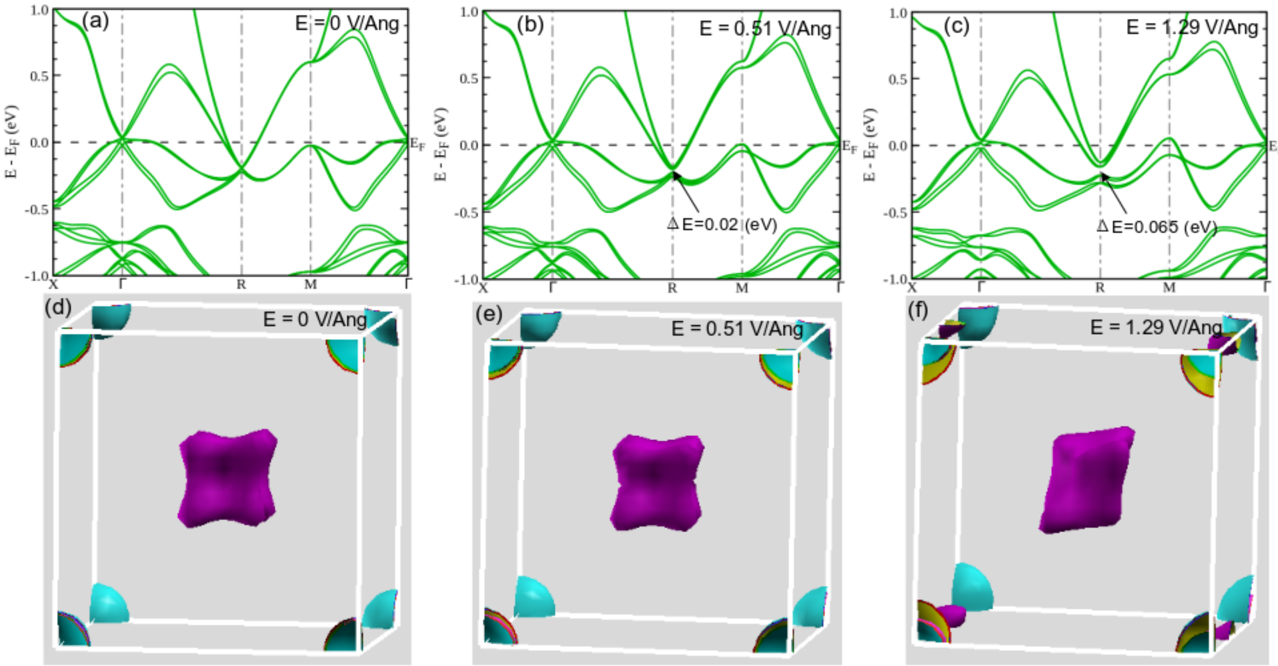

Figure 6.17: Band structure and Fermi surface of CoSi subject to varying external electric fields. Panel (a) and (d) illustrate the baseline band structure and Fermi surface at $E = 0$ V/Å. Panels (b) and (e) display changes in the band structure and modifications of the Fermi surface topology at $E = 0.51$ V/Å, demonstrating the impact of the electric field on electronic states. Panels (c) and (f) detail the substantial alterations in both band structure and Fermi surface at $E = 1.29$ V/Å, emphasizing the pronounced effects of enhanced electric field strength on the electronic properties.

These insights collectively provide a comprehensive view of how external electric fields can be used to tailor the electronic properties of CoSi. By manipulating the electric field strength, one can induce specific changes in the band structure and Fermi surface, paving the way for targeted electronic and quantum applications where control over electronic properties is crucial[266].

Charge density

In Fig. 6.18(a), which shows the charge density distribution of CoSi under no external electric field ($E = 0\ V/\text{Å}$), we observe a uniform distribution with distinct electron densities around the Co and Si atoms. This baseline condition indicates a balanced electronic structure, with electron densities prominently displayed around the atomic sites, conducive to the inherent electronic interactions of CoSi. Moving to Fig. 6.18(a), where an electric field of $E = 0.51\ V/\text{Å}$ is applied, there are noticeable changes in the charge density distribution. The color gradient shifts, indicating a redistribution of electrons. This redistribution is particularly evident near the Co atoms where the electron density appears to increase, while areas around the Si atoms show a slight decrease. This change suggests that the electric field induces electron migration towards lower energy states, mainly congregating around the Co atoms, which could be due to the field's alignment with the intrinsic electronic asymmetries of the material. At a higher electric field of $E = 1.29\ V/\text{Å}$, shown in Fig. 6.18(a), the localization of charge density becomes more pronounced. The color intensities around the Co atoms become more pronounced, indicating an increased localization of charge. This pattern of electron density suggests a redistribution of electrons, moving from higher to lower energy states as the electric field begins to influence the electronic structure. Such localized charge distributions can have profound implications on the electronic properties of CoSi, affecting everything from its conductivity to its chemical reactivity.

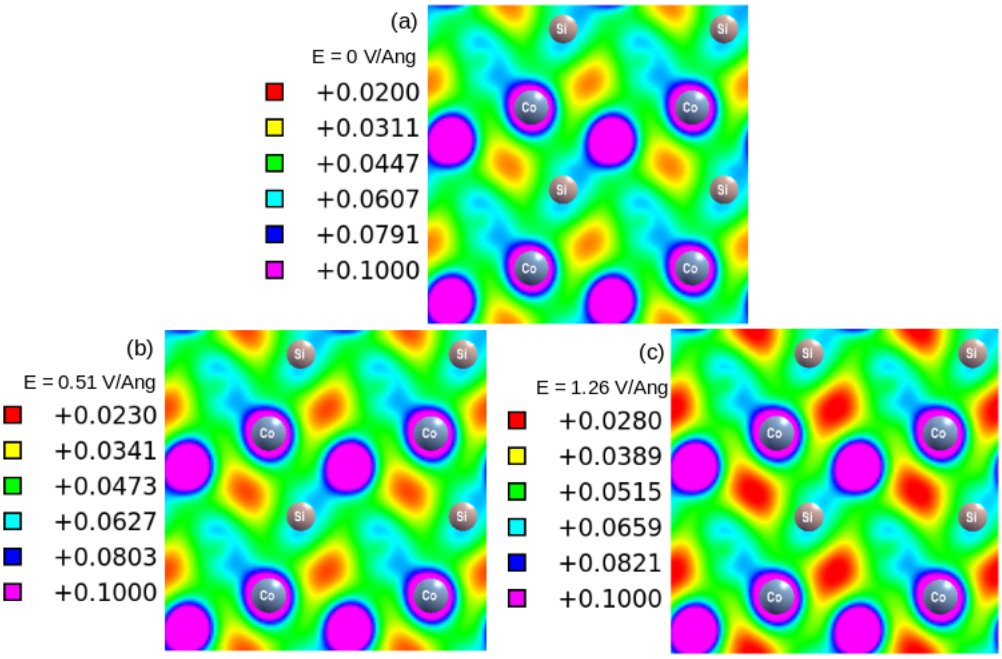

Figure 6.18: Charge density distribution in CoSi subject to varying external electric fields. Panel (a) presents the baseline electronic configuration without any applied electric field. Panel (b) shows the charge density under an external electric field of $E = 0.51$ V/Å, illustrating modifications in electronic density that reflect adaptive changes in the electronic environment. Panel (c) under an external electric field of $E = 1.29$ V/Å, highlights pronounced alterations in electronic density, evidencing a substantial response to the increased electric field strength.

These changes in the charge density under different electric field strengths illustrate how external electric fields can be used to manipulate the electronic structure of materials like CoSi. The electric field not only shifts the electron density but also modifies the electronic landscape, opening new possibilities for tuning material properties for specific applications such as semiconductors or electronic devices. The correlation between the observed charge density modifications and the band structure alterations previously discussed provides a comprehensive understanding of the material's response to external electric biases, highlighting the intricate relationship between an applied electric field and the material's electronic behavior.

b) Topological properties

Berry curvature and surface state

In Fig. 6.19(a), the Berry curvature of CoSi under no external electric field ($E = 0\ V/\text{Å}$) displays a uniform and symmetric distribution, reflecting the intrinsic topological properties of the material. This baseline condition suggests a stable electronic structure conducive to maintaining balanced topological features across the momentum space. When an electric field of $E = 0.51\ V/\text{Å}$ is applied, as shown in Fig. 6.19(b), there are noticeable shifts in the Berry curvature distribution. The curvature becomes more concentrated in specific regions, particularly near the Weyl points. This indicates that the electric field influences the localization and magnitude of the Berry curvature, suggesting alterations in the topological nature of the system. The electric field breaks certain symmetry properties, leading to an asymmetry in the curvature distribution, which may result in novel electronic behaviors. At a higher electric field of $E = 1.29\ V/\text{Å}$, displayed in Fig. 6.19(c), the changes in Berry curvature become more pronounced. The regions of concentration are more defined, and there are significant shifts in the magnitude of the curvature. These changes further underline the sensitivity of CoSi's topological properties to external electric fields, leading to enhanced topological phenomena or transitions under high field strengths. Correspondingly, the surface states in Figs. 6.19(d), (e), and (f) evolve significantly under these conditions. At $E = 0\ V/\text{Å}$, Fig. 6.19(a) shows well-defined surface states with clear dispersion relations, connected smoothly to the bulk states. This configuration indicates strong topological protection and a robust connection between surface and bulk electronic states. Upon the application of $E = 0.51\ V/\text{Å}$ in Fig. 6.19(e), the surface states begin to show shifts in their dispersion relations. These shifts suggest that the electric field alters the energy landscape of the surface states, affecting their connectivity to the bulk states and changing their nature and stability. This alteration might influence surface-related properties such as conductivity and reactivity, which are critical for applications in surface-sensitive devices. At the highest field of $E = 1.29\ V/\text{Å}$, shown in Fig. 6.19(f), the surface states undergo further modifications. The dispersion curves display significant changes, indicating a profound impact of the electric field on the surface electronic structure. The gap between surface and bulk states appears to widen, suggesting an increased isolation of the surface states from the bulk electronic properties. This could lead to distinct surface behaviors, useful for developing materials with tailored surface characteristics for advanced technological applications.

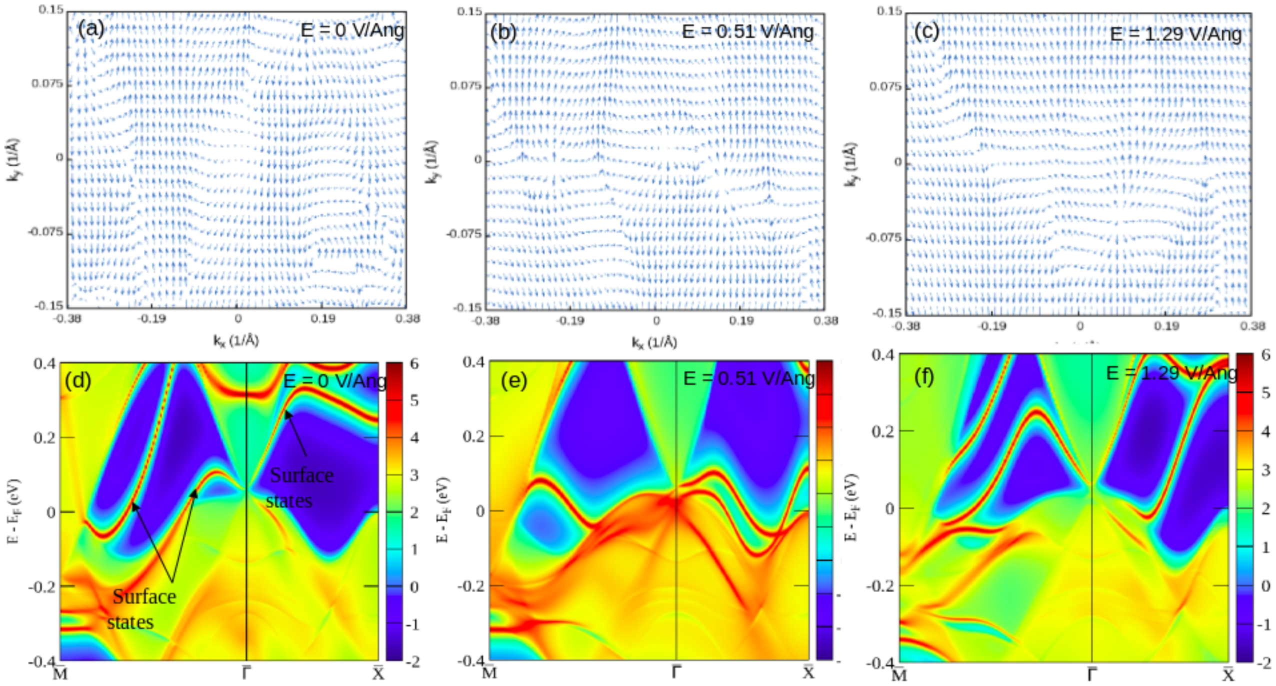

Figure 6.19: Berry curvature and surface state evolution in CoSi subject to varying external electric fields. Panels (a) and (d) depict the reference configuration without any applied electric field, providing a baseline for comparison. The Chern number $C \neq 0$. Panels (b) and (e) under an external electric field of $E = 0.51$ V/Å, illustrate the modifications in the topological properties, particularly highlighting shifts in Berry curvature and associated surface states. The Chern number $C = 0$. Panels (c) and (f) subjected to a higher electric field of $E = 1.29$ V/Å, showcase the progressive evolution and significant transformation of topological features as a response to increasing electric field strength. The Chern number $C \neq 0$.

These observations provide a comprehensive understanding of how external electric fields can manipulate the Berry curvature and surface states of CoSi. By controlling the field strength, one can induce specific topological and surface state changes, paving the way for materials engineering and the development of devices based on controlled electronic and topological properties[275].

Fermi arc

In Fig. 6.20(a), depicting the Fermi arc of CoSi under no external electric field ($E = 0\ V/\text{Å}$), the arcs display a coherent and continuous structure, connecting Weyl points across the momentum space with robustness and clarity. This baseline representation highlights the intrinsic stability and topological nature of CoSi's Fermi arcs, indicating their potential for maintaining electronic properties under standard conditions. Moving to Fig. 6.20(b), with an electric field of $E = 0.51\ V/\text{Å}$, the Fermi arcs begin to show noticeable changes in their configuration. The arcs elongate and undergo slight reorientation, altering their connection between Weyl points. These modifications suggest that the electric field begins to influence the topological stability and connectivity of the Fermi arcs. The change in shape and extent of these arcs under moderate electric field strength points to a dynamic response of the material's surface states to external electric biases, indicating possible shifts in electronic transport properties. At a higher electric field of $E = 1.29\ V/\text{Å}$, shown in Fig. 6.20(c), the Fermi arcs experience more pronounced transformations. The arcs are not only more elongated but also exhibit increased distortion and discontinuity. This suggests significant alterations in their connectivity and robustness, which indicate topological transitions under strong electric fields. The impact of such a high field strength demonstrates the susceptibility of Fermi arcs to external influences, leading to novel electronic behaviors.

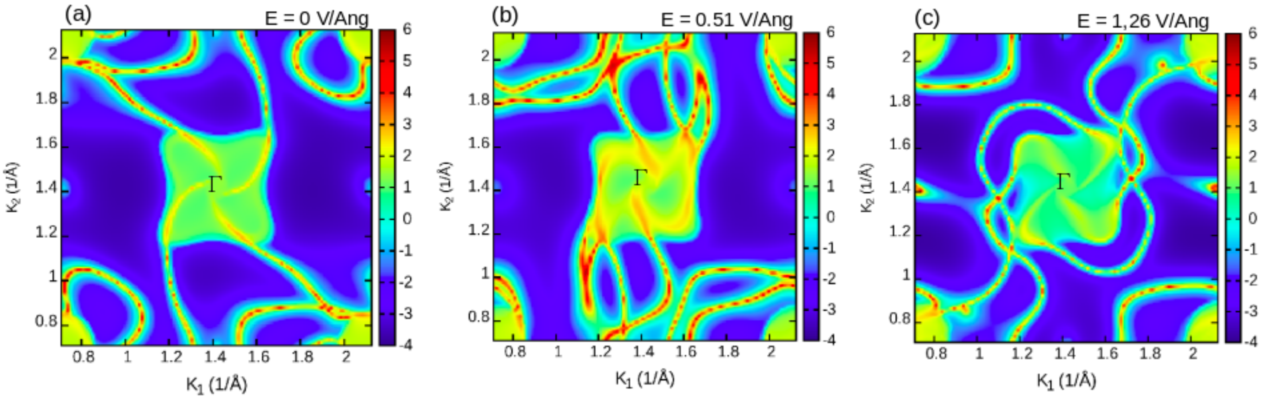

Figure 6.20: Visualization of the Fermi arcs in CoSi subject to varying external electric fields. Panel (a) shows the baseline topological state without any external electric field, establishing the reference condition for topological features. Panel (b) under an external electric field of $E = 0.51$ V/Å, demonstrates the changes in the Fermi arc structure, indicating modifications in topological characteristics in response to a moderate electric field. Panel (c) under a stronger electric field of $E = 1.29$ V/Å, highlights the significant evolution and deformation of the Fermi arcs, illustrating the dynamic response of topological states to increased electric field intensity.

These findings across the figures provide a comprehensive view of how external electric fields influence the Fermi arcs in CoSi. Starting from no field to a high-intensity field, the Fermi arcs show a progressive transformation in their structure and stability. This analysis underscores the sensitivity of topological properties to external conditions and offers insights into how such properties can be manipulated or controlled through the application of electric fields, catering to specific electronic and quantum technological applications[266]. It is important to highlight that Figure 6.20 reveals a notable observation: the electronic structure of CoSi is far less responsive to these external stimuli. Despite applying electric fields of increasing magnitudes, the changes in the Fermi arcs, while perceptible, are not as pronounced or dramatic as one might expect in more sensitive materials. This relative stability suggests that CoSi maintains a robust electronic structure, which is less susceptible to external electric fields. This characteristic is crucial for applications where material stability under external perturbations is essential.

6.3. Bulk NbP structure

6.3.1. Structural properties

NbP crystallizes in a non-centrosymmetric body-centered tetragonal (BCT) lattice, associated with the space group $I4_1md$ (No. 109)[46, 51, 276]. The lack of I symmetry in its structure is critical, as it results in the lifting of spin degeneracy in the band structure, an essential feature for the manifestation of Weyl semimetallic phases when combined with T symmetry. The lattice parameters of NbP are defined as a = b = 3.356438 Å and c = 11.436450 Å, which describe its tetragonal symmetry and further elucidate its geometric properties. The crystallographic configuration of NbP is illustrated in Fig. 6.21(a), highlighting its lattice arrangement. Fig. 6.21(c) depicts the BZ for the bulk structure of NbP. The projection of the (001) surface onto the BZ, as overlayed on the diagram, intersects with lines of high symmetry. This intersection is pivotal for the study of surface states, which are fundamental to understanding the topological characteristics of materials.

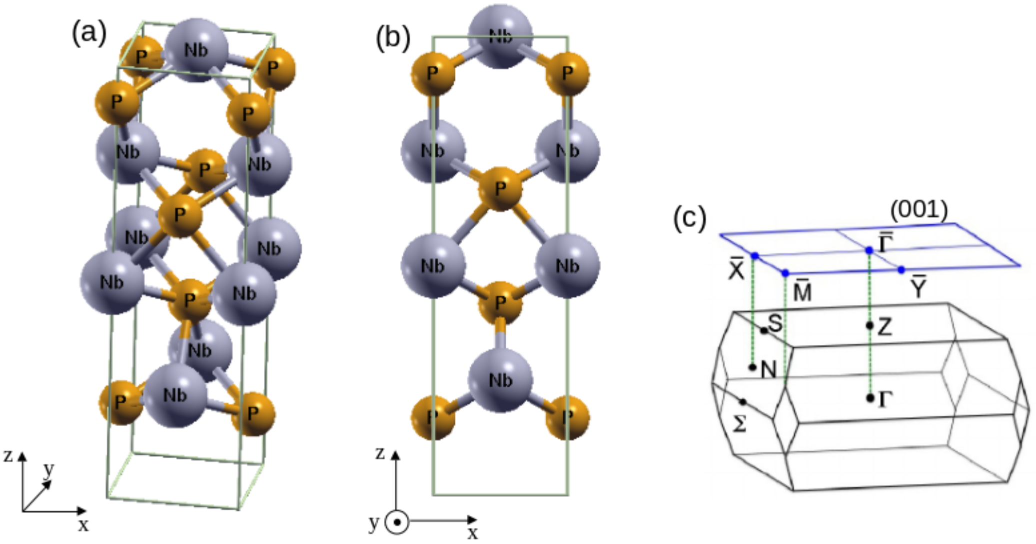

Figure 6.21: Bulk crystal Structure of NbP. Panel (a) diagram displaying the complete crystal structure of NbP. Panel (b) cross-sectional view of the crystal along the $x - z$ plane, showing internal atomic arrangement. Panel (c) illustration of the primitive BZ for NbP, detailing four unique high-symmetry points in the k-space. The diagram also includes the projection of the (001) surface BZ, with marked high-symmetry points.

6.3.2. Ground state electronic properties

The analysis of NbP's band structure in Figs. 6.22(a) and (b) offers insights into its topological properties and the role of SOC. Starting with Fig. 6.22(a), which represents the electronic band structure without SOC, we observe a more symmetric dispersion across the key symmetry points (Γ, Σ, Z, N, Γ) in the BZ. The bands near the Fermi level, E_F, appear to intersect at multiple points, suggesting potential Dirac-like features in the absence of SOC. This characteristic is critical, as it implies the presence of linear band crossings, which can be topologically non-trivial. Transitioning to Fig. 6.22(b), the inclusion of SOC alters the band structure significantly. The introduction of SOC leads to the lifting of degeneracies and the splitting of bands, particularly visible near the Fermi level. This splitting is indicative of the breaking of symmetrical spin degeneracy, a key factor in introducing topological insulator behavior. The modification of the band structure due to SOC is particularly pronounced in the $\Gamma - S$ direction, where the gap opening is evident. Such changes are crucial as they contribute to shifting the system's topology, leading to different electronic and topological phases. These result are consistent with the previous study[46, 51, 276].

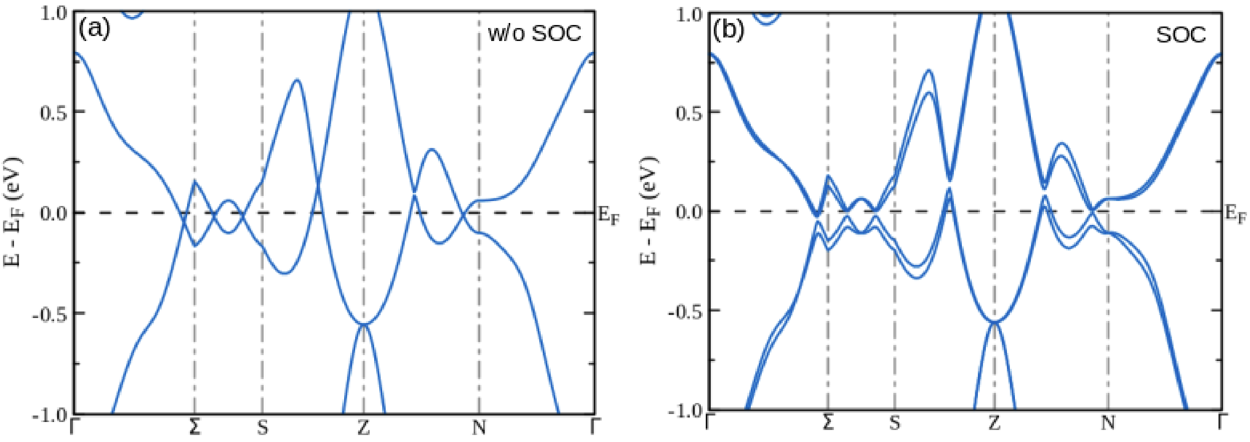

Figure 6.22: Band structure of NbP along high-symmetry lines in the BZ. Panel (a) depicts the band structure without the inclusion of SOC, illustrating the electronic states in their baseline configuration and highlighting the absence of relativistic effects. Panel (b) includes SOC, demonstrating the resultant band splitting as a direct consequence of relativistic interactions. The horizontal dotted lines indicate the Fermi level, serving as a reference for electronic state alignment.

These observations highlight the sensitivity of NbP's electronic properties to external perturbations such as SOC, underscoring the material's potential utility in spintronic applications where SOC effects are exploited[277]. The comparative analysis of the band structures with and without SOC provides a deeper understanding of how intrinsic symmetries and spin-orbit interactions influence the electronic and topological characteristics of NbP, paving the way for targeted manipulations in quantum material design.

6.3.3. Effect of applied strain

a) Electronic Properties

Band structure and Fermi surface

In Fig. 6.23(a), the band structure of NbP without any applied strain is depicted, showing a complex interaction of bands near the Fermi level, E_F. This unstrained state serves as the baseline for understanding the effects of tensile strain on electronic properties. The bands are densely packed around E_F, indicating a high DOS which is typical for (semi)metals and could contribute to high electrical conductivity. Fig. 6.23(b) illustrates the band structure with a 4% tensile strain applied. Here, notable changes include the opening of a gap of approximately 0.05 eV in the Γ - Σ direction. This alteration in the band structure signifies a transition in electronic properties, reducing electrical conductivity due to the decreased number of states at the Fermi level. Such changes are crucial for applications requiring controlled band gaps, such as semiconductors in electronic devices. Progressing to Fig. 6.23(c), with an 8% tensile strain, the band structure shows an additional modification around the Fermi level with a gap of about 0.035 eV. This continued alteration under higher strain levels further underscores the material's sensitivity to mechanical deformation, suggesting its suitability in sensor applications where strain-induced changes in electronic properties could be utilized. Turning to the Fermi surfaces in Fig. 6.23(d), the surface for the unstrained case displays several electron pockets, indicating regions of high electronic density. These pockets are crucial for the material's electronic and thermal transport properties. In Fig. 6.23(e), after applying 4% strain, the Fermi surface exhibits significant changes with reduced complexity and fewer electron pockets. This suggests a shift towards more localized electronic states, which could affect the material's conductivity. The absence of a Fermi surface plot for the 8% strained condition, as would have been shown in Fig. 6.23(f), is particularly telling. The lack of discernible Fermi surface features at this strain level implies a significant alteration in the electronic structure, leading to an insulating state or a state with very low electronic mobility. This drastic transformation underscores the potential use of NbP in applications where materials are needed to transition between conductive and non-conductive states under mechanical stress.

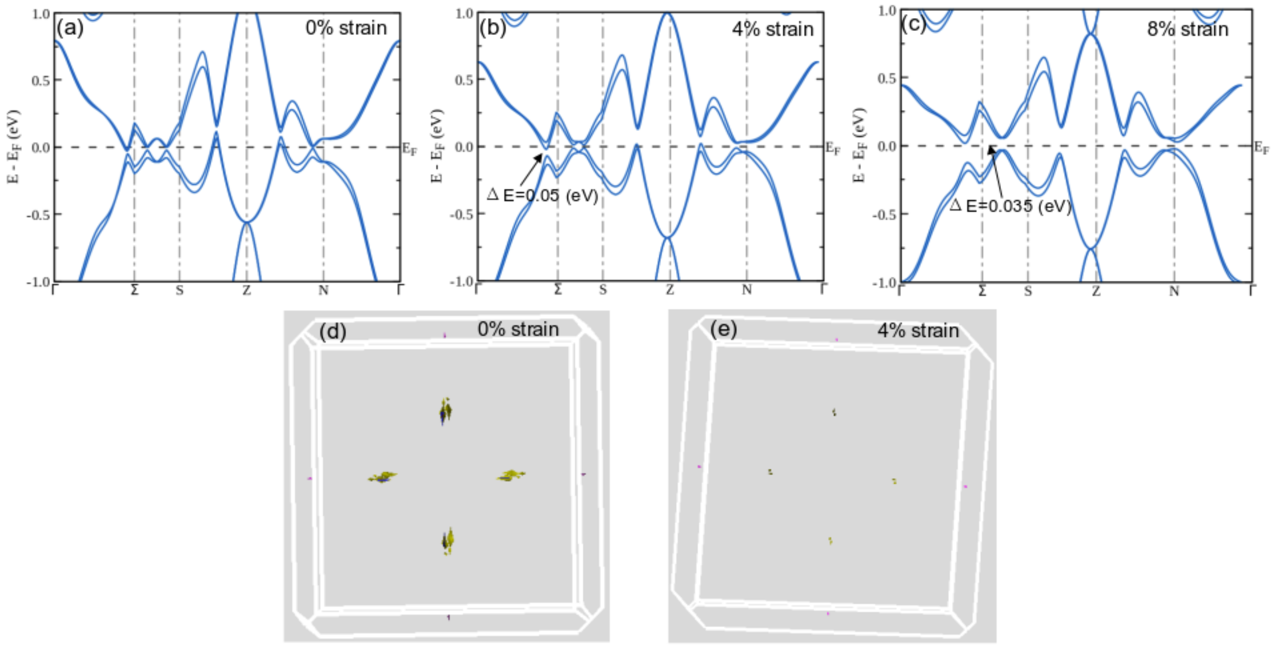

Figure 6.23: Band structure and Fermi surface of NbP under varying tensile strains. Panels (a) and (d) show the unstrained baseline configurations of the band structure and Fermi surface, respectively. Panels (b) and (e) illustrate the modifications at 4% tensile strain, highlighting adjustments in electronic states and alterations in Fermi surface topology. Panels (c) further detail the significant changes under 8% tensile strain, depicting the pronounced transformation in the Fermi surface morphology.

These results reveal how tensile strain can be a powerful tool in tuning the electronic properties of NbP, with implications for its use in strain sensors, flexible electronics, and other technologies where material properties need to be precisely controlled through mechanical means[274]. The alterations in both the band structure and Fermi surfaces highlight the complex interplay between mechanical and electronic properties in topological materials.

Charge density

Fig. 6.24(a) captures the charge density distribution in NbP under no strain. The visualization displays a relatively even distribution of charge density across the material, with higher densities around the Nb and P atomic sites. This uniformity reflects a stable electronic environment where electrons are distributed across the energy states near the Fermi level. The absence of external strain allows for an unbiased baseline of electronic interactions within NbP, serving as a critical reference for understanding strain-induced changes. In Fig. 6.24(b), with a 4% tensile strain applied, there is a notable shift in charge density, particularly around the Nb atoms. This redistribution suggests an alteration in the electronic structure as the strain influences the atomic spacing and, consequently, the electronic band structure. The appearance of denser regions around the Nb sites indicates a localization of charge density, which could imply enhanced electron-electron interactions or changes in bonding characteristics. This strain level also coincides with the opening of a gap near the Fermi level, as discussed previously, which leads to the migration of electrons from higher energy states to lower ones, affecting the overall charge distribution. Moving to Fig. 6.24(c), where an 8% strain is applied, the charge density shows even more pronounced changes. The increased strain further localizes the charge density around the Nb sites, while diminishing it near the P sites. This marked redistribution is indicative of significant alterations in the electronic landscape, where electrons are likely relocating to more stable, lower energy states due to the strain-induced modifications in the band structure. The gap opening at this strain level, although smaller than at 4%, continues to influence the electron density distribution by reducing the number of states available at the Fermi level, as visualized by the lesser intensity in regions previously occupied by these states.

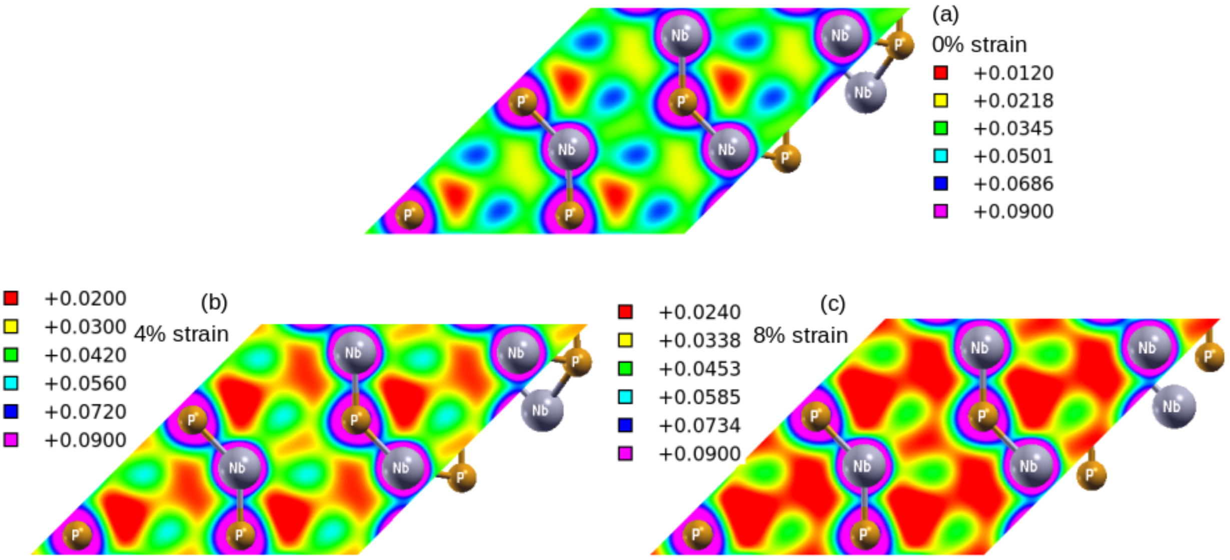

Figure 6.24: Charge density distribution of NbP under different tensile strains. Panel (a) displays the baseline electronic configuration without any applied strain, serving as the reference state. Panel (b) illustrates changes in electronic density at 4% tensile strain, detailing the moderate deformations in the electronic structure. Panel (c) depicts the extensive alterations in electronic density at 14% tensile strain, highlighting the significant effects of high mechanical stress on the material's electronic properties.

These changes in charge density across the figures directly correlate with the observed alterations in the band structure under varying tensile strains. As the strain modifies the atomic framework and electronic interactions within NbP, it shifts the electron density in ways that could impact the material's electronic properties and potential applications in semiconductor technology. Understanding these shifts is crucial for tailoring NbP's properties for specific applications, providing insights into how external mechanical biases like strain can be used to engineer desired electronic characteristics in novel materials.

b) Topological properties

Berry curvature and surface state

In Fig. 6.25(a), the Berry curvature for NbP under no strain shows a complex pattern, with localization of curvature near critical points in the momentum space. These localized regions are indicative of topological transitions and reflect the intrinsic symmetry of the crystal structure without external perturbations. The distribution and intensity of the Berry curvature are crucial as they relate directly to the quantum Hall effect and other topological phenomena, which rely on the integral of the Berry curvature over the BZ. Fig. 6.25(b) illustrates the Berry curvature under a 4% tensile strain. The curvature exhibits shifts in localization indicating a distortion in the topological characteristics of the material. These alterations can be attributed to strain-induced changes in the electronic band structure, which modify the conditions under which Weyl points and other topological features exist. The strain reduces symmetry in the Berry curvature distribution, leading to new electronic properties. In Fig. 6.25(c), with an 8% strain applied, the Berry curvature shows further dramatic changes. The pattern becomes more dispersed and less intense, suggesting a significant alteration or even a disappearance of certain topological features, such as Weyl points. This reduction in topological features indicate a transition to a topologically trivial phase, underlining the sensitivity of topological properties to mechanical deformations like strain.

Turning to the surface states, Fig. 6.25(d) displays the dispersion relations under no strain, with well-defined surface states crossing the Fermi level. These states are indicative of topologically protected modes that contribute to surface conductivity and potentially to phenomena like the quantum spin Hall effect. In Fig. 6.25(e), under 4% strain, the surface states show modifications in their dispersion relations. The bands appear to shift and bend differently compared to the unstrained case, reflecting changes in the connectivity between the surface and the bulk states. This strain level alters the energy levels at which these surface states exist, affecting the material's surface reactivity and electronic transport properties. Finally, Fig. 6.25(f) reveals that at 8% strain, the surface states show further modifications in their dispersion relations, indicative of a transition into a trivial topological phase. These alterations of the surface states significantly impact the electronic properties, especially in terms of reduced surface conductivity.

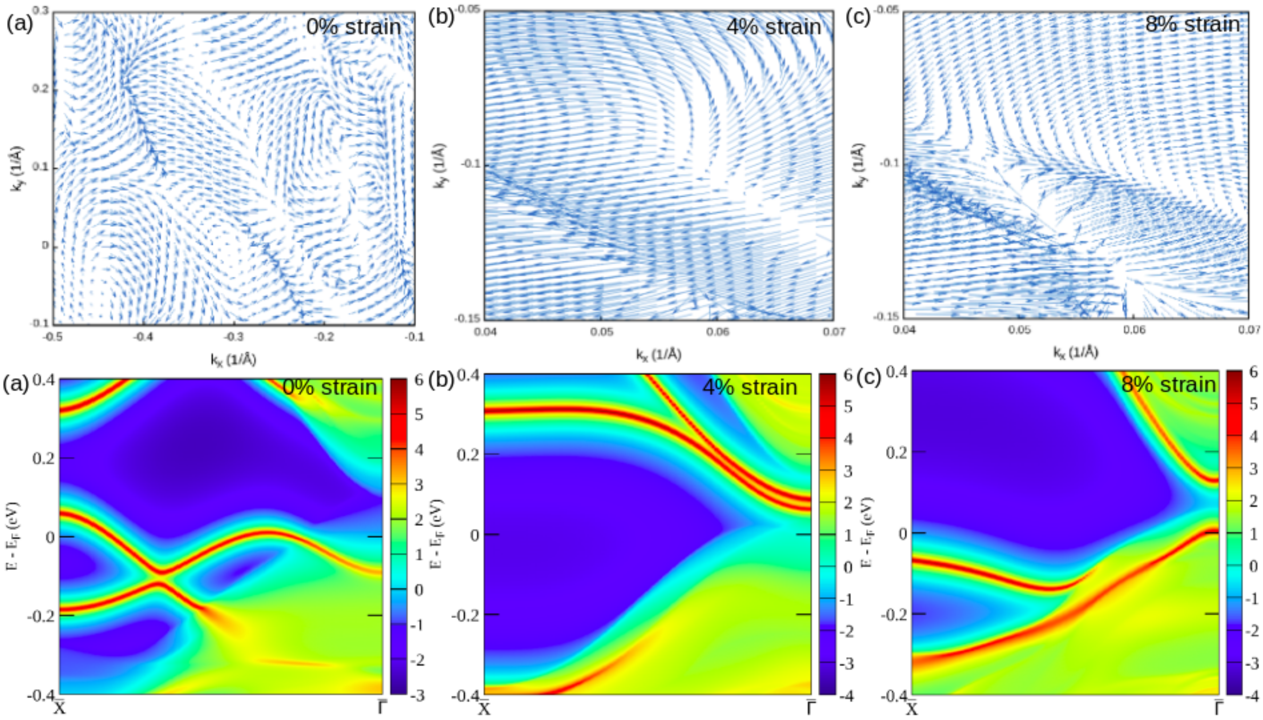

Figure 6.25: Berry curvature and surface state characteristics of NbP under increasing tensile strains. Panels (a) and (d) illustrate the baseline topological state without any applied strain, providing a reference for comparison. The Chern number $C \neq 0$. Panels (b) and (e) capture the impact of 4% tensile strain on the topological properties, detailing the induced changes in Berry curvature and surface states. The Chern number $C \neq 0$. Panels (c) and (f) further document the topological evolution at 8% tensile strain, highlighting significant transformations in both Berry curvature and surface state dynamics. The Chern number $C = 0$.

These observations from the Berry curvature and surface state analysis under different strain conditions provide a comprehensive view of how mechanical strain can be used to engineer the electronic and topological properties of NbP. The ability to control such properties through strain opens up new possibilities for designing materials with specific electronic characteristics for advanced technological applications[274].

Fermi arc

Fig. 6.26(a) depicts the Fermi arc structure in NbP under no strain, showcasing a complex pattern of arcs connecting Weyl points across the BZ. These arcs are characterized by their distinct shapes and extensive connectivity, indicative of the robust topological nature of the material. The arcs appear vibrant and widespread, suggesting strong topological protections and significant contributions to the surface state conductivity. Moving to Fig. 6.26(b), which shows the Fermi arc with a 4% tensile strain, there is a noticeable change in the shape and extent of the arcs. The arcs become reoriented, which is due to the strain altering the positions of the Weyl points within the BZ. This strain-induced modification affects the connectivity of these points, altering the topological characteristics of the material. The change in the shape of the Fermi arcs under strain suggests a less robust topological protection, which could influence the material's electronic properties, particularly in surface conductivity and topological quantum states. In Fig. 6.26(c), with an 8% strain, the Fermi arcs undergo further significant transformations. The arcs have almost vanished indicating a profound impact of high tensile strain on the topology of the material. The disappearance of the Fermi arc reflects a transition to a trival topological phase. This condition suggests that the Fermi arcs' robustness and stability are compromised under high strain, affecting the material's ability to maintain stable topological states and altering its utility in applications requiring robust topological features.

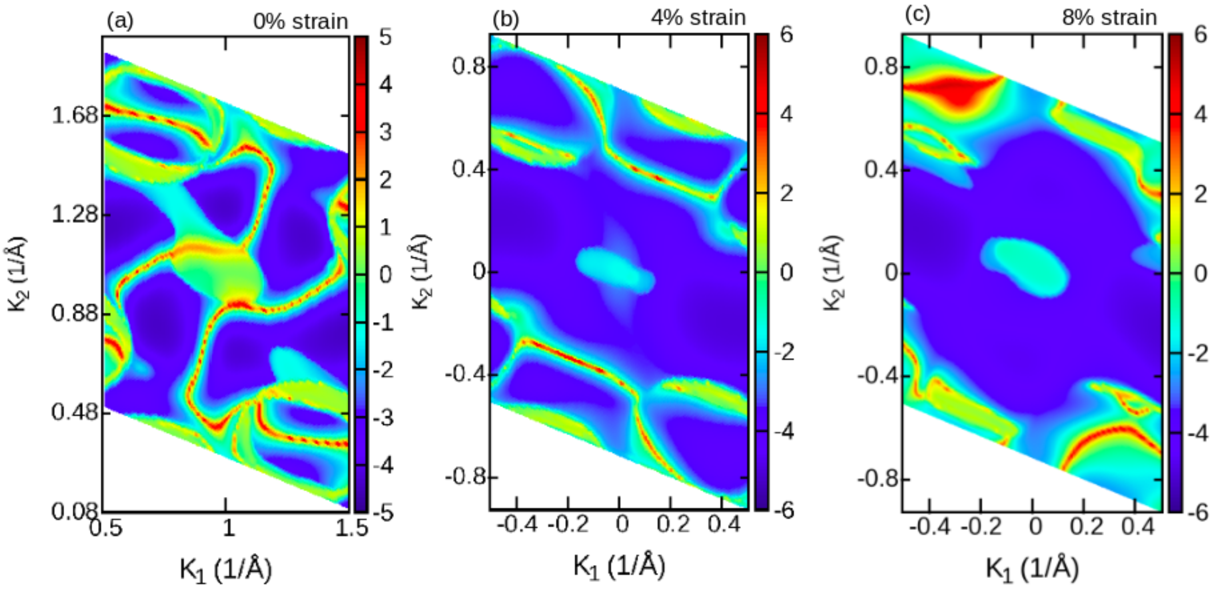

Figure 6.26: Visualization of Fermi arcs in NbP under different tensile strains. Panel (a) presents the baseline Fermi arc configuration without strain, serving as the reference state. Panel (b) depicts the Fermi arc structure under 4% tensile strain, illustrating moderate changes in arc morphology. Panel (c) highlights the further evolution and pronounced deformation of Fermi arcs under 8% strain, indicating significant adjustments in topological features due to increasing mechanical stress

These insights across the figures demonstrate how tensile strain can drastically influence the topological properties of NbP through modifications in the Fermi arc structure. The strain-dependent changes in the Fermi arcs, in correlation with the changes in band structure and Berry curvature discussed earlier, highlight the sensitivity of topological properties to mechanical deformations. Understanding these changes is crucial for designing and utilizing materials in applications where control over topological properties is required to achieve desired electronic functionalities[274].

6.3.4. With an external electric field applied

a) Electronic Properties

Band structure and Fermi surface

Fig. 6.27(a) presents the electronic band structure of NbP under no external electric field ($E = 0\ V/\text{Å}$). The bands are symmetric and contiguous, with no significant gaps around the Fermi level, E_F. This baseline scenario provides a clear understanding of the intrinsic electronic properties of NbP, with continuous band dispersion indicative of good semi-metallic conductivity. In Fig. 6.27(b), under a modest external electric field of $E = 0.51\ V/\text{Å}$, the band structure shows subtle changes. The impact of this electric field is minimal, as evidenced by the slight alterations in the band curvature near the high symmetry points. However, these changes are not enough to open a significant gap. This indicates that at lower field strengths, NbP maintains most of its electronic properties, with only minor perturbations affecting its electronic structure. Moving to Fig. 6.27(c), with a higher electric field of $E = 1.29\ V/\text{Å}$, a gap of approximately 0.02 eV opens in the $\Gamma - S$ direction. This change signifies a more pronounced response to the external electric field, altering the material's electronic structure significantly. The opening of this gap suggests a transition towards new topological phase, affecting the material's conductivity and electronic applications, such as in transistors where controlled gap modulation is crucial. Correspondingly, the Fermi surface in Fig. 6.27(d) (no electric field) shows a multi-pocketed structure, reflecting the semi-metallic nature of NbP and a high DOS at the Fermi level. These characteristics are typical for materials with good electrical conductivity. In Fig. 6.27(e), with an electric field of $E = 0.51\ V/\text{Å}$, the Fermi surface exhibits slight modifications, with minor reorientation and distortion of the pockets. These changes, while subtle, indicate the beginning of electron delocalization, affecting how electrons are distributed across the Fermi surface, though the overall semi-metallic nature remains largely intact. Finally, Fig. 6.27(f), under an electric field of $E = 1.29\ V/\text{Å}$, shows more noticeable changes in the Fermi surface. The pockets appear more fragmented and localized, correlating with the band gap opening observed in the band structure. This localizing effect reduces the number of available states at the Fermi level, which can lead to decreased electrical conductivity and a shift towards more localized electronic behavior.

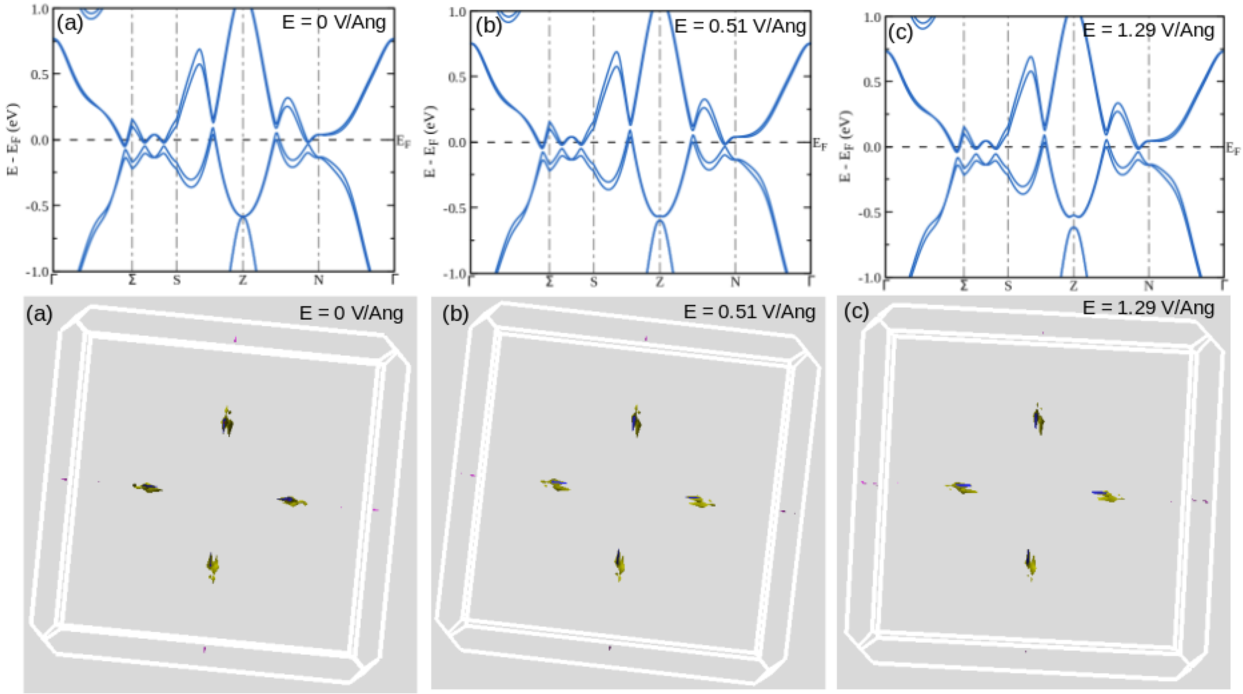

Figure 6.27: Band structure and Fermi surface of NbP under varying external electric fields. Panels (a) and (d) showcase the band structure and Fermi surface at $E = 0$ V/Å, establishing the baseline state. Panels (b) and (e) depict the band structure and Fermi surface at $E = 0.51$ V/Å, illustrating the adjustments in electronic states and the resulting alterations in Fermi surface topology due to the electric field. Panels (c) and (f) detail the band structure and Fermi surface at $E = 1.29$ V/Å, highlighting the significant modifications in electronic properties as a result of increased electric field strength.

These observations illustrate how external electric fields can be used to manipulate the electronic properties of NbP, with potential applications in electronic devices where the control of electronic properties such as conductivity and band gap is essential. The results demonstrate a clear correlation between the applied electric field strength, band structure modifications, and the corresponding changes in the Fermi surface, providing insights into the tunable electronic properties of NbP under varying external conditions[266].

Charge density

Fig. 6.28(a) displays the charge density distribution in NbP under no external electric field ($E = 0\,V/Å$). The distribution is relatively uniform with prominent electron density concentrated around the Nb and P atoms, reflecting the intrinsic electronic structure of NbP. This baseline condition highlights a stable and delocalized charge density characteristic of semimetals, where electron mobility is high, facilitating conductivity. Transitioning to Fig. 6.28(b), where a moderate electric field of $E = 0.51\ V/\text{Å}$ is applied, noticeable changes in the charge density distribution are evident. The electric field induces localization of charge density around specific atomic sites, particularly around Nb atoms. This indicates a redistribution of electrons, transitioning from higher to lower energy states as the electric field starts to affect the electronic structure. The increase in localization near specific sites suggests a potential for altered electronic properties, such as increased reactivity at these sites or modified transport properties. In Fig. 6.28(c), under a stronger electric field of $E = 1.29\ V/\text{Å}$, the charge density undergoes further significant redistribution. The localization around Nb atoms intensifies, and the overall charge density landscape shows a more pronounced contrast between high and low-density regions. This pattern indicates a strong influence of the electric field on the electronic structure, leading to more distinct regions of charge accumulation and depletion. The gap opening induced by the electric field, as discussed previously, correlates with a decrease in charge density at the Fermi level, further validating the observed changes in charge distribution.

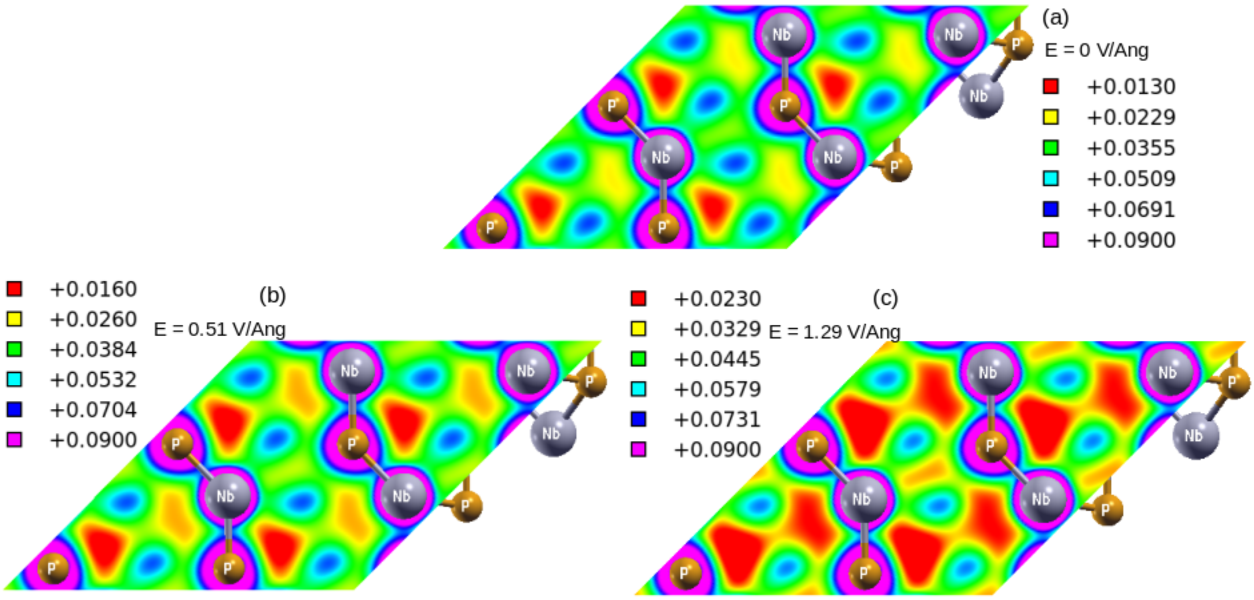

Figure 6.28: Charge density distribution in NbP under varying external electric fields. Panel (a) without an applied electric field, serving as a reference for the baseline electronic configuration. Panel (b) under an external electric field of $E = 0.51\ V/\text{Å}$, showing the modifications in electronic density as a result of the moderate electric field, indicating changes in the electronic environment. Panel (c) under an external electric field of $E = 1.29\ V/\text{Å}$, demonstrating significant alterations in electronic density in response to the increased field strength, highlighting the impact on electronic structure.

These modifications in charge density under varying electric field strengths demonstrate the material's responsiveness to external electric biases, which can be crucial for applications that rely on controlled electronic behavior, such as in semiconductor devices where precise manipulation of charge carriers is needed. The redistribution and localization of charge density not only affect the material's electronic and optical properties but also its interaction with other materials. Understanding these changes is essential for tailoring NbP's properties for specific applications, providing valuable insights into how external conditions can be used to engineer material properties at the atomic level.

b) Topological properties

Berry curvature and surface state

Fig. 6.29(a) displays the Berry curvature in NbP without an external electric field. The curvature pattern is widespread and uniform, indicative of a symmetric distribution without external perturbation. This uniformity highlights the intrinsic topological features of NbP. In Fig. 6.29(b), with an external electric field of $E = 0.51\ V/Å$, the Berry curvature starts to exhibit localized regions of enhanced curvature. The external field disrupts the symmetry of the Berry curvature distribution, resulting in a shift of the curvature distribution. This modification suggests a field-induced alteration in the topological invariants of the system, leading to novel electronic behaviors. Fig. 6.29(c) under a stronger external electric field of $E = 1.29\ V/Å$ shows a more dramatic transformation in the Berry curvature. The pattern becomes highly localized and intense around specific points in momentum space, showing significant deviations from the initial state. This indicates a substantial impact of the electric field on the material's topological properties. Moving to the surface states, Fig. 6.29(d) without an electric field shows typical topologically protected surface states that bridge the bulk band gaps. These states are crucial for surface conductivity and are indicative of NbP's inherent topological insulator characteristics. In Fig. 6.29(e), with $E = 0.51\ V/Å$, the surface states exhibit a noticeable shift in their dispersion relations. The energy bands are visibly altered, suggesting changes in the energy landscape at the surface. These alterations may affect the connectivity between surface and bulk states, altering the material's surface electronic properties and possibly affecting phenomena like surface conductivity. Finally, Fig. 6.29(f) under an electric field of $E = 1.29\ V/Å$ shows further shifts in the surface states. This could denote a significant reconfiguration of the material's surface electronic structure, potentially diminishing the robustness of topologically protected states under high electric fields.

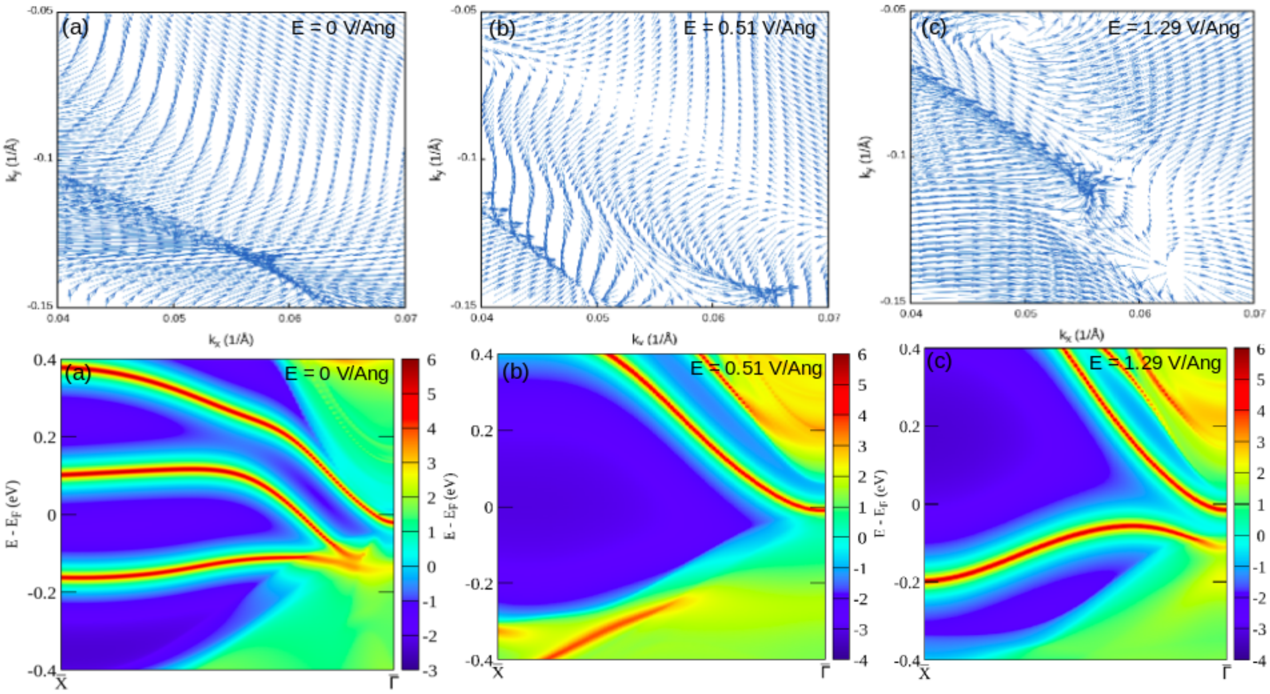

Figure 6.29: Berry curvature and surface state characteristics of NbP under varying external electric fields. The Chern number $C \neq 0$. Panels (a) and (d) without an applied electric field, providing a baseline for the reference configuration. The Chern number $C = 0$. Panels (b) and (e) under an electric field of $E = 0.51\ V/\text{Å}$, illustrating modifications in the topological properties induced by the electric field. The Chern number $C = 0$. Panels (c) and (f) under a higher electric field of $E = 1.29\ V/\text{Å}$, emphasizing the further development of topological features with increasing field strength.

These insights illustrate how NbP's electronic and topological properties can be dynamically controlled through external electric fields. This control is vital for applications in electronic devices, where the ability to modulate electronic properties on demand is crucial. The results underscore the sensitivity of topological materials to external perturbations and provide a pathway for tuning material properties for specific technological applications[278].

Fermi arc

Figure 6.30(a) illustrates the Fermi arc distribution in NbP under no external electric field ($E = 0\ V/\text{Å}$). The arcs exhibit and interconnected pattern. The connectivity and extensive reach of these arcs are essential for the unique surface properties of NbP, such as high surface conductivity and unusual quantum behaviors. Moving to Fig. 6.30(b), under a moderate electric field of $E = 0.51\ V/\text{Å}$, the Fermi arcs begin to show subtle changes in their configuration. The arcs appear slightly contracted and reoriented, suggesting an influence of the electric field on the topological nature of the material. These changes can be indicative of a shift in the locations or even the nature of the Weyl points, as the electric field begins to modify the underlying electronic structure. Although the arcs remain continuous, their altered geometry points to modifications in the surface electronic properties that could affect device performance based on these topological states. In Fig. 6.30(c), with a stronger electric field of $E = 1.29\ V/\text{Å}$, the Fermi arcs undergo more pronounced transformations. The arcs are notably more constricted and show significant distortion, which might reflect a substantial reconfiguration of the band structure under high electric fields. This modification can lead to a reduction in the stability of the topologically protected states, altering the material's electronic properties, such as its surface conductivity and the overall robustness of its topological insulator behavior.

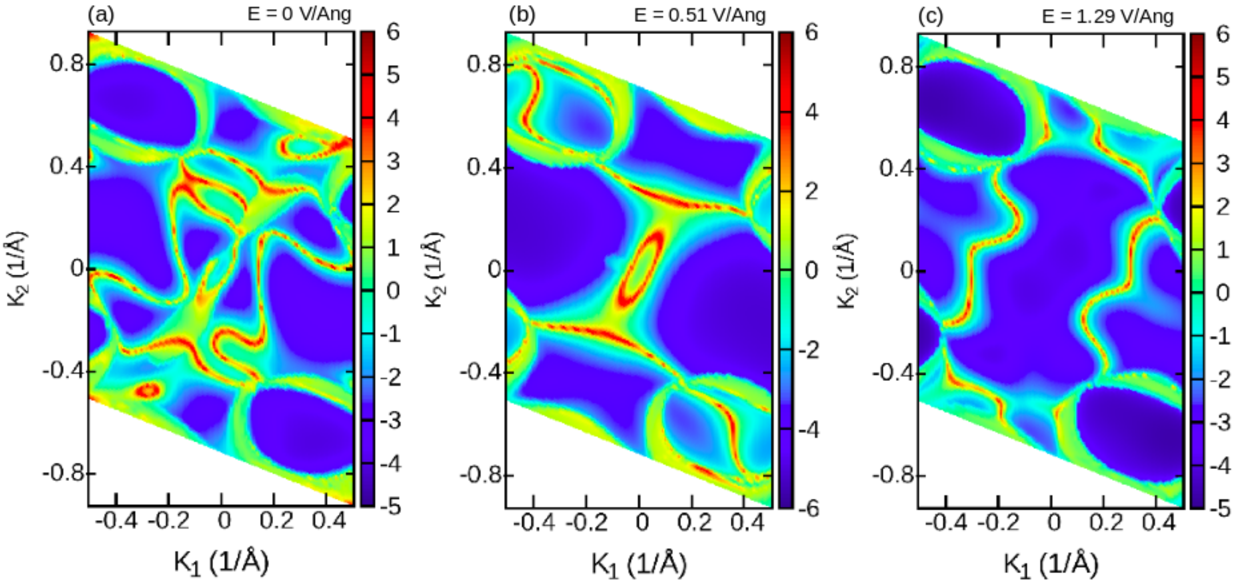

Figure 6.30: Visualization of the Fermi arcs in NbP under varying external electric fields. Panel (a): with no applied electric field, showing the baseline topological state. Panel (b): under an electric field of $E = 0.51\ V/\text{Å}$, indicating modifications in topological characteristics due to the moderate electric field. Panel (c) under a stronger electric field of $E = 1.29\ V/\text{Å}$, demonstrating the impact of increased field strength on the topological properties.

The observed changes in the Fermi arcs across these conditions demonstrate how external electric fields can effectively tune the topological and electronic properties of NbP. By affecting the connectivity and integrity of Fermi arcs, an electric field can control the material's quantum properties, offering potential avenues for developing electronic devices that leverage these unique characteristics. This control mechanism is particularly relevant for technologies that rely on topological phenomena, such as quantum computing and advanced sensing systems, where the precise manipulation of electronic states is crucial. The analysis of these Fermi arcs under varying electric field strengths underscores the dynamic nature of topological materials and their susceptibility to external perturbations, providing valuable insights into their application in next-generation electronic systems[279].

To conclude this part of the chapter, note that we used a range of lattice deformations and bias fields for each material in our calculations, then selected the strain and field magnitudes (strain ≈ 4-15%; E ~ 0.5-1.3 V/Å (~ 10^{10} - 10^{11} V/m)) that produced the most pronounced changes in electronic structure. The fact that these values cluster so closely across $SrSi_2$, CoSi, and NbP can be understood as follows:

- Linear-elastic and exploratory regime. Bulk covalent and intermetallic materials support elastic strains up to ≈ 1% under experimental conditions; beyond this, plasticity or fracture ensues[280]. However, first-principles simulations routinely impose larger lattice deformations (up to ≈ 15%) in order to explore extreme structural regimes and to map out phase boundaries without invoking defects or non-affine relaxations[281]. Staying within strain ≤ 15% ensures mechanical stability in DFT while enabling a thorough survey of strain-induced topological transitions.
- Electronic-energy matching. Fields of order 0.5-1.3 V/Å (~ 10^{10} - 10^{11} V/m) produce potential drops of roughly 10-25 eV over an interatomic spacing (~ 2 Å)[282]. These bias energies lie squarely within the range of first-ionization and band-gap scales for Sr (5.69 eV), Si (8.15 eV), Co (7.60 eV), Nb (6.76 eV), and P (10.49 eV), maximizing band-structure modulation without unphysical charge emission in a periodic cell.

By using the same strain and field magnitudes across all three materials, we enable a direct comparison under identical conditions, ensuring that observed differences stem from their intrinsic properties.

As can be seen, the external fields used in our DFT calculations ($10^{10} - 10^{11}$ V/m) greatly exceed the intrinsic dielectric strength of typical insulating solids, which lies between 10^6 and 10^9 V/m. In periodic DFT this does not trigger actual breakdown, but instead modifies the potential landscape. The electrostatic energy density in a medium of relative permittivity ε_r under a uniform field E is:

$$U = \frac{1}{2}\ \varepsilon_0 \varepsilon_r E^2, \tag{6.1}$$

where ε_0 is the vacuum permittivity. To compare the electrostatic energy with ionization energies of constituent atoms, we estimate the energy contained in a representative atomic-scale volume of 1 $Å^3$. For $\varepsilon_r \approx 10$ and $E = 10^{11}$ V/m, this yields an energy density of $U \approx 4.4 \times 10^{11}$ J/m^3, corresponding to $\approx$ 2.76 eV per $Å^3$. An electron moving across an interatomic distance $d \approx 2$ Å sees a potential drop $\Delta V = E \cdot d \approx 20$ eV. These energy scales are on the order of, or below, the first ionization energies of the constituent atoms of $SrSi_2$ (Sr: 5.69 eV, Si: 8.15 eV), CoSi (Co: 7.60 eV, Si: 8.15 eV), and NbP (Nb: 6.76 eV, P: 10.49 eV)[283]. Although these fields exceed experimental breakdown thresholds, in the simulation framework they do not induce real ionization. Instead, they produce bias energies on the order of electronic excitation scales, allowing us to probe how extreme potential gradients tune band alignments and topological responses without unphysical charge emission.

Direct experimental studies of topological characteristics under external bias are scarce for $SrSi_2$, CoSi, and NbP. However, related experimental work in each material family provides valuable benchmarks. For $SrSi_2$, ARPES at ambient pressure shows no clear Weyl nodes or Fermi arcs, while high-pressure ARPES and transport measurements reveal pressure-induced Weyl states and superconductivity above 20 GPa[284, 285]. In the CoSi family (space group $P2_13$), ARPES has unambiguously detected unconventional chiral fermions - spin-1 and charge-2 modes - connected by giant surface Fermi arcs, and magnetotransport confirms their chiral anomaly via negative longitudinal magnetoresistance[16, 44]. NbP (space group $I4_1md$) has been probed by high-resolution ARPES and scanning tunneling microscopy (STM/S), revealing Fermi-arc surface states, nonequivalent terminations on Nb- and P-surfaces, and detailed Fermi-surface shapes from quantum-oscillation studies[55, 286, 287]. While direct measurements under external bias remain to be performed, these experimental precedents both validate the theoretical predictions and guide future experimental designs for our systems.

6.4. Renormalization techniques applied to the study of bulk $SrSi_2$ structure mapped on graphene

Renormalization offers a straightforward computational method to explore how physical models behave under changes in scale. In this context, it demonstrates the use of external influences to adjust the electronic band structure from trivial to non-trivial states and back. This serves as a computational tactic to validate the theoretical assumptions behind the renormalization group approach. In this part of the chapter, we explore the intriguing parallels between WSMs and graphene, particularly focusing on $SrSi_2$, a notable WSM characterized by its chiral space group and absence of I symmetry. Renowned for their linear dispersion and massless fermionic excitations, WSMs are often considered as 3D counterparts to graphene. These materials not only mirror the high mobility and conductivity found in graphene due to their linear energy-momentum relationship, but they also exhibit unique topological features, such as protected Weyl points and consequential Fermi arcs, which mark significant departures from graphene's two-dimensional constraints. Here, we will delve into the renormalization of bulk $SrSi_2$ to a graphene-like sheet under external biases, aiming to elucidate the comparative dynamics and topological phenomena in these materials. Through a computational analysis, we anticipate shedding light on how external perturbations can modulate the electronic band structures from trivial to topologically non-trivial states, leveraging the principles of the renormalization group approach.

6.4.1. Impact of external fields on the renormalized band structure of $SrSi_2$

To study the effect of external fields on the renormalized band structure of bulk $SrSi_2$ along with the transport properties, we model a graphene supercell. This supercell consists of 50 atoms, created by repeating the basic hexagonal unit cell of graphene, which typically contains two carbon atoms, five times in each lattice direction, as shown in Fig. 6.31.

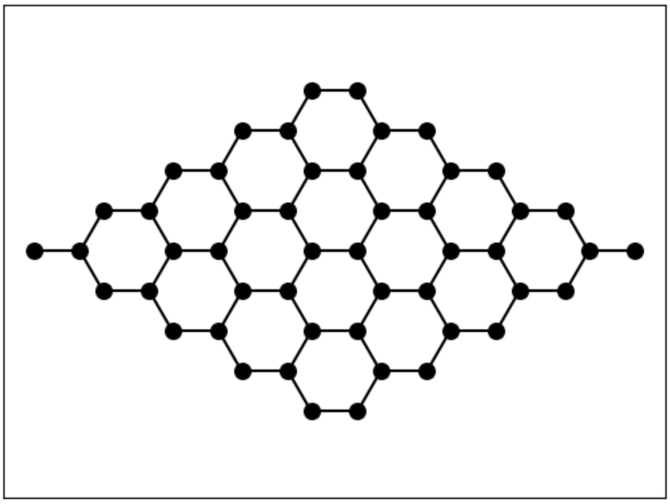

Figure 6.31: Supercell configuration of graphene with 50 atoms. the structure illustrates a 5 × 5 repetition of the basic hexagonal unit cell, containing two carbon atoms each.

Figure 6.32(a) showcases the band structure of $SrSi_2$ without the inclusion of SOC. Here, the key observation is the touching of two bands at points situated below and above the Fermi level, respectively. This characteristic is indicative of a semimetallic nature, where valence and conduction bands meet at specific points in the BZ, typically leading to high electron mobility and novel transport properties. The addition of SOC in Fig. 6.32(b), however, introduces a splitting in these bands. This splitting, observable at similar high-symmetry points, effectively lifts the degeneracy and is a direct representation of the intrinsic spin-orbit interactions within the material. In Fig. 6.32(c) and (d), the focus shifts to a graphene sheet model under the influence of external fields, aimed at mimicking the behaviors observed in $SrSi_2$. Figure 6.32(c) displays the band structure without SOC, where the application of an anti-Haldane field of $0.08t$ mirrors the crossings in the Γ - X direction seen in Fig. 6.32(a). This similarity supports the validity of using renormalization techniques to transpose the 3D characteristics of $SrSi_2$ onto a 2D graphene lattice. With the introduction of a KM SOC of $0.01t$ and an exchange field $J_z = 0.01$, depicted in Fig. 6.32(d), the bands further split, akin to the effects seen in Fig. 6.32(b) for $SrSi_2$. This not only confirms the effectiveness of the external fields in modifying band structures but also highlights the robustness of the renormalization approach in preserving the essential physical properties across dimensionalities. Therefore, to functionalize the renormalization method, we use $SrSi_2$ as a model for Dirac materials.

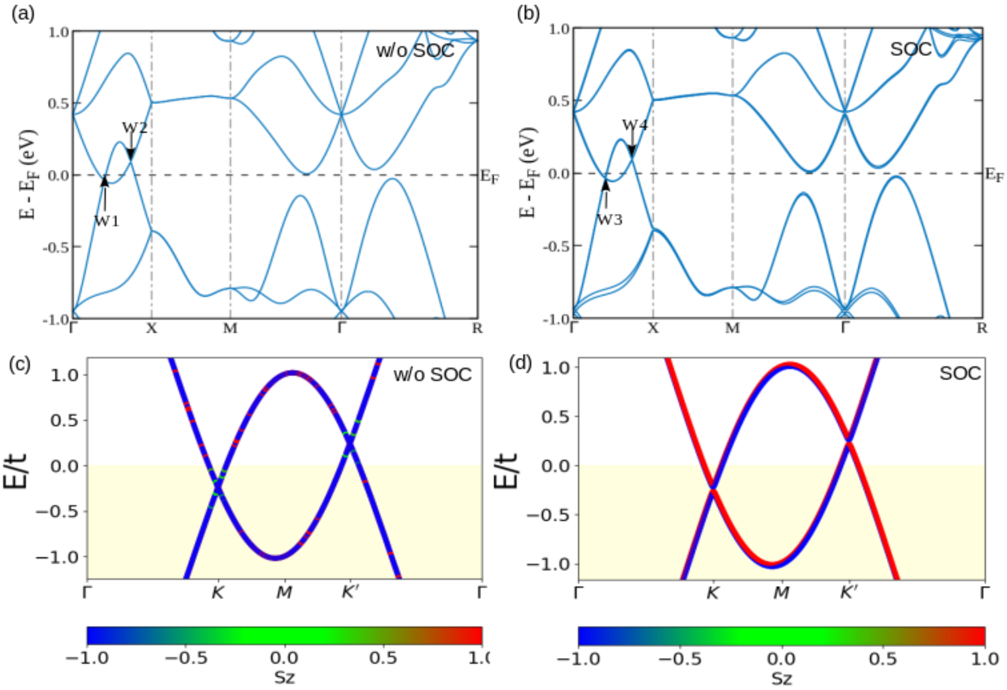

Figure 6.32: Comparative analysis of band structures in SrSi$_2$ and renormalized graphene. Panel (a) Electronic band structure of SrSi$_2$ without SOC, highlighting the semimetallic character with band crossings in the Γ - X direction. Panel (b) Band structure of SrSi$_2$ with SOC, showing band splitting and lifted degeneracies at high symmetry points. Panel (c) Band structure of graphene under anti-Haldane field (0.08t) without SOC, aligning with SrSi$_2$'s band characteristics in the Γ - X direction. Panel (d) Graphene band structure with KM SOC (0.01t) and exchange field (J_z = 0.01t), illustrating further band splitting and alignment with the band features observed in SrSi$_2$ with SOC.

In SrSi$_2$, the band structures in panels (a) and (b) are plotted along the cubic Brillouin-zone path X-M-Γ-R, capturing band inversion and splitting at these three-dimensional high-symmetry points. By contrast, the renormalized graphene results in panels (c) and (d) follow the hexagonal path K-M-K'-Γ, highlighting the Dirac cones at K and K' and their evolution under spin-orbit coupling. This distinction in symmetry directions reflects the different lattice geometries and ensures that renormalization traces the relevant quantum-phase behavior in each system.

The intricate interplay between SOC, external fields, and the band structures of SrSi$_2$ and graphene demonstrates the potential of renormalization techniques in exploring new quantum phases and electronic properties. The comparative analysis provided by these figures effectively bridges the gap between 3D and 2D materials, offering insights into the emergent transport characteristics and topological phenomena induced by external perturbations. Such studies are pivotal for advancing our understanding of Dirac materials and leveraging their properties in technological applications.

a) Fermi surface of the renormalized graphene

Figure 6.33(a) presents the 2D Fermi surface of renormalized graphene under an anti-Haldane field (0.08t) without the inclusion of SOC. The Fermi surface features distinct hotspots that correspond to regions of high electron density. These features correlate directly with the band structure observed in Fig. 6.32(c), where the absence of SOC maintains a degenerate band crossing, reflected here as enhanced electron localization at specific k-space coordinates. The electron localization phenomenon is indicative of the preserved symmetry and absence of SOC-induced band splitting, maintaining a more traditional Fermi surface akin to pristine graphene but modified slightly by the anti-Haldane field. In contrast, Fig. 6.33(b) illustrates the Fermi surface after the inclusion of KM SOC (0.01t) combined with an exchange field ($J_z = 0.01$). This inclusion noticeably transforms the Fermi surface, as evidenced by the emergence of new features at different k-space points. The impact of SOC is manifest in the redistribution and partial localization of electron density, which creates a more complex Fermi surface pattern. This transformation is linked to the band splitting observed in Fig. 6.32(d), where SOC and the exchange field lift the degeneracy of the bands, leading to distinct energy states for different spin orientations. Consequently, this induces a variation in electron density across the Fermi surface, highlighting SOC's profound effect on altering electronic properties. The evolution of the Fermi surface with SOC demonstrates how topological modifications induced by SOC can lead to new electronic behaviors, influencing transport properties and electronic applications of the material.

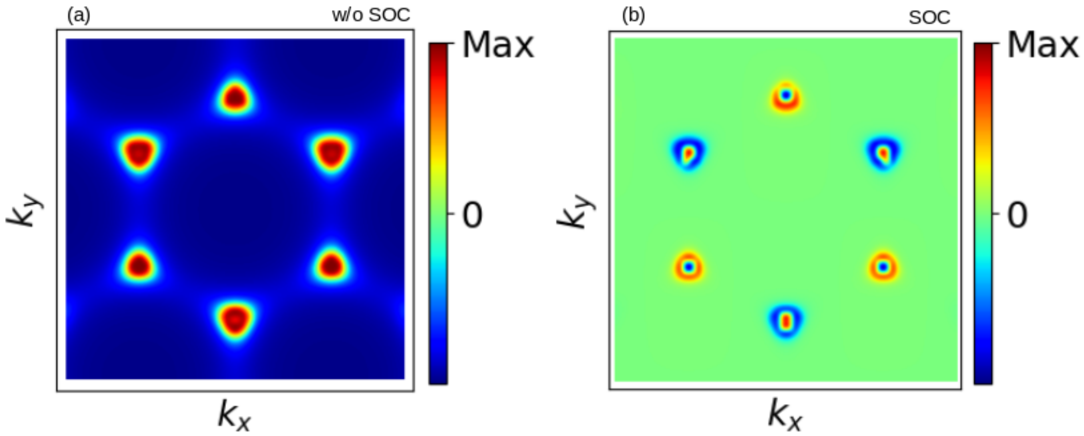

Figure 6.33: Two-dimentioanl Fermi surface of renormalized graphene. Panel (a) under an anti-Haldane field ($0.08t$) without SOC, showing localized electron density at specific k-space points. Panel (b) with the inclusion of KM SOC ($0.01t$) and an exchange field ($J_z = 0.01t$), depicting the transformation and redistribution of electron density at new k-space points.

The analysis of the Fermi surfaces in Figs. 6.33(a) and (b) provides a deep insight into the electronic structure dynamics of renormalized graphene under varying conditions. Without SOC, the Fermi surface remains relatively simple and reflects traditional graphene characteristics, although slightly altered by the external field. The introduction of SOC, however, revolutionizes this scenario by introducing complexity and underscoring topological effects' influence on electronic properties. This complexity is evident in Fig. 6.33(b), which shows how the inclusion of KM SOC and an exchange field redistributes the electron density compared to panel (a). On the same color scale (red = maximum density, blue = minimum), the six sharp red peaks at the k-points shrink and a green background appears, indicating that spectral weight has spread into the surrounding k-space. New, smaller red spots at slightly shifted k-coordinates mark the relocated density maxima. This pattern reveals that SOC and magnetic exchange partially delocalize the Fermi surface weight and reshape the electronic structure of renormalized graphene. These changes are crucial for understanding the potential applications of renormalized graphene in devices where SOC can be manipulated to tailor material properties.

b) Topological properties of the renormalized graphene

Figure 6.34(a) displays the 2D Berry curvature of renormalized graphene under an anti-Haldane field of $0.08t$, without the inclusion of SOC. The curvature is diffusely spread across the momentum space, with slight concentrations visible in a somewhat random pattern. This diffuse distribution indicates a lack of strong localization, which is typical in systems where SOC is absent, as SOC generally plays a critical role in sharpening and defining features in the Berry curvature. The absence of SOC preserves certain symmetry properties in the curvature distribution, as there are no SOC-induced asymmetries to disrupt the underlying lattice symmetries. Conversely, Fig. 6.34(b) shows the 2D Berry curvature with the inclusion of KM SOC ($0.01t$) and an exchange field ($J_z = 0.01$). Here, the curvature exhibits clear, localized peaks, distinctly positioned at specific points in momentum space. This localization reflects the breaking of certain symmetries due to SOC, which introduces anisotropies in the electronic structure, thereby enhancing the localization of Berry curvature. These sharp features highlight the impact of SOC in creating topologically non-trivial properties in the material, crucial for applications that exploit the quantum geometric properties of materials. Moving to Fig. 6.34(c), the Chern number calculated for the system without SOC is zero across the momentum space. This uniformity reflects the topologically trivial nature of the renormalized graphene without SOC, consistent with the absence of the localized

Berry curvature that would indicate topological non-triviality. In Fig. 6.34(d), the inclusion of SOC changes the scenario dramatically. The Chern number varies significantly across different regions of momentum space, with values reaching up to 20. This variation and the appearance of non-zero Chern numbers underscore the topological transition induced by SOC. The areas of high Chern number correlate with the peaks in Berry curvature seen in Fig. 6.34(b), indicating regions of high topological significance and the potential for exotic quantum phenomena such as the quantum anomalous Hall effect.

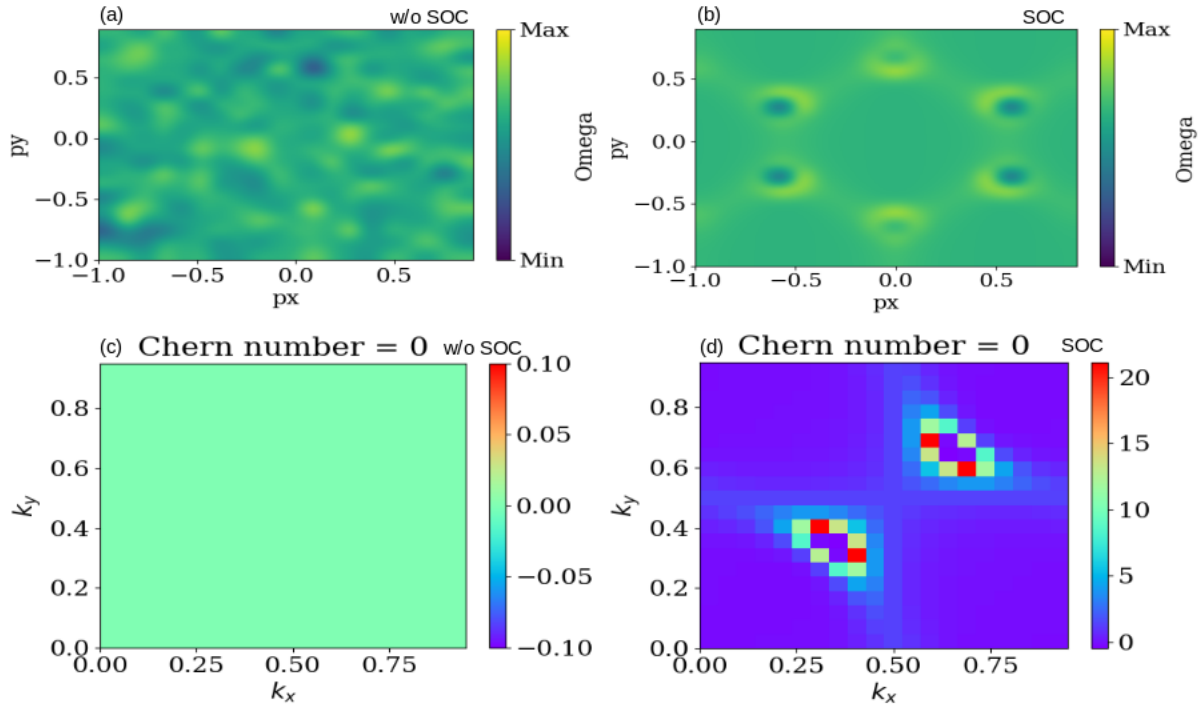

Figure 6.34: 2D Berry curvature and chern numbers in renormalized graphene under various conditions. Panel (a) under an anti-Haldane field ($0.08t$) without SOC, exhibiting a diffuse distribution across momentum space. Panel (b) with the inclusion of KM SOC ($0.01t$) and an exchange field ($J_z = 0.01t$), showing localized peaks indicating topological non-triviality. Panel (c) Chern number for the condition without SOC, uniformly zero across all momentum space, reflecting the topologically trivial nature of the system. Panel (d) Chern number with SOC, varying significantly, with high values in regions corresponding to peaks in the Berry curvature, indicating the emergence of topologically non-trivial states.

The comparative analysis of Berry curvature and Chern numbers in Figs. 6.34(a)-(d) demonstrates how the introduction of SOC and external fields fundamentally alters the topological landscape of renormalized graphene. Without SOC, the system remains topologically trivial, with a diffuse Berry curvature and zero Chern number. However, the inclusion of SOC not only localizes the Berry curvature but also engenders a topologically non-trivial state as evidenced by the non-zero

Chern numbers, pointing towards profound implications for the electronic and quantum properties of the material. This analysis highlights the critical role of SOC in engineering topological states in materials science.

6.4.2. Topological quantum phase transition in renormalized graphene

a) Opening of the gap

Figure 6.35(a) presents the electronic band structure of $SrSi_2$ under the influence of an external electric field of magnitude $0.15\ V/\text{Å}$. The application of this electric field results in a notable opening of the band gap at high-symmetry points in the BZ. This gap opening is critical as it demonstrates the ability to manipulate the electronic properties of $SrSi_2$ through external fields, thereby tuning the material's electronic phase from a semimetallic to an insulating state. The controlled introduction of the electric field induces a shift in the energy levels, leading to a separation between the conduction and valence bands, which is essential for the emergence of insulating properties. In Fig. 6.35(b), the band structure of renormalized graphene is shown with an increased KM SOC strength of $0.02t$ and an exchange field of $J_z = 0.01$. The increase in KM SOC strength effectively induces a band gap at points K and K', analogous to the gap observed in $SrSi_2$ under the electric field. This gap is a quintessential marker of a TQPT, where the material transitions from a normal to a topological insulator state, characterized by the presence of protected edge states within the gap. The introduction of SOC not only splits the bands due to the spin-orbit interaction but also locks the spins in a way that results in non-trivial topological properties.

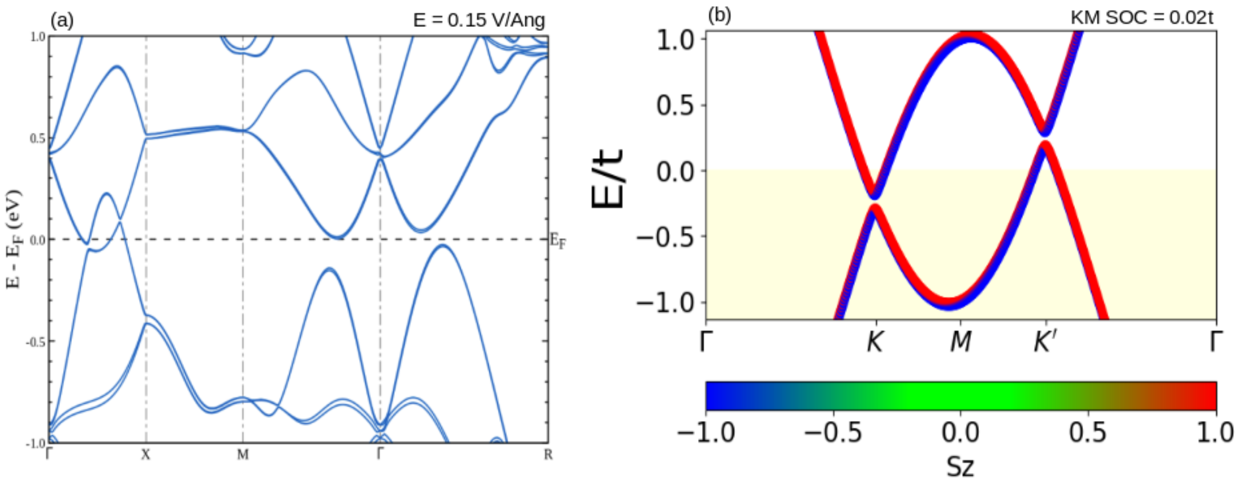

Figure 6.35: Band structures indicating TQPTs in $SrSi_2$ and renormalized graphene. Panel (a) Band structure of $SrSi_2$ under an external electric field ($E = 0.15\ V/\text{Å}$), showcasing the opening of a band gap in the Γ - X direction, facilitating a transition from semimetallic to insulating state. Panel (b) Band structure of renormalized graphene with increased KM SOC strength ($0.02t$) and an exchange field ($J_z = 0.01t$), demonstrating a band gap at points K and K', indicative of a TQPT to a topological insulator state.

The analysis of Figures 6.35(a) and (b) reveals the parallel mechanisms through which external perturbations influence the electronic properties of both $SrSi_2$ and renormalized graphene. In $SrSi_2$, the application of an electric field opens a band gap, pushing the material into an insulating phase. Similarly, in renormalized graphene, increasing the KM SOC strength leads to a band gap opening that signifies a transition into a topological insulating phase. These results underscore the sensitivity of these materials to external fields and SOC, highlighting their potential for applications in quantum computing and electronic devices where phase control is crucial.

b) Emergence of topological quantum phases

As previously discussed, Fig. 6.36(a) showcases the renormalized graphene band structure with KM SOC ($0.02t$) and exchange field ($J_z = 0.01t$), where a gap is opened at points K and K'. This configuration indicates a topological insulating phase due to the introduction of SOC and minimal exchange interaction. The corresponding Fermi surface shown in Fig. 6.36(d) illustrates a lack of states at the Fermi level within the gap, confirming the insulating nature of this phase with well-defined gaps around symmetrical points in the BZ. Figure 6.36(b) represents a significant alteration in the system's parameters with KM SOC increased to ($0.03t$) and exchange field raised to ($J_z = 0.1t$). This change leads to the closure of the previously observed gap, allowing for band crossings at points K and K' and the emergence of a topological semimetallic phase. This transition is captured in the corresponding Fermi surface in Fig. 6.36(e), where the formation of pockets indicates states at the Fermi level, characteristic of semimetallic behavior. Moving to Fig. 6.36(c), the parameters are further altered by maintaining KM SOC at (0.03t) while introducing additional exchange fields ($J_z = 0.2t$ and $J_x = 0.2t$). This modification results in the re-opening of the band gap at points K and K' with band inversion, a hallmark of a more complex topological phase, suggesting a transition to a different type of topological insulator. The corresponding Fermi surface in Fig. 6.36(f) shows a reduction in the DOS at the Fermi level, with clear gaps at K and K' and localized states around these points, further evidencing the band inversion and the robustness of the topological phase under these conditions.

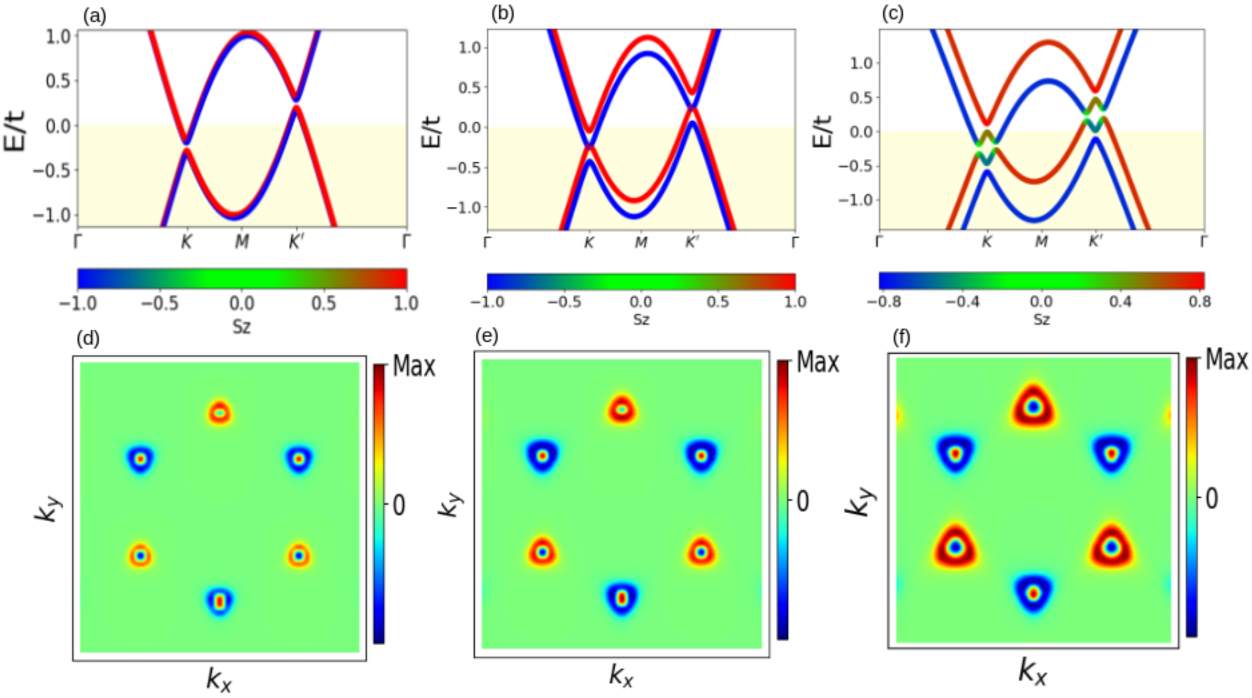

Figure 6.36: Band structures and corresponding Fermi surfaces of renormalized graphene under varying KM SOC and exchange fields, indicating Topological Transitions. Panel (a) Band structure with initial KM SOC (0.02t) and exchange field ($J_z = 0.01t$) showing a topological insulating phase with a gap at points K and K'. Panel (d) Corresponding Fermi surface lacking states at the Fermi level, affirming the insulating nature. Panel (b) Band structure with increased KM SOC (0.03t) and higher exchange field ($J_z = 0.1t$) displaying a closure of the gap and emergence of a topological semimetallic phase. Panel (e) Corresponding Fermi surface with pockets indicating semimetallic behavior. Panel (c) Band structure with the same KM SOC and additional exchange fields ($J_z = 0.2t$ and $J_x = 0.2t$) showing band inversion and re-opening of the gap at K and K', suggesting a transition to a another topological phase. Panel (f) Corresponding Fermi surface showing localized states, corroborating the topological characteristics.

The transitions observed in Fig. 6.36(a) through (f) provide a detailed view of the effects of varying SOC and magnetic exchange fields on the electronic structure of renormalized graphene. These changes not only demonstrate the tunability of topological phases through external parameters but also highlight the sensitive balance between SOC and magnetic interactions in dictating the electronic and topological properties of the material. Each step of the parameter variation leads to distinct electronic states, from insulating to semimetallic to a potentially more exotic topological insulating state, underscoring the complex interplay of spin-orbit and magnetic effects in engineered graphene systems. This analysis underscores the potential for using these tunable parameters to explore new quantum electronic applications and enhance our understanding of topological materials.

Figure 6.37(a) presents the Berry curvature for renormalized graphene with KM SOC ($0.02t$) and exchange field ($J_z = 0.01t$), parameters corresponding to a topological insulating phase as seen in Fig. 6.36(a). The Berry curvature is relatively uniform with minor fluctuations across the momentum space, indicating a lack of significant topological features under these conditions. This is consistent with a system in a trivial topological phase where the Chern number, shown in Fig. 6.37(d), is zero. The absence of pronounced peaks in the Berry curvature supports the insulating behavior without any exotic topological characteristics. Moving to Fig. 6.37(b), the Berry curvature is mapped with increased KM SOC ($0.03t$) and a higher exchange field ($J_z = 0.1t$). This setup correlates with the emergence of a topological semimetallic phase as observed in Fig. 6.36(b). The curvature shows more pronounced peaks, suggesting the presence of non-trivial topological features. The corresponding Chern number in Fig. 6.37(e) totals to 1, confirming the non-trivial topological nature of the phase. This shift to a Chern number of 1 is indicative of a topological phase transition driven by the adjusted KM SOC and magnetic field strengths, which align with the observed band crossings in the band structure. In Fig. 6.37(c), the Berry curvature is depicted for parameters including KM SOC ($0.03t$) with additional exchange fields ($J_z = 0.2t$ and $J_x = 0.2t$), leading to band inversions as seen in Fig. 6.36(c). The curvature here shows varied intensities and localized peaks, which are indicative of a strong topological influence resulting from the complex interplay of SOC and multidirectional exchange fields. The corresponding Chern number plot in Fig. 6.37(f) shows a return to 0, suggesting that despite the presence of band inversions and apparent complex topological features, the overall topological charge of the system remains neutral.

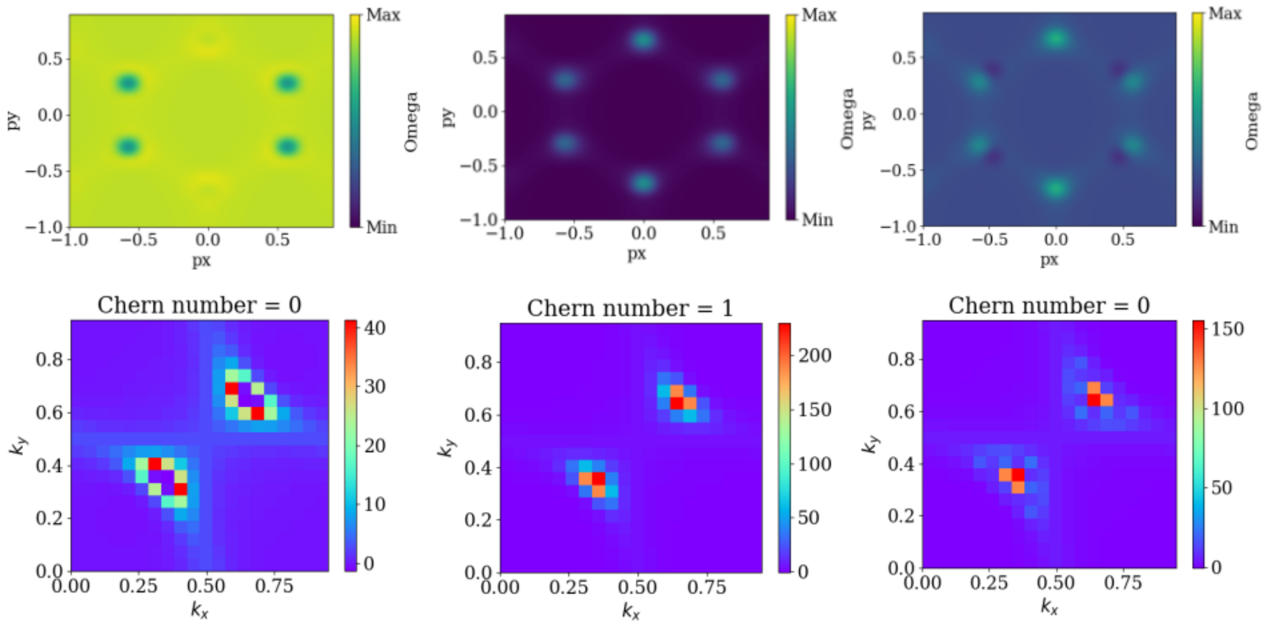

Figure 6.37: Berry curvature and corresponding Chern numbers of renormalized graphene under varied KM SOC and exchange field conditions. Panel (a) with KM SOC ($0.02t$) and exchange field ($J_z = 0.01t$), displaying minimal fluctuations, consistent with a topologically trivial phase. Panel (d) corresponding Chern number plot showing a total of 0, confirming the trivial nature. Panel (b) with increased KM SOC ($0.03t$) and higher exchange field ($J_z = 0.1t$), featuring more pronounced peaks, indicative of a non-trivial topological semimetallic phase. Panel (e) corresponding Chern number plot with a total of 1, verifying the non-trivial topological characteristics. Panel (c) with further enhanced KM SOC ($0.03t$) and additional exchange fields ($J_z = 0.2t$ and $J_x = 0.2t$), showing varied intensities and localized peaks, linked to complex topological features. Panel (f) corresponding Chern number plot returning to 0, suggesting a neutral topological charge despite apparent complexities.

The results from Fig. 6.37(a) through (f) illustrate the profound impact of SOC and exchange field manipulations on the topological properties of renormalized graphene. Transitioning from trivial to non-trivial and back to trivial topological phases under varying conditions demonstrates the tunable nature of topological properties in graphene-based systems. These findings not only underscore the sensitivity of Berry curvature and Chern numbers to external parameters but also highlight the potential for engineering topological states in materials for advanced technological applications. This detailed examination of Berry curvature and Chern numbers deepens our understanding of the relationship between electronic structure alterations and topological properties.

For $SrSi_2$, the Berry curvature and surface state analyses under various conditions, such as strain and external electric fields, reveal significant changes in topological properties. Notably, under no strain and no external electric field, $SrSi_2$ exhibits non-zero Chern numbers, consistent with the

presence of non-trivial topological phases similar to those observed in the graphene models with adjusted SOC and exchange fields. These Chern numbers, indicative of robust topological features, provide a quantitative measure of the system's topological invariants, directly corresponding to the observed Berry curvature distributions. As strain or electric field strength increases, the topology of $SrSi_2$ evolves, as evidenced by the varying Chern numbers. This transition parallels the behavior seen in renormalized graphene when adjusting SOC and magnetic interactions, where Chern numbers also transition between non-zero to zero values, reflecting a shift from non-trivial to trivial topological phases. These observations underscore the consistency across different material systems and the impact of external perturbations on topological characteristics. Thus, the connection between these DFT results and the theoretical models used in the study of renormalized graphene not only confirms the consistency of gauge fixing concepts across disparate systems but also enriches our understanding of how external conditions influence quantum topological states. This comparative approach enhances our grasp of complex topological phenomena, providing a clearer picture of the underlying mechanisms driving these QPTs.
It is worth mentioning that we chose all exchange field values by scanning a range of J_z in our tight-binding model (for example, from 0.005 t up to 0.02 t) and, for each trial value, comparing key features - band dispersions, gap openings, and Fermi surface intensity - to our DFT results. The values reported here are those that best reproduced the DFT observables, ensuring quantitative agreement between the model and first-principles calculations.

To conclude this chapter, the results of this study reveal that $SrSi_2$, CoSi, and NbP offer concrete pathways toward devices that exploit their strain- and field-tunable topological properties. For example, the ability to open and close small band gaps in $SrSi_2$ and NbP under controlled strain or electric bias suggests these materials could serve as low-dissipation switches or filters in high-frequency electronics, where a small, strain-induced gap modulates carrier flow with minimal energy loss. In CoSi, the anisotropic response of different Brillouin-zone points to strain and field points to applications in directional sensors or transducers, where mechanical deformation or applied voltage produces a measurable change in conductivity or optical absorption. More broadly, the robust surface states and Fermi arcs in these compounds - tunable via external perturbations - could underpin topological qubits for fault-tolerant quantum computing, as such states are inherently protected against disorder and backscattering[59, 61]. Strain engineering thus provides a practical means to tailor the operational window of these devices, bridging our computational predictions with real-world performance requirements. In photonics, the field-induced symmetry breaking that gaps Weyl nodes can yield switchable optical activity, useful in modulators or isolators, while the sensitivity of Berry curvature to lattice distortions opens opportunities for novel magneto-optic sensors. By mapping how small, experimentally accessible strains and fields drive phase transitions and modify transport, this work lays out clear design rules for integrating $SrSi_2$, CoSi, and NbP into next-generation electronics, spintronics, and quantum technologies.

Chapter 7

Conclusion

The research explored in this thesis focused on the investigation of the ground-state electronic structures and topological properties of $SrSi_2$, CoSi, and NbP under the effects of tensile strain and external electric fields using advanced computational methods. It specifically examined how these external perturbations influence electronic band structures, Berry curvature, Fermi surfaces, and charge density distributions. Additionally, computational experiments were conducted to elucidate the mechanisms of QPTs in $SrSi_2$, using a suitably renormalized ground state within the graphene lattice. Major findings include the identification of distinct changes in band structures and Fermi surfaces induced by strain and electric fields, with key results for each material contributing to a deeper understanding of QPTs and their predictive modeling.

Prior work on $SrSi_2$, CoSi, and NbP underscores both foundational insights and practical directions in topological materials. First-principles studies and transport experiments on cubic $SrSi_2$ reveal a narrow, pressure- and alloy-tunable bandgap alongside predictions of double Weyl fermions, pointing to promising photogalvanic and thermoelectric applications. Investigations of chiral CoSi have mapped spin-3/2 Rarita-Schwinger and spin-1 triple fermions emerging from symmetry-protected band crossings, with tunneling spectroscopy confirming robust surface states and strain studies highlighting transitions beyond simple Weyl physics. In NbP, quantum oscillations and band-structure calculations expose coexisting hole pockets and tilted Weyl cones, accounting for its colossal, nonsaturating MR and direct signatures of the chiral anomaly. By combining fundamental theory and predictions with practical materials making and testing, research on this trio of materials boosts innovation in many areas. The diversity of exotic quasiparticles, tunable band topology via strain and defects, negative MR, and thermoelectric or low-power device prospects highlights rich opportunities. Next, tracking Berry curvature, band-crossing degeneracies, and Fermi arcs under bias and strain will reveal new phases and control mechanisms. Developing advanced mapping of phase boundaries and topology-linked phenomena sets the stage for the material-specific findings that follow.

For $SrSi_2$, the application of tensile strain and an external electric field revealed a rich interplay of topological and electronic transitions. Under a 12% tensile strain, a small gap of approximately 0.055 eV emerged along the Γ - X direction, breaking the symmetry responsible for the semimetallic state and driving the material toward reduced metallic conductivity. Similarly, the application of an external electric field demonstrated a progressive evolution in electronic structure. At a moderate field strength of $E = 0.51$ V/Å, the symmetry of the band structure began to break, initiating gap openings between Weyl nodes. At a higher field strength of $E = 1.29$ V/Å, a more pronounced gap of approximately 0.058 eV formed around the Fermi level, confirming the transition from a conductive to a predominantly insulating phase. For CoSi, the application of tensile strain and external electric fields revealed distinct and tunable modifications in its electronic properties. A 10% tensile strain induced a band gap of approximately 0.035 eV at the Γ point, highlighting significant changes in the electronic states and transport properties. However, no gap was observed at the R point, indicating the anisotropic response of the electronic structure to strain. Increasing the strain to 15% widened the gap at the Γ point to 0.11 eV, suggesting a strengthening of band splitting, while the R point remained robustly gapless. In contrast, under an external electric field, a gap of approximately 0.02 eV emerged at the R point for a moderate field strength of $E = 0.51$ V/Å, breaking symmetry selectively in this region while leaving the Γ point gapless. As the field increased to $E = 1.29$ V/Å, the gap at the R point widened significantly to about 0.065 eV. For NbP, the application of tensile strain and external electric fields revealed distinct modifications in its electronic properties, highlighting its tunability under external stimuli. Under a 4% tensile strain, a band gap of approximately 0.05 eV emerged in the $\Gamma - \Sigma$ direction, signifying a reduction in electrical conductivity due to fewer states at the Fermi level. Increasing the strain to 8% introduced further changes, with a gap of about 0.035 eV forming around the Fermi level. In contrast, a moderate external electric field of $E = 0.51$ V/Å caused only subtle changes in the band curvature, leaving the electronic structure largely intact. However, at a stronger field of $E = 1.29$ V/Å, a band gap of approximately 0.02 eV opened in the Γ - S direction, signaling a transition toward a new topological phase. These results demonstrate the sensitivity and tunability of the electronic structure of $SrSi_2$, CoSi, and NbP under both tensile strain and external electric fields, offering a pathway for designing systems with tailored electronic and topological properties. The computational experiments on $SrSi_2$, using the Quantum Lattice software, further elucidated the mechanisms of QPTs, revealing parallels with renormalized graphene system and demonstrating how SOC and magnetic interactions govern topological phase behavior.

The insights gained contribute to the broader understanding of topological materials under external perturbations. The observed changes in band structure, Berry curvature, and Fermi arcs upon the application of tensile strain and external electric fields align with theoretical predictions of topological phase transitions and provide computational evidence supporting these phenomena. By quantifying the effects of external conditions on key properties, this research bridges the gap between theoretical predictions and practical implications, enriching our understanding of the mechanisms underlying QPTs and advancing predictive models for emergent quantum phenomena.

The implications of this research extend across multiple fields, particularly in the development of next-generation technologies. The ability to manipulate electronic properties through external means such as electric fields and mechanical strain demonstrates potential for applications in semiconductor devices, spintronics, and sensors. These findings pave the way for designing materials with customized properties, enhancing the performance of electronic and photonic devices. Additionally, the study's methodologies, combining DFT, TB, and computational experiments, establish a robust framework for exploring the electronic and topological properties of other materials.

The study, while extensive, has its limitations. The computational models used rely on approximations that may not fully account for all quantum mechanical interactions. Moreover, computational constraints limit the system size and accuracy in simulations of larger-scale interactions. Future research should focus on refining these models to capture more complex interactions and extending the analysis to additional material systems. Exploring other external perturbations, such as magnetic fields, and extending the study to magnetic topological materials could further expand the scope of this work and its applicability in advanced materials science. Another possible outlook is to investigate the Berry curvature dipole (BCD) in $SrSi_2$, CoSi, and NbP. Because these materials lack inversion symmetry, they can exhibit a finite BCD that drives a second-order nonlinear Hall response even without time-reversal breaking. By extending our Wannier-based tight-binding models to compute the momentum-space derivative of the Berry curvature - namely the dipole tensor $D_{ab} = \sum_n \int_{\mathrm{BZ}} \frac{d\mathbf{k}}{(2\pi)^3} \frac{\partial \Omega_{n,b}(\mathbf{k})}{\partial k_a} f\left(\epsilon_n(\mathbf{k})\right)$, where $f\left(\epsilon_n(\mathbf{k})\right)$ is the Fermi-Dirac distribution, and $\Omega_{n,b}(\mathbf{k})$ is the b-th Cartesian component of the Berry curvature for band n at momentum $\mathbf{k}$[288] - we can predict how bias or strain shifts the Fermi level to enhance or invert D_{ab} . Experimentally, such tunable BCDs would manifest as bias-dependent nonlinear Hall voltages, offering a clear probe of Berry curvature - driven phenomena and a direct test of our theoretical framework.

Ultimately, this research underscores the critical role of computational studies in understanding material behavior under external influences. By revealing the intricate interplay between electronic structures and topological properties, this work provides a solid foundation for predicting and manipulating material characteristics at the quantum level. The findings align with ongoing efforts to develop computationally efficient models for material design, advancing both theoretical understanding and practical applications. These contributions are expected to inspire further research in condensed matter physics and material science, driving innovation in the development of technologies leveraging quantum phenomena.

References

[1] C.Q. Choi. A Beginner's Guide to Topological Materials. *IEEE Spectr.*, March 2023.

[2] S.M. Young and C.L. Kane. Dirac semimetals in two dimensions. *Phys. Rev. Lett.*, 115(12): 126803, 2015.

[3] B. Yan and C. Felser. Topological materials: Weyl semimetals. *Annu. Rev. Condens. Matter Phys.*, 8(1):337–354, March 2017. ISSN 1947-5462.

[4] S. Gupta and A. Saxena. *The Role of Topology in Materials*, volume 189. Springer, 2018.

[5] Topological Materials Explained. URL `https://www.nanowerk.com/nanotechnology-glossary/topological-materials.php`. [Online; accessed 4. Nov. 2024].

[6] Y. Qiu, K.N. Sanders, J. Dai, J.E. Medvedeva, W. Wu, P. Ghaemi, T. Vojta, and Y.S. Hor. Time reversal symmetry breaking superconductivity in topological materials, 2015.

[7] C.-Z. Chen, J.J. He, M.N. Ali, G.-H. Lee, K.C. Fong, and K.T. Law. Asymmetric josephson effect in inversion symmetry breaking topological materials. *Phys. Rev. B*, 98(7):075430, 2018.

[8] L. Du, T. Hasan, A. Castellanos-Gomez, G.-B. Liu, Y. Yao, C.N. Lau, and Z. Sun. Engineering symmetry breaking in 2D layered materials. *Nat. Rev. Phys.*, 3(3):193–206, 2021.

[9] A. Amaricci, J.C. Budich, M. Capone, B. Trauzettel, and G. Sangiovanni. First-order character and observable signatures of topological quantum phase transitions. *Phys. Rev. Lett.*, 114(18):185701, 2015.

[10] L.T. Hoa, H.V. Phuc, and L.T.T. Phuong. Electrical and thermal properties of strain-and electric field-induced topological crystalline insulators. *Chem. Phys.*, 536:110845, 2020.

[11] J.-Y. You, X.-J. Dong, B. Gu, and G. Su. Electric field induced topological phase transition and large enhancements of spin-orbit coupling and curie temperature in two-dimensional ferromagnetic semiconductors. *Phys. Rev. B*, 103(10):104403, 2021.

[12] P. Li, X. Yang, Q.-S. Jiang, Y.-Z. Wu, and W. Xun. Built-in electric field and strain tunable valley-related multiple topological phase transitions in $VSiXN_4$ (X = C, Si, Ge, Sn, Pb) monolayers. *Phys. Rev. Mater.*, 7(6):064002, 2023.

[13] B. Singh, G. Chang, T.-R. Chang, S.-M. Huang, C. Su, M.-C. Lin, H. Lin, and A. Bansil. Tunable double-Weyl fermion semimetal state in the $SrSi_2$ materials class. *Sci. Rep.*, 8(1): 10540, 2018.

[14] S.-M. Huang, S.-Y. Xu, I. Belopolski, C.-C. Lee, G. Chang, T.-R. Chang, B. Wang, N. Alidoust, G. Bian, M. Neupane, et al. New type of Weyl semimetal with quadratic double Weyl fermions. *Proc. Natl. Acad. Sci. U.S.A.*, 113(5):1180–1185, 2016.

[15] B. Xu, Z. Fang, M.-Á. Sánchez-Martínez, J. W. F. Venderbos, Z. Ni, T. Qiu, K. Manna, K. Wang, J. Paglione, C. Bernhard, et al. Optical signatures of multifold fermions in the chiral topological semimetal CoSi. *Proc. Natl. Acad. Sci. U.S.A.*, 117(44):27104–27110, 2020.

[16] F. Balduini, A. Molinari, L. Rocchino, V. Hasse, C. Felser, M. Sousa, C. Zota, H. Schmid, A.G. Grushin, and B. Gotsmann. Intrinsic negative magnetoresistance from the chiral anomaly of multifold fermions. *Nat. Commun.*, 15(1):6526, 2024.

[17] P. Sergelius, J. Gooth, S. Baßler, R. Zierold, C. Wiegand, A. Niemann, H. Reith, C. Shekhar, C. Felser, B. Yan, et al. Berry phase and band structure analysis of the Weyl semimetal NbP. *Sci. Rep.*, 6(1):33859, 2016.

[18] Sudesh, P. Kumar, P. Neha, T. Das, and S. Patnaik. Evidence for trivial Berry phase and absence of chiral anomaly in semimetal NbP. *Sci. Rep.*, 7(1):46062, 2017.

[19] M. Imai, T. Naka, H. Abe, and T. Furubayashi. Pressure effect on the electrical resistance of $SrSi_2$. *Intermetallics*, 15(7):956–960, 2007.

[20] Y. Imai and A. Watanabe. Calculation of electronic properties of $SrSi_2$ within the framework of a band theory. *Intermetallics*, 14(6):666–671, 2006.

[21] Z.-J. Chen and D.B. Tian. First-principles calculations of electronic, optical, and thermodynamic properties of $SrSi_2$. *J. Appl. Phys.*, 109(3), 2011.

[22] M. Imai, A. Sato, T. Kimura, and T. Aoyagi. Basic properties of Sr_1 - $xBaxSi_2$. *Thin Solid Films*, 519(24):8496–8500, 2011.

[23] C.S. Lue, C.N. Kuo, J.Y. Huang, H.L. Hsieh, H.Y. Liao, B. Ramachandran, and Y.K. Kuo. Enhancement of thermoelectric performance driven by Ge substitution in $SrSi_2$ alloy. *J. Phys. D: Appl. Phys.*, 46(31):315303, 2013.

[24] M.A. Rahman. First-principles calculations of elastic and optical properties of $SrSi_2$.

[25] S.K. Singh and M. Imai. Thermoelectric properties of cubic Ba-substituted strontium disilicide, Sr_1-xBaxSi2, with ba content above solid solubility limit. *Intermetallics*, 127:106981, 2020.

[26] D. Shiojiri, T. Iida, T. Kadono, M. Yamaguchi, T. Kodama, S. Yamaguchi, S. Takahashi, Y. Kayama, K. Hiratsuka, M. Imai, et al. Re-evaluation of the electronic structure and thermoelectric properties of narrow-gap semiconducting α-$SrSi_2$: A complementary experimental and first-principles hybrid-functional approach. *J. Appl. Phys.*, 129(11), 2021.

[27] B. Sadhukhan and T. Nag. Electronic structure and unconventional nonlinear response in double Weyl semimetal $SrSi_2$. *Phys. Rev. B*, 104(24):245122, 2021.

[28] M.-Y. Yao, J. Noky, K. Manna, N. Kumar, V.N. Strocov, C. Shekhar, Y. Sun, and C. Felser. Observation of chirality-neutral Fermi surface in Weyl semimetal candidate $SrSi_2$. *arXiv preprint arXiv:2106.11332*, 2021.

[29] S. Barua, B.R. Rano, I.M. Syed, and S.H. Naqib. An ab initio approach to understand the structural, thermophysical, electronic, and optical properties of binary silicide $SrSi_2$: A double Weyl semimetal. *Results Phys.*, 42:105973, 2022.

[30] A. Shende, S.K. Gupta, A. Kore, and P. Singh. Pressure driven Weyl-topological insulator phase transition in Weyl semimetal $SrSi_2$. *arXiv:2305.15980*, 2023.

[31] D.A. Pshenay-Severin, Y.V. Ivanov, A.A. Burkov, and A.T. Burkov. Band structure and unconventional electronic topology of CoSi. *J. Phys.: Condens. Matter*, 30(13):135501, 2018.

[32] D. Takane, Z. Wang, S. Souma, K. Nakayama, T. Nakamura, H. Oinuma, Y. Nakata, H. Iwasawa, C. Cacho, T. Kim, et al. Observation of chiral fermions with a large topological charge and associated Fermi-arc surface states in CoSi. *Phys. Rev. Lett.*, 122(7):076402, 2019.

[33] P. Tang, Q. Zhou, and S.-C. Zhang. Multiple types of topological fermions in transition metal silicides. *Phys. Rev. Lett.*, 119(20):206402, 2017.

[34] Q.-Q. Yuan, L. Zhou, Z.-C. Rao, S. Tian, W.-M. Zhao, C.-L. Xue, Y. Liu, T. Zhang, C.-Y. Tang, Z.-Q. Shi, et al. Quasiparticle interference evidence of the topological Fermi arc states in chiral fermionic semimetal CoSi. *Sci. Adv.*, 5(12):eaaw9485, 2019.

[35] P. Dutta and S.K. Pandey. Electronic correlation effect on nontrivial topological fermions in CoSi. *Eur. Phys. J. B*, 94:1–11, 2021.

[36] X. Xu, X. Wang, T.A. Cochran, D.S. Sanchez, G. Chang, I. Belopolski, G. Wang, Y. Liu, H.-J. Tien, X. Gui, et al. Crystal growth and quantum oscillations in the topological chiral semimetal CoSi. *Phys. Rev. B*, 100(4):045104, 2019.

[37] Y.V. Kudryavtsev, V.A. Oksenenko, Y.P. Lee, J.Y. Rhee, and Y.D. Kim. Optical properties of co silicides: Experiment and density functional theory. *J. Appl. Phys.*, 102(10), 2007.

[38] H. Wang, S. Xu, X.-Q. Lu, X.-Y. Wang, X.-Y. Zeng, J.-F. Lin, K. Liu, Z.-Y. Lu, and T.-L. Xia. de Haas–van Alphen quantum oscillations and electronic structure in the large-chern-number topological chiral semimetal CoSi. *Phys. Rev. B*, 102(11):115129, 2020.

[39] B.J. Wieder, B. Bradlyn, J. Cano, Z. Wang, M.G. Vergniory, L. Elcoro, A.A. Soluyanov, C. Felser, T. Neupert, N. Regnault, et al. Topological materials discovery from crystal symmetry. *Nat. Rev. Mater.*, 7(3):196–216, 2022.

[40] S. Nikolaev, D. Pshenay-Severin, Y. Ivanov, and A. Burkov. Effect of deformation on topological properties of cobalt monosilicide. *Crystals*, 11(2):143, 2021.

[41] G.H. Fecher, J. Kubler, and C. Felser. Chirality in the solid state: Chiral crystal structures in chiral and achiral space groups. *Materials*, 15(17):5812, 2022.

[42] Z.-C. Rao, H. Li, T.-T. Zhang, S.-J. Tian, C.-H. Li, B.-B. Fu, C.-Y. Tang, L. Wang, Z.-L. Li, W.-H. Fan, et al. New classes of chiral topological nodes with non-contractible surface Fermi arcs in CoSi. *arXiv:1901.03358*, 2019.

[43] Z. Rao, Q. Hu, S. Tian, Q. Qu, C. Chen, S. Gao, Z. Yuan, C. Tang, W. Fan, J. Huang, et al. Charge instability of topological Fermi arcs in chiral crystal CoSi. *Sci. Bull.*, 68(2):165–172, 2023.

[44] Z. Rao, H. Li, T. Zhang, S. Tian, C. Li, B. Fu, C. Tang, L. Wang, Z. Li, W. Fan, et al. Observation of unconventional chiral fermions with long Fermi arcs in CoSi. *Nature*, 567 (7749):496–499, 2019.

[45] Y. Sun, S.-C. Wu, and B. Yan. Topological surface states and Fermi arcs of the noncentrosymmetric Weyl semimetals TaAs, TaP, NbAs, and NbP. *Phys. Rev. B*, 92(11):115428, 2015.

[46] C.-C. Lee, S.-Y. Xu, S.-M. Huang, D.S. Sanchez, I. Belopolski, G. Chang, G. Bian, N. Alidoust, H. Zheng, M. Neupane, et al. Fermi surface interconnectivity and topology in Weyl fermion semimetals TaAs, TaP, NbAs, and NbP. *Phys. Rev. B*, 92(23):235104, 2015.

[47] C. Shekhar, A.K. Nayak, Y. Sun, M. Schmidt, M. Nicklas, I. Leermakers, U. Zeitler, Y. Skourski, J. Wosnitza, Z. Liu, et al. Extremely large magnetoresistance and ultrahigh mobility in the topological Weyl semimetal candidate NbP. *Nat. Phys.*, 11(8):645–649, 2015.

[48] R.D. Dos Reis, S.-C. Wu, Y. Sun, M.O. Ajeesh, C. Shekhar, M. Schmidt, C. Felser, B. Yan, and M. Nicklas. Pressure tuning the Fermi surface topology of the Weyl semimetal NbP. *Phys. Rev. B*, 93(20):205102, 2016.

[49] Z.-P. Guo, P.-C. Lu, T. Chen, J.-F. Wu, J. Sun, and D.-Y. Xing. High-pressure phases of Weyl semimetals NbP, NbAs, TaP, and TaAs. *Sci. China Phys. Mech. Astron.*, 61:1–9, 2018.

[50] Y. Zhou, P. Lu, Y. Du, X. Zhu, G. Zhang, R. Zhang, D. Shao, X. Chen, X. Wang, M. Tian, et al. Pressure-induced new topological Weyl semimetal phase in TaAs. *Phys. Rev. Lett.*, 117(14):146402, 2016.

[51] S.-C. Wu, Y. Sun, C. Felser, and B. Yan. Hidden type-II Weyl points in the Weyl semimetal NbP. *Phys. Rev. B*, 96(16):165113, 2017.

[52] A.C. Niemann, J. Gooth, S.-C. Wu, S. Baßler, P. Sergelius, R. Hühne, B. Rellinghaus, C. Shekhar, V. Süss, M. Schmidt, et al. Chiral magnetoresistance in the Weyl semimetal NbP. *Sci. Rep.*, 7(1):43394, 2017.

[53] Y.-L. Fu, H.-B. Sang, W. Cheng, and F.-S. Zhang. Topological properties after light ion irradiation on Weyl semimetal niobium phosphide from first principles. *Mater. Today Commun.*, 24:100939, 2020.

[54] B. Tilmann, A.K. Pandeya, G. Grinblat, L. de S. Menezes, Y. Li, C. Shekhar, C. Felser, S.S.P. Parkin, A. Bedoya-Pinto, and S.A. Maier. Ultrafast sub-100 fs all-optical modulation and efficient third-harmonic generation in Weyl semimetal niobium phosphide thin films. *Adv. Mater.*, 34(15):2106733, 2022.

[55] F. Balduini, L. Rocchino, A. Molinari, T. Paul, G. Mariani, V. Hasse, C. Felser, C. Zota, H. Schmid, and B. Gotsmann. Probing the shape of the Weyl Fermi surface of NbP using transverse electron focusing. *Phys. Rev. Lett.*, 133(9):096601, 2024.

[56] M. Nakahara. *Geometry, topology and physics*. CRC Press, 2018.

[57] D.J. Thouless, M. Kohmoto, M.P. Nightingale, and M. den Nijs. Quantized Hall conductance in a two-dimensional periodic potential. *Phys. Rev. Lett.*, 49(6):405, 1982.

[58] D. Xiao, M.-C. Chang, and Q. Niu. Berry phase effects on electronic properties. *Rev. Mod. Phys.*, 82(3):1959, 2010.

[59] M.Z. Hasan and C.L. Kane. Colloquium: Topological insulators. *Rev. Mod. Phys.*, 82(4): 3045, 2010.

[60] A. Altland and B. Simons. *Condensed Matter Field Theory*. Cambridge University Press, 2016.

[61] X.-L. Qi and S.-C. Zhang. Topological insulators and superconductors. *Rev. Mod. Phys.*, 83 (4):1057, 2011.

[62] A.H.C. Neto, F. Guinea, N.M.R. Peres, K.S. Novoselov, and A.K. Geim. The electronic properties of graphene. *Rev. Mod. Phys.*, 81(1):109–162, 2009.

[63] X. Wan, A.M. Turner, A. Vishwanath, and S.Y. Savrasov. Topological semimetal and Fermi-arc surface states in the electronic structure of pyrochlore iridates. *Phys. Rev. B*, 83(20): 205101, 2011.

[64] K.-Y. Yang, Y.-M. Lu, and Y. Ran. Quantum Hall effects in a Weyl semimetal: Possible application in pyrochlore iridates. *Phys. Rev. B*, 84(7):075129, 2011.

[65] A.A. Burkov and L. Balents. Weyl semimetal in a topological insulator multilayer. *Phys. Rev. Lett.*, 107(12):127205, 2011.

[66] G. Xu, H. Weng, Z. Wang, X. Dai, and Z. Fang. Chern semimetal and the quantized anomalous Hall effect in $HgCr_2Se_4$. *Phys. Rev. Lett.*, 107(18):186806, 2011.

[67] W. Witczak-Krempa and Y.B. Kim. Topological and magnetic phases of interacting electrons in the pyrochlore iridates. *Phys. Rev. B*, 85(4):045124, 2012.

[68] S.M. Young, S. Zaheer, J.C.Y. Teo, C.L. Kane, E.J. Mele, and A.M. Rappe. Dirac semimetal in three dimensions. *Phys. Rev. Lett.*, 108(14):140405, 2012.

[69] Z. Wang, Y. Sun, X.-Q. Chen, C. Franchini, G. Xu, H. Weng, X. Dai, and Z. Fang. Dirac semimetal and topological phase transitions in A_3Bi (A = Na, K, Rb). *Phys. Rev. B*, 85(19): 195320, 2012.

[70] Z. Wang, H. Weng, Q. Wu, X. Dai, and Z. Fang. Three-dimensional Dirac semimetal and quantum transport in Cd_3As_2. *Phys. Rev. B*, 88(12):125427, 2013.

[71] H. Weng, C. Fang, Z. Fang, B.A. Bernevig, and X. Dai. Weyl semimetal phase in noncentrosymmetric transition-metal monophosphides. *Phys. Rev. X*, 5(1):011029, 2015.

[72] S.-M. Huang, S.-Y. Xu, I. Belopolski, C.-C. Lee, G. Chang, B. Wang, N. Alidoust, G. Bian, M. Neupane, C. Zhang, et al. A Weyl fermion semimetal with surface Fermi arcs in the transition metal monopnictide TaAs class. *Nat. Commun.*, 6(1):1–6, 2015.

[73] T.O. Wehling, A.M. Black-Schaffer, and A.V. Balatsky. Dirac materials. *Adv. Phys.*, 63(1): 1–76, 2014.

[74] S.A. Yang, H. Pan, and F. Zhang. Dirac and Weyl superconductors in three dimensions. *Phys. Rev. Lett.*, 113(4):046401, 2016.

[75] A.A. Burkov. Weyl metals. *Annu. Rev. Condens. Matter Phys.*, 9:359–378, 2018.

[76] N.P. Armitage, E.J. Mele, and A. Vishwanath. Weyl and Dirac semimetals in three-dimensional solids. *Rev. Mod. Phys.*, 90(1):015001, 2018.

[77] Z.K. Liu, B. Zhou, Y. Zhang, Z.J. Wang, H.M. Weng, D. Prabhakaran, S.-K. Mo, Z.X. Shen, Z. Fang, X. Dai, et al. Discovery of a three-dimensional topological Dirac semimetal, Na_3Bi. *Science*, 343(6173):864–867, 2014.

[78] M. Neupane, S.-Y. Xu, R. Sankar, N. Alidoust, G. Bian, C. Liu, I. Belopolski, T.-R. Chang, H.-T. Jeng, H. Lin, et al. Observation of a three-dimensional topological Dirac semimetal phase in high-mobility Cd_3As_2. *Nat. Commun.*, 5(1):1–8, 2014.

[79] S.-Y. Xu, I. Belopolski, N. Alidoust, M. Neupane, G. Bian, C. Zhang, R. Sankar, G. Chang, Z. Yuan, C.-C. Lee, et al. Discovery of a Weyl fermion semimetal and topological Fermi arcs. *Science*, 349(6248):613–617, 2015.

[80] B.Q. Lv, H.M. Weng, B.B. Fu, X.P. Wang, H. Miao, J. Ma, P. Richard, X.C. Huang, L.X. Zhao, G.F. Chen, et al. Experimental discovery of Weyl semimetal TaAs. *Phys. Rev. X*, 5 (3):031013, 2015.

[81] L. Lu, Z. Wang, D. Ye, L. Ran, L. Fu, J.D. Joannopoulos, and M. Soljačić. Experimental observation of Weyl points. *Science*, 349(6248):622–624, 2015.

[82] P.A.M. Dirac. The quantum theory of the electron. *Proc. R. Soc. Lond., Ser. A*, 117(778): 610–624, 1928.

[83] D. McMahon. *Quantum field theory demystified*. McGraw Hill Professional, 2008.

[84] S. Murakami. Phase transition between the quantum spin Hall and insulator phases in 3D: Emergence of a topological gapless phase. *New J. Phys.*, 9(9):356, 2007.

[85] M.Z. Hasan. New topological phases of matter: Platform for emergent Dirac, Majorana and Weyl fermions, October 2016. URL `http://pmaweb.caltech.edu/PhysColl/abstracts/16-17/Hasan%20ppt%20slides/CalTech_Physcolloq_2016.pdf`. [Online; accessed 6. Jan. 2024].

[86] T.-R. Chang. Exploring fundamental physics in topological materials, March 2016. URL `https://phy08.phy.ntnu.edu.tw/~cms/download.php?id=119&kind=talk`. [Online; accessed 6. Jan. 2024].

[87] T.-R. Chang. Lecture 12 topological materials, August 2017. URL `http://www.phys.nthu.edu.tw/~spin/course/106F/Lecture%2012%20Topological%20materials%20-2.pdf`. [Online; accessed 6. Jan. 2024].

[88] H. Gao, J.W.F. Venderbos, Y. Kim, and A.M. Rappe. Topological semimetals from first principles. *Annu. Rev. Mater. Res.*, 49:153–183, 2019.

[89] S. Sachdev. Quantum phase transitions. *Phys. World*, 12(4):33, 1999.

[90] S. Sachdev. The landscape of the Hubbard model. In *String Theory And Its Applications: TASI 2010 From meV to the Planck Scale*, pages 559–620. World Scientific, 2012.

[91] L. Janssen. Lecture notes and exercises on quantum phase transitions, 2024. URL https://tu-dresden.de/mn/physik/itp/ressourcen/dateien/arbeitsgruppe-quantum-critical-matter/qpt-ss24/qpt-pokart.pdf?lang=en. [Online; accessed 2025-05-14].

[92] E. Christou, F. de Juan, and F. Krüger. Criticality of Dirac fermions in the presence of emergent gauge fields. *Phys. Rev. B*, 101(15):155121, 2020.

[93] H. Yerzhakov. Studies of quantum phase transitions in Dirac electron systems, 2021. URL https://era.library.ualberta.ca/items/ed20417c-112e-41f2-8d25-8eecf97d584d/view/f1ca0621-cc82-4fcf-a7c6-4540602e8b94/Yerzhakov_Hennadii_202101_PhD.pdf. [Online; accessed 2025-05-14].

[94] S.M. Young, S. Chowdhury, E.J. Walter, E.J. Mele, C.L. Kane, and A.M. Rappe. Theoretical investigation of the evolution of the topological phase of Bi_2Se_3 under mechanical strain. *Phys. Rev. B*, 84(8):085106, 2011.

[95] B. Sa, J. Zhou, Z. Sun, and R. Ahuja. Strain-induced topological insulating behavior in ternary chalcogenide $Ge_2Sb_2Te_5$. *EPL*, 97(2):27003, 2012.

[96] J.A. Steinberg, S.M. Young, S. Zaheer, C.L. Kane, E.J. Mele, and A.M. Rappe. Bulk Dirac points in distorted spinels. *Phys. Rev. Lett.*, 112(3):036403, 2014.

[97] J. Liu, Y. Xu, J. Wu, B.-L. Gu, S.B. Zhang, and W. Duan. Manipulating topological phase transition by strain. *Acta Crystallogr. Sect. C*, 70(2):118–122, 2014.

[98] F. Utermohlen. Tight-Binding model for graphene. URL https://cpb-us-w2.wpmucdn.com/u.osu.edu/dist/3/67057/files/2018/09/graphene_tight-binding_model-1ny95f1.pdf. [Online; accessed 28. Dec. 2023].

[99] H. Weyl et al. Electron and gravitation. *Z. Phys.*, 56:330–352, 1929.

[100] P.B. Pal. Dirac, Majorana, and Weyl fermions. *Am. J. Phys.*, 79(5):485–498, 2011.

[101] C.L. Kane. *Topological Insulators: Chapter 1. Topological Band Theory and the Z_2 Invariant*, volume 6. Elsevier Inc. Chapters, 2013.

[102] A. Messiah. *Quantum mechanics*. Courier Corporation, 2014.

[103] M.V. Berry. Quantal phase factors accompanying adiabatic changes. *Proc. R. Soc. Lond., Ser. A*, 392(1802):45–57, 1984.

[104] Kelvin–Stokes theorem, October 2023. URL `http://handwiki.org/wiki/Physics:Kelvin%E2%80%93Stokes_theorem#cite_note-iwahori-1`. [Online; accessed 11. Jan. 2024].

[105] J. Stewart. Calculus early transcendentals, 7th. *Belmont, CA: Brooks/Cole*, 2003.

[106] M. Nakahara. Geometry, topology and physics, graduate student series in physics. *Adam Hilger, Bristol etc*, 1990.

[107] B. Yan and C. Felser. Topological materials: Weyl semimetals. *Annu. Rev. Condens. Matter Phys.*, 8:337–354, 2017.

[108] A.K. Pariari. Atoms to topological electronic materials: A bedtime story for beginners. *Indian J. Phys.*, pages 1–22, 2020.

[109] K.S. Novoselov, A.K. Geim, S.V. Morozov, D. Jiang, Y. Zhang, S.V. Dubonos, I.V. Grigorieva, and A.A. Firsov. Electric field effect in atomically thin carbon films. *Science*, 306 (5696):666–669, 2004.

[110] K.S. Novoselov, V.I. Fal' ko, L. Colombo, P.R. Gellert, M.G. Schwab, and K. Kim. A roadmap for graphene. *Nature*, 490(7419):192–200, 2012.

[111] A.K. Geim and I.V. Grigorieva. Van der waals heterostructures. *Nature*, 499(7459):419–425, 2013.

[112] R. Peierls. Quelques propriétés typiques des corps solides. In *Ann. Inst. Henri Poincaré*, volume 5, pages 177–222, 1935.

[113] L.D. Landau and E.M. Lifshitz. *Course of theoretical physics*. Elsevier, 2013.

[114] N.D. Mermin. Crystalline order in two dimensions. *Phys. Rev.*, 176(1):250, 1968.

[115] J.W. Evans, P.A. Thiel, and M.C. Bartelt. Morphological evolution during epitaxial thin film growth: Formation of 2D islands and 3D mounds. *Surf. Sci. Rep.*, 61(1-2):1–128, 2006.

[116] N. Blomquist. Large-scale nanographite exfoliation for low-cost metal-free supercapacitors. 2016.

[117] A.K. Geim and K.S. Novoselov. The rise of graphene. *Nat. Mater.*, 6(3):183–191, 2007.

[118] N.M.R. Peres and R.M. Ribeiro. Focus on graphene. *New J. Phys.*, 11(9):095002, 2009.

[119] M.A. Poothanari, Y.B. Pottathara, and S. Thomas. Carbon nanostructures for electromagnetic shielding applications. In *Industrial applications of nanomaterials*, pages 205–223. Elsevier, 2019.

[120] A.W. Tsen, L. Brown, M.P. Levendorf, F. Ghahari, P.Y. Huang, R.W. Havener, C.S. Ruiz-Vargas, D.A. Muller, P. Kim, and J. Park. Tailoring electrical transport across grain boundaries in polycrystalline graphene. *Science*, 336(6085):1143–1146, 2012.

[121] Y.-M. Lin, A. Valdes-Garcia, S.-J. Han, D.B. Farmer, I. Meric, Y. Sun, Y. Wu, C. Dimitrakopoulos, A. Grill, P. Avouris, et al. Wafer-scale graphene integrated circuit. *Science*, 332(6035):1294–1297, 2011.

[122] S. Garaj, W. Hubbard, A. Reina, J. Kong, D. Branton, and J.A. Golovchenko. Graphene as a subnanometre trans-electrode membrane. *Nature*, 467(7312):190–193, 2010.

[123] D. Voiry, J. Yang, J. Kupferberg, R. Fullon, C. Lee, H.Y. Jeong, H.S. Shin, and M. Chhowalla. High-quality graphene via microwave reduction of solution-exfoliated graphene oxide. *Science*, 353(6306):1413–1416, 2016.

[124] M. Xu, D. Fujita, and N. Hanagata. Perspectives and challenges of emerging single-molecule DNA sequencing technologies. *Small*, 5(23):2638–2649, 2009.

[125] Y. Liu. Application of graphene oxide in water treatment. In *IOP Conf. Ser.: Earth Environ. Sci.*, volume 94, page 012060. IOP Publishing, 2017.

[126] S. Bae, H. Kim, Y. Lee, X. Xu, J.-S. Park, Y. Zheng, J. Balakrishnan, T. Lei, H. Ri Kim, Y.I. Song, et al. Roll-to-roll production of 30-inch graphene films for transparent electrodes. *Nat. Nanotechnol.*, 5(8):574–578, 2010.

[127] J.-C. Charlier, P.C. Eklund, J. Zhu, and A.C. Ferrari. Electron and phonon properties of graphene: Their relationship with carbon nanotubes. *Carbon nanotubes: advanced topics in the synthesis, structure, properties and applications*, pages 673–709, 2008.

[128] K.S. Novoselov, A.K. Geim, S.V. Morozov, D. Jiang, M.I. Katsnelson, I.V. Grigorieva, S.V. Dubonos, and A.A. Firsov. Two-dimensional gas of massless Dirac fermions in graphene. *Nature*, 438(7065):197–200, 2005.

[129] Y. Zhang, Y.-W. Tan, H.L. Stormer, and P. Kim. Experimental observation of the quantum Hall effect and Berry's phase in graphene. *Nature*, 438(7065):201–204, 2005.

[130] I. Bialynicki-Birula and Z. Bialynicka-Birula. Berry's phase in the relativistic theory of spinning particles. *Phys. Rev. D*, 35(8):2383, 1987.

[131] W. Hermann. Elektron und gravitation. I. *Z. Phys.*, 56(5-6):330–352, 1929.

[132] T. Ojanen. Helical Fermi arcs and surface states in time-reversal invariant Weyl semimetals. *Phys. Rev. B*, 87(24):245112, 2013.

[133] A.C. Potter, I. Kimchi, and A. Vishwanath. Quantum oscillations from surface Fermi arcs in Weyl and Dirac semimetals. *Nat. Commun.*, 5(1):5161, 2014.

[134] Z. Fang, N. Nagaosa, K.S. Takahashi, A. Asamitsu, R. Mathieu, T. Ogasawara, H. Yamada, M. Kawasaki, Y. Tokura, and K. Terakura. The anomalous Hall effect and magnetic monopoles in momentum space. *Science*, 302(5642):92–95, 2003.

[135] G.B. Halász and L. Balents. Time-reversal invariant realization of the Weyl semimetal phase. *Phys. Rev. B*, 85(3):035103, 2012.

[136] A.A. Zyuzin, S. Wu, and A.A. Burkov. Weyl semimetal with broken time reversal and inversion symmetries. *Phys. Rev. B*, 85(16):165110, 2012.

[137] A.A. Burkov. Topological semimetals. *Nat. Mater.*, 15(11):1145–1148, 2016.

[138] M. Vojta. Quantum phase transitions. *Rep. Prog. Phys.*, 66(12):2069, 2003.

[139] Transitions in focus, March 2008. ISSN 1745-2481. [Online; accessed 12. Jan. 2024].

[140] L. Bayha, M. Holten, R. Klemt, K. Subramanian, J. Bjerlin, S.M. Reimann, G.M. Bruun, P.M. Preiss, and S. Jochim. Observing the emergence of a quantum phase transition shell by shell. *Nature*, 587(7835):583–587, 2020.

[141] C. Li, G. Zhang, S. Lin, and Z. Song. Quantum phase transition induced by real-space topology. *Sci. Rep.*, 6(1):39416, 2016.

[142] S.H. Mousavi, A.B. Khanikaev, and Z. Wang. Topologically protected elastic waves in phononic metamaterials. *Nat. Commun.*, 6(1):8682, 2015.

[143] D. Leykam, K.Y. Bliokh, C. Huang, Y.D. Chong, and F. Nori. Edge modes, degeneracies, and topological numbers in non-hermitian systems. *Phys. Rev. Lett.*, 118(4):040401, 2017.

[144] A. Bansil, H. Lin, and T. Das. Colloquium: Topological band theory. *Rev. Mod. Phys.*, 88 (2):021004, 2016.

[145] B. Huckestein. Scaling theory of the integer quantum Hall effect. *Rev. Mod. Phys.*, 67(2): 357, 1995.

[146] X.-L. Qi, T.L. Hughes, and S.-C. Zhang. Topological field theory of time-reversal invariant insulators. *Phys. Rev. B*, 78(19):195424, 2008.

[147] J. Yu and C.-X. Liu. Piezoelectricity and topological quantum phase transitions in two-dimensional spin-orbit coupled crystals with time-reversal symmetry. *Nat. Commun.*, 11 (1):2290, 2020.

[148] S. Ganeshan, K. Sun, and S.D. Sarma. Topological zero-energy modes in gapless commensurate Aubry-André-Harper models. *Phys. Rev. Lett.*, 110(18):180403, 2013.

[149] H. Pan, Z. Li, C.-C. Liu, G. Zhu, Z. Qiao, and Y. Yao. Valley-polarized quantum anomalous Hall effect in silicene. *Phys. Rev. Lett.*, 112(10):106802, 2014.

[150] H.M. Eiding. Ab initio studies of molecules, 2014. URL `https://www.semanticscholar.org/paper/Ab-Initio-Studies-of-Molecules-Eiding/e79d1d33da4aa5a4f860e64cd47a3390901d9feb`. [Online; accessed 8. Nov. 2024].

[151] P. Giraud. Study of the electronic structure of hexagonal boron nitride on metals substrates, 2014. URL `https://nano-bio.ehu.es/files/paulgiraud_masterthesis.pdf`. [Online; accessed 8. Nov. 2024].

[152] O.A. Salawu. Calculations of phonons and phonon dispersion in LiFeP pnictide superconductor, 2017. URL `https://repository.aust.edu.ng/xmlui/bitstream/handle/`

123456789/532/SALAWU%20OMOTAYO%20AKANDE.pdf?sequence=1&isAllowed=y. [Online; accessed 8. Nov. 2024].

[153] R.G. Parr. Density functional theory of atoms and molecules. In *Horizons of quantum chemistry*, pages 5–15. Springer, 1980.

[154] W. Yang and R.G. Parr. Density functional theory of atoms and molecules. *New York*, page 25, 1989.

[155] F. Giustino. *Materials modelling using density functional theory: Properties and predictions*. Oxford University Press, 2014.

[156] V. Levitin. *Interatomic bonding in solids: Fundamentals, simulation, and applications*. John Wiley & Sons, 2014.

[157] T. Tsuneda. Density functional theory in quantum chemistry. 2014.

[158] C. Fiolhais, F. Nogueira, and M.A.L. Marques. *A primer in density functional theory*, volume 620. Springer Science & Business Media, 2003.

[159] D. Sholl and J.A. Steckel. *Density functional theory: A practical introduction*. John Wiley & Sons, 2011.

[160] M. Born and R. Oppenheimer. Zur quantentheorie der molekeln. *Ann. Phys.*, 389(20): 457–484, 1927.

[161] M. Born and K. Huang. *Dynamical theory of crystal lattices*. Clarendon Press, 1954.

[162] V. Fock. Näherungsmethode zur lösung des quantenmechanischen mehrkörperproblems. *Z. Phys.*, 61(1-2):126–148, 1930.

[163] J.C. Slater. Quantum theory of molecular and solids. *The self-Consistent Field for Molecular and solids*, 4, 1974.

[164] L. Piela. *Ideas of quantum chemistry*. Elsevier, 2006.

[165] P. Hohenberg and W. Kohn. Inhomogeneous electron gas. *Phys. Rev.*, 136(3B):B864, 1964.

[166] W. Kohn and L.J. Sham. Self-consistent equations including exchange and correlation effects. *Phys. Rev.*, 140(4A):A1133, 1965.

[167] D.J. Singh and L. Nordström. *Planewaves, Pseudopotentials, and the LAPW method*. Springer Science & Business Media, 2006.

[168] M.C. Payne, M.P. Teter, D.C. Allan, T.A. Arias, and J.D. Joannopoulos. Iterative minimization techniques for ab initio total-energy calculations: Molecular dynamics and conjugate gradients. *Rev. Mod. Phys.*, 64(4):1045, 1992.

[169] K. Capelle. A bird's-eye view of density-functional theory. *Brazilian J. Phys.*, 36:1318–1343, 2006.

[170] N. Zettili. Quantum mechanics: Concepts and applications, 2003. URL `https://books.google.com.gh/books?id=6jXlpJCSz98C&printsec=copyright&redir_esc=y#v=onepage&q&f=false`. [Online; accessed 8. Nov. 2024].

[171] M. Levy. Universal variational functionals of electron densities, first-order density matrices, and natural spin-orbitals and solution of the v-representability problem. *Proc. Natl. Acad. Sci. U.S.A.*, 76(12):6062–6065, 1979.

[172] M. Levy. Electron densities in search of hamiltonians. *Phys. Rev. A*, 26(3):1200, 1982.

[173] E.H. Lieb. Density functionals for coulomb systems. In *Inequalities*, pages 269–303. Springer, 2002.

[174] J.P. Perdew and Y. Wang. Pair-distribution function and its coupling-constant average for the spin-polarized electron gas. *Phys. Rev. B*, 46(20):12947, 1992.

[175] J.P. Perdew, K. Burke, and M. Ernzerhof. Generalized gradient approximation made simple. *Phys. Rev. Lett.*, 77(18):3865, 1996.

[176] C. Kittel, P. McEuen, and P. McEuen. *Introduction to Solid State Physics*, volume 8. Wiley, New York, 1996.

[177] N.W. Ashcroft, N.D. Mermin, et al. *Solid state physics*, volume 2005. Holt, Rinehart and Winston, New York; London, 1976.

[178] F. Bloch. Über die quantenmechanik der elektronen in kristallgittern. *Z. Phys.*, 52(7-8):555–600, 1929.

[179] C. Friedrich. Tetrahedron integration method for strongly varying functions: Application to the G T self-energy. *Phys. Rev. B*, 100(7):075142, 2019.

[180] P. Lambin and J.-P. Vigneron. Computation of crystal green's functions in the complex-energy plane with the use of the analytical tetrahedron method. *Phys. Rev. B*, 29(6):3430, 1984.

[181] H.J. Monkhorst and J.D. Pack. Special points for brillouin-zone integrations. *Phys. Rev. B*, 13(12):5188, 1976.

[182] D.R. Hamann, M. Schlüter, and C. Chiang. Norm-conserving pseudopotentials. *Phys. Rev. Lett.*, 43(20):1494, 1979.

[183] G.B. Bachelet, D.R. Hamann, and M. Schlüter. Pseudopotentials that work: From H to Pu. *Phys. Rev. B*, 26(8):4199, 1982.

[184] D. Vanderbilt. Soft self-consistent pseudopotentials in a generalized eigenvalue formalism. *Phys. Rev. B*, 41(11):7892, 1990.

[185] S.V. Ramanujam. *Band Structure of Graphene Using Empirical Pseudopotentials*. PhD thesis, Arizona State University, 2015.

[186] P.E. Blochl. Projector augmented-wave method. *Phys. Rev. B*, 50(24):17953, 1994.

[187] X. Gonze and F. Finocchi. Pseudopotentials plane waves–projector augmented waves: A primer. *Phys. Scr.*, 2004(T109):40, 2004.

[188] G. Kresse and D. Joubert. From ultrasoft pseudopotentials to the projector augmented-wave method. *Phys. Rev. B*, 59(3):1758, 1999.

[189] N.A.W. Holzwarth, G.E. Matthews, R.B. Dunning, A.R. Tackett, and Y. Zeng. Comparison of the projector augmented-wave, pseudopotential, and linearized augmented-plane-wave formalisms for density-functional calculations of solids. *Phys. Rev. B*, 55(4):2005, 1997.

[190] M.-S. Dupuy. Projector augmented-wave method: An analysis in a one-dimensional setting. *arXiv preprint arXiv:1712.04685*, 2017.

[191] C. Rostgaard. The projector augmented-wave method. *arXiv preprint arXiv:0910.1921*, 2009.

[192] P.E. Blöchl. Generalized separable potentials for electronic-structure calculations. *Phys. Rev. B*, 41(8):5414, 1990.

[193] C.G. Van de Walle and P.E. Blöchl. First-principles calculations of hyperfine parameters. *Phys. Rev. B*, 47(8):4244, 1993.

[194] P. Margl, K. Schwarz, and P.E. Blöchl. Finite-temperature characterization of ferrocene from first-principles molecular dynamics simulations. *J. Chem. Phys.*, 100(11):8194–8203, 1994.

[195] J. Sarnthein, K. Schwarz, and P.E. Blöchl. Ab initio molecular-dynamics study of diffusion and defects in solid Li_3N. *Phys. Rev. B*, 53(14):9084, 1996.

[196] P.L. Taylor and O. Heinonen. *A quantum approach to condensed matter physics*. Cambridge University Press, 2002.

[197] C. Herring. A new method for calculating wave functions in crystals. *Phys. Rev.*, 57(12): 1169, 1940.

[198] L.L. Foldy and S.A. Wouthuysen. On the Dirac theory of spin-1/2 particles and its non-relativistic limit. *Phys. Rev.*, 78(1):29, 1950.

[199] L.L. Foldy. The electromagnetic properties of Dirac particles. *Phys. Rev.*, 87(5):688, 1952.

[200] S. Weinberg. *Lectures on quantum mechanics*. Cambridge University Press, 2015.

[201] M.W. Wu, J.H. Jiang, and M.Q. Weng. Spin dynamics in semiconductors. *Phys. Rep.*, 493 (2-4):61–236, 2010.

[202] N. Nagaosa, J. Sinova, S. Onoda, A.H. MacDonald, and N.P. Ong. Anomalous Hall effect. *Rev. Mod. Phys.*, 82(2):1539, 2010.

[203] P. Ehrenfest. Bemerkung über die angenäherte gültigkeit der klassischen mechanik innerhalb der quantenmechanik. *Z. Phys.*, 45(7-8):455–457, 1927.

[204] J.C. Slater and G.F. Koster. Simplified LCAO method for the periodic potential problem. *Phys. Rev.*, 94(6):1498, 1954.

[205] J.L. Fry, N.E. Brener, F.C. Case, and N.L. Desai. Two-center approximation in the quantum theory of solids. *Phys. Rev. B*, 15(12):5811, 1977.

[206] Y.F. Suprunenko, E.V. Gorbar, V.M. Loktev, and S.G. Sharapov. Effect of next-nearest-neighbor hopping on the electronic properties of graphene. *Low Temp. Phys.*, 34(10):812–817, 2008.

[207] A. Armano and S. Agnello. Two-dimensional carbon: A review of synthesis methods, and electronic, optical, and vibrational properties of single-layer graphene. *C*, 5(4):67, 2019.

[208] S.J. Chae, F. Güneş, K.K. Kim, E.S. Kim, G.H. Han, S.M. Kim, H.-J. Shin, S.-M. Yoon, J.-Y. Choi, M.H. Park, et al. Synthesis of large-area graphene layers on poly-nickel substrate by chemical vapor deposition: Wrinkle formation. *Adv. Mater.*, 21(22):2328–2333, 2009.

[209] S.S. Dindorkar, A.S. Kurade, and A.H. Shaikh. Magical moiré patterns in twisted bilayer graphene: A review on recent advances in graphene twistronics. *Chem. Phys. Impact*, page 100325, 2023.

[210] G.H. Wannier. The structure of electronic excitation levels in insulating crystals. *Phys. Rev.*, 52(3):191–197, 1937.

[211] W. Kohn. Analytic properties of bloch waves and wannier functions. *Phys. Rev.*, 115(4): 809–821, 1959.

[212] N. Marzari and D. Vanderbilt. Maximally localized generalized wannier functions for composite energy bands. *Phys. Rev. B*, 56(20):12847–12865, 1997.

[213] D. Vanderbilt. *Berry Phases in Electronic Structure Theory: Electric Polarization, Orbital Magnetization and Topological Insulators*. Cambridge University Press, 2018.

[214] D.J. Thouless et al. Quantized Hall conductance in a two-dimensional periodic potential. *Phys. Rev. Lett.*, 49(6):405–408, 1982.

[215] A.A. Soluyanov and D. Vanderbilt. Computing topological invariants without inversion symmetry. *Phys. Rev. B*, 83(23):235401, 2011.

[216] P. Giannozzi et al. QUANTUM ESPRESSO: A modular and open-source software project for quantum simulations of materials. *J. Phys.: Condens. Matter*, 21(39):395502, 2009.

[217] R.M. Martin. *Electronic Structure: Basic Theory and Practical Methods*. Cambridge University Press, 2004.

[218] G. Kresse and J. Furthmueller. Efficiency of ab-initio total energy calculations for metals and semiconductors using a plane-wave basis set. *Comput. Mater. Sci.*, 6(1):15–50, 1996.

[219] G. Kresse and J. Furthmueller. Efficient iterative schemes for ab initio total-energy calculations using a plane-wave basis set. *Phys. Rev. B*, 54(16):11169, 1996.

[220] P. Giannozzi et al. Advanced capabilities for materials modelling with Quantum ESPRESSO. *J. Phys.: Condens. Matter*, 29(46):465901, 2017.

[221] P. Giannozzi et al. Quantum ESPRESSO toward the exascale. *J. Chem. Phys.*, 152(15): 154105, 2020.

[222] H.J. Monkhorst and J.D. Pack. Special points for brillouin-zone integrations. *Phys. Rev. B*, 13:5188–5192, 1976. doi: 10.1103/PhysRevB.13.5188.

[223] M.P. Methfessel and A.T. Paxton. High-precision sampling for brillouin-zone integration in metals. *Phys. Rev. B*, 40(6):3616, 1989.

[224] N.W. Ashcroft and N.D. Mermin. *Solid State Physics*. Holt, Rinehart and Winston, 1976.

[225] P. Kratzer and J. Neugebauer. The basics of electronic structure theory for periodic systems. *Front. Chem.*, 7:106, 2019.

[226] K. Choudhary and F. Tavazza. Convergence and machine learning predictions of Monkhorst-Pack k-points and plane-wave cut-off in high-throughput DFT calculations. *Comput. Mater. Sci.*, 161:300–308, 2019.

[227] C. Kittel. *Introduction to Solid State Physics*. John Wiley & Sons, 8 edition, 2004.

[228] Free electron model, 10 2004. URL https://en.wikipedia.org/wiki/Free_electron_model. [Online; accessed 2025-05-14].

[229] Nearly free electron model | Condensed Matter Physics class notes. URL https://library.fiveable.me/condensed-matter-physics/unit-2/free-electron-model/study-guide/tUjdGCkARCDkvE4P. [Online; accessed 2025-05-14].

[230] Van Hove singularity, 1 2006. URL https://en.wikipedia.org/wiki/Van_Hove_singularity. [Online; accessed 2025-05-14].

[231] J.P. Perdew and M. Levy. Physical content of the exact Kohn-Sham orbital energies: band gaps and derivative discontinuities. *Phys. Rev. Lett.*, 51(20):1884, 1983.

[232] Electronic band structure, 6 2004. URL https://en.wikipedia.org/wiki/Electronic_band_structure. [Online; accessed 2025-05-14].

[233] J. Moore. Berry phases of Bloch electrons, December 2009. URL https://www.ens-lyon.fr/CBP/topiso/Talks_Online_files/Moore_Lyon2009.pdf. [Online; accessed 10. Nov. 2024].

[234] F.P. Sabino, X.G. Zhao, G.M. Dalpian, and A. Zunger. Impact of symmetry breaking and spin-orbit coupling on the band gap of halide perovskites. *Phys. Rev. B*, 110(3):035160, 2024.

[235] R.P. Feynman. Forces in molecules. *Physical review*, 56(4):340, 1939.

[236] K. Kunc and R. Resta. External fields in the self-consistent theory of electronic states: A new method for direct evaluation of macroscopic and microscopic dielectric response. *Phys. Rev. Lett.*, 51(8):686, 1983.

[237] P. Umari and A. Pasquarello. Density functional theory with finite electric field. *Int. J. Quantum Chem.*, 101(6):666–670, 2005.

[238] J. Tóbik and A. Dal Corso. Electric fields with ultrasoft pseudo-potentials: Applications to benzene and anthracene. *J. Chem. Phys.*, 120(21):9934–9941, 2004.

[239] K. Kunc and R. Resta. External electric field in the self-consistent theory of electronic structure. *Phys. Rev. B*, 28(12):6756–6764, 1983.

[240] A.A. Mostofi, J.R. Yates, G. Pizzi, Y.-S. Lee, I. Souza, D. Vanderbilt, and N. Marzari. An updated version of wannier90: A tool for obtaining maximally-localised wannier functions. *Comput. Phys. Commun.*, 185(8):2309–2310, 2014.

[241] Q. Wu, S.-N. Zhang, H.-F. Song, M. Troyer, and A.A. Soluyanov. Wanniertools: An open-source software package for novel topological materials. *Comput. Phys. Commun.*, 224: 405–416, 2018.

[242] J. Lado. Quantum-lattice: User-friendly open-source software to design and solve tight-binding models, addressing electronic properties, topology, interactions, non-collinear magnetism, and unconventional superconductivity, among others. URL https://github.com/joselado/quantum-lattice. (Accessed on 12/31/2023).

[243] J.L. Villanueva. *Topological electronic phases in graphene*. PhD thesis, Universidade de Santiago de Compostela, 2016.

[244] C.L. Kane and E.J. Mele. Z_2 topological order and the quantum spin Hall effect. *Phys. Rev. Lett.*, 95(14):146802, 2005.

[245] C.L. Kane and E.J. Mele. Quantum spin Hall effect in graphene. *Phys. Rev. Lett.*, 95(22): 226801, 2005.

[246] X.-G. Wen. *Quantum field theory of many-body systems: From the origin of sound to an origin of light and electrons*. OUP Oxford, 2004.

[247] B.A. Bernevig. *Topological insulators and topological superconductors*. Princeton University Press, 2013.

[248] G.E. Pringle. The structure of $SrSi_2$: A crystal of class o (432). *Acta Crystallogr. Sect. B*, 28(8):2326–2328, 1972.

[249] J. Evers, G. Oehlinger, and A. Weiss. Solid solutions M_1-xSrxSi$_2$ (M = Ca, Eu, Ba) and BaSi$_2$ - yGey with SrSi$_2$ - type structure. *J. Less-Common Met.*, 69(2):399–402, 1980.

[250] P.I. Kripyakevich and E.I. Gladyshevskii. The crystal structure of strontium disilicide. *Crystallography*, 11:818, 1966.

[251] J. Evers. Transformation of three-dimensional three-connected silicon nets in $SrSi_2$. *J. Solid State Chem.*, 24(2):199–207, 1978.

[252] C.S. Boland, Y. Sun, and D.G. Papageorgiou. Bandgap engineering of 2D materials toward high-performing straintronics. *Nano Lett.*, 24(41):12722–12732, 2024.

[253] C.K. Maiti and T.K. Maiti. *Strain-engineered mosfets*. CRC press, 2012.

[254] S. Sharma and A.S. Banerjee. Strain induced topological phase transitions in split and line graphs of bipartite lattices featuring flat bands. *arXiv:2501.11783*, 2025.

[255] M.Z. Hasan and J.E. Moore. Three-dimensional topological insulators. *Annu. Rev. Condens. Matter Phys.*, 2(1):55–78, 2011.

[256] A.-Q. Wang, X.-G. Ye, D.-P. Yu, and Z.-M. Liao. Topological semimetal nanostructures: From properties to topotronics. *ACS Nano*, 14(4):3755–3778, 2020.

[257] R.K. Goyal, S. Maharaj, P. Kumar, and M. Chandrasekhar. Exploring quantum materials and applications: A review. *J. Mater. Sci.: Mater. Electron.*, 20(1):4, 2025.

[258] Topological insulator, 7 2009. URL https://en.wikipedia.org/wiki/Topological_insulator. [Online; accessed 2025-05-15].

[259] A. Hirohata, K. Yamada, Y. Nakatani, I.-L. Prejbeanu, B. Diény, P. Pirro, and B. Hillebrands. Review on spintronics: Principles and device applications. *J. Magn. Magn. Mater.*, 509: 166711, 2020.

[260] M.Y. Toriyama and G.J. Snyder. Topological insulators for thermoelectrics: A perspective from beneath the surface. *The Innovation*, 2025.

[261] M.Y. Toriyama and G.J. Snyder. Are topological insulators promising thermoelectrics? *Mater. Horiz.*, 11(5):1188–1198, 2024.

[262] X. Ni, S. Yves, A. Krasnok, and A. Alù. Topological metamaterials. *Chem. Rev.*, 123(12): 7585–7654, 2023.

[263] X.-L. Tang, X.-Q. Zhang, T.-X. Ma, M. Kim, and Y.-S. Wang. Topological rainbow trapping and broadband piezoelectric energy harvesting of acoustic waves in gradient phononic crystals with coupled interfaces. *Appl. Acoust.*, 233:110630, 2025.

[264] G. Lee, D. Lee, J. Park, Y. Jang, M. Kim, and J. Rho. Piezoelectric energy harvesting using mechanical metamaterials and phononic crystals. *Commun. Phys.*, 5(1):94, 2022.

[265] J. Yang, L. Wei, Y. Li, L. Chen, W. Niu, S. Wang, F. Li, P. Liu, S. Zhou, and Y. Pu. Electric field control of nonlinear Hall effect in Weyl semimetal TaIrTe_4. *arXiv:2502.05960*, 2025.

[266] A. Ferraris. *Electric field control of topological Weyl semimetals*. PhD thesis, Politecnico di Torino, 2021.

[267] M. Ezawa. Pseudospin-3/2 fermions, type-II Weyl semimetals, and critical Weyl semimetals in tricolor cubic lattices. *Phys. Rev. B*, 94(19):195205, 2016.

[268] L. Liang and Y. Yu. Semimetal with both Rarita-Schwinger-Weyl and Weyl excitations. *Phys. Rev. B*, 93(4):045113, 2016.

[269] R.M. Geilhufe, S.S. Borysov, A. Bouhon, and A.V. Balatsky. Data mining for three-dimensional organic Dirac materials: Focus on space group 19. *Sci. Rep.*, 7(1):7298, 2017.

[270] C. Fang, M.J. Gilbert, X. Dai, and B.A. Bernevig. Multi-Weyl topological semimetals stabilized by point group symmetry. *Phys. Rev. Lett.*, 108(26):266802, 2012.

[271] Y. Xu and L.-M. Duan. Type-II Weyl points in three-dimensional cold-atom optical lattices. *Phys. Rev. A*, 94(5):053619, 2016.

[272] H.B. Nielsen and M. Ninomiya. No-go theorem for regularizing chiral fermions. Technical report, Science Research Council, 1981.

[273] S. Gupta. Topological materials: The future of quantum computing and electronics, 4 2025. URL `https://www.studyiq.com/articles/topological-materials/`. [Online; accessed 2025-05-30].

[274] J.M. Kim, M.F. Haque, E.Y. Hsieh, S.M. Nahid, I. Zarin, K.-Y. Jeong, J.-P. So, H.-G. Park, and S.W. Nam. Strain engineering of low-dimensional materials for emerging quantum phenomena and functionalities. *Adv. Mater.*, 35(27):2107362, 2023.

[275] Q. Liu, X. Zhang, L.B. Abdalla, A. Fazzio, and A. Zunger. Switching a normal insulator into a topological insulator via electric field with application to phosphorene. *Nano Lett.*, 15(2):1222–1228, 2015.

[276] D. Grassano, O. Pulci, A. Mosca Conte, and F. Bechstedt. Validity of Weyl fermion picture for transition metals monopnictides TaAs, TaP, NbAs, and NbP from ab initio studies. *Sci. Rep.*, 8(1):3534, 2018.

[277] J. Duan, S. Hu, P. Wang, D. Zhang, and Y. Jiang. Topological quantum materials for spintronics. *MetalMat*, 1(2):e24, 2024.

[278] G. Qiu, H.-Y. Yang, S.K. Chong, Y. Cheng, L. Tai, and K.L. Wang. Manipulating topological phases in magnetic topological insulators. *Nanomaterials*, 13(19):2655, 2023.

[279] B.-C. Lin, S. Wang, A.-Q. Wang, Y. Li, R.-R. Li, K. Xia, D. Yu, and Z.-M. Liao. Electric control of Fermi arc spin transport in individual topological semimetal nanowires. *Phys. Rev. Lett.*, 124(11):116802, 2020.

[280] Strain engineering, 1 2007. URL `https://en.wikipedia.org/wiki/Strain_engineering`. [Online; accessed 2025-05-14].

[281] M. Xu, J. T. Paci, J. Oswald, and T. Belytschko. A constitutive equation for graphene based on density functional theory. *Int. J. Solids Struct.*, 49(18):2582–2589, 2012.

[282] N. D. Drummond, V. Zolyomi, and V. I. Fal'Ko. Electrically tunable band gap in silicene. *Phys. Rev. B*, 85(7):075423, 2012.

[283] Ionization energies of the elements (data page), 3 2005. URL https://en.wikipedia.org/wiki/Ionization_energies_of_the_elements_%28data_page%29. [Online; accessed 2025-05-14].

[284] M.-Y. Yao, J. Noky, Q.-G. Mu, K. Manna, N. Kumar, V.N. Strocov, C. Shekhar, S. Medvedev, Y. Sun, and C. Felser. High pressure induced superconductivity and chirality-neutral Fermi surface in $SrSi_2$. *Physical Review B*, 110(22):224514, 2024.

[285] K. Manna, N. Kumar, S. Chattopadhyay, J. Noky, M. Yao, J. Park, T. Förster, M. Uhlarz, T. Chakraborty, B.V. Schwarze, et al. Three-dimensional quasiquantized Hall insulator phase in $SrSi_2$. *Phys. Rev. B*, 106(4):L041113, 2022.

[286] S. Souma, Z. Wang, H. Kotaka, T. Sato, K. Nakayama, Y. Tanaka, H. Kimizuka, T. Takahashi, K. Yamauchi, T. Oguchi, et al. Direct observation of nonequivalent Fermi-arc states of opposite surfaces in the noncentrosymmetric Weyl semimetal NbP. *Phys. Rev. B*, 93(16): 161112, 2016.

[287] H. Zheng, S.-Y. Xu, G. Bian, C. Guo, G. Chang, D.S. Sanchez, I. Belopolski, C.-C. Lee, S.-M. Huang, X. Zhang, et al. Atomic-scale visualization of quantum interference on a Weyl semimetal surface by scanning tunneling microscopy. *ACS Nano*, 10(1):1378–1385, 2016.

[288] H. Pang, G. Jin, and L. He. Tuning of Berry-curvature dipole in TaAs slabs: An effective route to enhance the nonlinear Hall response. *Phys. Rev. Mater.*, 8(4):043403, 2024.